Dedicated to Research in **Mechanical Engineering and Its Applications**

European Mechanical Science

Editor in Chief
Mustafa Ozcanli

ISSN: 2587-1110

December **2024**
Volume **8** · Issue **4**

Exploring Innovations in
Mechanical Science and Engineering

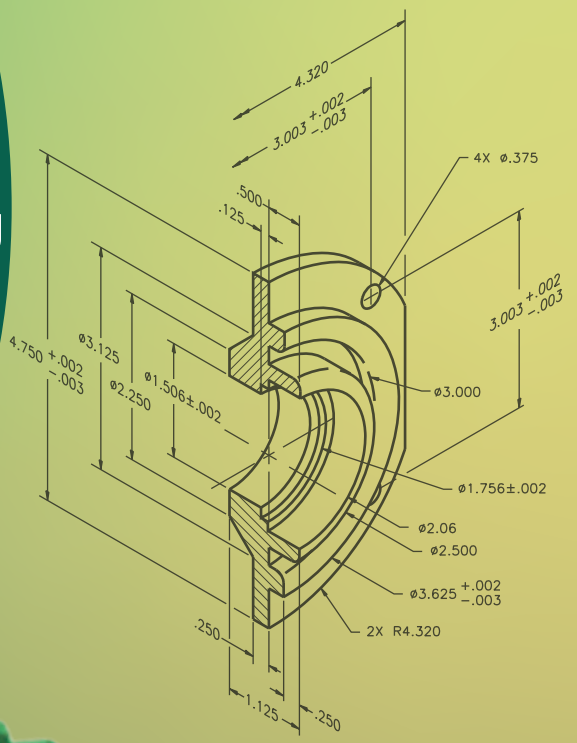

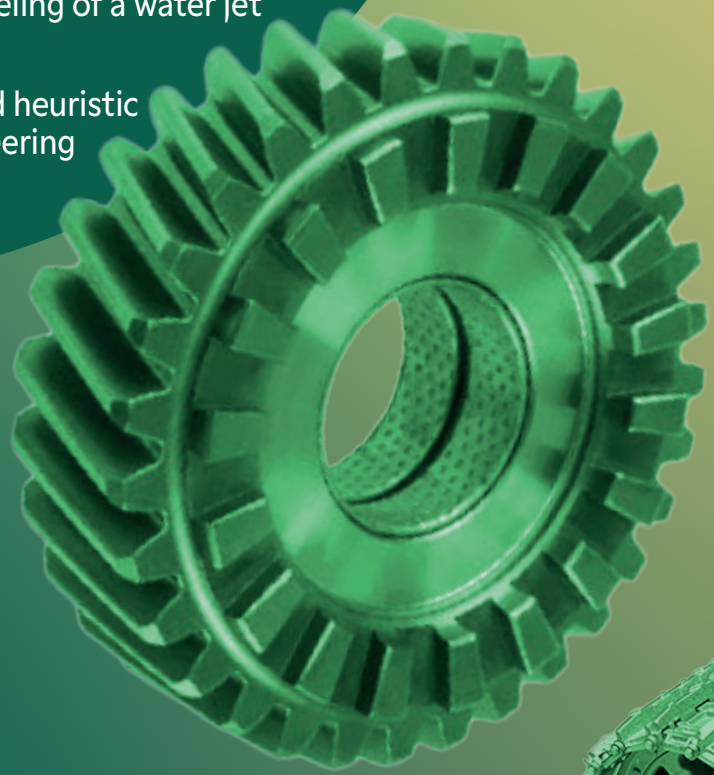

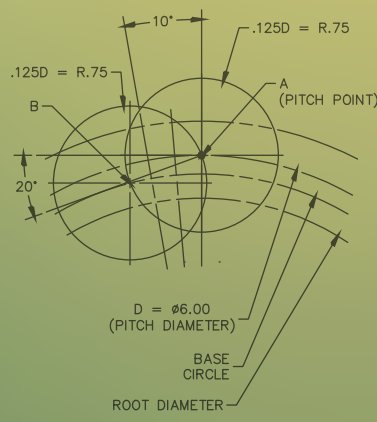

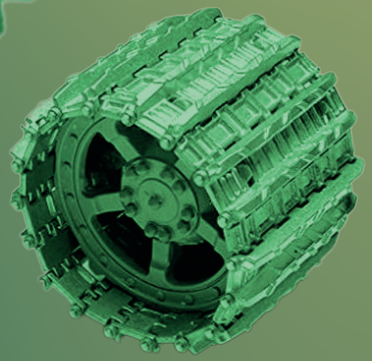

An International Journal Covering Advances in
Mechanical Engineering and Applied Sciences

97726367450090

OPEN ACCESS

EUROPEAN MECHANICAL SCIENCE
e-ISSN: 2587-1110

European Mechanical Science 2024, 8(4)

Editor in Chief

Editors

Technical Editors

Language Editorial Board

Indexed / Abstracted in:

TR-Dizin, EBSCO, Scilit, Index Copernicus, The Open Ukrainian Citation Index (OUCI), Paperity Open Science, Asian Science Citation Index

Aims and Scopes

European Mechanical Science (EMS) is an international, peer-reviewed journal that publishes full-length original research papers, and reviews related to all areas of Mechanical Engineering such as Solid Mechanics, Material, Automotive, Fluid Mechanics, Thermal, Engine and Power, Dynamics and Control, Robotics and Mechatronics, Transportation, Computational Mechanics, Design, Systems, Manufacturing, Biomedical, Process, and Aerospace published four times a year in March, June, September, and December. This is an open-access journal which means that all content is freely available without charge to the user or author's institution. EMS is a quarterly published journal operating an online submission and peer review system. It allows authors to submit articles online and track their progress via its web interface. This journal is a peer-reviewed open-access engineering journal published four times a year.

For inquiries and communication, please contact us at: emsjournal01@gmail.com

https://dergipark.org.tr/ems

Contents

– *Research Articles*

EUROPEAN MECHANICAL SCIENCE

Research Article

e-ISSN: 2587-1110

The effect of ageing on the tensile properties of greenhouses nets

Ines Tucman[1*], **Ana Pilipović**[1]

[1]University of Zagreb Faculty of Mechanical Engineering and Naval Architecture, Department of Technology, Chair for Polymer Processing, Ivana Lucica 5, 10000 Zagreb, Croatia

Abstract: Providing good protection for cultivated plants against weather conditions like hail, frost, and wind, as well as from animals like birds, insects, and wild boars, is important for enhancing plant growth and improving both production and quality. For this reason, plants are grown in covering systems (greenhouses) where covering materials play a major role. This paper analyses the effect of ageing on tensile properties of nets and the advantages of using nets as a covering part in greenhouses and explores their positive impact on plant protection and growth. The nets that were tested are made from different polymer materials, mostly polypropylene (PP) and high-density polyethylene (HDPE). The result shows that in the case of PP net (PA105N) and HDPE wind protection net (ZO95) the tensile strength decreases by 28% - 35% respectively after ageing. The elongation in most cases increases even up to 70% (net 70%). Additionally, there is a noticeable change in the shape of the nets after exposure to the atmospheric environment.

Keywords: ageing; nets; greenhouse; polymer materials; tensile properties.

1. Introduction

Greenhouses are fundamental to the advancement of facility agriculture and are crucial for achieving high-quality, efficient crop production. Accurate control of the greenhouse microclimate is a key technology for maximizing crop yield, quality, and efficiency. [1] There are different types of greenhouses with all-frame structures, including gable-shaped, tunnel-shaped/quonset-shaped, and gothic arch-shaped. Greenhouses that are quadrant-shaped, hapel-shaped, semi-gable-shaped, and semi-tunnelshaped usually have transparent apricus roofs, opaque shady roofs, and solid walls. The latter four types are hybrid load-bearing structures that encompass both frames and walls. Of the various shapes, gable-shaped and tunnel-shaped greenhouses are the most commonly used for growing crops. [2] Currently, the greenhouses that once used glass covering are increasingly started using plastic materials. The world consumption of plastics in agriculture amounts yearly to 6.5 million tons. This shift is primarily due to the cost-effectiveness, lightweight nature, and ability to construct larger structures offered by plastics when compared to glass. The plastic material type (nets or films) to be used depends on several factors, mainly the local tradition. [3]

Plastic nets are used mainly in countries with tropical and Mediterranean climates. A major problem confronting Mediterranean greenhouse horticulture is the excess of heat during summer. One of the methods to alleviate the heat load is shading with nets. They play a crucial role in covering applications to improve micro-climatic conditions for crops and are protecting crops from weather conditions like hail, wind, snow, and heavy rainfall, primarily in fruit cultivation and ornamental plant cultivation. One of the key advantages of using nets as a covering material in greenhouses is their ability to improve air circulation and ventilation. Traditional covering materials like glass or plastic films can restrict the movement of air, leading to stagnant conditions and increased humidity. Nets, on the other hand, allow air to flow freely, creating a well-ventilated environment. This enhanced air circulation helps prevent the buildup of moisture, reduces the risk of fungal diseases, and promotes the exchange of gases necessary for photosynthesis. They are also perfect to be used to shade mushroom-beds and shelters for cattle breeding. [3,4,5,6]

*Corresponding author:
Email: inestucman1997@gmail.com

Cite this article as:
Tucman, I., Pilipović, A. (2024). The effect of ageing on the tensile properties of greenhouses nets. *European Mechanical Science, 8*(4): 210-217. https://doi.org/10.26701/ems.1515141

History dates:
Received: 12.07.2024, *Revision Request*: 25.08.2024, *Last Revision Received*: 10.09.2024, *Accepted*: 23.09.2024

Plastic net coverings offer many advantages and environmental benefits. In particular, net covering can enhance productivity, quality and homogeneity of plants and fruits throughout the year in hot and sunny regions. [7]

Furthermore, these nets find utility in safeguarding crops against virus-carrying insects and birds, as well as aiding in harvesting and post-harvesting procedures. The most used raw material extensively used for producing agricultural nets is high density polyethylene (HDPE). Additionally, polypropylene (PP) is also utilized for this purpose. [8]

Within the market, nets are defined as both woven and non-woven variations. To avoid misunderstanding, the following definition of plastic nets is proposed: a plastic net is a product made of plastic fibres connected with each other, in a woven or knitted way forming a regular porous geometric structure and allowing fluids (gases and liquids) to go through. [3,8]

Net types are characterised by different structural features like kind of threads, fabrics, shape and dimensions of fibres and meshing, by physical properties like weight, colours, shading factor, durability, porosity, air permeability and mechanical characteristics such as stress, strength at break and elongation. Normally the available dimensions of nets vary a lot for both the width and the length. The width usually varies from 1 m to 6 m or from 12 to 20 m (depending on the type of net) and the length from 25 m to 300 m. Wider nets are constructed by joining the required number of widths. A first classification of nets can be based on the material, the kind of fabric, the colour and additives used. [9,10]

This study investigates the impact of ageing on the tensile properties of greenhouse nets, focusing on how different materials are affected by ageing and whether they need to be changed more often or not. Six nets for a variety of applications, such as sun, wind, insect and hail protection made from various polymer materials, including HDPE and PP, were selected for testing. Parameters such as tensile force, strength, elongation, and changes in net shape after ageing were analyzed.

2. Materials and Methods

2.1. Materials

Different structural attributes such as material composition, thread type, thread dimensions, texture, mesh size, solidity, and weight distinguish various types of nets. Nets can also have different colour, transmissivity, reflectivity, and shading factor. In addition, different net types have different physical traits like air permeability and various mechanical properties including tensile stress, durability, strength, and elongation at break. In this work, classification of nets will be based on type of material. The most used material for agricultural nets is high density polyethylene (ρHDPE = 940-960 kg/m^3). It is a non-toxic material, which can be used in direct contact with plants; it is completely recyclable; easily convertible; resistant to water; durable, if stabilized to ultraviolet (UV) radiation agents are added in the correct quantity; and has good mechanical characteristics such as tensile strength in the range from 20 to 37 MPa, elongation in the range from 200 to 600%). Except for HDPE, polypropylene is also widely used. Polypropylene (ρPP = 900-910 kg/m^3) is used as raw material in the production of non-woven layers. This kind of membrane is in horticulture and in orchards applied as direct cover on plants to protect cultivations from rain, frost, or wind. Non-woven layers are characterized by a very low structural resistance and cannot be used as coverings of structural frames. PP is also used as fibers and filaments produced by extrusion and is used in agriculture for piping, sheeting, nets, and twines. [9, 10]

In this work, six types of commercially available nets were selected for various applications. Different nets (for different applications like sun, wind, insect and hail protection) made from the same type of material (HDPE) were selected, along with one net made from a different material (PP), to enable a more accurate comparison of properties and to determine whether the material affects these properties. Additionally, this approach aimed to assess whether such nets can withstand long continuous exposure to the sun's rays.. The ▶**Table 1** shows images of the nets, also enlarged under a Digital microscope *Stemi 508*, from the manufacturer *Zeiss*. The scale bars in the magnified net images presented in ▶**Table 1** are 1000 μm.

2.2. Methods

Six different types of nets were used in this research. From each net sample six specimens were cut off. Three of them were put in the ageing chamber. Dimensions of specimens, cut out of net samples, were 50 mm × 300 mm with gauge length 200 mm, in accordance with the ISO 13934-1:2013 (▶**Figure 1**). The nets test specimens were not folded over twice at the gripping areas, the grips of the tensile testing machine clamped the test specimens at the edges. During the test, none of the nets broke in the jaws. The thickness of nets is listed in ▶**Table 1**.

Ageing was carried out in Solarbox xenon test chamber (▶**Figure 2**) that has xenon-arc light in the presence of moisture, so there is a possibility of regulating temperature, humidity and/or wetting. The radiant heat emitted by the Xenon Lamp in Solarbox xenon test chamber is continuously monitored and regulated using a Black Standard Thermometer (B.S.T.), which is positioned in the plane of the test panels near the

Table 1. Listed nets and their descriptions

Name of the net	Picture of the net	Net material	Description
8/10	 Thickness: 0.482 mm	-HDPE	- Anti-insect nets allow an effective protection against harmful insects in the context of biological and integrated pest management. White color ensures maximum brightness, and the different sizes of the hole allow the protection against various types of insects.
20/10	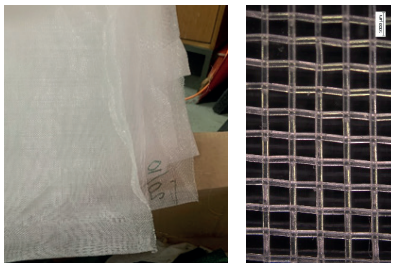 Thickness: 0.54 mm	-HDPE	- Anti-insect nets allow an effective protection against harmful insects in the context of biological and integrated pest management. White color ensures maximum brightness, and the different sizes of the hole allow the protection against various types of insects.
PA105N	 Thickness: 0.272 mm	-PP	-Groundcover provides a clean surface to walk on while keeping the soil free from weeds. It is strong, durable, and permeable to water. It also reduces the water evaporation by keeping the soil moist. It drastically reduces herbicides and maintenance costs.
ZO95	 Thickness: 0.498 mm	-HDPE	- ZO[5 is HDPE UV stabilized net which is mostly used in protection against the wind from air currents and sun.
70%	 Thickness: 0.612 mm	-HDPE	- Shading nets create a better microclimate, reduce evaporati-on, avoid the sunburn, decrease the thermal shock, protect from hail and wind, create areas of privacy, with various effects depending on the density of meshes. The nets are supplied in standard rolls or in sewn cloths on demand.
APRO	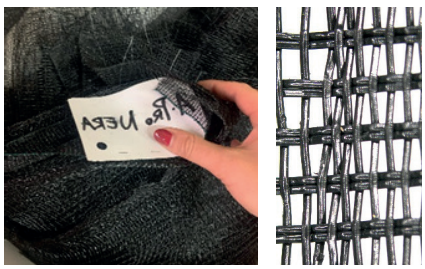 Thickness: 0.55 mm	- HDPE	-APRO is professional anti-hail net HDPE UV stabilized. Some properties of this net are: weft yarn: ø 0.32 mm, mesh size: 8.5x2.8 mm, black color shading: 16%, reinforcements: center and edges, widths: da 0,50 a 6 mt (from 0,50 to 6 mt), widths over 6 mt with sewing.

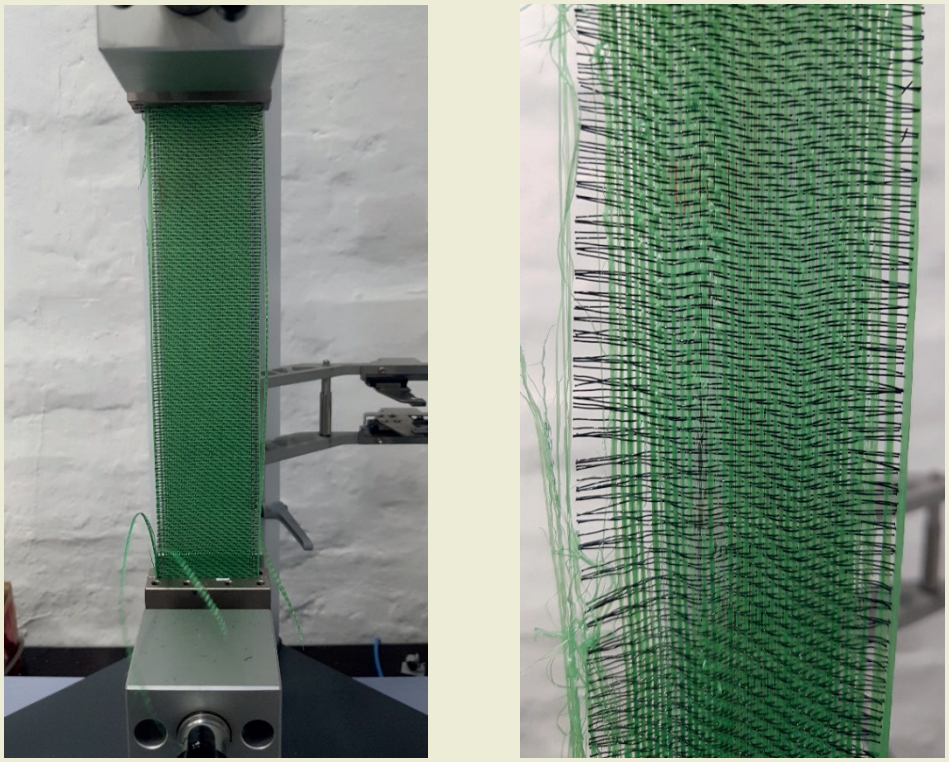

a) b)

Figure 1. Tensile test of nets: a) during the testing, b) after the testing

a) b)

Figure 2. Solarbox xenon test chamber: a) the whole chamber, b) nets in the chamber

samples. The B.S.T. allows for the control and display of the black standard temperature within a range of 35 °C to 100 °C. The significance of temperature in the weathering degradation process lies in the fact that the rate of chemical reactions tends to double with every 10 °C increase in temperature. As temperature plays a critical role in accelerating the ageing process, precise control of the B.S.T. during exposure to filtered Xenon

radiation is crucial for ensuring accurate and reliable test results. Solarbox xenon test chamber has ultimate filtered Xenon light exposure and weathering instruments which simulate realistic natural outdoor weathering conditions. The ageing was done according to ISO-4892-2 at an irradiation of 550 W/m², a temperature of 65 °C and humidity 65% for 1000 h. Ageing in xenon test chamber in duration of 1000 h roughly corresponds to 3 years of actual ageing under atmospheric condition. After ageing, the specimens are marked with symbol K. Given that the goal of the work is to establish whether the tensile properties of the net have changed after ageing, the nets were tested before and after ageing. Tensile properties were tested on tensile machine Shimadzu AGS-X with max force 10 kN. All results are presented in ▶**Table 2**.

Figure 3. Curling of the nets after ageing

3. Results and Discussions

To understand the effects of ageing on the tensile properties of greenhouse nets, various observations were made before and after the ageing process. The analysis aimed to evaluate how prolonged exposure to environmental conditions impacts the physical characteristics of these nets. Initial findings indicate that the ageing process causes noticeable changes in the nets, such as curling, as depicted in ▶**Figure 3**. This section discusses these changes in detail, presenting the data on tensile force, strength, and elongation along with visual evidence of the physical alterations observed.

Results of tensile force and elongation is given in the ▶**Table 2** and ▶**Figure 4**. In the ▶**Table 2** is presented average values with standard deviation.

From the conducted tests, it can be concluded that the tensile force of all nets, although UV-stabilized, decreases during ageing, but their tensile elongation increases. For the PA105N net, the tensile force decreased by 27%, while for the ZO95 net, the tensile force decreased by 34%. The only net whose tensile force did not decrease is the 70% net; after ageing, its tensile force increased by 4%. The APRO and 8/10 nets experienced a slight decrease of around 3%, and the 20/10 net showed a tensile force decrease of 14%. All nets, except for the ZO95 net (whose elongation increased by 70%), did not show significant differences in elongation before and after ageing. For PA105N the tensile strenght decreases by 27%, for ZO95 decreased by 34%. The 70% net is only net that shows increase in tensile strenght. And other nets have slight decresed values which can be seen better in ▶**Figure 5**.

Comparing the results from the tables in many other research, it can be noticed that the results are very similar. In other studies, it is reported that anti-hail, anti-insect, and anti-wind nets made from HDPE have an elongation at break ranging from approximately 20% to 40%. In this research, the values similarly fall within

Table 2. Testing results

Name	Max. force, N	Break disp, mm	Break force, N	Max. break disp, mm	Max. Stress, N/mm²
PA105N	775.816±61.9371	30.3970±3.42141	523.261±114.415	34.7582±0.44422	57.0453±4.55424
K-PA105N	567.382±19.2071	22.2418±2.53476	455.056±81.2193	24.9471±1.79342	41.7193±1.41226
ZO95	1445.15±107.791	41.8066±1.74068	1294.78±102.407	43.6695±0.67983	58.0379±4.32892
K-ZO95	958.072±324.002	62.6417±7.33512	871.508±350.793	74.1747±5.68667	38.4767±13.0120
70%	672.640±35.0809	41.6945±1.38087	216.116±30.6572	54.1693±2.78258	21.9817±1.14645
K-70%	699.033±49.0850	47.1527±4.07053	435.633±36.4331	60.6363±9.86550	22.8442±1.60410
APRO	268.194±25.4491	33.2070±4.17501	232.578±33.4858	35.8528±1.95411	9.75252±0.92542
K-APRO	260.450±10.0347	34.7823±1.39186	229.980±58.8926	38.1527±2.93355	9.47090±0.36489
20/10	557.525±35.8535	41.9526±3.13471	252.944±149.229	49.8252±1.76057	20.6490±1.32789
K-20/10	496.882±17.4388	42.1140±5.58894	363.989±62.0107	48.2915±7.00628	18.4030±0.64588
8/10	837.713±5.80287	38.2862±2.32484	661.409±168.481	40.8689±3.90539	34.7599±0.24080
K-8/10	823.190±47.4025	37.9974±1.70967	707.461±112.293	41.1302±1.55311	34.1573±1.96690

https://doi.org/10.26701/ems.1515141

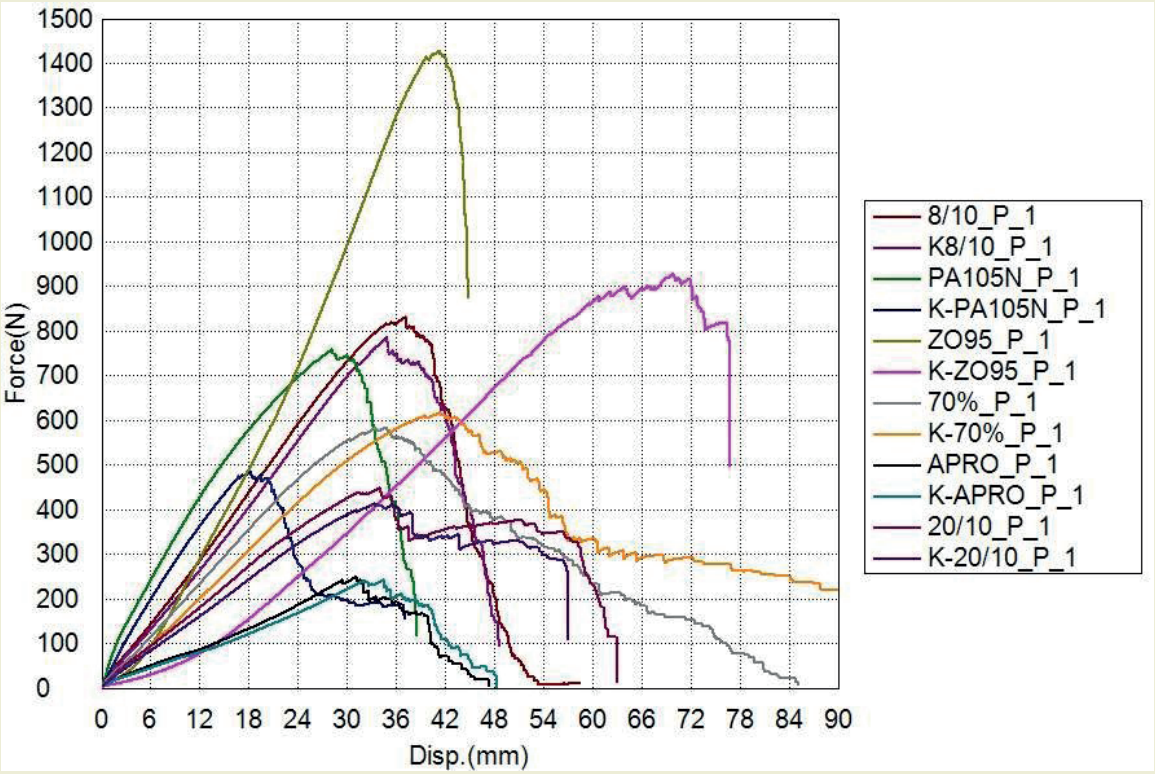

Figure 4. Tensile force – displacement curve (average curves for all nets)

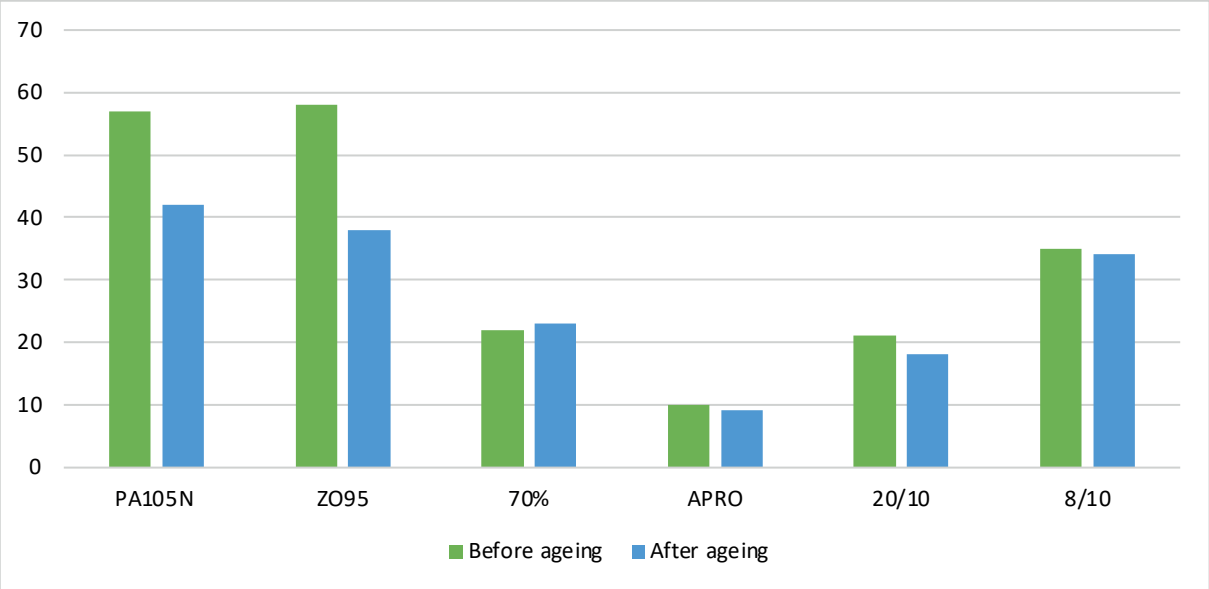

Figure 5. Comparison of tensile strength of the nets

this range. Tests have shown that the best properties are the nets that are mostly used in agriculture, HDPE nets. Compared to other studies, where the values for HDPE nets typically range around 25 N/mm^2 and some are around 7 N/mm^2. It really depends on type of the net. In one study, the max. break disp values are approximately 60 mm for windbreak nets used in agriculture align closely with our own testing results. Similarly, the tensile force values are also comparable as values are little bit higer. [11,12,13]

4. Conclusions

This paper examines the effect of ageing on various nets used as greenhouse covers for plants. The results indicate that the tensile force of the nets decreases with ageing, despite being UV-stabilized, but their elongation remains similar.

According to the standard in the Republic of Croatia, this chamber test simulates approximately 3 years of

real-world conditions. It can be concluded that the nets maintain their properties and could continue to be used for an extended period without replacement. However, as ▶**Figure 3** illustrates, degradation is evident in the change of the net's shape; it no longer retains its original form and begins to curl. Interestingly, the net made from PP (while others are made from HDPE) exhibits similar properties, showing no significant difference between these two materials.

This test expedites the selection process of suitable materials for protecting greenhouse plantations (including plants, fruits, and vegetables). However, its efficacy heavily relies on seasonal variations and climate factors such as rainfall, hail size, sunlight intensity, and wind speed. It's crucial to note that in Croatia, the orientation of the greenhouse plays a pivotal role. In the continental region, it's advisable to use nets and films that allow higher light transmission, essential for early and late-season crop production. A north-south orientation is preferred with these materials. Conversely, in coastal areas, diffuse nets and films are more common. While they allow less sunlight penetration, they provide better thermal insulation in winter and effective shading in summer. The orientation of the greenhouse is less critical with these materials. Furthermore, the covering material must possess high transparency, transmitting at least 80% of the visible spectrum, up to 20% of the ultraviolet spectrum, and no more than 10% of the infrared spectrum.

After laboratory tests, which in this case correspond to 3 years of actual exposure to UV rays, the majority of tested nets showed that tensile forces and strength do not change over time. The PP mesh for covering the ground and the mesh against the wind showed slightly worse properties in terms of tensile strength. In further research, we will include the process of rain (i.e. immersion in water) and different percentages of moisture and see how this affects the properties of the nets. In addition to the nets, in future research it is also planned to examine the plastic films that are used to protect plants in greenhouses. Furthermore, in order to establish why such phenomena occur in future research, FTIR and TGA testing will be performed on all nets before and after ageing. Also a continuation of the study, there will be an analysis of the impact of ageing on meshes cut perpendicular to the manufacturing direction.

Acknowledgments

The work was created as part of the project Development of an innovative mobile system for covering and protection of plantations (Project code: KK.01.2.1.02.0311) financed from the Operational Program "Competitiveness and Cohesion 2014-2020" from the European Fund for Regional Development as part of the call KK.01.2.1.02 - Increasing the development of new products and services resulting from research and development activities (IRI) - phase II. The authors would like to thank the European Union for funding this project.

Research ethics

Not applicable.

Author contributions

Conceptualization: Ines Tucman and Ana Pilipović, Methodology: Ines Tucman, Formal Analysis: Ines Tucman and Ana Pilipović, Investigation: Ines Tucman, Data Curation: Ana Pilipović, Writing - Original Draft Preparation: Ines Tucman, Writing - Review & Editing: Ana Pilipović, Visualization: Ana Pilipović, Supervision: Ana Pilipović, Project Administration: Ana Pilipović

Competing interests

The author(s) state(s) no conflict of interest.

Research funding

Project code: KK.01.2.1.02.0311) financed from the Operational Program "Competitiveness and Cohesion 2014-2020" from the European Fund for Regional Development as part of the call KK.01.2.1.02 - Increasing the development of new products and services resulting from research and development activities (IRI) - phase II.

Data availability

The raw data can be obtained on request from the corresponding author.

Orcid

Ines Tucman https://orcid.org/0000-0003-4520-3584
Ana Pilipović https://orcid.org/0000-0003-1330-6458

Reference

[1] Wang, L., Xu, M., Zhang, Y., & Wang, B. (2024). Benefit-prioritized greenhouse environment dual-time domain multi-layered closed-loop control strategy. *Computers and Electronics in Agriculture, 225*, 109284. https://doi.org/10.1016/j.compag.2024.109284

[2] Ding, D. (2024). Design strategies of passive solar greenhouses: A bibliometric and systematic review. *Ain Shams Engineering Journal, 15*(5), 102680. https://doi.org/10.1016/j.asej.2024.102680

[3] Scarascia-Mugnozza, G., Sica, C., & Russo, G. (2012). Plastic materials in European agriculture: Actual use and perspectives. *Journal of Agricultural Engineering, 42*(3), 15. https://doi.org/10.4081/jae.2011.3.15

[4] Vuković, M., Jurić, S., Maslov Bandić, L., Levaj, B., Fu, D.-Q., & Jemrić, T. (2022). Sustainable food production: Innovative netting concepts and their mode of action on fruit crops. *Sustainability, 14*(15), 9264. https://doi.org/10.3390/su14159264

[5] Teitel, M., Gahali, Y., Barak, M., Lemcoff, H., Antler, A., Wenger, E., Amir, R., Gantz, S., & Harhel, D. (2012). The effect of shading nets on greenhouse microclimate. *Acta Horticulturae, 952*, 731-738. https://doi.org/10.17660/ActaHortic.2012.952.92

[6] Castronuovo, D., Statuto, D., Muro, N., Picuno, P., & Candido, V. (2017). The use of shading nets for the greenhouse cultivation of sweet pepper in the Mediterranean area. *Acta Horticulturae, 1170*. https://doi.org/10.17660/ActaHortic.2017.1170.46

[7] Statuto, D., Picuno, P., & Abdel-Ghany, A. M. (2019). Shading methods for crops protection under greenhouse in Mediterranean areas. In *47th Symposium Actual Tasks on Agricultural Engineering* (pp. 297-306). Opatija, Croatia.

[8] Al-Helal, I. M., & Abdel-Ghany, A. M. (2010). Responses of plastic shading nets to global and diffuse PAR transfer: Optical properties and evaluation. *NJAS - Wageningen Journal of Life Sciences, 57*(2), 125–132. https://doi.org/10.1016/j.njas.2010.02.002

[9] Briassoulis, D., Mistriotis, A., & Eleftherakis, D. (2007). Mechanical behaviour and properties of agricultural nets - Part I: Testing methods for agricultural nets. *Polymer Testing, 26*, 822–832. https://doi.org/10.1016/j.polymertesting.2007.05.007

[10] Castellano, S., Scarascia-Mugnozza, G., Russo, G., Briassoulis, D., Mistriotis, A., Hemming, S., & Waaijenberg, D. (2008). Plastic nets in agriculture: A general review of types and applications. *Applied Engineering in Agriculture, 24*(6), 799–808. https://doi.org/10.13031/2013.25368

[11] Castellano, S., Scarascia-Mugnozza, G., Russo, G., Briassoulis, D., Mistriotis, A., Hemming, S., & Waaijenberg, D. (2008). Design and use criteria of netting systems for agricultural production in Italy. *Applied Engineering in Agriculture, 3*, 31-42. https://doi.org/10.13031/2013.25368

[12] Giannoulis, A., Briassoulis, D., Papardaki, N. G., & Mistriotis, A. (2021). Evaluation of insect-proof agricultural nets with enhanced functionality. *Biosystems Engineering, 208*, 98-112. https://doi.org/10.1016/j.biosystemseng.2021.05.012

[13] Maraveas, C. (2020). The sustainability of plastic nets in agriculture. *Sustainability, 12*(9), 3625. https://doi.org/10.3390/su12093625

EUROPEAN MECHANICAL SCIENCE

Research Article

e-ISSN: 2587-1110

Investigation of mechanical behavior of reinforced u-profile composites under low velocity impact

Merve Uslu[1], Mete Onur Kaman[1], Mustafa Albayrak[2*], Cenk Yanen[1], Serkan Dag[3], Serkan Erdem[1], Kadir Turan[4]

[1]Firat University, Engineering Faculty, Department of Mechanical Engineering, Elazig, Türkiye
[2]Inonu University, Department of Machine and Metal Technologies, Industrial Zone Vocational School, Malatya, Türkiye
[3]Middle East Technical University, Engineering Faculty, Department of Mechanical Engineering, Ankara, Türkiye
[4]Dicle University, Engineering Faculty, Department of Mechanical Engineering, Diyarbakir, Türkiye

Abstract: In this study, the impact resistance of reinforced composite panels with unsupported, and U profile supported by I profile was numerically examined. For this purpose, firstly, unsupported glass fiber/epoxy composite panels were designed, and then I-profile composite supports were added to these panels. The impact strength, and damage behavior of supported, and unsupported specimens under low-velocity impact were compared numerically. In the analysis, the MAT22 material card, also known as the Chang-Chang damage model for composite material, was used in the LS-DYNA program. As a result of the analysis, maximum damage load of the unsupported specimen is determined to be approximately 294 N. It was determined that by adding an I profile to the structure, the maximum damage load increased to 543 N. It was seen that the added I profile supports increased the maximum contact force of the composite structure by approximately 85%. Fiber breakage damages were observed in both supported, and unsupported specimens. However, with the use of I profile support, the damaged area was further reduced. It has been determined that under low-velocity impact, supported specimens exhibit more rigid material behavior than unsupported specimens.

Keywords: u-profile composite; Chang-Chang failure criteria; I profile; impact; MAT22.

1. Introduction

Fiber reinforced polymer (FRP) composites have the characteristics of low density, high strength, high hardness, and corrosion resistance. In recent years, FRP structures have been preferred in many areas, especially aviation, and spacecraft applications, due to these superior properties. When the fuselage, and wing structure designs of civil, and military aircraft are examined, it is seen that composite panels are widely preferred. Reinforced composite panels are used as the basic building blocks that form the main body in aircraft (▶**Figure 1**). Reinforced panels with U-profile provide superior bending strength, and torsional stiffness to the structure, unlike "T-shaped", and "I-shaped" long beams. Therefore, they are one of the most important parts of the structure. Thanks to reinforced composite panels produced from FRP composites, it is possible to obtain structures that have superior material properties, and at the same time prioritize structural safety. With correct damage analysis, it is possible to design safe aircraft wings, and maintain structural integrity. Thanks to the uniquely designed reinforced panels, the lateral forces, and radial forces caused by the bending of the fuselage or wing will be compensated. Hou, et al. investigated the low-velocity impact, and post-impact crushing behavior of reinforced CFRP panels experimentally, and numerically. Experimental tests were initially developed on panels reinforced with T-, and I-shaped beams [1]. Hu, et al. designed a three-dimensional model to predict the mechanical behavior of T-profile reinforced composite structures. They examined the effect of the added profile by subjecting the

*Corresponding author:
Email: mustafaalbayrak@inonu.edu.tr

Cite this article as:
Uslu M., *etal.* (2024). Investigation of mechanical behavior of reinforced u-profile composites under low velocity impact. *European Mechanical Science*, *8*(4): 218-225. https://doi.org/10.26701/ems.1490393

History dates:
Received: 27.05.2024, *Revision Request*: 25.06.2024, *Last Revision Received*: 26.08.2024, *Accepted*: 29.08.2024

model to axial pressure tests under various equipment [2]. CAI tests of foam-filled reinforced composite panels subjected to low-velocity impacts were carried out by Liu et al. The effect of damage at different impact locations on strength is discussed [3]. Liu and Xu examined the effects of filler-reinforced composite panels on post-crushing impact damage. They investigated the effect of the added filler material on the damage load, and damage behavior [4]. Meng, et al. performed impact, and post-impact compression tests on reinforced panels. They investigated the damage morphology/mechanisms for three types of impact positions [5]. Peng, et al. experimentally, and numerically examined the effect of impact positions on the post-impact crushing performance of T-shaped reinforced composite panels [6]. Shi, Xiong, Cai, and others conducted a series of impact experiments with a hammer platform falling on reinforced panels. In these experiments, high-velocity deflection fields during short impact duration were recorded and examined using the 3D-DIC (Digital Image Correlation) system [7]. Tan, et al. conducted experiments to investigate the effect of reinforced composite panels with L-shaped reinforcement on the impact behavior and examined the types of damage occurring in the specimens [8]. Wang, Liu, and others investigated the structural deformation mechanism of reinforced plates used in marine structures under impact load. In the test results, they evaluated the deformation state of the reinforced plate [9]. Wu, et al., examined the compressive buckling, and post-buckling behavior of J-type composite reinforced panels before, and after impact load using theoretical, numerical, and experimental methods. They theoretically predicted the load-bearing properties of reinforced panels, including buckling strength, ultimate strength, and damage process [10]. Zhou et al. conducted shear fatigue experiments to investigate the fatigue behavior, and damage mechanism of reinforced composite panels. The shear fatigue behavior of hardened panels subjected to impact was examined. They conducted fatigue experiments at two load levels to investigate the initiation, and propagation of delamination. They discussed the fatigue shear behavior, and damage mechanisms based on experimental results [11]. Zhou, and Gao investigated the effect of adhesive interface properties on the post-buckling response of composite I-profile reinforced panels with lateral beam support under axial pressure [12]. Zou et al. investigated the damage development, and damage mechanism of foam-filled reinforced composite panels at different positions, and different energies under low-velocity impact, and post-impact crushing using experimental, and numerical simulation methods. Delamination damage caused by low-velocity impact was detected by ultrasonic progressive C scanning [13]. Studies in the literature focus on damage analysis, especially in laminates.

There are different studies based on the finite element method by examining the impact resistance, and crushing behavior of the composite structure, reinforced with

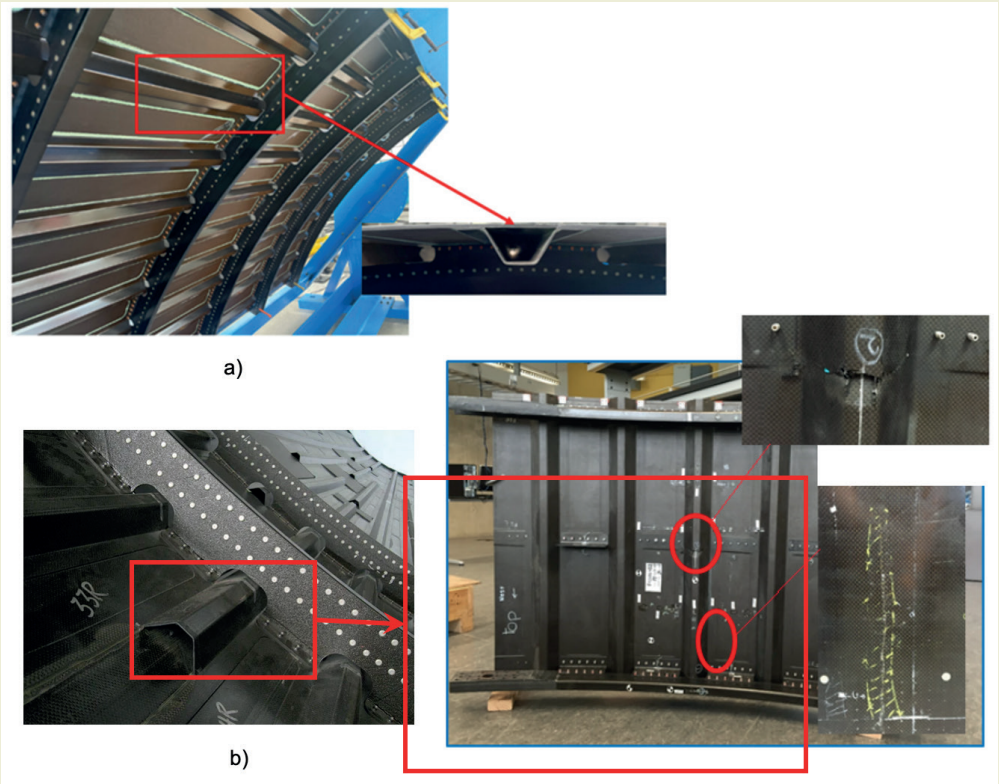

Figure 1. a) reinforced panels [14], and b) damages [15] in aircraft structures

a U-profile, separately. Within the scope of this study, unlike the literature, the impact resistance of I-profile, and supported, and unsupported U-profile composite panels was examined numerically for the first time. The effect of adding support rods into the U-profile on impact strength was revealed for the first time in this study. The development of numerical solution techniques, and finite element programs has provided the opportunity to numerically examine problems that are difficult to solve experimentally. The problem was solved in the LS-DYNA program, and force displacement graphs of supported, and unsupported specimens were obtained. In addition, damage images after the impact are compared, and presented.

2. Materials and Methods

1.4 mm thick glass fiber composite models were designed to perform impact tests on U-profile supported, and unsupported glass fiber composite panels. The model shown in ▶**Figure 2**; It is the assembled image of U-profile, and composite plate, that is, glued with adhesive. ▶**Figure 3** shows the addition of support bars to the reinforced panel. Glass fiber materials are both cheaper than carbon fiber, and more advantageous in their production, and use, considering human health. Within the scope of the study, 2x2 glass fiber fabric with 300g/m2 twill weave type was used as a reinforcement element. The matrix material comprised MGSH160 resin, and MGSL160 hardener. Both materials are commercial products obtained from Dost Kimya A.Ş., Istanbul, Türkiye.

2.1. Low velocity drop weight impact test method

Upper, and lower molds are needed to fix U profile composites. ▶**Figure 4** shows these molds, and their fixed shape. The striker has a weight of 5.5 kg, and diameter of 20 mm. As a result of the analysis, reaction force, and damage images were obtained according to time.

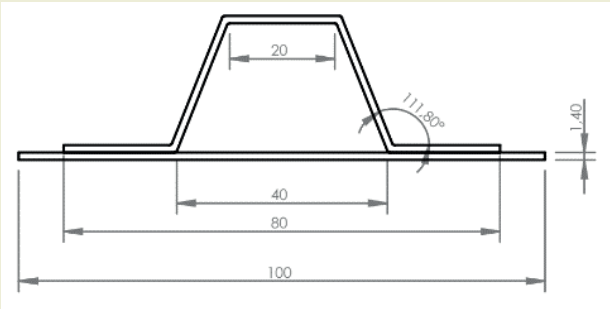

Figure 2. Front view of unsupported composite model.

Table 1. Glass fiber reinforced composite material properties.

Thickness	0.23mm
Weaving type	Twill
Weight	300gr/m²
Witdh	100 cm

2.2. Numerical Model

Low-velocity impact analyzes were carried out in the LS-DYNA finite element program. 8-node solid element type was used in modeling composite plates. To obtain realistic boundary conditions, upper, and lower dies were modeled instead of fixing the boundary nodes. As shown in ▶**Figure 5**, the upper, and lower molds, and the striker model are defined as rigid. The dies are fixed in the x, y, and z directions relative to the global axis tool. The batter is only allowed to move in the z direction. In the analysis, the MAT22 material card was selected for the composite material in the LS-DYNA program. Damage conditions for the Chang-Chang damage model are given in equations 1-7. Here, when any corresponding damage criterion exceeds the value 1, the relevant element is damaged for that mode. For longitudinal tension

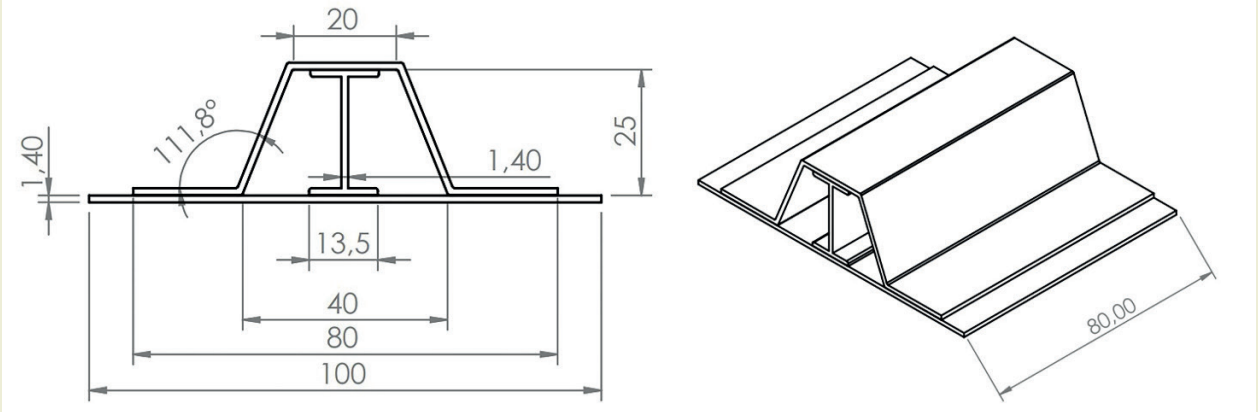

Figure 3. Supported specimen example a) Front view of the model b) Three-dimensional view of the model.

$$\left(\frac{\sigma_1}{X_t}\right)^2 + \bar{\tau} > 1, \quad \sigma_1 > 0 \tag{1}$$

Transverse tension

$$\left(\frac{\sigma_2}{Y_t}\right)^2 + \bar{\tau} > 1, \quad \sigma_1 > 0 \tag{2}$$

Transverse compression

$$\left(\frac{\sigma_2}{2S_{12}}\right)^2 + \left[\left(\frac{Y_c}{2S_{12}}\right)^2 - 1\right]\frac{\sigma_2}{Y_c} + \bar{\tau} > 1 \tag{3}$$

where σ_1, σ_2 are the tension in the fiber direction, and matrix direction, respectively. Likewise, X_t, and Y_t are the longitudinal, and transverse tensile strength, respectively. $\bar{\tau}$ is fiber matrix shearing term, S_{12} is in-plane shear strength, and Y_c is transverse compressive strength.

$$\bar{\tau} = \frac{\frac{\tau_{12}^2}{2G_{12}} + \frac{3}{4}\alpha\tau_{12}^4}{\frac{S_{12}^2}{2G_{12}} + \frac{3}{4}\alpha\tau_{12}^4} \tag{4}$$

The in-plane stress–strain relationships are as follows.

$$\varepsilon_2 = \frac{1}{E_1}(\sigma_1 - \vartheta_{12}\sigma_2) \tag{5}$$

$$\varepsilon_2 = \frac{1}{E_2}(\sigma_2 - \vartheta_{12}\sigma_1) \tag{6}$$

$$\varepsilon_{12} = \frac{\tau_{12}}{2G_{12}}(\sigma_1 - \vartheta_{12}\sigma_2) \tag{7}$$

where E_1 is strain in fiber direction, ϑ_{12} is Poisson's ratio, E_2 is strain in the transverse direction, and $2\varepsilon_{12}$ is shear strain. If index 2 is replaced by 3 in any above criteria, failure theories are applied for the planes 1–3 [16].

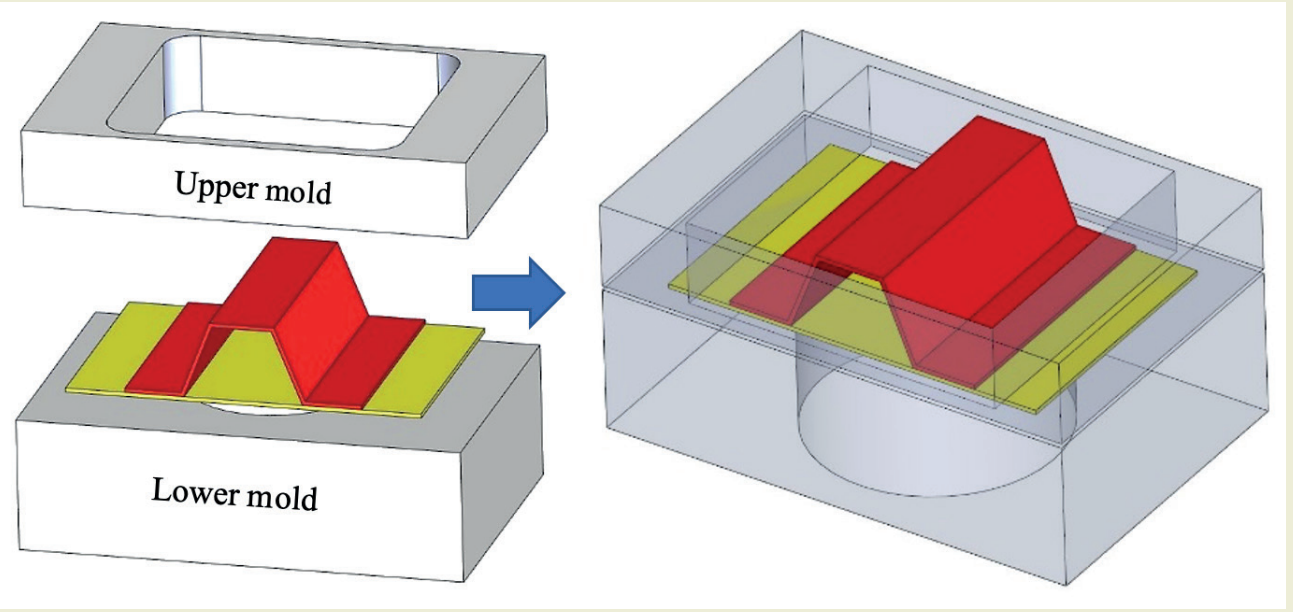

Figure 4. Molds designed to fix the composite panel on the impact test analysis.

Table 2. Mechanical properties of glass fiber reinforced composite [16]

Symbol	Properties	Value	Unit
ρ	Density	1500	kg/m3
E_x, E_v	Elasticity modulus x, and y direction	43.7	GPa
E_z	Elasticity modulus z direction	14.57	GPa
v	Poisson	0.21	-
G_{xv}	Modulus of rigidity in xy plane	14.18	GPa
G_{vz}	Modulus of rigidity in yz plane	14.65	GPa
G_{zx}	Modulus of rigidity in zx plane	14.65	GPa

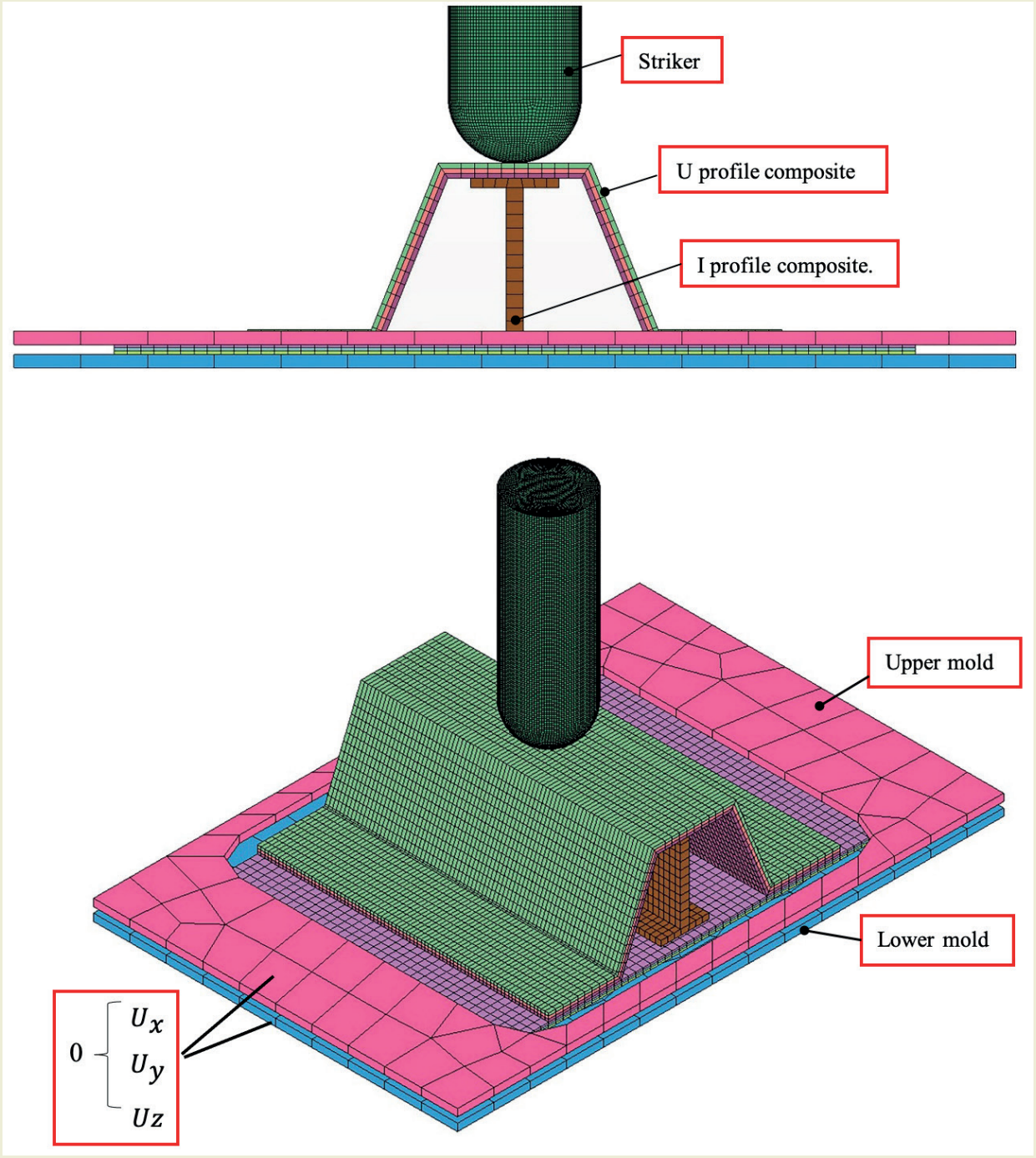

Figure 5. Finite element model of I profile supported composite.

3. Results and Discussions

The mechanical behavior of I-profile supported, and unsupported composites under impact load was examined. The effect of the I profile support added to the composite structure on the damage load, and damage behavior of the structure was evaluated. ▶**Figure 6** shows the reaction force-time graph for supported, and unsupported specimens. According to the graph, it was seen that the reaction force increased in the elastic region with the contact of the striker with the U-profile composite, and after reaching the maximum point, the structure was damaged. When the slope of the force increase in the elastic region was compared, it was determined that the supported specimens exhibited more rigid material behavior. In the supported specimens, the impact was rebounded by the impact of the I profile upon impact with the specimen, and its contact with the specimen was less than that of the unsupported specimen. In the first stage of contact, slight oscillations were observed due to the elastic vibration caused by the initial contact between the striking tip, and the composite plate. The

initial sudden force decrease is due to the decrease of bending stiffness, and reaching the delamination damage threshold because of the brittle impact damage behavior of the glass fiber composite. Continuing small force decreases thereafter indicate crack growth [17]. In ▶**Figure 7**, the maximum damage loads of the specimens are compared.

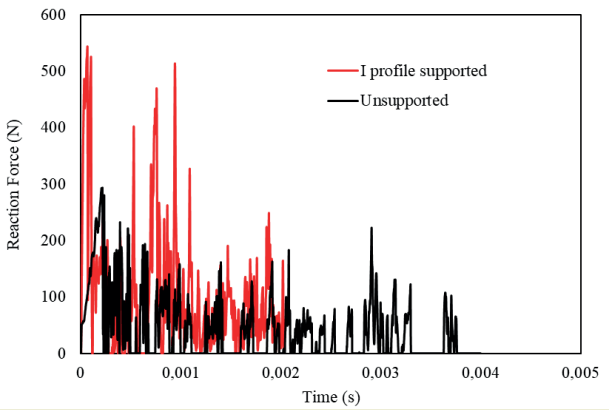

Figure 6. Reaction force-time graph of supported, and unsupported U-profile composites.

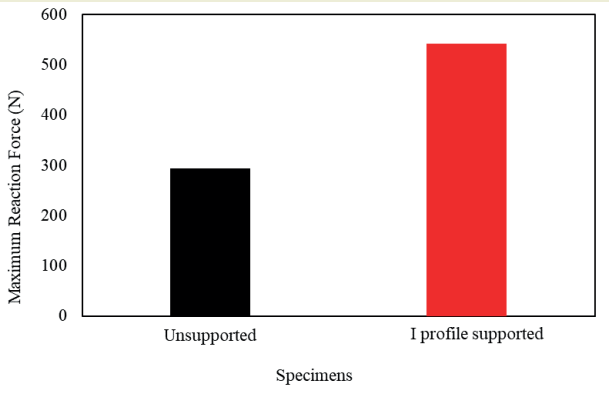

Figure 7. Reaction force- time graph of supported, and unsupported U-profile composites.

When the graph is examined, the maximum damage load of the unsupported specimen is determined to be approximately 294 N. It was determined that by adding an I profile to the structure, the maximum damage load increased to 543 N. Accordingly, it was determined that the increase in the maximum reaction force was approximately 85%. Hou et al. stated in their study that I, and T-reinforced composites increased the impact strength, and post-impact compressive strength. ▶**Figures 8**, and 9 show the images of unsupported, and supported specimens after the impact test. As can be seen, fiber breakage was observed under impact loads on the surface where the U profile, and the striker encountered the unsupported specimens. The MAT22 material model shows fiber breaks by destroying the elements in this region. When the damage image of the supported structure given in ▶**Figure 9** is examined, it is again possible to see fiber breaks. However, as can be seen, fewer damage areas were observed compared to the unsupported specimens.

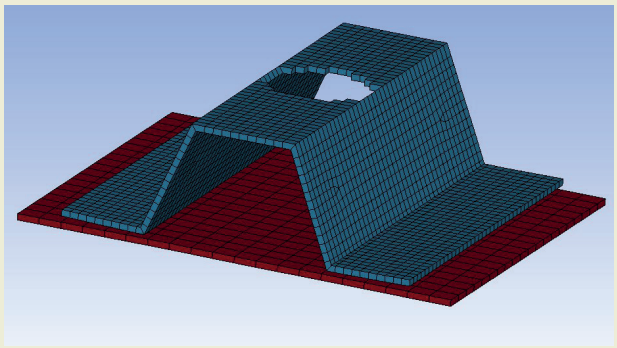

Figure 8. After-impact image of the unsupported U-profile composite.

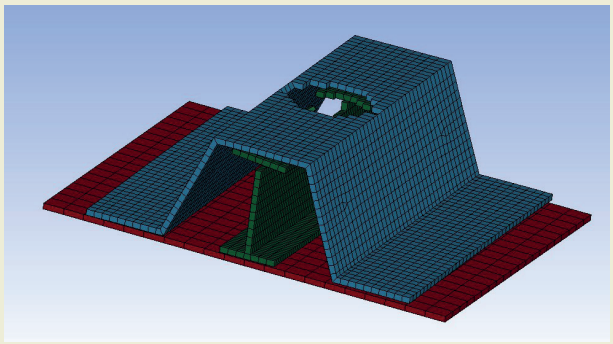

Figure 9. After-impact image of the I profile supported U-profile composite.

4. Conclusions

In the study, supported, and unsupported glass fiber composites with U profiles were designed. Afterwards, impact tests were carried out on the specimens with an impact energy of 27.55J. The results are compared, and summarized as follows.

- It has been determined that the maximum damage load of the structure increases by approximately 85% by adding I profile support to unsupported U profile composites.
- It has been determined that supported specimens exhibit more rigid material behavior than unsupported specimens under impact load.
- After the impact analysis, it was observed that the damage area was reduced on the upper surface of the U profile, which was contacted by the striker, thanks to the I profile support.

- Adding an I profile to reinforced panels with a U-profile is recommended to designers, both in terms of structural integrity, and the damage load it can carry.

Acknowledgments

This study was supported by Scientific, and Technological Research Council of Turkey (TUBITAK) under the Grant Number 123M357. The authors thank to TUBITAK for their supports.

Research ethics

Not applicable.

Author contributions

Methodology: [Mete Onur Kaman], Formal Analysis: [Mustafa Albayrak], Investigation: [Merve Uslu], Resources: [Cenk Yanen], Data Curation: [Serkan Erdem], Writing - Original Draft Preparation: [Merve Uslu], Writing - Review & Editing: [Serkan Dağ], Visualization: [Kadir Turan]

Competing interests

The author(s) state(s) no conflict of interest.

Research funding

This study was supported by Scientific, and Technological Research Council of Turkey (TUBITAK) under the Grant Number 123M357

Data availability

The raw data can be obtained on request from the corresponding author.

Peer-review

Externally peer-reviewed.

Orcid

Merve Uslu https://orcid.org/0000-0001-7819-8377
Mete Onur Kaman https://orcid.org/0000-0003-0178-6079
Mustafa Albayrak https://orcid.org/0000-0002-2913-6652
Cenk Yanen https://orcid.org/0000-0002-5092-8734
Serkan Dag https://orcid.org/0000-0003-4608-3924
Serkan Erdem https://orcid.org/0000-0002-2504-0135
Kadir Turan https://orcid.org/0000-0002-4065-9649

References

[1] Hou, Y., Huang, J., Liu, Y., Meng, L., Sapanathan, T., & Xu, Y. (2024). Low-velocity impact and compression after impact behaviors of rib-stiffened CFRP panels: Experimental and numerical study. Aerospace Science and Technology, *146*, 108948.

[2] Hu, C., Xu, Z., Huang, M., Cai, C., Wang, R., & He, X. (2024). An insight into the mechanical behavior and failure mechanisms of T-stiffened composite structures with through-interface debonding defects. Ocean *Engineering, 300*, 117342.

[3] Liu, D., Bai, R., Lei, Z., Guo, J., Zou, J., Wu, W., & Yan, C. (2020). Experimental and numerical study on compression-after-impact behavior of composite panels with foam-filled hat-stiffener. Ocean *Engineering, 198*, 106991.

[4] Liu, L., & Xu, W. (2022). Effects of fillers on the impact damage and compressive residual properties of single hat-stiffened composite panels. Thin-*Walled Structures, 180*, 109705.

[5] Meng, Z., Huang, L., Wang, P., Zhang, W., Sun, J., Zhao, M., Yun, Z., Ai, X., & Li, N. (2024). Investigation on damage behavior of composite T-shaped stiffened panels under compression after multi-point impact considering impact positions. Thin-*Walled Structures, 196*, 111514.

[6] Peng, A., Deng, J., Ren, T., Wu, D., Zhou, G., & Wang, X. (2023). On damage behavior and stability of composite T-shaped stiffened panels under compression after impact considering impact locations. Thin-Walled Structures, 182, 110295.

[7] Shi, G.-J., Xiong, Y., Cai, S.-J., & Wang, D.-Y. (2023). Experiment study of dynamic buckling for stiffened panels under longitudinal impact. Ocean *Engineering, 284*, 115243.

[8] Tan, R., Xu, J., Guan, Z., Sun, W., Ouyang, T., & Wang, S. (2020). Experimental study on effect of impact locations on damage formation and compression behavior of stiffened composite panels with L-shaped stiffener. Thin-*Walled Structures, 150*, 106707.

[9] Wang, Z., Liu, K., Yu, T., Zong, S., & Wang, X. (2022). Structural deformation mechanism of the hat-stiffened plate used in marine structures under impact load. Ocean *Engineering, 266*, 112736.

[10] Wu, X., Chen, Q., Zhao, B., Zhang, K., Wang, P., & Yue, Z. (2022). Experimental behavior and shear bearing capacity simulation of stiffened composite panels subjected to invisible damage impact. Thin-*Walled Structures, 178*, 109454.

[11] Zhou, J., Guan, Z., Ouyang, T., Wang, X., Li, Z., & Hu, H. (2022). Experimental investigation of shear fatigue behavior of composite stiffened panels with impact damage. Thin-*Walled Structures, 181*, 110118.

[12] Zhou, R., & Gao, W. (2021). Influence of adhesive interface properties on the post-buckling response of composite I-stiffened panels with lateral support under axial compression. Journal *of Adhesion Science and Technology, 35*(12), 1337–1355.

[13] Zou, J., Lei, Z., Bai, R., Liu, D., Jiang, H., Liu, J., & Yan, C. (2021). Damage and failure analysis of composite stiffened panels under low-velocity impact and compression after impact. Composite *Structures, 262*, 113333.

[14] Li, B., Gong, Y., Gao, Y., Hou, M., & Li, L. (2022). Failure analysis of hat-stringer-stiffened aircraft composite panels under four-point bending loading. Materials, *15*(7), 2430.

[15] Capriotti, M., Kim, H. E., Lanza di Scalea, F., & Kim, H. (2017). Non-Destructive inspection of impact damage in composite aircraft panels by ultrasonic guided waves and statistical processing. Materials, *10*(6), 616.

[16] Albayrak, M., Kaman, M. O., & Bozkurt, I. (2023). Experimental and Numerical Investigation of the Geometrical Effect on Low Velocity Impact Behavior for Curved Composites with a Rubber Interlayer. In Applied *Composite Materials* (Vol. 30, Issue 2). Springer Netherlands. https://doi.org/10.1007/s10443-022-10094-5

[17] Berk, B., Karakuzu, R., & Toksoy, A. K. (2017). An experimental and numerical investigation on ballistic performance of advanced composites. Journal *of Composite Materials, 51(25),* 3467–3480.

[18] García-Moreno, I., Caminero, M. Á., Rodríguez, G. P., & López-Cela, J. J. (2019). Effect of thermal ageing on the impact damage resistance and tolerance of carbon-fibre-reinforced epoxy laminates. Polymers, *11(1),* 160.

EUROPEAN MECHANICAL SCIENCE

Research Article

e-ISSN: 2587-1110

Computational hemodynamic non-newtonian fluid-structure interaction simulation in a curved stenotic artery

Sireetorn Kuharat[1*], M. A. Chaudhry[1], O. Anwar Bég[1], Tasveer A. Bég[2]

[1] Salford University, Dept. Mechanical/Aeronautical Engineering, MPESG, Corrosion Lab, 3-08, SEE Building, M54WT, England, United Kingdom
[2] Engineering Mechanics Research, Israfil House, Dickenson Rd., Manchester, M13, England, United Kingdom.

Abstract: This paper focuses on deploying Computational Fluid Dynamics (CFD) and Fluid-Structure Interaction (FSI) to investigate key characteristics associated with Cardiovascular Diseases (CVDs), a leading cause of global mortality. CVDs encompass various heart and blood vessel disorders, including coronary artery disease, stroke and atherosclerosis, which significantly impact arteries. Risk factors such as high blood pressure and obesity contribute to atherosclerosis, which is characterized by narrowed arteries due to fatty deposits, impeding blood flow and increasing heart attack and stroke risks. To simulate blood flow behaviour and its effects on artery stenosis formation, ANSYS-based CFD and monolithic (one-way) FSI analyses are deployed in this work. Extensive visualization of blood flow patterns relevant to patient-specific conditions is included using the non-Newtonian (Carreau shear-thinning) bio-rheological model. These simulations start with creating a three-dimensional patient artery model, followed by applying CFD/FSI methodologies to solve the equations iteratively with realistic boundary conditions. Velocity, pressure, wall shear stress (WSS), Von Mises stress and strain characteristics are all computed for multiple curvature cases and different stenotic depths. Factors such as blood viscosity, density and its non-Newtonian behaviour due to red blood cells are considered. FSI analysis extends CFD by including the interaction between blood flow and deformable (elastic) arterial walls, accounting for the arterial mechanical properties and the flow-induced pressure changes. Here we do not consider the two-way case where deformation in turn affects the flow, only the one-way case where the blood flow distorts the arterial wall. This approach allows for deeper insight into the interaction between rheological blood flow and elastic arterial walls which aids in highlighting high stress zones, recirculation and hemodynamic impedance of potential use in identifying rupture or plaque formation, contributing significantly to the management and prevention of CVDs. The novelties of the present study are the simultaneous consideration of rigorous visualization of hemodynamic characteristics for a wide range of stenotic depths of direct relevance to patient-specific conditions (both diastolic and systolic phases are included), inclusion of non-Newtonian (Carreau shear-thinning) bio-rheology, multiple arterial curvatures, and also flow-structural interaction analysis. Previous studies have invariably considered only aspects of these multiple features. This article therefore generalizes and significantly extends previous studies and will be of benefit to clinicians and other researchers engaged in computational medical fluid dynamics.

Key words: CFD; Monolithic FSI; hemodynamics; stenotic; non-Newtonian Carreau model.

1. Introduction

Cardiovascular diseases (CVDs) are a leading cause of global mortality. They include coronary artery disease, stroke, heart failure and peripheral artery disease, among many others. A key focus is on how these diseases affect arteries, which are vital for transporting oxygen-rich blood throughout the body. Many risk factors contribute to CVDs, such as high blood pressure, high cholesterol, diabetes, obesity, ethnic background and lifestyle choices. A particularly prevalent cause of CVDs is atherosclerosis. Atherosclerosis is characterized by narrowed arteries due to fatty deposits, poses significant

*Corresponding author:
Email: S.Kuharat2@salford.ac.uk

Cite this article as:
Kuharat, S., Chaudhry, M. A., Bég, O.A., Bég, T. A. (2024). Computational hemodynamic non-newtonian fluid-structure interaction simulation in a curved stenotic artery. *European Mechanical Science, 8*(4): 226-256. https://doi.org/10.26701/ems.1492905

History dates:
Received: 31.05.2024, ***Revision Request***: 25.06.2024, ***Last Revision Received***: 25.09.2024, ***Accepted***: 30.09.2024

risks for heart attack, stroke, and reduced oxygen supply to organs [1]. Fluid dynamic studies of blood flow have motivated significant attention in engineering sciences over the past 5 decades. An excellent perspective of hemodynamic modelling was provided by Goldsmith and Skalak [2] who reviewed both large and small arterial transport and identified many key aspects including Newtonian and non-Newtonian behaviour, pulsatile and pressure wave propagation, bifurcations, curvature, bends, obstructions and stenoses. They emphasized the importance of including curvature and rheological effects, in particular, in the microcirculation and the contribution to the genesis of atherosclerotic and other pathological states. More recently Ku [3] reviewed key progress in the two decades following the review of Goldsmith and Skalak [2], focusing on unsteady characteristics in cardiovascular flows, multiple branching, Womersley number, curvature and computational and diagnostic tools. Further excellent perspectives on hemodynamic simulation have been given by Taylor and Figueroa [4] addressing finite element and fluid-structure interaction for patient-specific geometries and Wong *et al.* [5] on coronary artery hemodynamics focusing on Computed Tomography (CT) imaging, WSS and wall pressure (WPG) and their contribution to atherosclerosis and plaque formation, which in turn leads to myocardial ischemia and infarction. A particularly important geometrical configuration in hemodynamicis a stenosis. Atherosclerotic disease is confirmed to be localized in zones where there is a narrowing of the artery lumen; this is known as a stenosis. The stenosis can induce significant modifications in velocity distribution, experiences impedance via viscous head losses and flow choking. Berger [6] has further identified that stenotic conditions are more prevalent in zones where the vessel is curved, exhibits a split (bifurcation), junction, side branch or rapid change in geometry. These flows may also feature flow reversal, separation, low and oscillating wall shear stresses, secondary vortices etc, which are very challenging to simulate. Substantially high shear stresses may arise in the vicinity of the throat of the stenosis which in turn can activate platelets and this can accelerate the onset of thrombosis manifesting in serious blockage to blood flow to the heart or brain. Stenotic hydrodynamics is therefore a very important aspect of blood flow modelling. Mathematical modelling of stenotic and/or curved arterial transport can therefore significantly benefit early detection and quantification of stenosis and advise clinicians in terms of surgical intervention, stenting or coronary bypass surgery. Many interesting studies in both these areas have been communicated in recent years. Dash *et al.* [7] investigated Newtonian blood flow in a catheterized curved artery with stenosis under steady and laminar conditions. They derived double series perturbation solutions for the case of small curvature and mild stenosis. They computed the effect of catheterization on pressure drop, impedance and the wall shear stress for a range of catheter size and Reynolds numbers, noting significant variation across the stenotic lesion and that elevation in catheter size enhances all flow characteristics. They also demonstrated that the effect of stenosis is more dominant than that of the curvature. Kim *et al.* [8] deployed modified coronary angiography, to measure the functional significance of a stenosis, specifically pressure drop across the stenosis. They also simulated the regime with 3D finite element simulations for thirty-three patient-specific coronary stenoses. They identified that pressure drop is principally attributable to curvature as well as the area-reduction ratio of the stenosis before the minimal luminal area (MLA), although it is also influenced significantly by the area-expansion ratio after the MLA due to flow separation. Santamarina *et al.*, [9] investigated the hemodynamics in a curved tube model of the coronary artery with sinusoidally time-varying curvature using CFD-ACE software. They considered an inlet steady uniform velocity corresponding to a Reynolds number of 300 and observed a variation in wall shear rates in excess of 50% relative to the static mean wall shear rate within a region of 10 tube diameters from the inlet. to, flow patterns that have been associated with atherogenesis. Hoque *et al.* [10] investigated the biomagnetic blood flow in a curved tube arterial model with a spectral numerical method, as a simulation of ionic behaviour in streaming hemodynamics. They computed Dean vortex structures for a range of magnetic Hartmann numbers and also curvature ratios. Many other investigations have been communicated in curved conduit biological fluid dynamics. Chiang *et al.* [11] used a finite volume method (FVM) to simulate the viscous Newtonian unsteady blood flow and vortex patterns in a 180° curved arterial geometry. Ali *et al.* [12] who examined peristaltic blood flow in a curved conduit with the Carreau rheological model, forward time centre spaced (FTCS) finite difference and variational finite element methods. Tripathi *et al.* [13] deployed the Nakayama-Sawada bi-viscosity non-Newtonian model and MATLAB quadrature for curved tube biological transport. Narla *et al.* [14] considered axial electrical field effects on nano-doped blood flows in a curved microvascular geometry. Khan *et al.* [15] utilized integral and Mathematica shooting methods to compute the electrokinetic peristaltic pumping of ionic blood with viscous heating in a curved micro-channel. Bég *et al.* [16] visualized the Dean vortex patterns in curved arterial magnetized blood flow with numerical methods. Many complex stenotic hemodynamics simulations have also been reported recently using both Newtonian and non-Newtonian formulations. Non-Newtonian models better represent the complex properties of blood in smaller geometries which are associated with suspensions in including blood cells, proteins, lipids etc. These alter the rheology of streaming blood. Zaman *et al.* [17] computed the time-dependent magnetic pseudoplastic blood flow with body acceleration in an overlapping stenotic artery containing porous media (fatty deposits) with finite difference techniques. They showed that with higher values of permeability parameter, there is a boost in velocity, flow rate and wall shear stress increase and a concomitant reduction in hemodynamic impedance and also contraction in the magnitude of trapped boluses of blood. They further not-

ed that stronger transverse extra-corporeal magnetic field retards the blood flow, enhances impedance and modifies the post-stenotic flow distribution significantly. Wajihah and Sankar [18] reviewed a variety of stenotic hemodynamic models utilizing the single-layered viscoelastic rheological and also four-layered fluid models (combinations of Newtonian peripheral and core non-Newtonian power-law models). Sriyab *et al.* [19] computed the blood flow in power-law non-Newtonian blood flow through different stenoses, namely bell- and cosine shaped geometries. They noted that blood flow in the cosine geometry experiences greater impedance compared with the bell geometry, whereas the latter produces higher wall shear stress magnitudes. They also computed the influence of stenosis depth and stenosis height on flow characteristics over a range of values of the rheological power law index. Lakzian *et al.* [20] investigated the Newtonian/non-Newtonian unsteady pulsatile entry blood flow inside a 3D curved stenosed artery using the power-law model to characterize shear thinning or shear thickening behaviour. They applied a clinically robust pulsatile waveform at the inlet of the artery, and examined the impact of is curvature ratios, percentage and length ratio of stenosis and shear-thickening on hemodynamic characteristics, noting that the maximum wall shear stress arises in the vicinity of the stenosis (constriction) and that wall shear stress is elevated with a reduction in stenosis length. Zaman *et al.* [21] numerically studied the transient non-Newtonian blood flow through a diseased catheterized artery featuring both a stenosis and post-stenotic dilated region, using the Eringen micropolar model. They noted that blood velocity and flow rate are suppressed whereas hemodynamic impedance is enhanced with an increment in size of catheter radius, critical height parameter and micropolar parameter in the stenotic region, whereas the opposite behaviour is computed in the post-stenotic dilated region. They further visualized the post-stenotic vortex patterns and noted that the strength of recirculating zones appearing in this location is also an increasing function of catheter radius, critical height parameter and micropolar parameter. Further investigations of stenotic hemodynamics include Vasu *et al.* [22] (who deployed FreeFEM++ software and also considered nanoparticle drug diffusion), Tripathi *et al.* [23] (who considered magnetohydrodynamic control in nano-doped blood flow in an axisymmetric overlapped stenotic artery), Dubey *et al.* [24] (who utilized a Sisko viscoelastic model for Ag-Au nanoparticle blood transport in an irregular symmetric stenosis) and Roy and Bég [25] (who used asymptotic methods to study Taylor dispersion in time-dependent blood flow and mass diffusion in multiple irregular stenoses). Other computational models of stenotic blood flows have deployed the Cross rheological model [27], Oldroyd-b viscoelastic model [28], Reynolds exponential viscosity model [29] and Sisko viscoelastic and Buongiorno nanoscale models [30].

The above studies, while they have all confirmed the significant modification in hemodynamic characteristics with rheology, have neglected deformability of the blood vessel. When the blood flow distorts the vessel geometry and this geometry then alters the blood flow, this two-way coupling is known as fluid structure interaction (FSI). It is very prominent in the cardiovascular system as exemplified by the beating of the human heart, expansion and contraction of arterial and venous segments. It also arises in human respiration, intestinal peristalsis etc. To more accurately represent actual hemodynamic transport therefore, FSI models are required. Understandably the simulation of blood flow/vessel structural interaction is computationally much more challenging than purely hemodynamic modelling. Recent advances in algorithms available in commercial computational fluid dynamics (CFD) software and hardware however have enabled FSI computations to be conducted in reasonable compilation times and with much improved accuracy. FSI enables simultaneously the computation of both fluid dynamic characteristics (pressure, velocity, vorticity, wall shear stress) and also structural characteristics (deformation, stress and strain). Many excellent studies have therefore been communicated in the past decade. Bukač *et al.* [31] used a loosely coupled partitioned finite element method to compute the FSI between a curved (tortuous) coronary artery with an implanted stent, pulsatile Newtonian blood flow, and heart contractions. They considered a variety of stent geometries (Palmaz-like stent, an Express-like stent, Cypher-like stent and a Xience-like stent) and simulated the arterial walls as multi-layered different structures (the intimal layer with the internal elastic laminae as a nonlinearly elastic membrane and the media–adventitia complex as a 3D linearly elastic material). Bukač *et al.* [32] further investigated hemodynamic FSI problems with a coupled partitioned numerical scheme allowing non-zero longitudinal displacement in which arterial walls were simulated as linearly viscoelastic, cylindrical Koiter shells and a Newtonian viscous model was deployed for blood. Mendez *et al.* [33] studied 2-way FSI in blood flow in ascending thoracic aortic aneurysms (ATAAs) with both a bicuspid aortic valve (BAV) and separately with a tricuspid aortic valve (TAV). Carvalho *et al.* [34], motivated by elaborating more precisely the artery wall interaction with streaming blood, utilized both computational fluid dynamics and fluid-structure interaction modelling analysis to investigate if the arterial wall compliance affect considerably the hemodynamic results obtained in idealized stenotic coronary models. They confirmed that the impact of wall compliance on wall shear stress distribution is significantly greater than on the time-averaged wall shear stress and on the oscillatory shear index. This study is also notable for emphasizing the importance of mesh quality for accurate simulations and utilized a 50% stenosis model without curvature, which limits the understanding of wall shear effects but provides valuable insights into fluid properties and modelling. Luraghi *et al.* [35] deployed HYPERMESH, ANSYS and LS-DYNA finite element codes to compute the FSI in blood flow in bio-inspired polymeric heart valves (PHVs). They noted that, FSI simulations are substantially more accurate

than purely CFD or Finite element stress simulations to describe the actual behaviour of PHVs as they can replicate the valve-fluid interaction while providing realistic fluid dynamic results. Failer *et al.* [37] conducted monolithic (one way) FSI simulations of Newtonian blood flow in curved elastic arteries. They evaluated the impact of FSI on the wall shear stress distribution, fractional flow reserve and on the damping effect of a stenosis on the pressure amplitude during the pulsatile cycle. Further investigations of stenotic FSI blood flows include Balzani *et al.* [37] (who deployed both different nonlinear wall models to better simulate vascular elasticity including anisotropic and simple, isotropic Neo–Hooke models), Deparis *et al.* [38] (who used Steklov–Poincaré Formulation for FSI coupling in blood flow in compliant arteries), Gasser *et al.* [39] (who considered FSI simulations in biomechanical rupture risk assessment of abdominal aortic aneurysms), Turek *et al.* [40] (who utilized monolithic multigrid finite element codes) and Bertaglia *et al.* [41] (who employed viscoelastic wall models).

Motivated by exploring in more detail fully 3D stenotic and curved arterial geometry hemodynamics with wall compliance, in this article CFD and FSI approaches are utilized to investigate key characteristics of blood flow behaviour and its effects on artery stenosis formation. ANSYS-based CFD and FSI analyses are deployed in this work. Extensive visualization of blood flow patterns relevant to patient-specific conditions is included using both the non-Newtonian (Carreau shear-thinning) bio-rheological model. Velocity, pressure, wall shear stress (WSS), stress and strain characteristics are all computed for multiple curvature cases and different stenotic depths. These simulations start with creating a three-dimensional patient-specific artery model, followed by applying CFD and FSI methodologies to solve the equations iteratively with realistic boundary conditions. FSI analysis extends CFD by including the interaction between blood flow and deformable (elastic) arterial walls, accounting for the arterial mechanical properties and the flow-induced pressure changes. Detailed contour plots are presented with extensive interpretation of the results and clinical implications for cardiovascular disease. The present study has identified that thus far there has been an absence in computational hemodynamics literature with regard to the *simultaneous consideration of rigorous visualization of hemodynamic characteristics for a wide range of stenotic depths of direct relevance to patient-specific conditions (both diastolic and systolic phases are included), inclusion of non-Newtonian (Carreau shear-thinning) bio-rheology, multiple arterial curvatures, and also flow-structural interaction analysis.* These are all addressed for the first time in the present article which generalizes and pushes forward on previous studies which were restricted to only aspects of these multiple features and did not consider all these features. This article therefore generalizes and significantly extends previous studies and will be of benefit to clinicians and other researchers engaged in computational medical fluid dynamics.

2. Methodolog

2.1. Fluid Dynamic Models and Wall shear stress

The basic viscous flow model available in ANSYS FLUENT is Newtonian for which we adopt the incompressible Navier–Stokes and the continuity equations as shown below:

$$\nabla \cdot \boldsymbol{u} = 0 \tag{1}$$

$$\mu_0 = 0.0560 Pa \cdot s \tag{2}$$

Here, $\boldsymbol{u}$ *is the velocity vector,* ρ *is density, t is time, p is pressure and* μ *is dynamic viscosity.* The flow is modelled as incompressible and laminar with a density of 1060 kg/m^3 following McDonald [42]. However, due to the capacity of red blood cells to deform and aggregate, blood is actually a non-Newtonian fluid. In this work, we therefore adopt the *non-Newtonian Carreau* model which accurately represents the shear-thinning blood behaviour, and is defined by equation below:

$$\mu = \mu_\infty + (\mu_0 - \mu_\infty)[1 + \lambda\gamma^2]^{\frac{n-1}{2}} \tag{3}$$

Here the μ is viscosity,$\mu_\infty = 0.00345\ Pa \cdot s$. is the infinite shear viscosity, $\mu_0 = 0.0560 Pa \cdot s$ .is the blood viscosity at zero shear rate, λ =3.13s is the time constant, γ is the instantaneous shear rate and $n = 0.3568$ is the rheological power-law index. Selection of the Carreau model option in ANSYS FLUENT modifies the appropriate terms in the basic Newtonian viscous model. Many applications of this model have been communicated in previous studies in blood flows [43-50]. A key hemodynamic parameter is the WSS which is useful for predicting and estimating distributed flow conditions and the development of local atherosclerotic plaque. WSS is calculated using:

$$\tau_w = \mu \frac{\partial u}{\partial y} = \mu \cdot \dot{\gamma} \tag{4}$$

Here $\dot{\gamma}$ is deformation rate and $\frac{\partial u}{\partial y}$ is axial spatial velocity gradient.

2.2. Boundary Conditions

In terms of the boundary conditions applied in this investigation, a medically precise pulsatile velocity profile was set at the inlet and is shown in ▶**Figure 1** and 80 mmHg of pressure was predicated for the outflow based on the study done by Carvalho *et al.* [34]. The inlet and outlet are fixed in all directions, and the vessel wall boundaries are established as a fluid-structure interface. The pulsative velocity profile is converted into a text file and inserted into the analysis as shown in the ▶**Figure 1**.

The elastic artery wall material has a density of ρ =1120 kg/m^3. The ANSYS Fluent software applies the finite discretisation method to divide the fluid domain into finite control volumes and apply conservation equations to each volume. The semi-implicit approach for the pressure-linked equations (SIMPLE) methodology is employed for the velocity-pressure coupling [34]. The CFD simulation is set as transient due to the heartbeat and pulsation effect. The results for CFD analysis include velocity plots, wall shear stress and pressure at the peak points of systole (0.4) and diastole (0.6). These points are chosen due to the extreme conditions applied to the system.

2.3. Hemodynamic Geometry

In the present simulations, we study various degrees of curvature of the arteries and different percentages of stenosis. Properties of the artery are taken from [34]. The maximum thickness of this artery is considered to be 0.8mm. The solid geometry is used in CFD, and the shell geometry is used in the FSI analysis. The fluid domain is created using design modular in Ansys workbench [51]. The straight length of the artery is estimated to be 20mm long and the diameter is 2.9mm based on the study [42]. Three different curvatures are given to the geometry with the angles of 30°, 60° and 90°. The percentage of stenosis severity is illustrated in ▶**Figures 2-4** for each angle. The blood flow travels from the bottom of the curved artery to the top.

2.4. Meshing

After creating the geometry, it is discretised using a mesh tool before boundary conditions can be applied. The element size of 0.11mm is used to discretize the fluid domain into hexahedral elements. The artery due its cylindrical shape will require an inflation feature closer to the wall which allows elements to be smaller in the near wall region. This is done to capture more precisely the wall velocity profile and wall shear stress. Five inflation layers are applied near to the wall area with a growth rate of 1.2 transitioning smoothly along the wall. The meshes are visualized in ▶**Figure 5**.

The smallest possible element size of 0.11mm is used to generate mesh. To ensure the quality of the mesh, the skewness and orthogonal quality are evaluated. The maximum skewness and minimum Orthogonal quality parameters as documented in ▶**Table 1** below show that the mesh quality is reliable, and convergence is achieved.

3. Numerical CFD And FSI Contour Results Visualization

Detailed simulations have been conducted. The sim-

Table 1. Mesh independence tests conducted with skewness

Curvature (degree)	% Stenosis	No of Element	Min Orthogonal Quality	Max Skewness
30	20	441688	0.338	0.662
60	20	427180	0.335	0.665
90	20	366639	0.56	0.44
30	40	441688	0.338	0.662
60	40	427180	0.335	0.665
90	40	366639	0.557	0.443
30	60	441688	0.338	0.662
60	60	427180	0.336	0.664
90	60	366639	0.55	0.451
30	80	444912	0.338	0.662
60	80	430404	0.337	0.663
90	80	369733	0.506	0.502

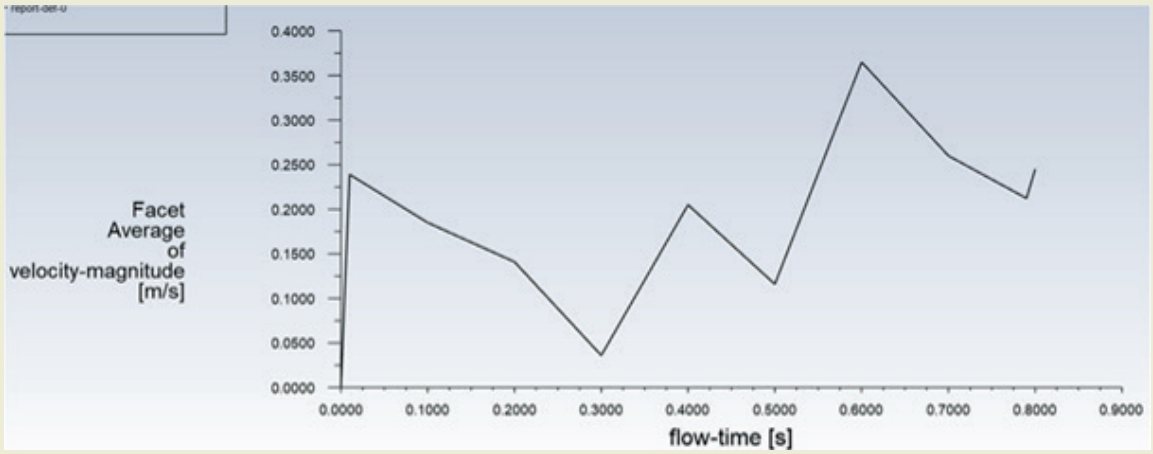

Figure 1. Pulsatile wave form deployed in simulations.

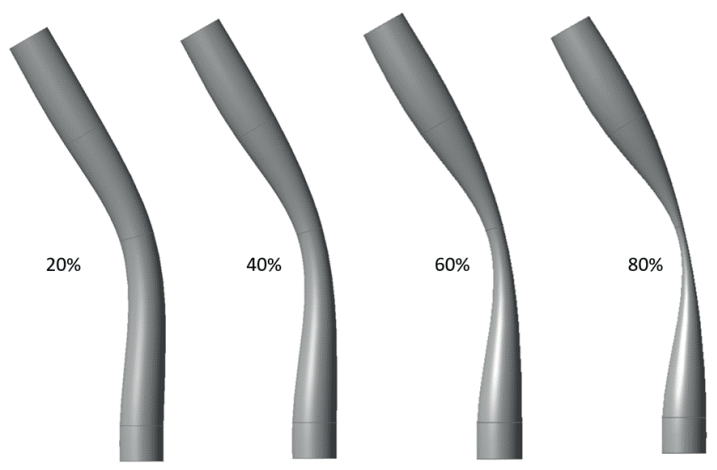

Figure 2. 30-degree curved arteries with different percentage of stenosis

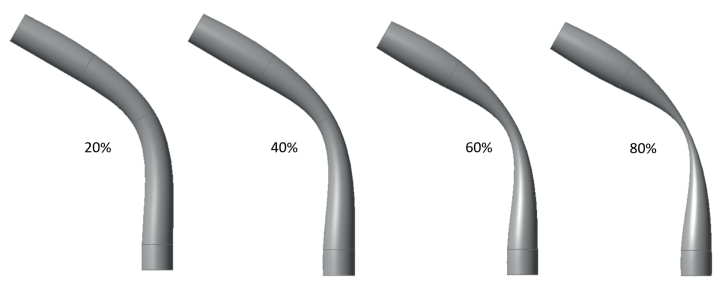

Figure 3. 60-degree curved arteries with different percentage of stenosis.

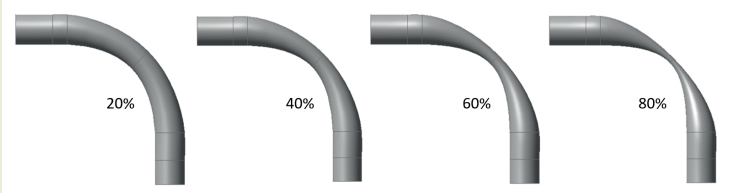

Figure 4. 90-degree curved arteries with different percentage of stenosis.

ulations have been grouped according to curvature with corresponding variations in stenosis percentage for each case of curvature. It is important again to mention that only one-way coupling is considered in the FSI simulations, wherein the blood flow distorts the arterial walls; the arterial walls do not modify the blood flow. This was selected as a first step in order to establish a rigorous methodology for cardiovascular FSI. In subsequent studies the authors will examine the full two-way coupling problem and also explore other non-Newtonian models e.g. power-law model, Casson viscoplastic model etc, which are also available in the ANSYS workbench platform.

3.1. CFD Visualizations

We present first the CFD results for velocity (streamlines), pressure, wall shear stress and finally 3D velocity vector plots for 3 curvature cases (30, 60, 90 degrees) each with 4 stenosis depths (20, 40, 60, 80%). The results are therefore grouped in 12 sets in 4 subsections (A, B, C, D). In each figure we provide 2 graphs, one for the *systole* (the part of the cardiac cycle during which some chambers of the heart contract after refilling with blood) and the other for the *diastole* (relaxed phase of the cardiac cycle when the chambers of the heart are refilling with blood. The contrasting phase is systole when the heart chambers are contracting).

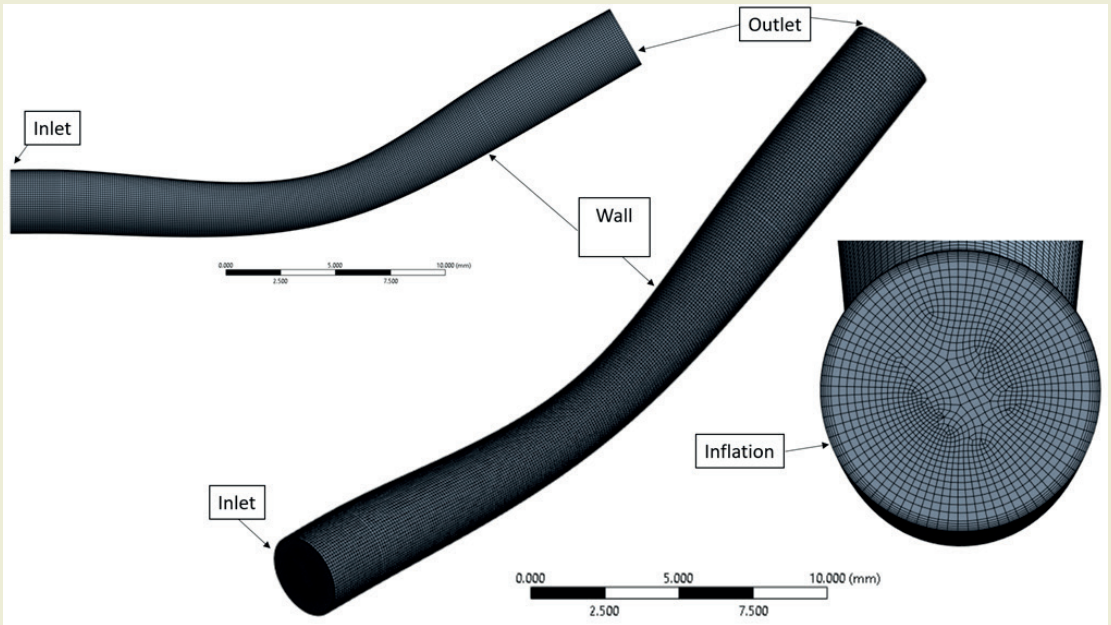

Figure 5. 3D finite element mesh deployed for the curved stenosed artery.

3.1-1 Velocity contours for different curvatures and stenoses

A] Velocity contour of 30-degree curvature

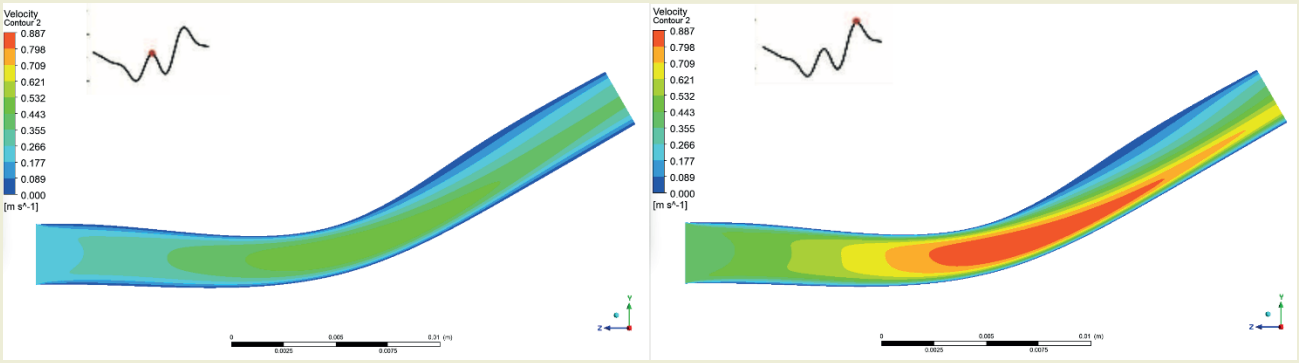

Figure 6. Velocity contour of systole (left) and diastole (right) with 20% stenosis.

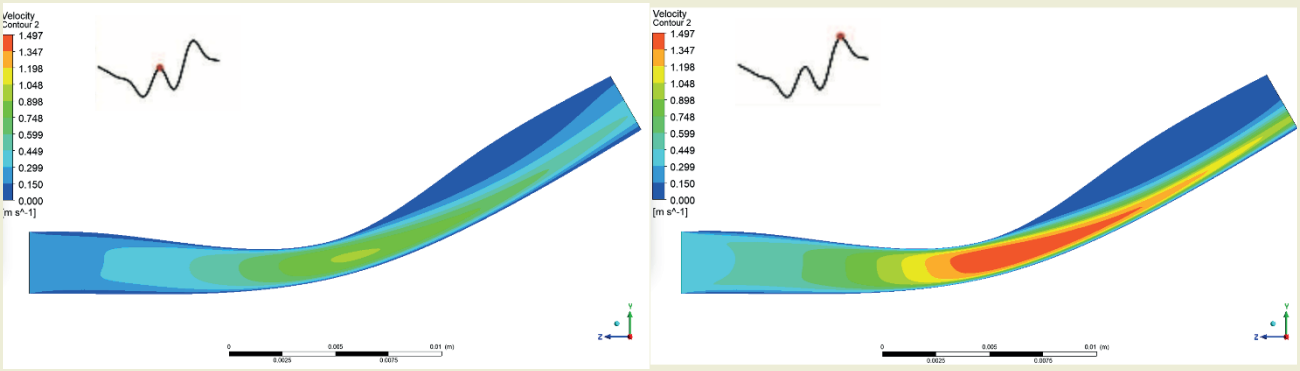

Figure 7. Velocity contour of systole (left) and diastole (right) with 40% stenosis.

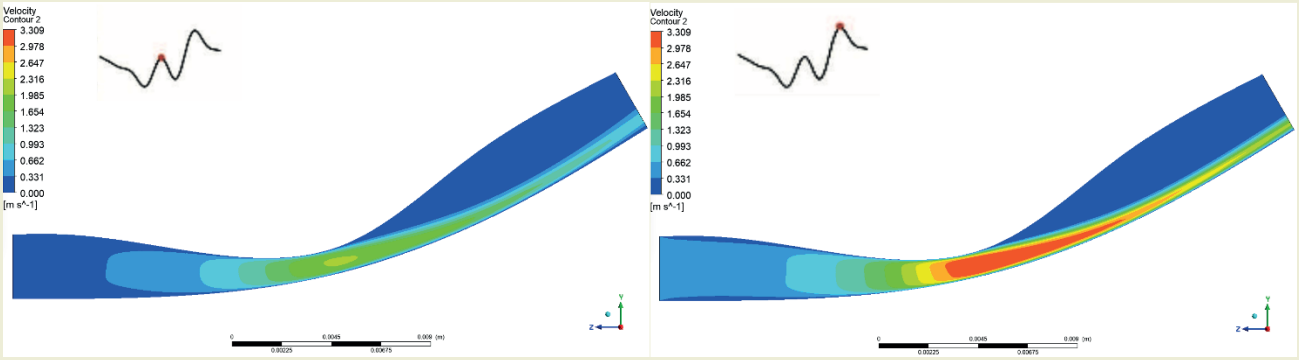

Figure 8. Velocity contour of systole (left) and diastole (right) with 60% stenosis.

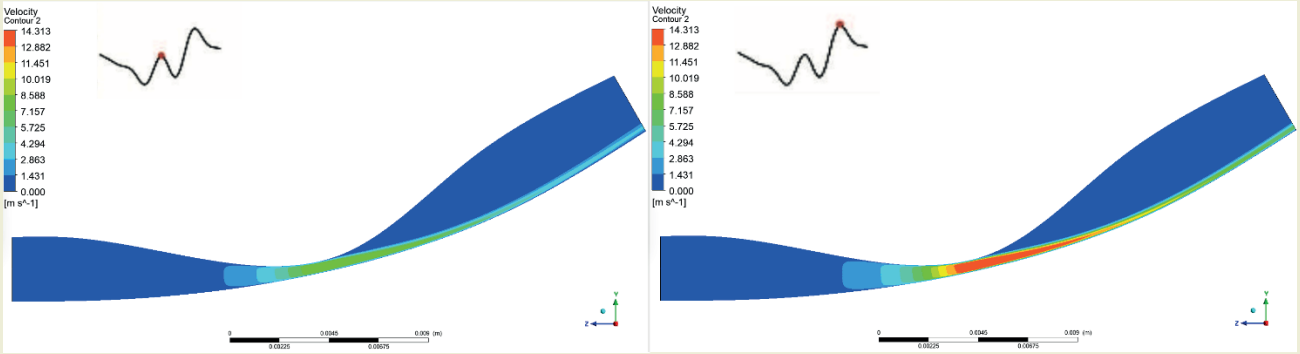

Figure 9. Velocity contour of systole (left) and diastole (right) with 80% stenosis.

B] Velocity contour of 60-degree curvature

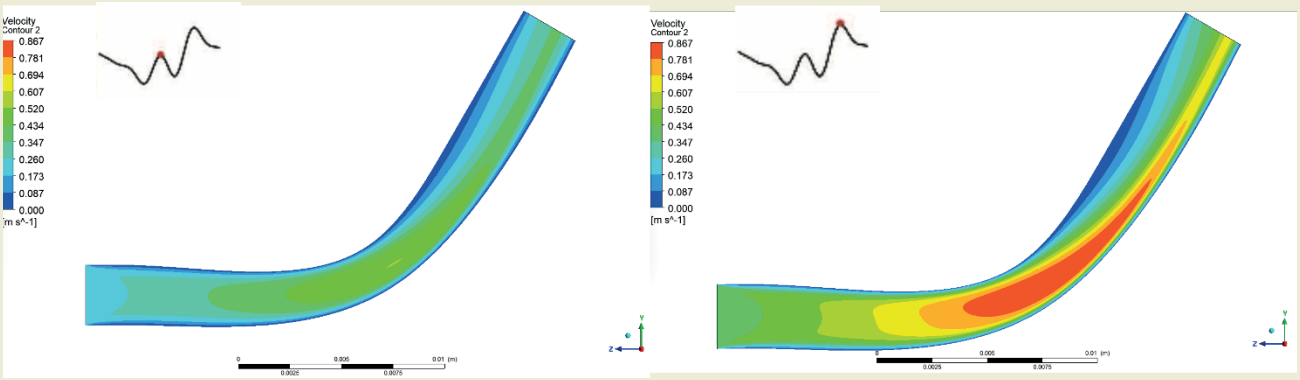

Figure 10. Velocity contour of systole (left) and diastole (right) with 20% stenosis.

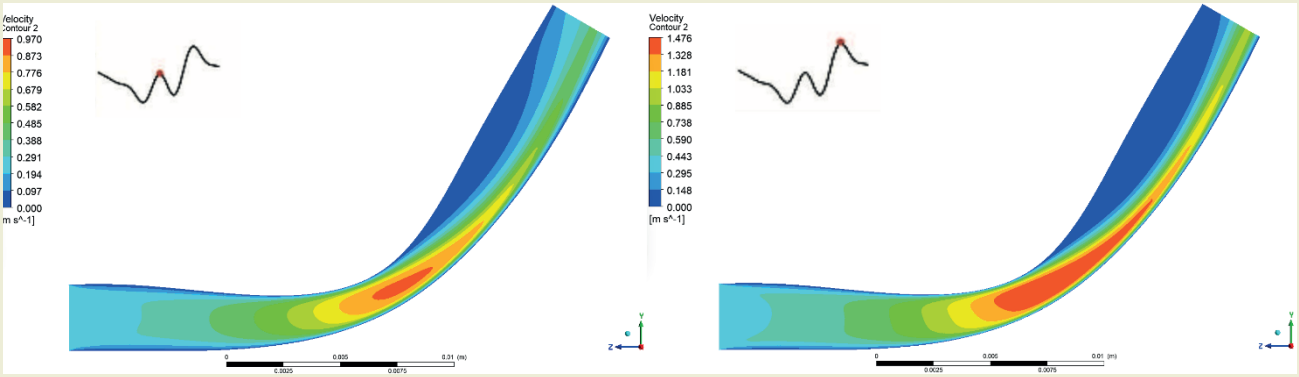

Figure 11. Velocity contour of systole (left) and diastole (right) with 40% stenosis.

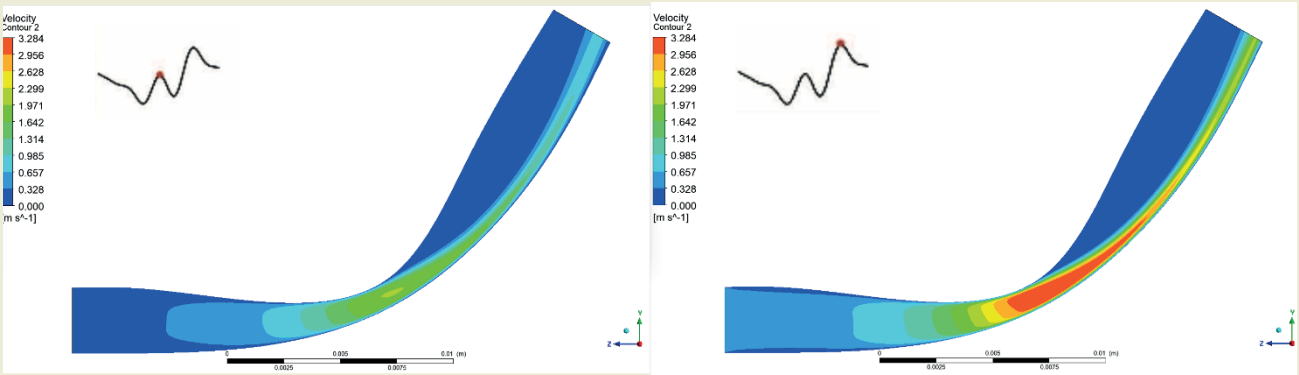

Figure 12. Velocity contour of systole (left) and diastole (right) with 60% stenosis.

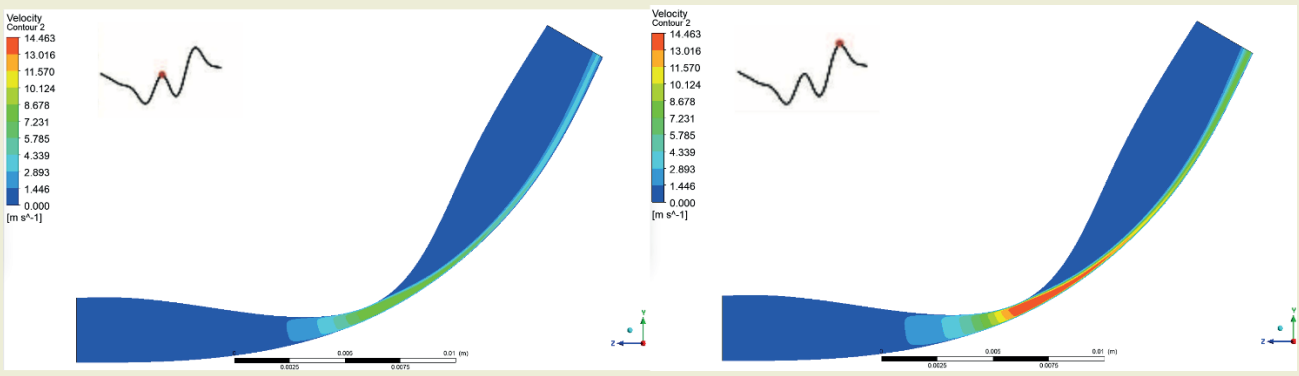

Figure 13. Velocity contour of systole (left) and diastole (right) with 80% stenosis.

C] Velocity contour of 90-degree curvature

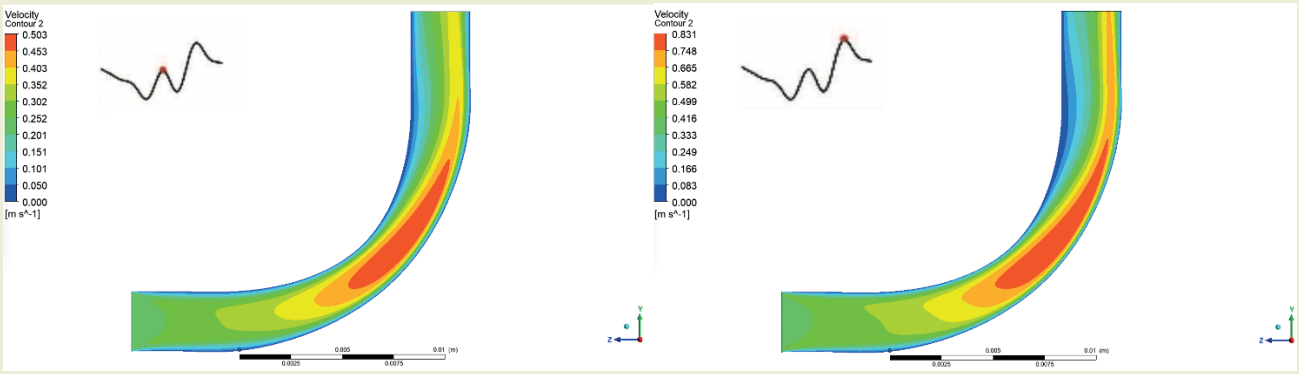

Figure 14. Velocity contour of systole (left) and diastole (right) with 20% stenosis.

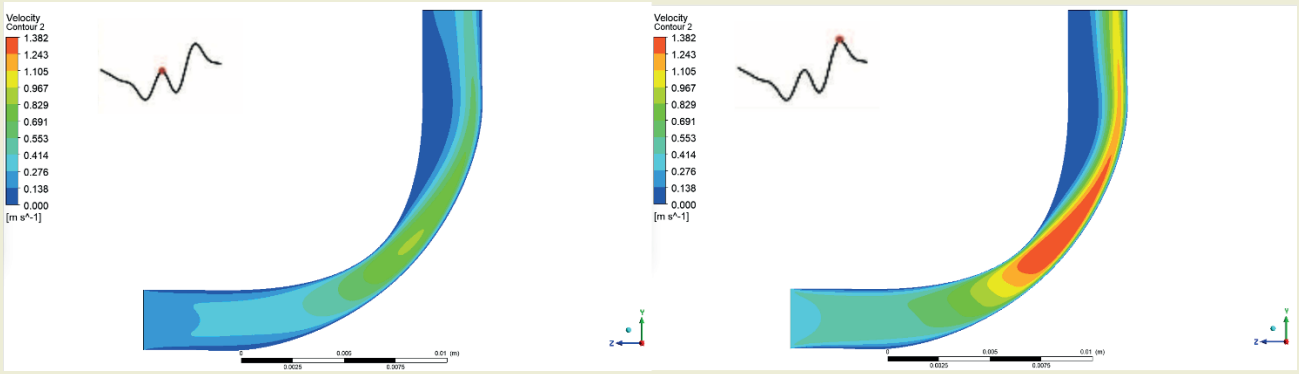

Figure 15. Velocity contour of systole (left) and diastole (right) with 40% stenosis.

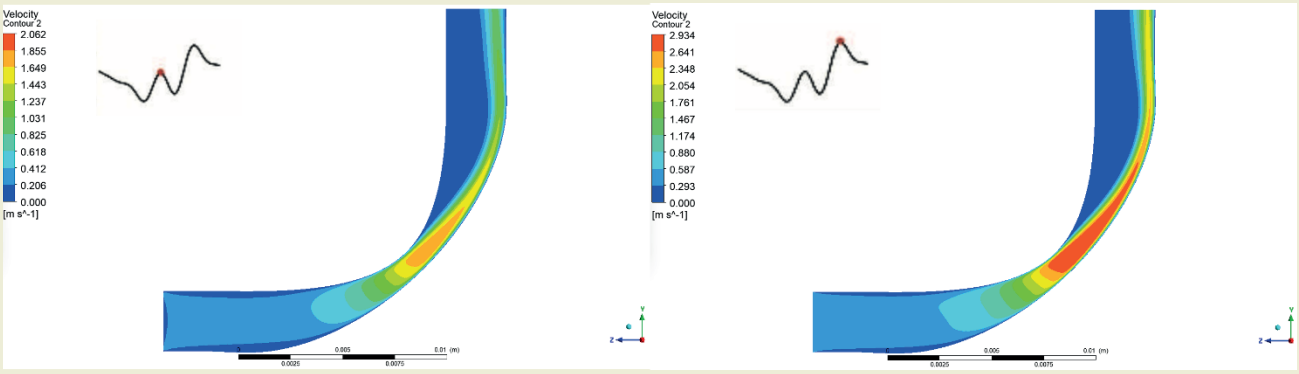

Figure 16. Velocity contour of systole (left) and diastole (right) with 60% stenosis.

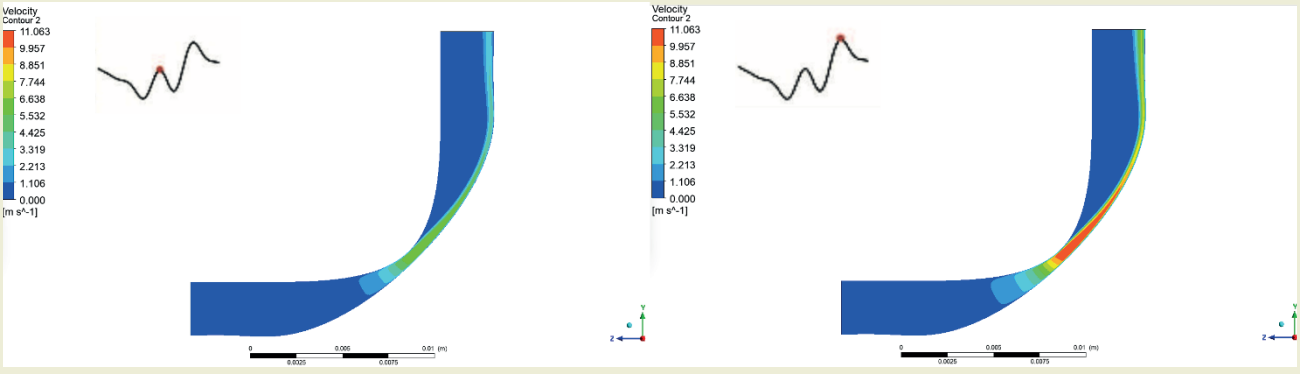

Figure 17. Velocity contour of systole (left) and diastole (right) with 80% stenosis.

3.1-2 Pressure contours for different curvatures and stenoses

A] Pressure contour of 30-degree curvature

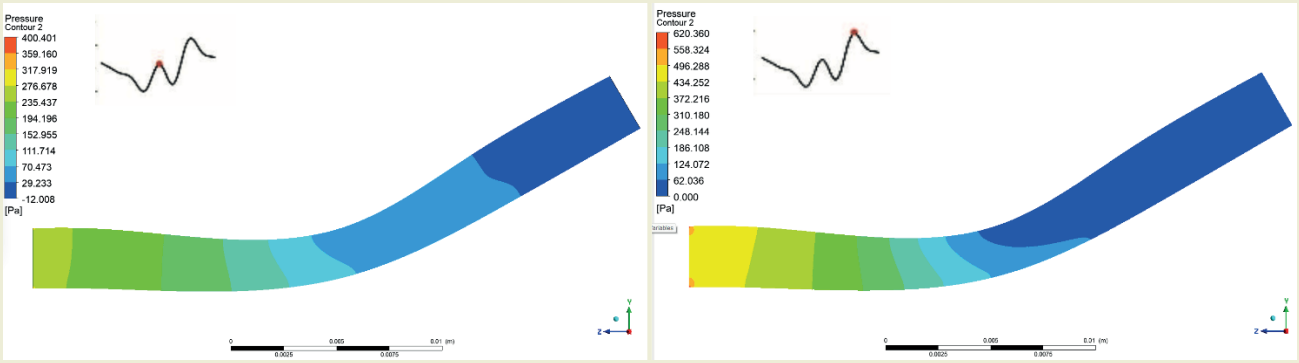

Figure 18. Pressure contour of systole (left) and diastole (right) with 20% stenosis.

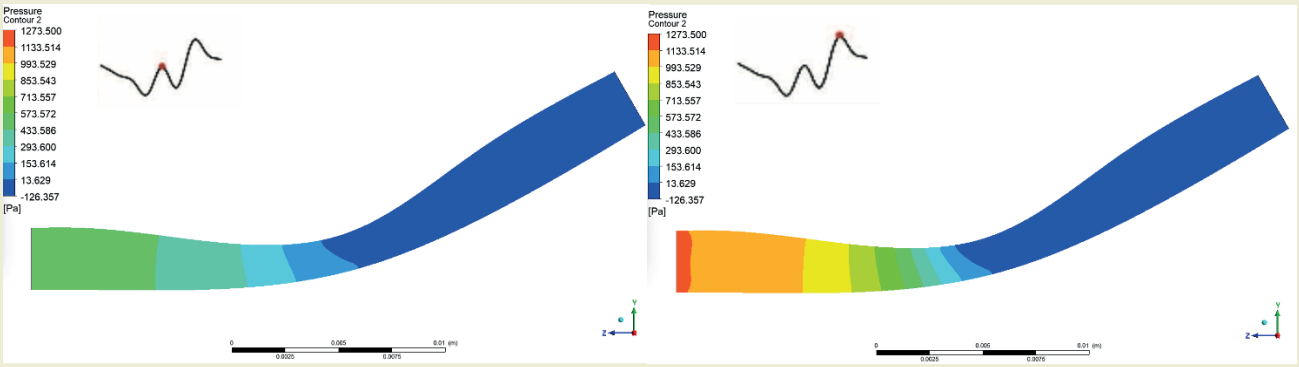

Figure 19. Pressure contour of systole (left) and diastole (right) with 40% stenosis.

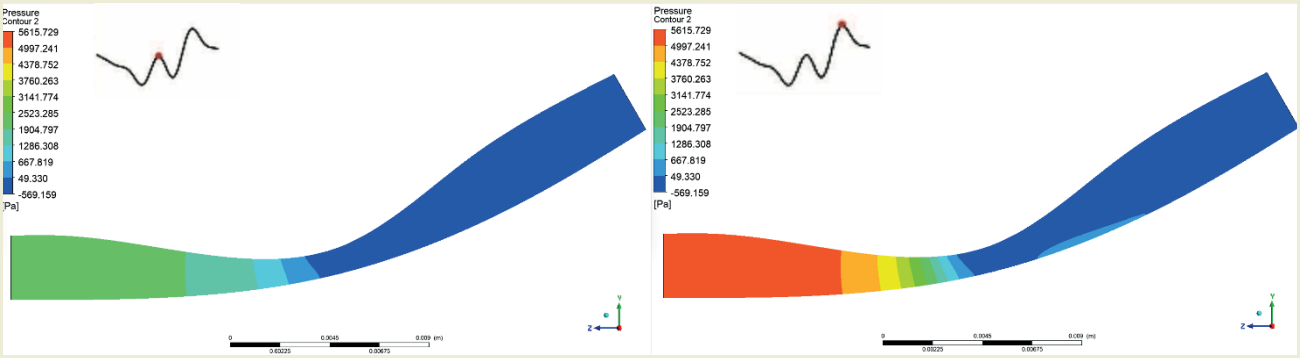

Figure 20. Pressure contour of systole (left) and diastole (right) with 60% stenosis.

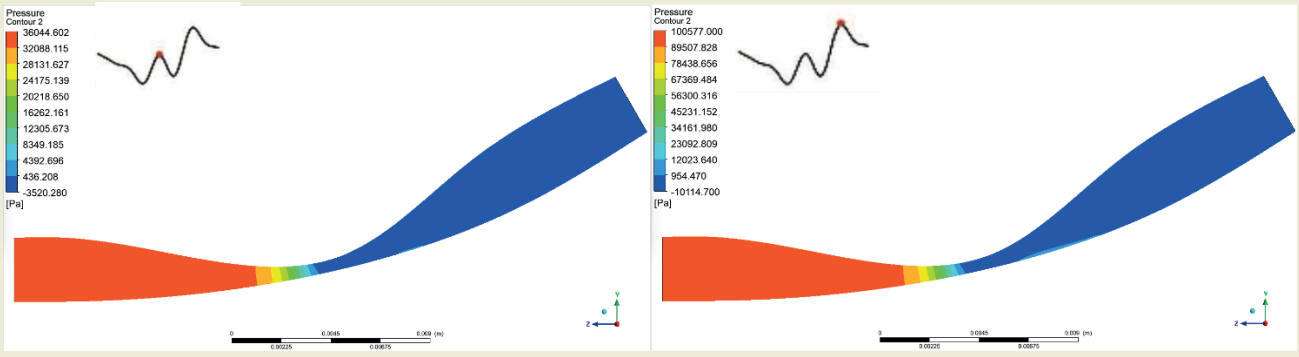

Figure 21. Pressure contour of systole (left) and diastole (right) with 80% stenosis.

B] Pressure contour of 60-degree curvature

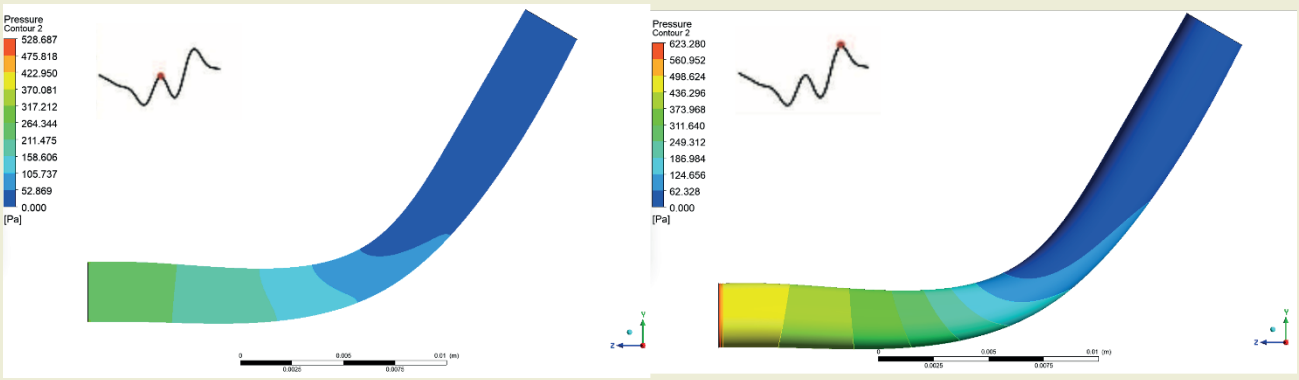

Figure 22. Pressure contour of systole (left) and diastole (right) with 20% stenosis.

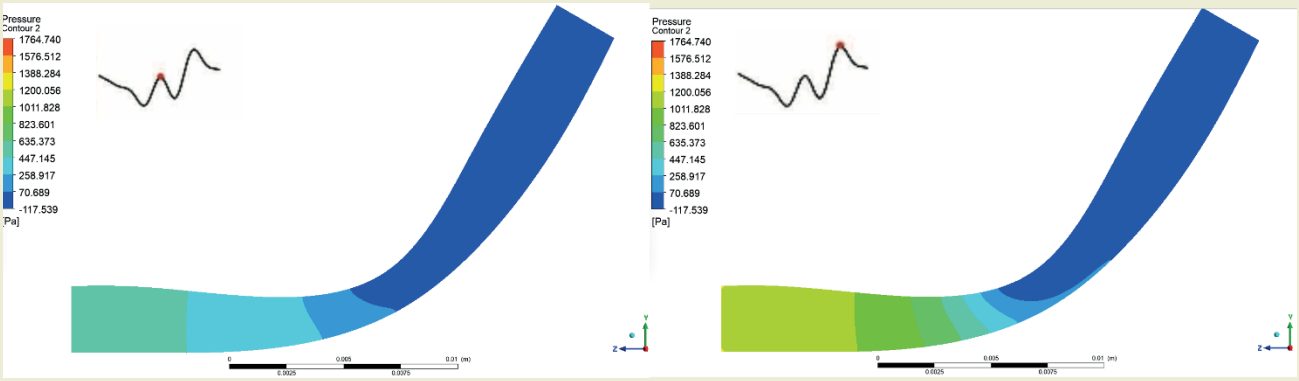

Figure 23. Pressure contour of systole (left) and diastole (right) with 40% stenosis.

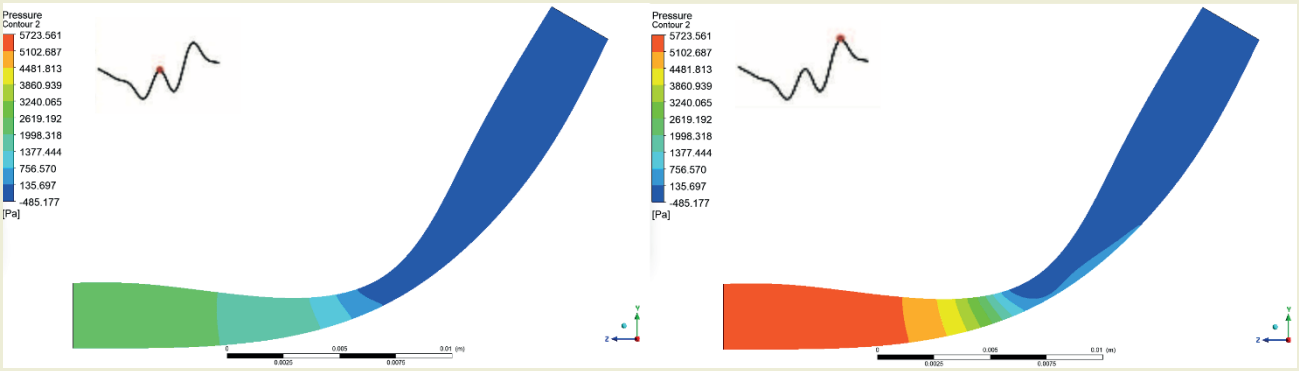

Figure 24. Pressure contour of systole (left) and diastole (right) with 60% stenosis.

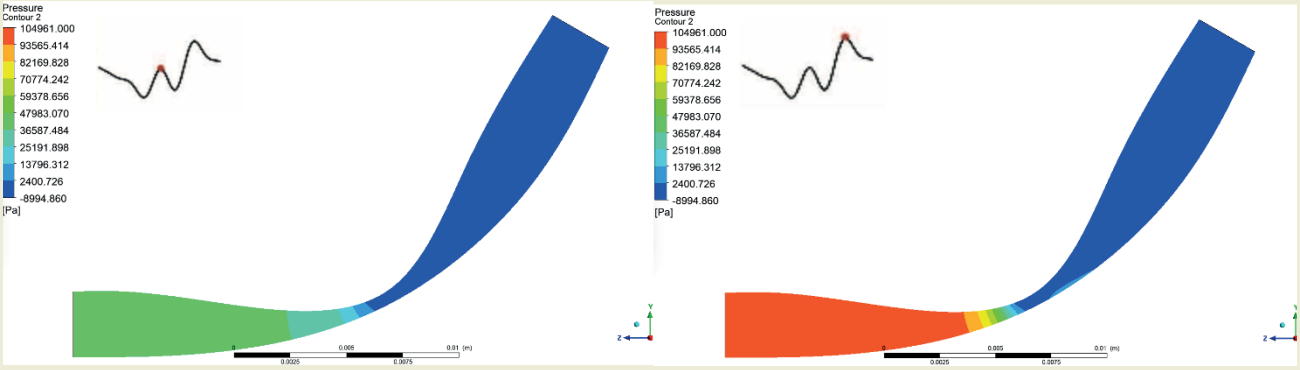

Figure 25. Pressure contour of systole (left) and diastole (right) with 80% stenosis.

C] Pressure contour of 90-degree curvature

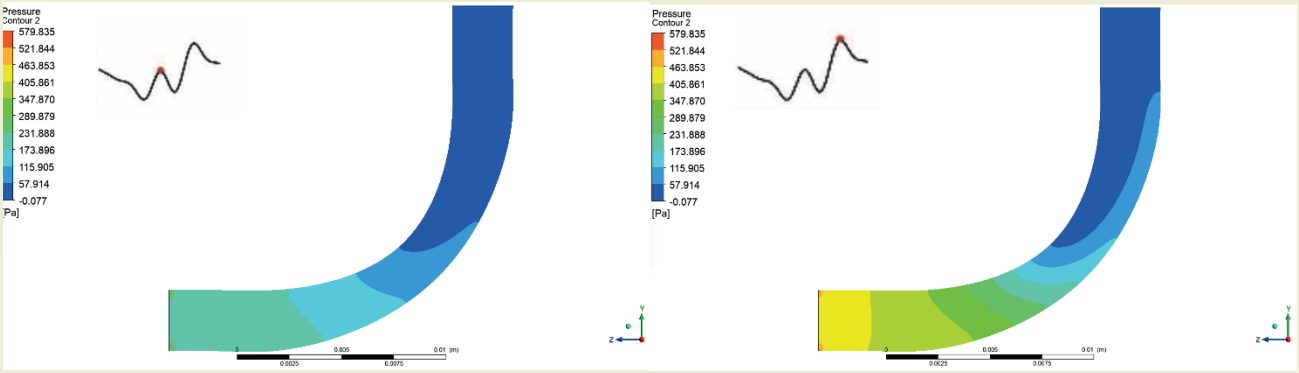

Figure 26. Pressure contour of systole (left) and diastole (right) with 20% stenosis.

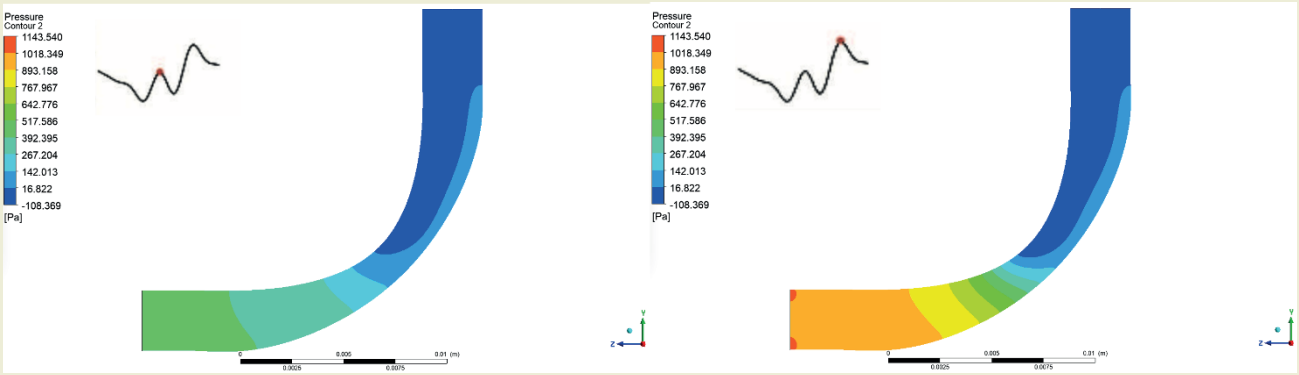

Figure 27. Pressure contour of systole (left) and diastole (right) with 40% stenosis.

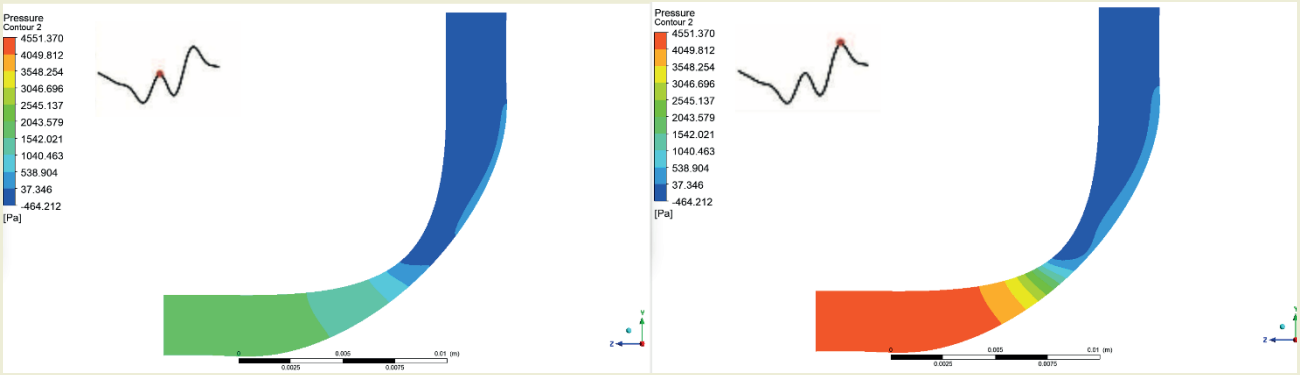

Figure 28. Pressure contour of systole (left) and diastole (right) with 60% stenosis.

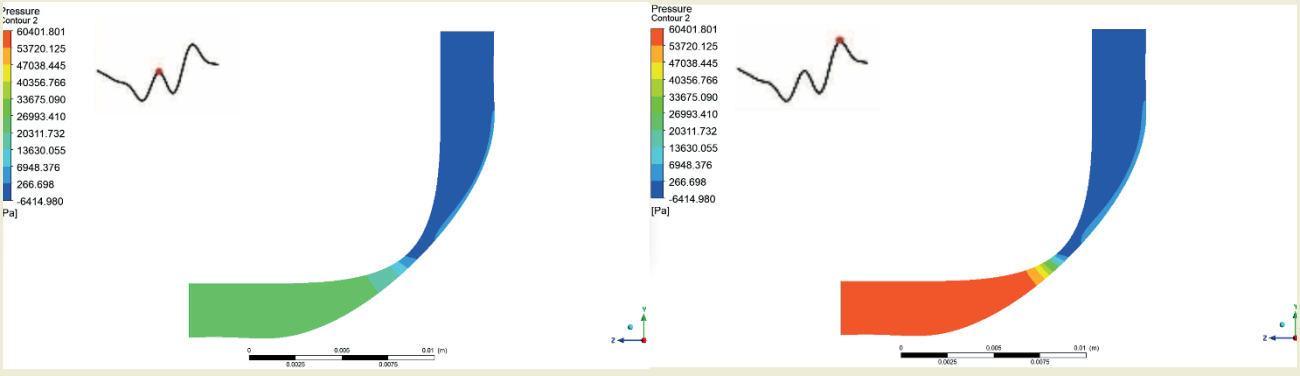

Figure 29. Pressure contour of systole (left) and diastole (right) with 80% stenosis.

3.1-3 WSS contours for different curvatures and stenoses

A] WSS contour of 30-degree curvature

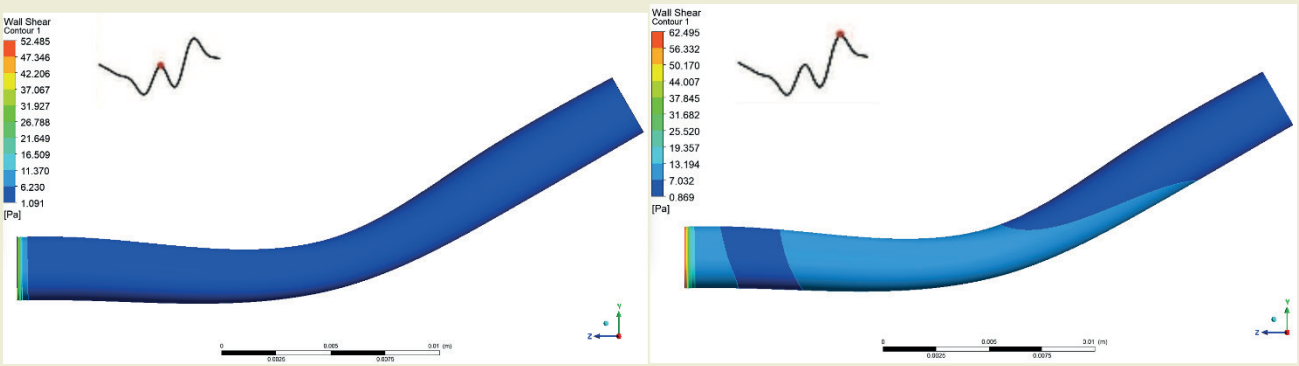

Figure 30. Wall shear stress (WSS) contour of systole (left) and diastole (right) with 20% stenosis.

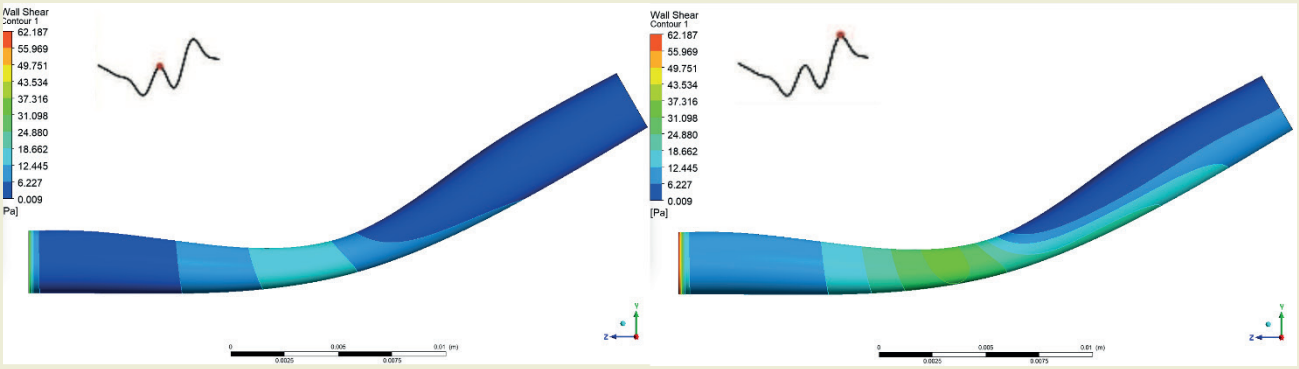

Figure 31. Wall shear stress (WSS) contour of systole (left) and diastole (right) with 40% stenosis.

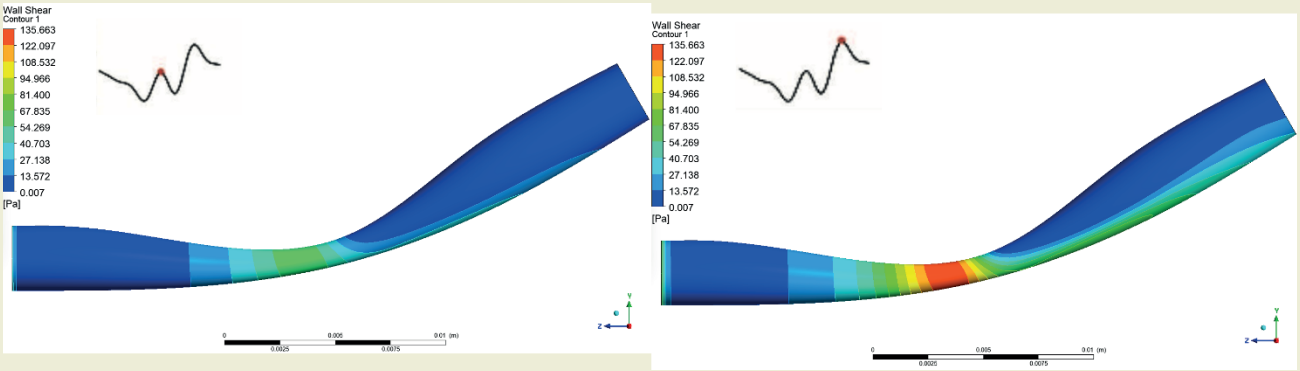

Figure 32. Wall shear stress (WSS) contour of systole (left) and diastole (right) with 60% stenosis.

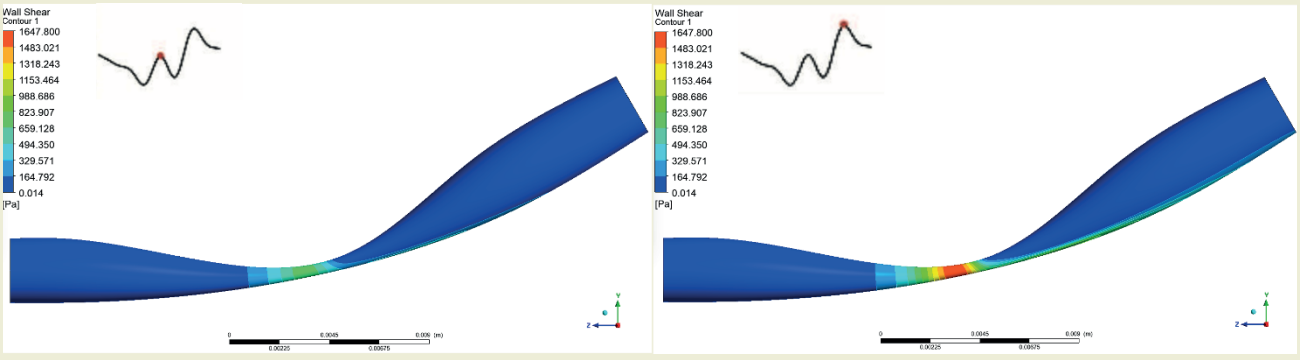

Figure 33. Wall shear stress (WSS) contour of systole (left) and diastole(right) with 80% stenosis.

B] WSS contour of 60-degree curvature

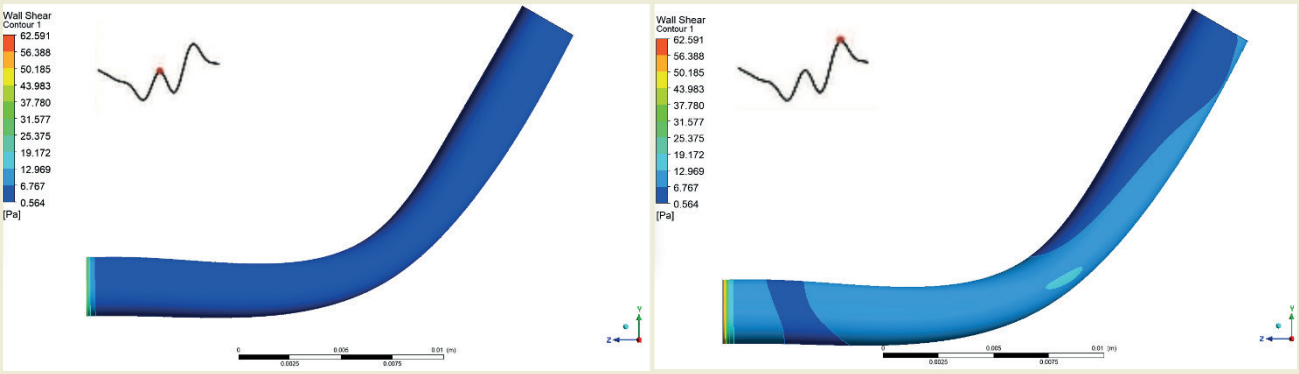

Figure 34. Wall shear stress (WSS) contour of systole (left) and diastole (right) with 20% stenosis.

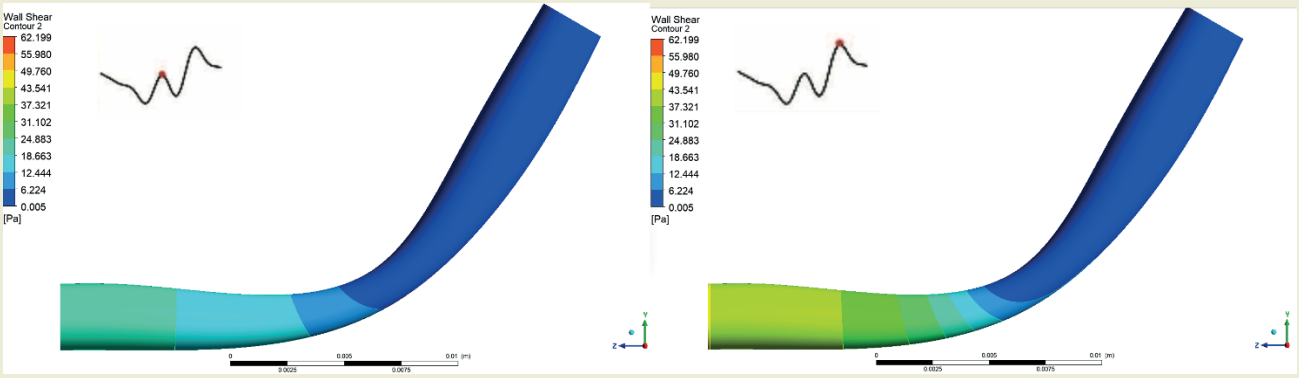

Figure 35. Wall shear stress (WSS) contour of systole (left) and diastole(right) with 40% stenosis.

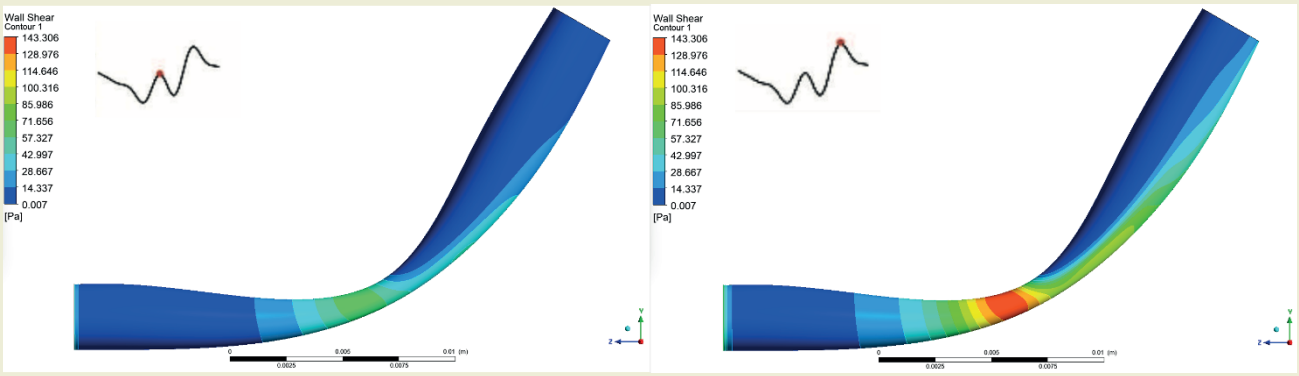

Figure 36. Wall shear stress (WSS) contour of systole (Left) and Diastole(right) with 60% stenosis.

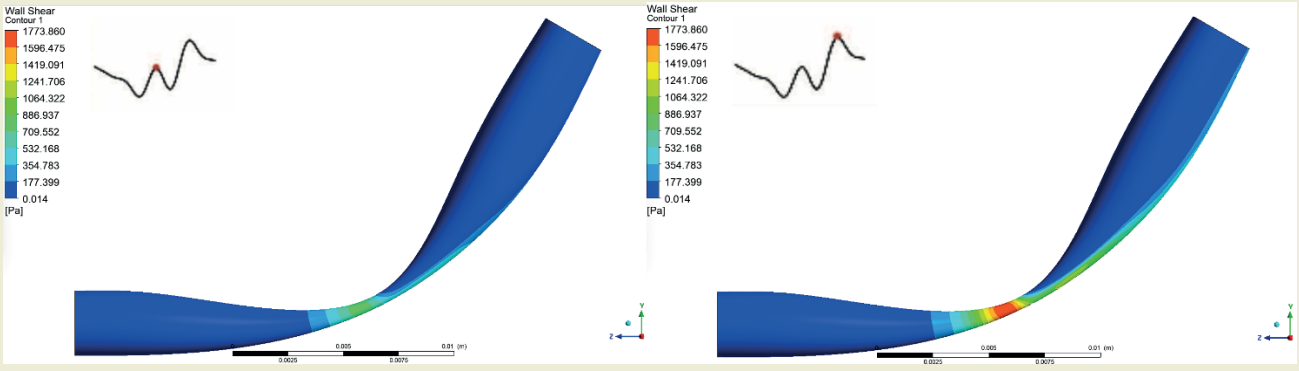

Figure 37. Wall shear stress (WSS) contour of systole (left) and diastole (right) with 80% stenosis.

C] WSS contour of 90-degree curvature

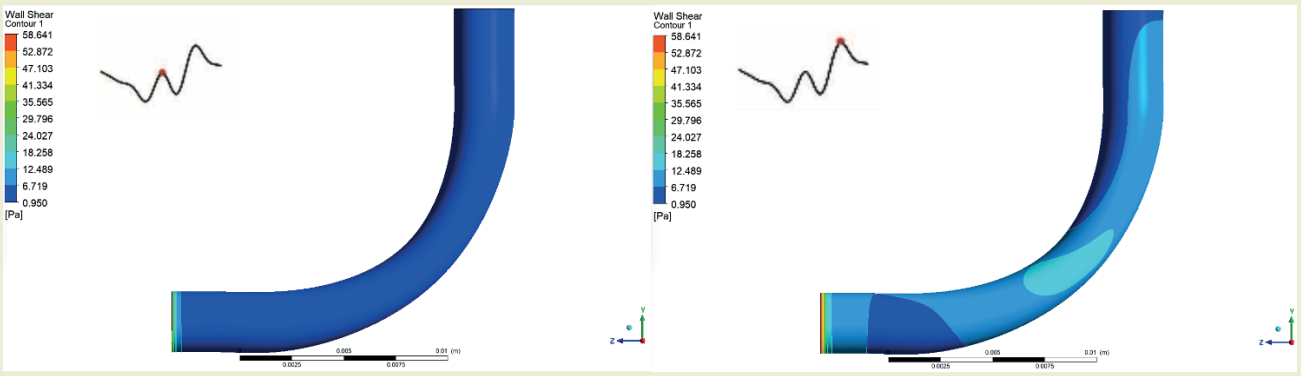

Figure 38. Wall shear stress (WSS) contour of systole (left) and diastole (right) with 20% stenosis.

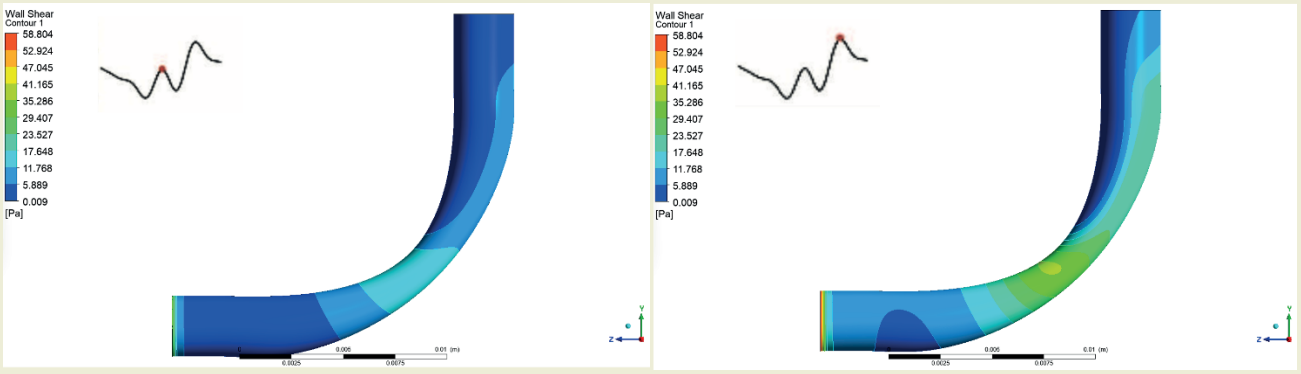

Figure 39. Wall shear stress (WSS) contour of systole (left) and diastole (right) with 40% stenosis.

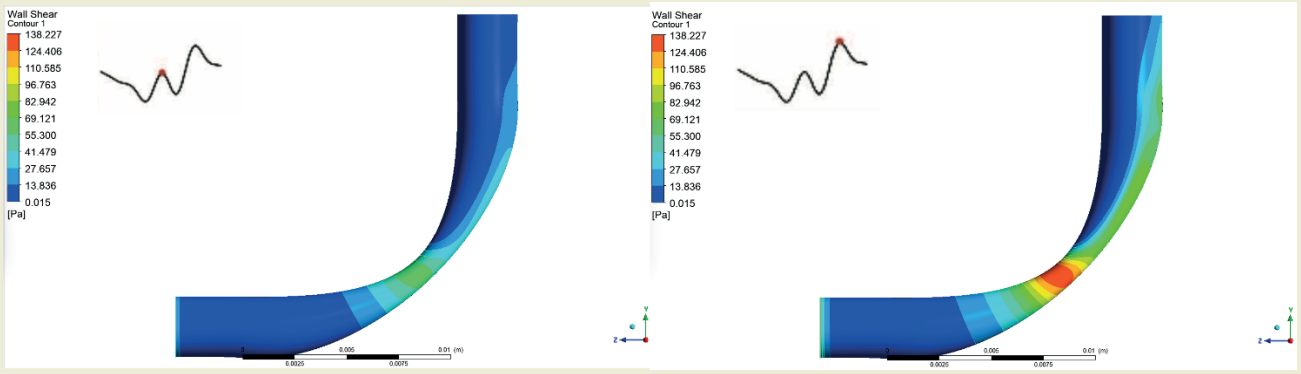

Figure 40. Wall shear stress (WSS) contour of systole (left) and diastole (right) with 60% stenosis.

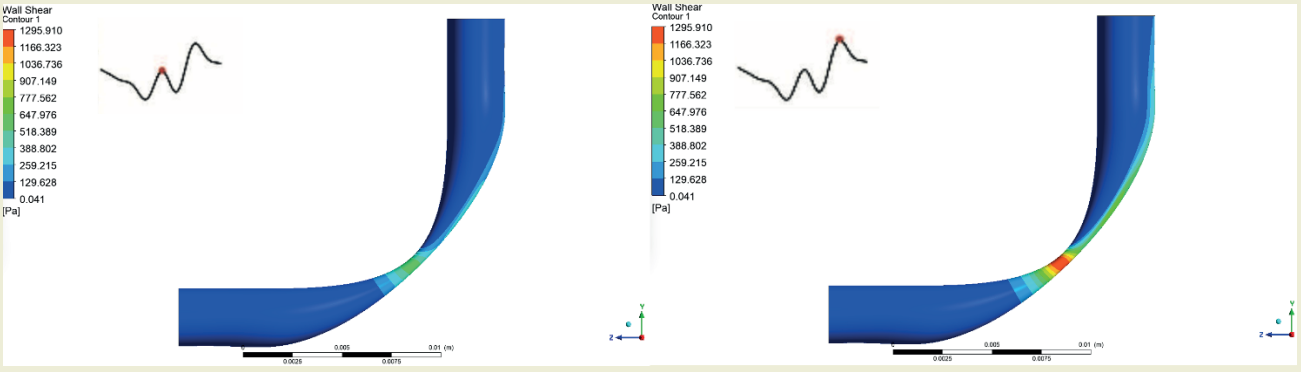

Figure 41. Wall shear stress (WSS) contour of systole (left) and diastole (right) with 80% stenosis.

3.1-4 Velocity vector contour plots for different curvatures and stenoses

A] Velocity vector plot of 30-degree curvature

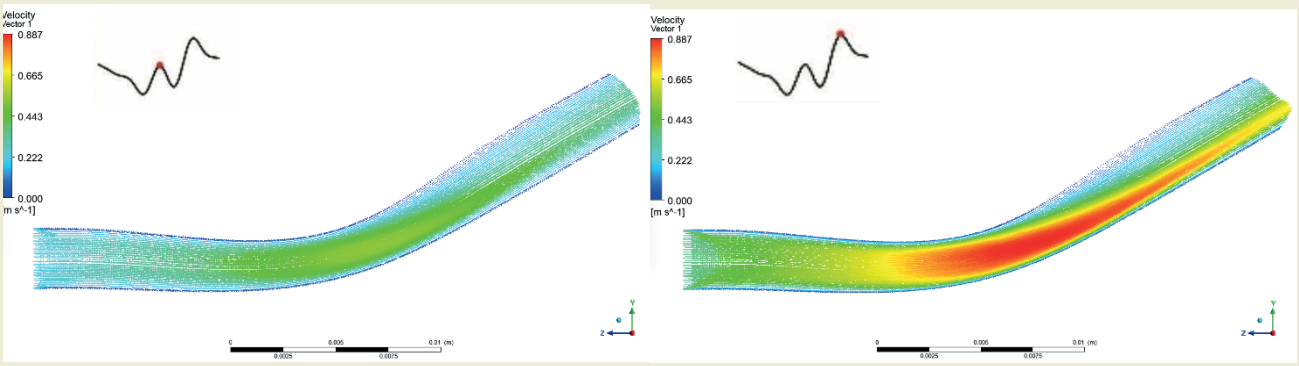

Figure 42. Velocity vector plot of systole (left) and diastole (right) with 20% stenosis.

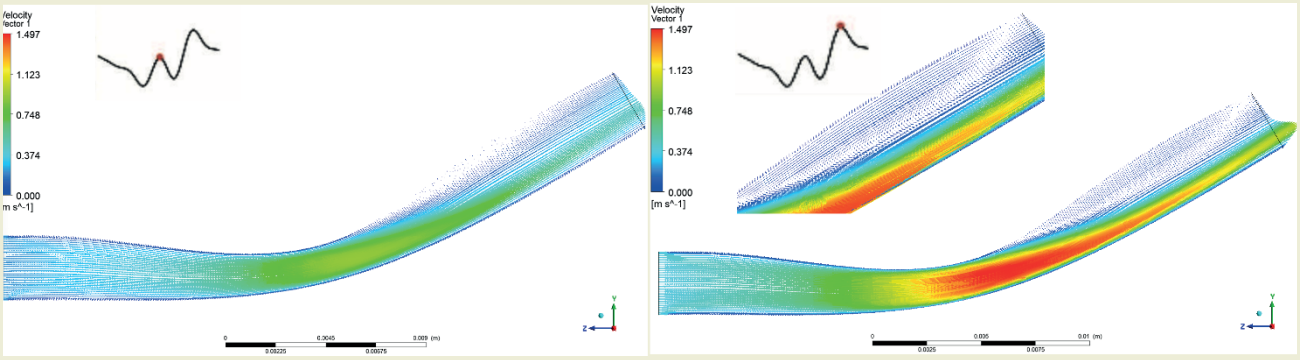

Figure 43. Velocity vector plot of systole (left) and diastole (right) with 40% stenosis.

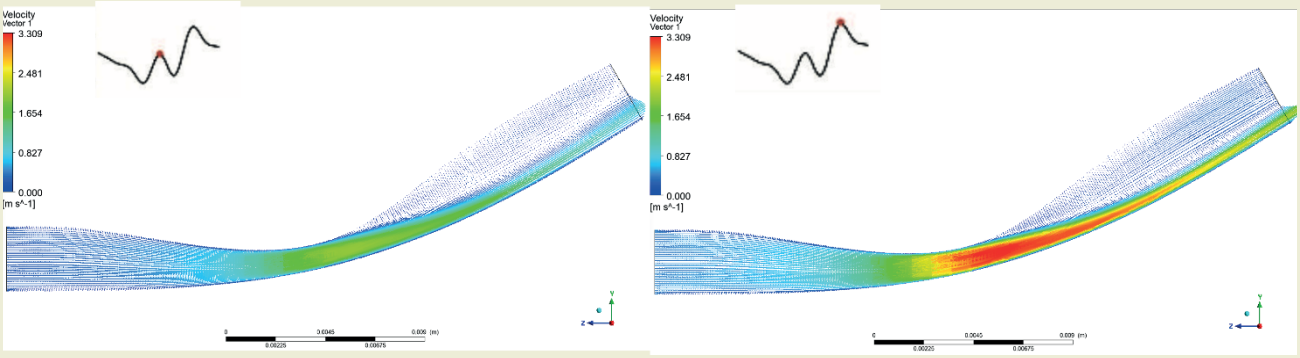

Figure 44. Velocity vector plot of systole (left) and diastole (right) with 60% stenosis.

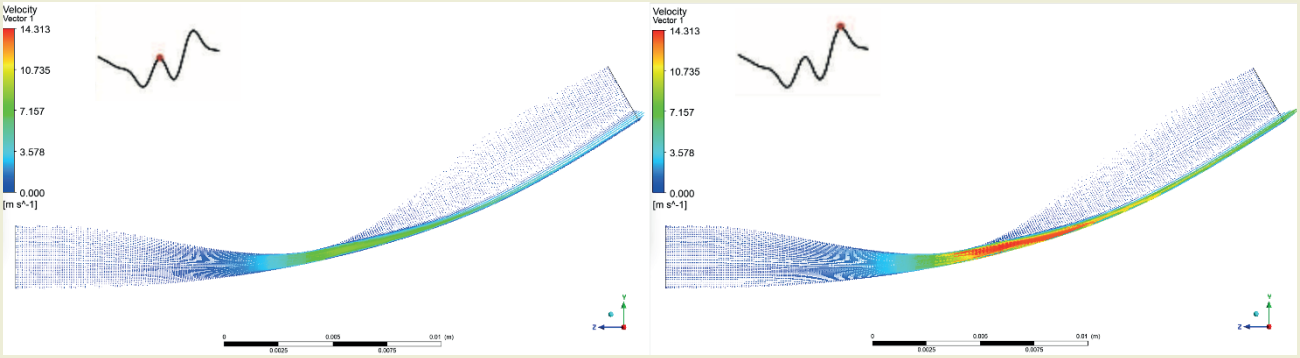

Figure 45. Velocity vector plot of systole (left) and diastole (right) with 80% stenosis.

B] Velocity vector plot of 30-degree curvature

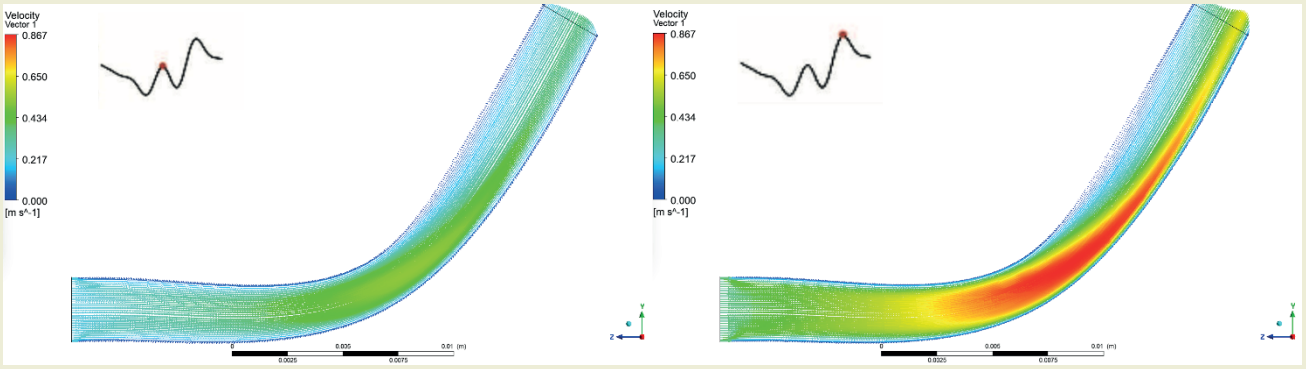

Figure 46. Velocity vector plot of systole (left) and diastole (right) with 20% stenosis.

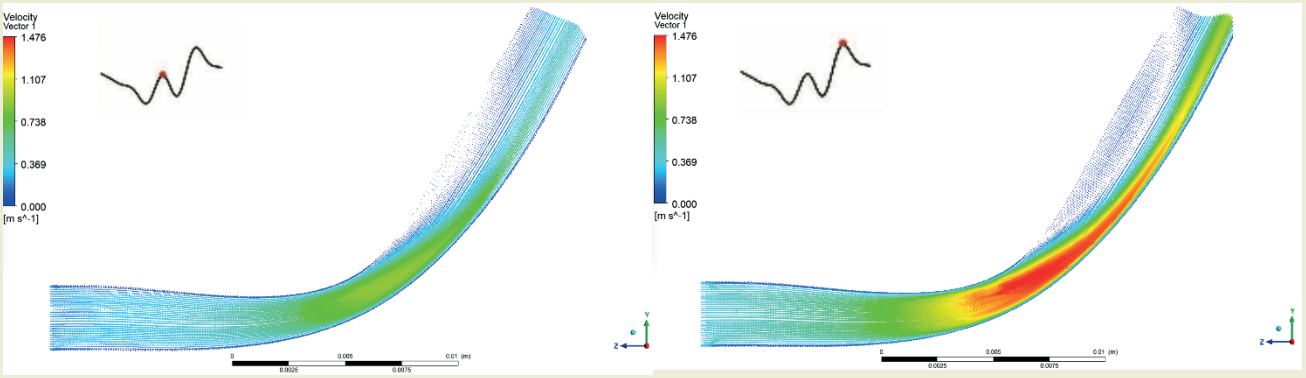

Figure 47. Velocity vector plot of systole (left) and diastole (right) with 40% stenosis.

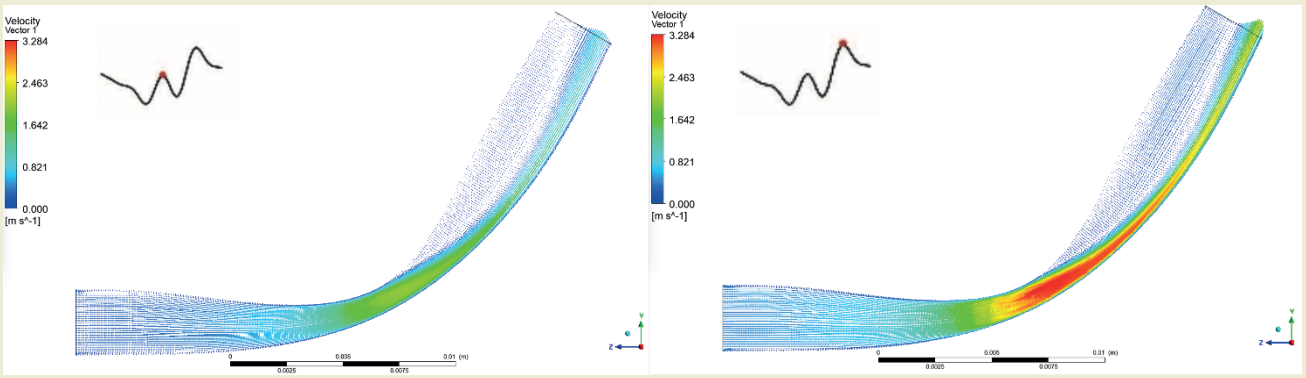

Figure 48. Velocity vector plot of systole (left) and diastole (right) with 60% stenosis.

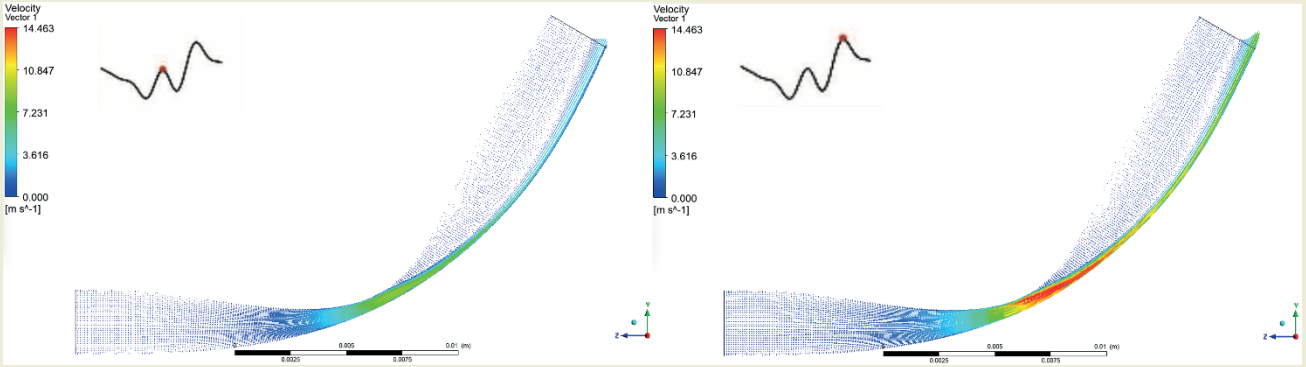

Figure 49. Velocity vector plot of systole (left) and diastole (right) with 80% stenosis.

C] Velocity vector plot of 90-degree curvature

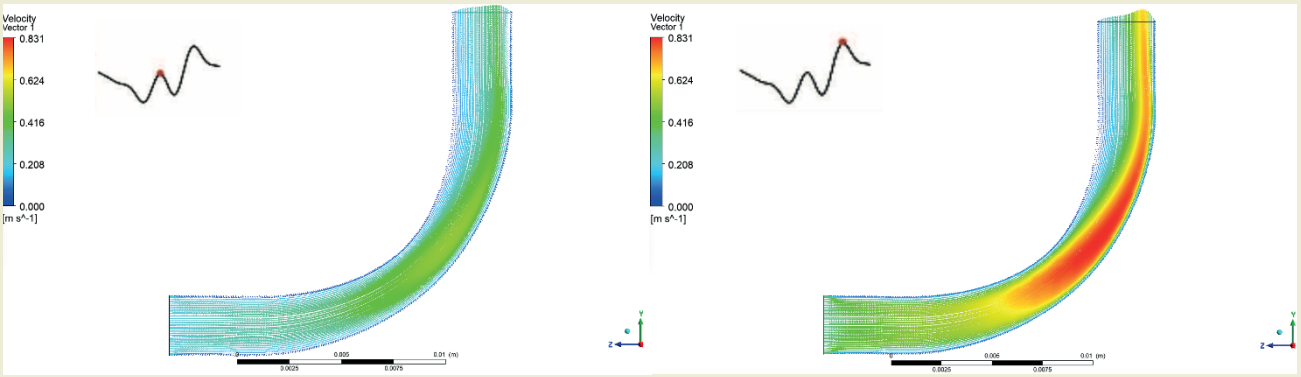

Figure 50. Velocity vector plot of systole (left) and diastole (right) with 20% stenosis.

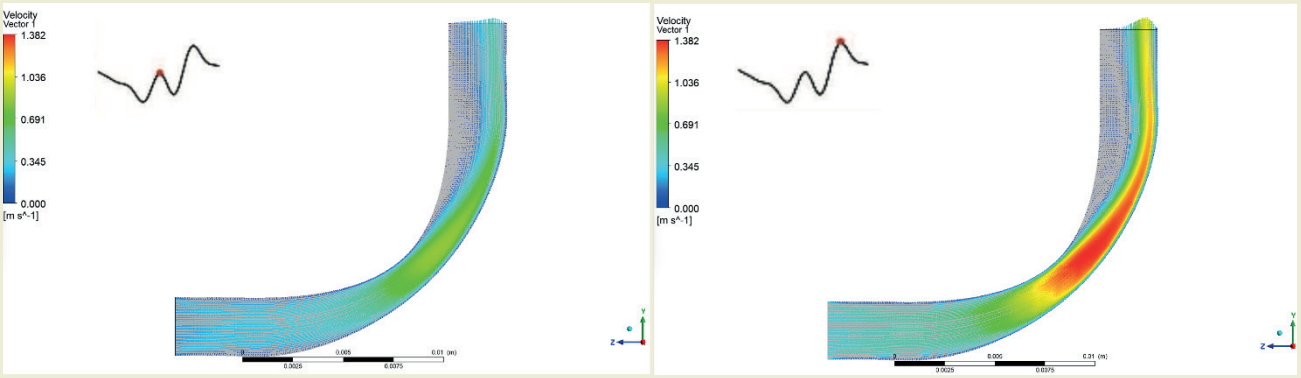

Figure 51. Velocity vector plot of systole (left) and diastole (right) with 40% stenosis.

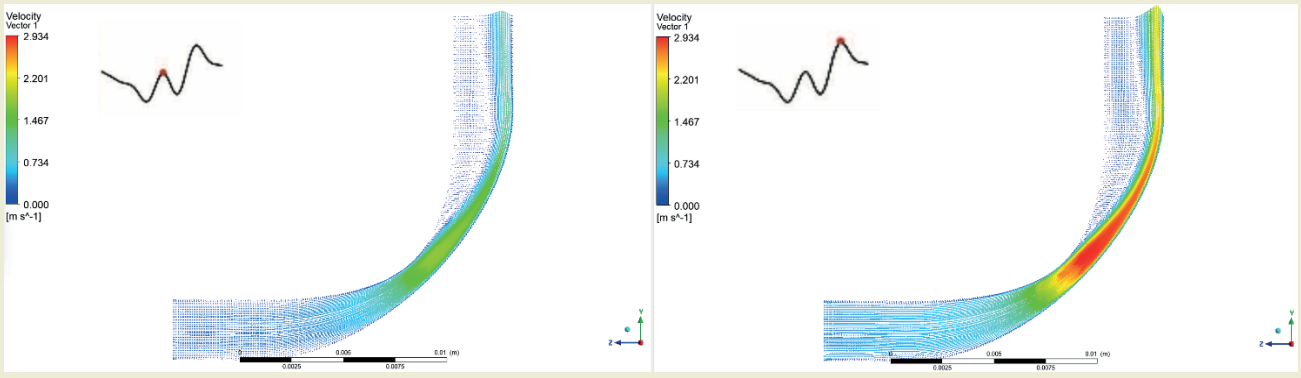

Figure 52. Velocity vector plot of systole (left) and diastole (right) with 60% stenosis.

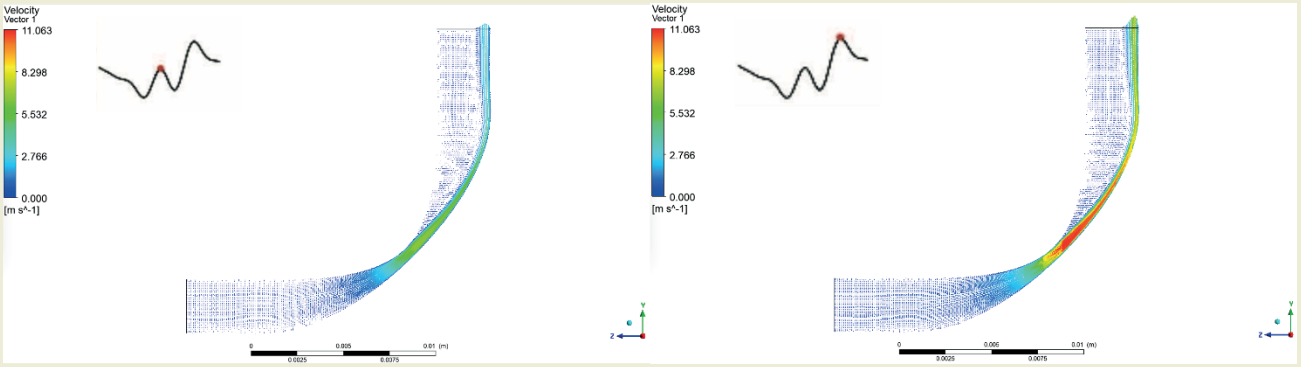

Figure 53. Velocity vector plot of systole (left) and diastole (right) with 80% stenosis.

3.2. FSI (arterial stress and deformation) Visualizations

Next, we present the structural (stress) results, for Von Mises stress and total deformation (displacement) of the artery structure, again for 3 curvature cases (30, 60, 90 degrees) each with 4 stenosis depths (20, 40, 60, 80%). The results are therefore grouped in 12 sets in 2 subsections (A, B). In each figure we provide 2 graphs, one for the systole and the other for the diastole.

3.2-1 Von Mises stress contour plots for different curvatures and stenoses

A] Von Mises stress contour of 30-degree curvature

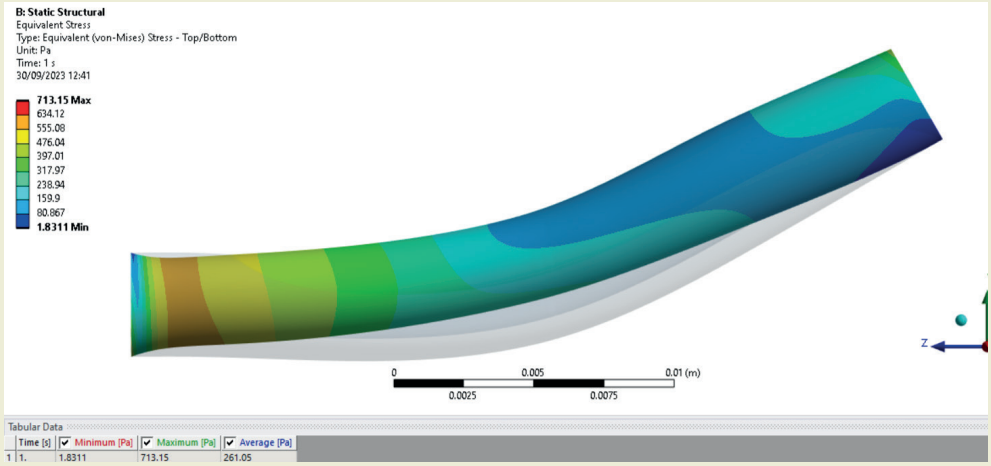

Figure 54. Von Mises stress of artery with 20% stenosis.

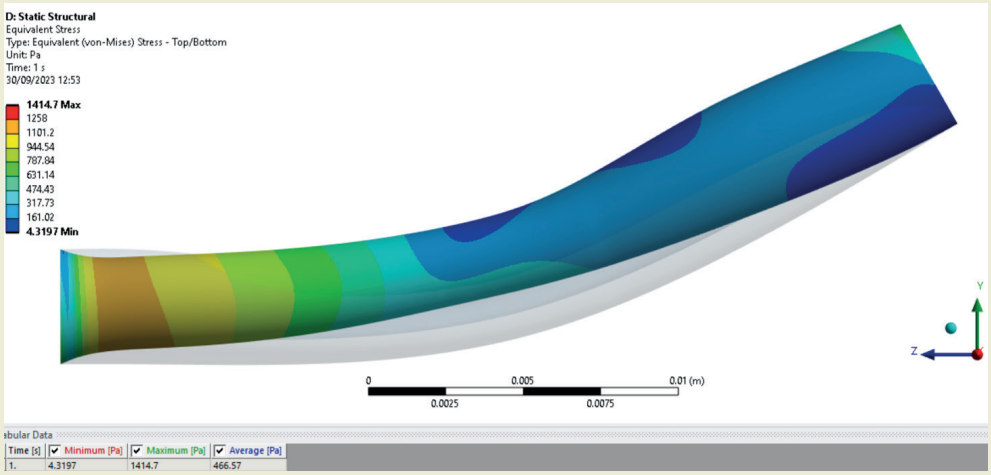

Figure 55. Von Mises stress of artery with 40% stenosis.

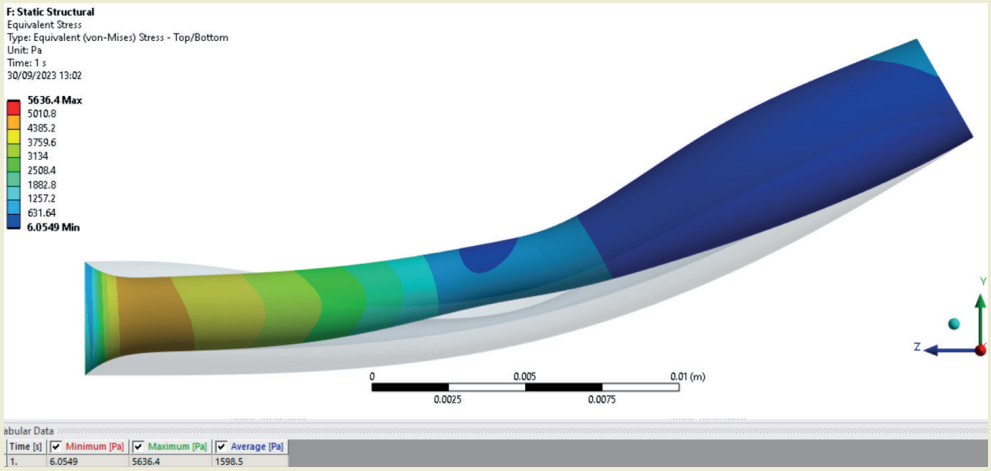

Figure 56. Von Mises stress of artery with 60% stenosis.

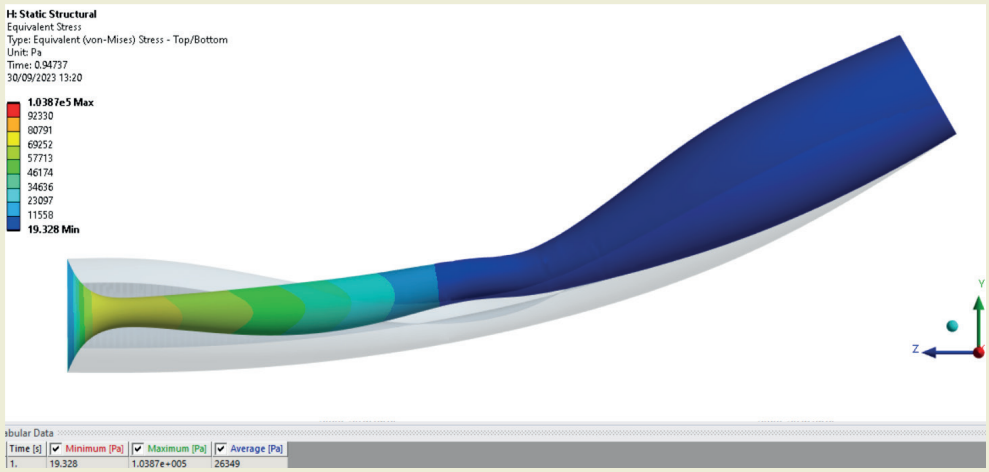

Figure 57. Von Mises stress of artery with 80% stenosis.

B] Von Mises stress contour of 60-degree curvature

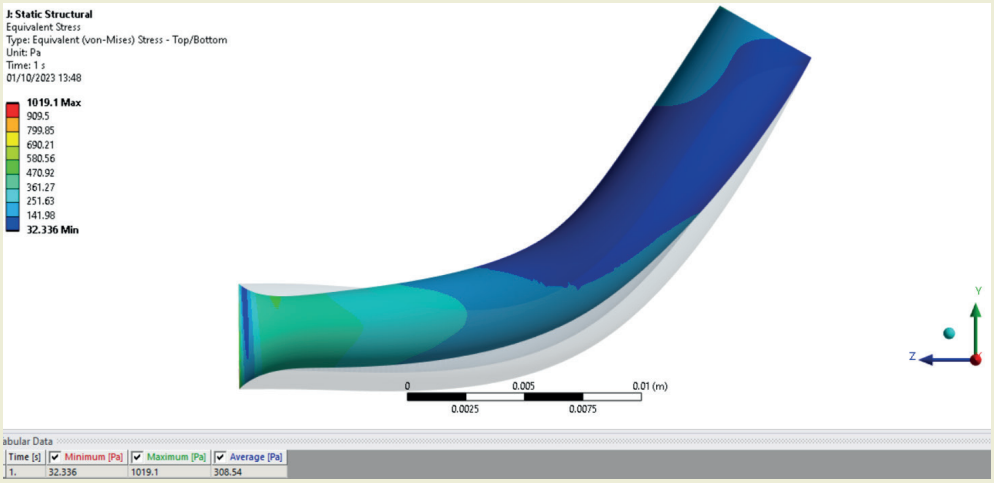

Figure 58. Von Mises stress of artery with 20% stenosis.

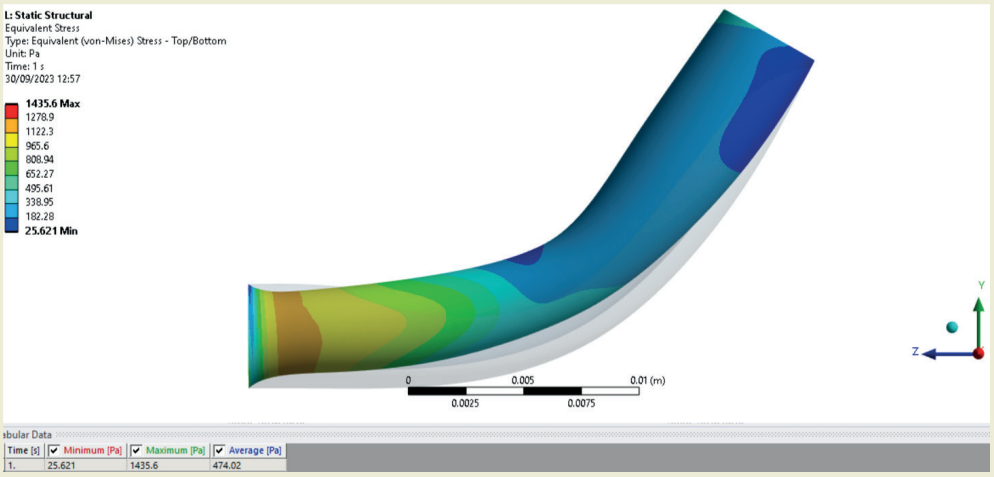

Figure 59. Von Mises stress of artery with 40% stenosis.

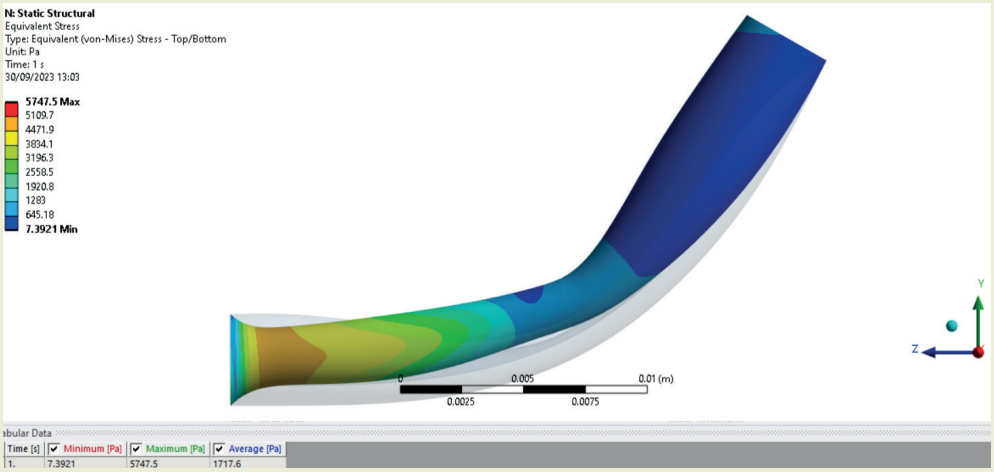

Figure 60. Von Mises stress of artery with 60% stenosis.

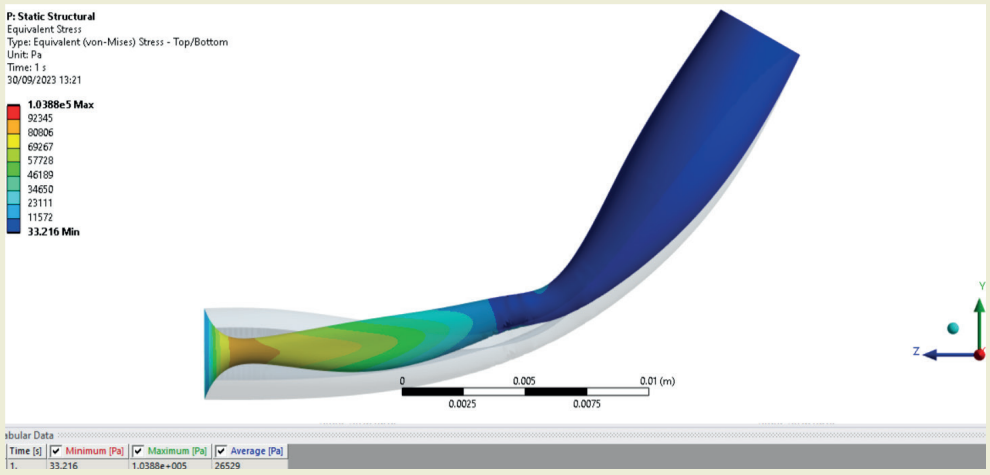

Figure 61. Von Mises stress of artery with 80% stenosis.

C] Von Mises stress contour of 90-degree curvature

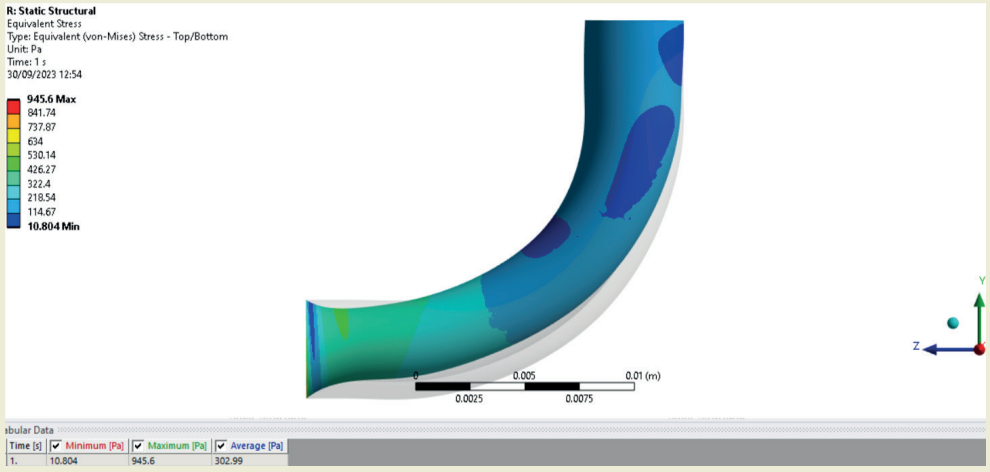

Figure 62. Von Mises stress of artery with 20% stenosis.

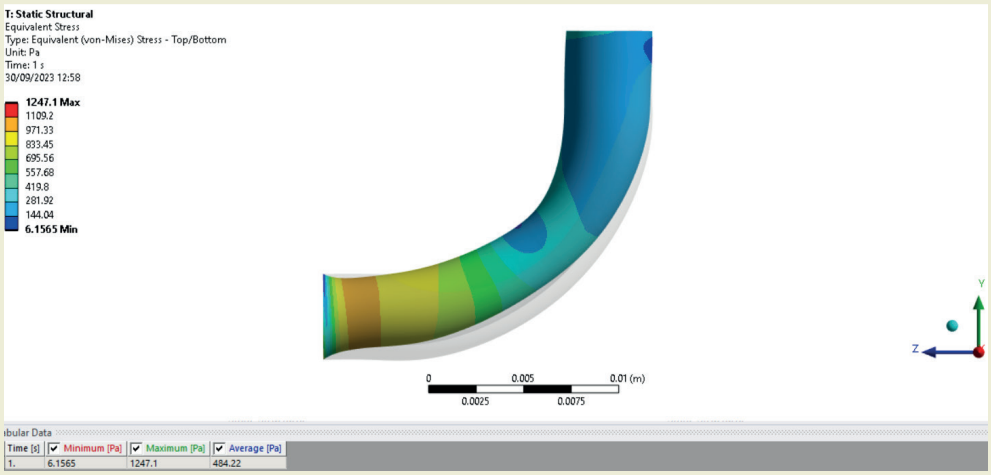

Figure 63. Von Mises stress of artery with 40% stenosis.

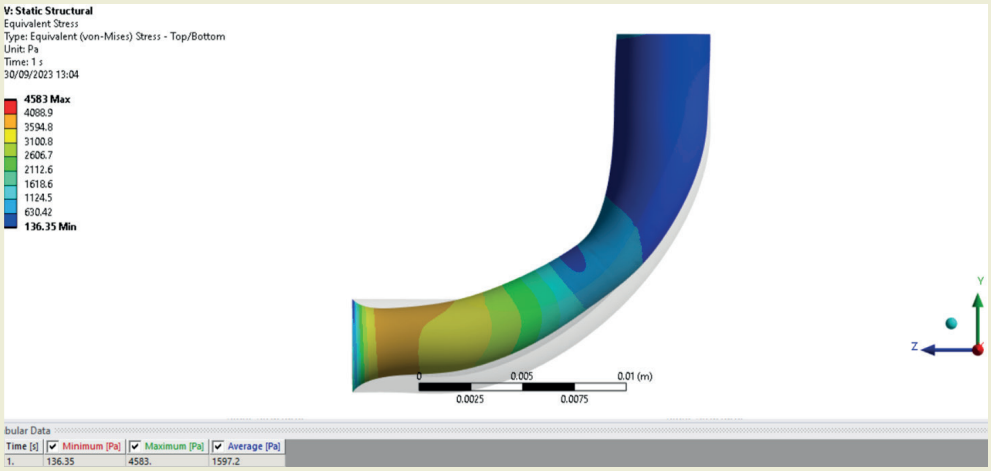

Figure 64. Von Mises stress of artery with 60% stenosis.

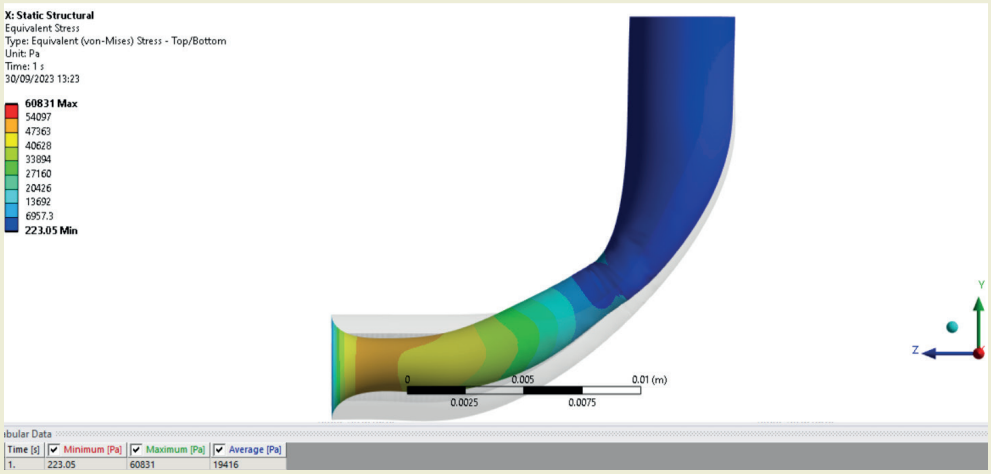

Figure 65. Von Mises stress of artery with 80% stenosis.

3.2-2 Total displacement (deformation) contour plots for different curvatures and stenoses

A] Total displacement contour of 30-degree curvature

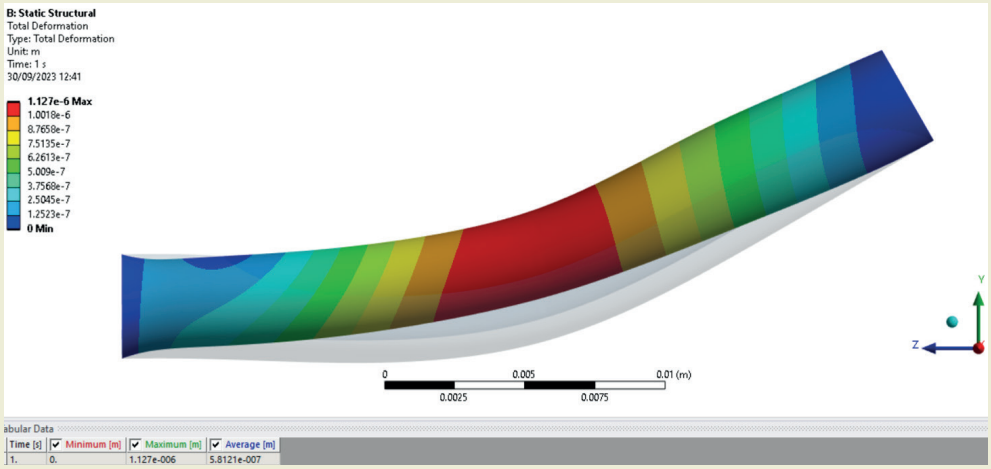

Figure 66. Total displacement of artery with 20 % stenosis.

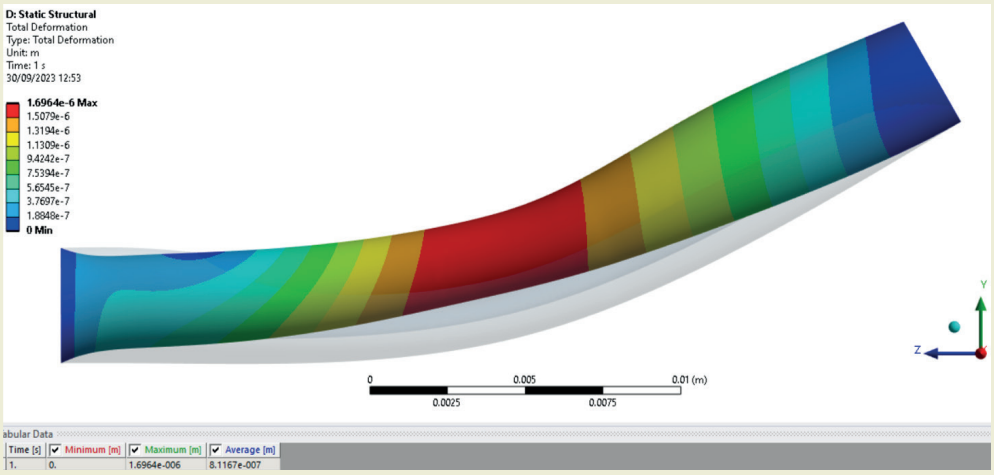

Figure 67. Total displacement of artery with 40% stenosis.

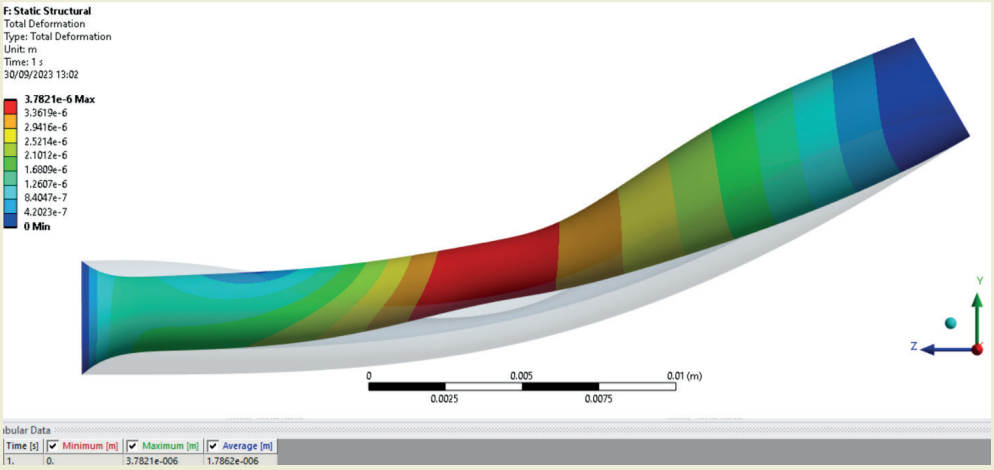

Figure 68. Total displacement of artery with 60% stenosis.

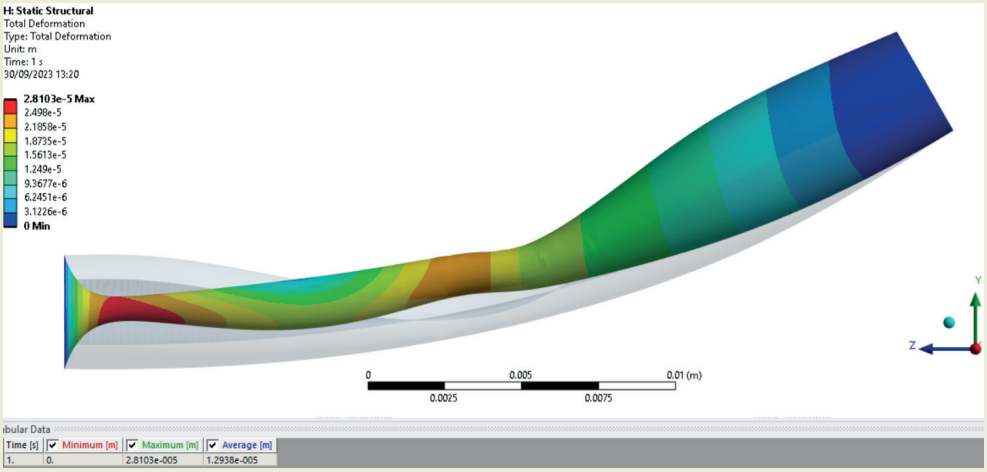

Figure 69. Total displacement of artery with 80 % stenosis.

B] Total displacement contour of 60-degree curvature

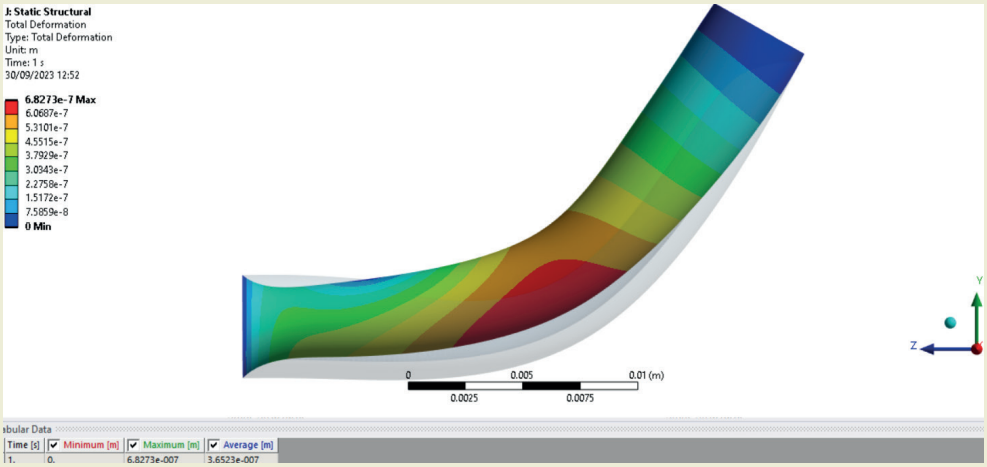

Figure 70. Total displacement of artery with 20 % stenosis.

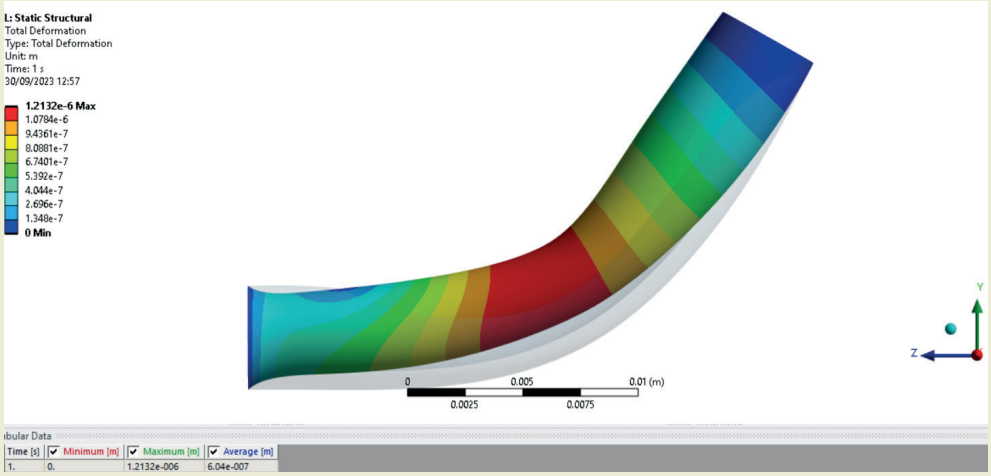

Figure 71. Total displacement of artery with 40 % stenosis.

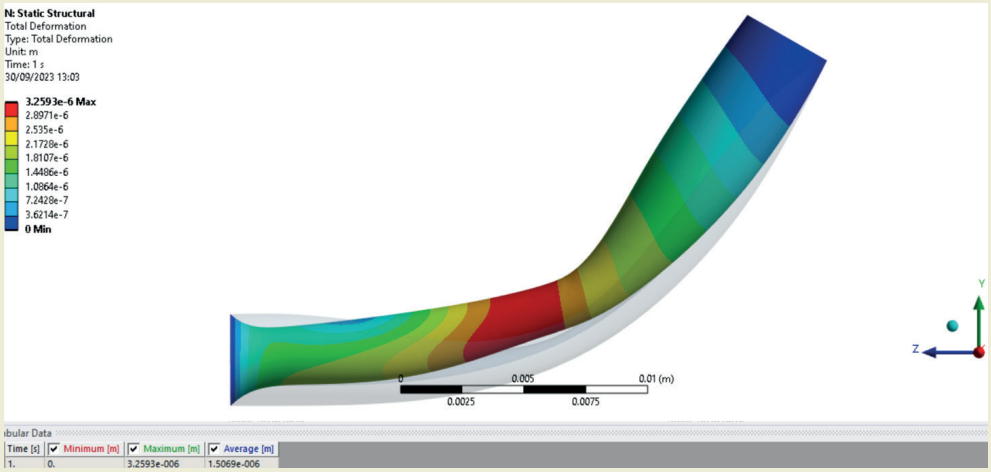

Figure 72. Total displacement of artery with 60 % stenosis.

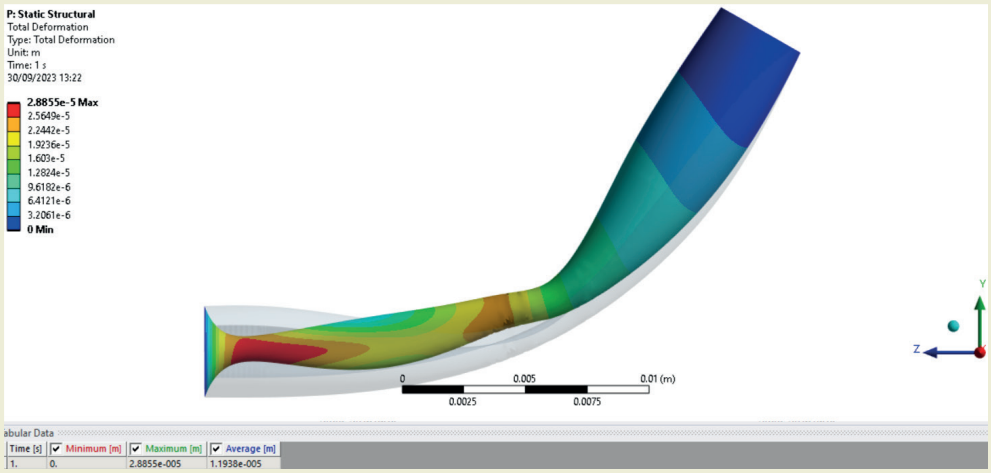

Figure 73. Total displacement of artery with 80 % stenosis.

C] Total displacement contour of 90-degree curvature

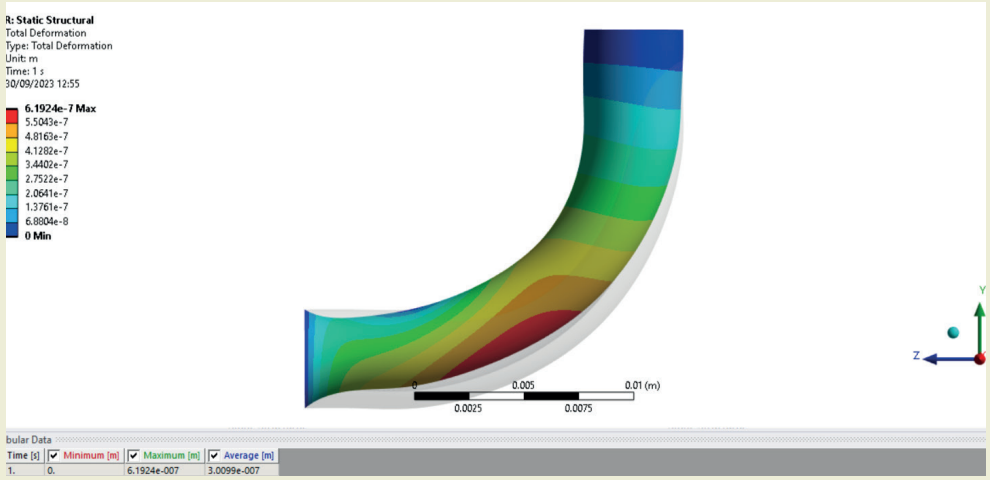

Figure 74. Total displacement of artery with 20 % stenosis.

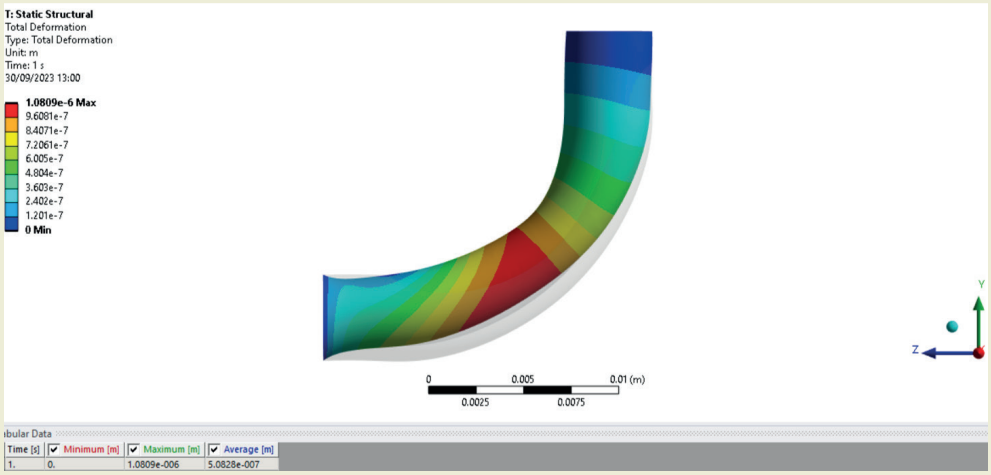

Figure 75. Total displacement of artery with 40 % stenosis.

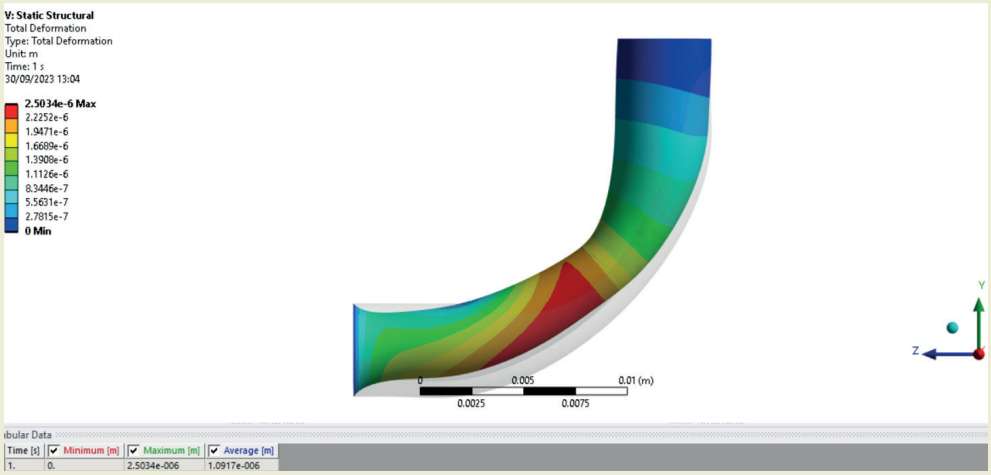

Figure 76. Total displacement of artery with 60 % stenosis.

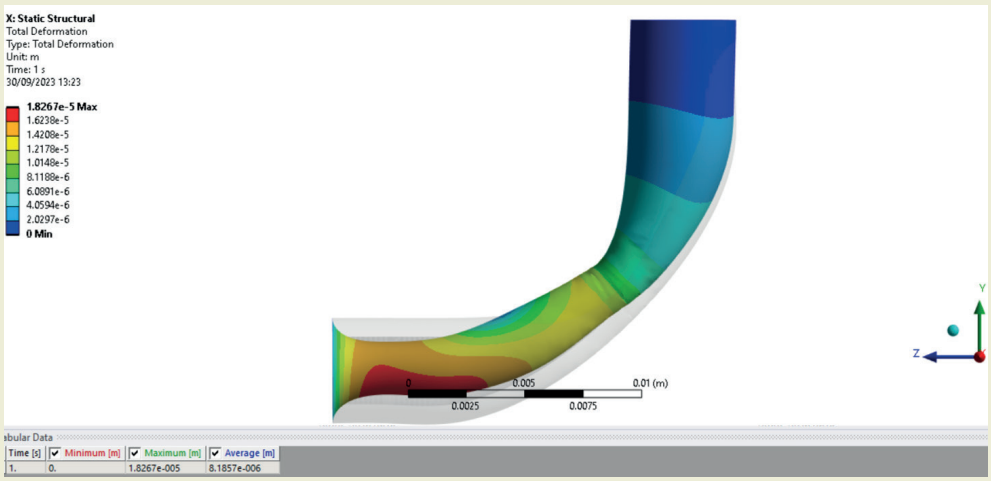

Figure 77. Total displacement of artery with 80 % stenosis.

4. Discussion

Inspection of the CFD results as depicted in ▶**Figures 6-17**, i.e. velocity contours, for the three sets of curvatures considered (30, 60, 90 degrees), the estimated velocity profiles are different both in systole (0.4s) and diastole (0.8s) and are significantly modified by both curvature and stenosis depth (percentage). Velocity is clearly much higher in the diastole compared to the systole for all cases. This is due to the compression in the artery by the contraction of the myocardium during systole, therefore, most of the blood flow occurs during diastole, increasing the blood flow. The maximum velocity is noted at the throat area (stenosis) and slowly reduces at it reaches the outlet. The velocity also changes when compared with different percentages of stenosis. The velocity magnitude increases as the percentage of stenosis increases; however larger high velocity zones are computed for the 40% case (red area) relative to other stenosis depths. The variation in the post-stenotic region is quite apparent and is exacerbated with greater curvature and larger stenosis depths. The blue low velocity zones far downstream from the stenosis significantly expand with greater stenosis for the low curvature cases (30 degrees); a similar effect is observed for the other two curvature cases. The low entry velocity zones (blue) are also very evident for the 30 and 60-degrees curvature cases at all stenotic depths; however, for the 90-degree bend case, much greater velocities precede the stenosis region at least up to a stenotic depth of 40%. However, with subsequent increment in the stenosis to 60& and 80% (▶**Figures 16 and 17**) the blue deceleration zones dominate, and the red high acceleration zone is progressively constricted in the vicinity of the outer curved wall. Poiseuille's law implies that the flow rate is highly dependent on the radius. In an artery without stenosis, the pressure gradient increases due to an increase in flow rate. However, this is not the case with the presence of a stenosis. The narrowing of the artery causes additional pressure modifications. This can be described as a quadratic polynomial. At some point, the pressure coefficient is independent of flow rate in higher flow rates. Then, it is dependent on the degree of stenosis. The velocity is higher at the outer curvature of the wall when compared with the inner side of the artery downstream. This indicates the pressure drops at the stenosis area and creates zones of low pressure, contracting the artery and forcing blood to accelerate. The flow also increases in speed even before reaching the throat area, as noted by Ku [3]. Since non-Newtonian (Carreau) blood is considered the shear rate and viscosity differs from conventional Newtonian blood flow simulations. The velocity contours (streamlines) are therefore different also. Inspection of the pressure contour plots in ▶**Figures 18-29** (again for all three curvature cases with 4 stenotic depths per case) demonstrates that the pressure is generally much higher upstream of the stenosis when compared to the downstream. The local pressure drop after the flow passes through stenosis is attributable to the constriction which induces acceleration but by virtue of Bernoulli's equation, manifests in a pressure slump. The pressure drops further with the flow rate increase, the pressure difference is elevated as the stenosis is increased.

Since stenosis is responsible for restricting the flow, a larger wall shear stress (WSS) magnitude is induced at the throat. The WSS predicted along the artery wall are compared in ▶**Figures 30-41**, again for the three curvature cases with 4 different stenotic depths. Apparently in all scenarios low wall shear stress arises at the entry zone (pre-stenotic) and again in the exit zone (post-stenotic), although initially for the 30 degrees curvature at low stenosis there is a higher wall shear stress immediately at the entry. However, the high WSS is identified generally along the stenosis throat zone indicating that flow acceleration here produces faster shearing in the Carreau blood along both the internal inner and outer walls of the artery. For example, in ▶**Figures 30-33** (30 degrees curvature), the initially blue (low WSS) stenotic zone morphs into a green/yellow zone as the stenotic depth increases and then culminates in a red high WSS zone for 60% stenotic depth. However, with further increment to 80% stenotic depth this red high WSS zone contracts. The relationship is therefore complex. The diastole case always exhibits higher WSS at any stenotic depth. For the 60 degrees curvature case, ▶**Figures 34-37** show that while the low WSS patterns arise at low stenotic depth (20%), with a small higher WSS zone at the entry, when stenotic depth is increased to 40%, a higher WSS develops along the pre-stenotic zone with maximum WSS again at the entry point and progressive decay in WSS towards the stenotic zone, with low WSS computed again after the stenotic throat (blue zone). The extent of this higher WSS zone is much smaller for the systole case relative to the diastole case. At 60 degrees stenosis, a higher WSS zone emerges at the stenotic throat (green/yellow) for the systole case with a thin boundary layer growing at the inner surface of the outer arterial wall for some distance in the post-stenotic zone. However, for the diastole case, much greater WSS magnitudes are computed at the stenotic zone (red/orange contours) and the growth of the post stenotic near-wall zone is much greater extending almost to the end of the post-stenotic region. This complex variation in WSS is also related to the velocity distribution and influenced by the shear-thinning nature of the Carreau rheological blood. At maximum stenosis depth, the stenotic and post-stenotic acceleration zones are both diminished although a high WSS is sustained at the central stenotic zone in the latter. Low WSS generally dominate the pre- and post-stenotic regimes at this maximum stenotic depth (blue contour zones). These effects are further amplified as the degree of curvature is increased to 90 degrees ▶**Figures 38-41**. The downstream outer wall experiences higher WSS. WSS contours also spread at the outer bend of the arterial wall near the throat and downstream, which is associated with promoting further development of plaque (deposits on the inner walls associated with the greater

stenotic depths). This also increases the risk of atherosclerosis plaque rupture. Again, the maximum acceleration zone in the 90-degree curvature case arises with 60 % stenosis, not the maximum stenotic depth (80%). The final computations for the CFD analysis are the velocity vector plots which permit a clearer visualization of the direction of the Carreau blood flow as depicted in ▶**Figures 42-53**. The results indicate the existence of flow re-circulation downstream of the stenosis. The recirculation is evident at the 40% stenosis and the re-circulation zones is substantially amplified for all three curvature cases (30, 60, 90 degrees) as the stenosis depth is increased. This is due to the artery expansion caused by the pulsatile flow. This flow after the stenosis has laminar characters with clear reversed flow in the vicinity of the arterial wall. The most significant accentuation in re-circulation of the Carreau blood flow in the post-stenotic zone is associated with the 60% and 80% stenoses for the 90-degree curvature case ▶**Figures 52, 53**. Again, the vector plots indicate significant deviation in non-Newtonian blood flow relative to conventional Newtonian blood flow, as evident in previous Newtonian studies [6-8].

The structural (stress) analysis computations are shown in ▶**Figures 54-77** for the FSI analysis. These contour plots are strongly dependent on the elasticity of the artery wall. The Von Mises stress ▶**Figures 54-65** is highly dependent on the thickness and the curvature of the artery. As mentioned above; to maintain the flow rate, the upstream artery walls experience high stresses which cause contraction in the arteries. The stress is generally higher with larger stenosis. The downstream arterial wall generally experiences low Von Mises stress (blue zones) for all curvatures and stenosis depths. Clearly a significant modification does arise due to the hemodynamic influence on the arterial stress states (one-way coupling). Peak Von Mises stress is always located in the pre-stenotic zone and maximized at the throat stenosis with progressive reduction in the post-stenotic zone. Finally, ▶**Figures 66-77** display the deformation (total displacement) contours which exhibit a similar trend with the change in stenosis, to the Von Mises elastic stresses. As the stenosis increases, the deformation affects the throat area until it reaches 80% stenosis, where the inlet outer wall of curvature is most severely affected. This indicates a greater potential for rupture of the artery. At higher (90 degrees) curvature, the localization of high displacement in the stenotic region also tends to spread to other locations on the arterial wall, however the high displacement zones are generally sustained for some distance downstream of the stenosis also.

5. Conclusions

Detailed CFD and FSI simulations of non-Newtonian hemodynamics in a curved arterial section with different stenosis depths have been described. ANSYS FLUENT has been deployed for the CFD computations with one-way FSI utilized in ANSYS workbench for stress analysis of the arterial walls. Extensive visualization of blood flow patterns relevant to patient-specific conditions is included using both the non-Newtonian (Carreau shear-thinning) bio-rheological model for 30, 60 and 90-degrees curvatures, and 20, 40, 60 and 80% stenotic depths. Velocity, pressure, wall shear stress (WSS), Von Mises stress and strain characteristics are all computed for these curvature and stenotic depth scenarios. The results presented accurately predicted the characteristics contributing to cardiovascular diseases in rheological blood flow. The main conclusions of the simulations can be summarized as follows:

(i) The Von Mises stress is substantially influenced by the thickness and the curvature of the artery and is generally higher with larger stenosis. The downstream arterial wall generally experiences low Von Mises stress (blue zones) for all curvatures and stenosis depths. Clearly a significant modification does arise due to the hemodynamic influence on the arterial stress states (one-way coupling). Peak Von Mises stress is always located in the pre-stenotic zone and maximized at the throat stenosis with progressive reduction in the post-stenotic zone.

(ii) Wall deformation (total displacement) contours show similar patterns with the change in stenosis, to the Von Mises elastic stresses. As the stenosis increases, the deformation affects the throat area until the most severe case of 80% stenosis, where the inlet outer wall of curvature is most severely affected. This indicates a greater potential for rupture of the artery.

(iii) Hemodynamic velocity is substantially greater in the diastole compared to the systole for all cases, owing to the compression in the artery by the contraction of the myocardium during systole. Principal blood flow occurs during diastole, increasing the blood flow. The maximum velocity is computed at the throat area (stenosis) and slowly reduces at it reaches the outlet. The velocity magnitude increases as the percentage of stenosis increases; however larger high velocity zones are computed for the 40% case (red area) relative to other stenosis depths. The variation in the post-stenotic region is quite apparent and is exacerbated with greater curvature (60 and 90 degrees) and larger stenosis depths.

(iv) Low wall shear stress arises at the entry zone (pre-stenotic) and again in the exit zone (post-stenotic), although initially for the 30 degrees curvature at low stenosis there is a higher wall shear stress immediately at the entry. However, the high WSS is identified generally along the stenosis throat zone indicating that flow acceleration here produces faster shearing in the Carreau blood along both the internal inner and outer walls of the artery. At 60 degrees stenosis, a higher WSS zone emerges at the stenotic throat (green/yellow) for the

systole case with a thin boundary layer growing at the inner surface of the outer arterial wall for some distance in the post-stenotic zone. However, for the diastole case, much greater WSS magnitudes are computed at the stenotic zone (red/orange contours) and the growth of the post stenotic near-wall zone is much greater extending almost to the end of the post-stenotic region. This complex variation in WSS is also related to the velocity distribution and influenced by the shear-thinning nature of the Carreau rheological blood. At maximum stenosis depth, the stenotic and post-stenotic acceleration zones are both diminished although a high WSS is sustained at the central stenotic zone in the latter. These effects are further amplified as the degree of curvature is increased to 90 degrees. WSS contours also spread at the outer bend of the arterial wall near the throat and downstream, which is associated with promoting further development of plaque (deposits on the inner walls associated with the greater stenotic depths).

(v) For all three curvature cases (with 4 stenotic depths per case) the pressure in the Carreau blood flow is generally much higher upstream of the stenosis when compared to the downstream. The local pressure drop after the flow passes through stenosis is attributable to the constriction which induces acceleration but by virtue of Bernoulli's equation, manifests in a pressure slump. The pressure drops further with the flow rate increase, the pressure difference is elevated as the stenosis is increased, which is associated with clinical diseases and plaque deposition.

Overall, using CFD and FSI, the risk of plaque formation can be predicted, and the computations described provide an understanding of the parameters which are most influential in predicting plaque formation and plaque rupture. The wall shear stress obtained from CFD simulations can be used to predict such phenomena; however, FSI provides the most accurate picture of how the artery reacts to the formation of stenosis with different curvature. Of course, as in all simulations, there are some assumptions involved in the analysis which restrict the full understanding of the study. Since the blood flow behaves in a pulsatile manner, an unsteady FSI analysis is required which can be explored in future investigations. Furthermore, more detailed visualization of the dual Dean vortex structure may be addressed with more refined mesh densities and also the effect of oscillatory parameters (e.g. Womersley number) can be examined to determine the frequency and phase of the flow. Additionally, pressure gradients may also be of a decaying nature which contribute to the continuous decrease of velocity in a blood flow. Finally other non-Newtonian models may be deployed for the hemo-rheology e. g. Casson and viscoelastic user defined models. All these aspects are under consideration and efforts in these directions are underway and will be reported imminently.

Acknowledgements

The authors are grateful to both reviewers for their comments which have improved the clarity of the present article.

Research ethics

Not applicable.

Author contributions

Conceptualization: [S. Kuharat, M. A. Chaudhary], Methodology: [All 4 authors], Formal Analysis: [M. A. Chaudhary], Investigation: [All 4 authors], Resources: [SKuharat and M. A. Chaudhary], Data Curation: [M. A. Chaudhary], Writing - Original Draft Preparation: [All 4 authors], Writing - Review & Editing: [All A authors, Visualization: [M. A. Chaudhary, Supervision: [S. Kuharat and O. A. Beg], Project Administration: [S. Kuharat]

Competing interests

The author(s) declare(s) no conflict of interest.

Research funding

None declared.

Data availability

Not applicable.

Peer-review

Externally peer-reviewed.

Orcid

Sireetorn Kuharat https://orcid.org/0009-0000-5739-9137
M. A. Chaudhry https://orcid.org/0000-0001-7611-9356
O. Anwar Bég https://orcid.org/0000-0001-5925-6711
Tasveer A. Bég https://orcid.org/0009-0004-1023-8255

References

[1] Papageorgiou, N. (2016). *Cardiovascular diseases: Genetic susceptibility, environmental factors and their interaction*. Academic Press.

[2] Goldsmith, H. L., & Skalak, R. (1975). Hemodynamics. *Annual Review of Fluid Mechanics, 7*(1), 213-247.

[3] Ku, D. N. (1997). Blood flow in arteries. *Annual Review of Fluid Mechanics, 29*(1), 399-434.

[4] Taylor, C. A., & Figueroa, C. A. (2009). Patient-specific modelling of cardiovascular mechanics. *Annual Review of Biomedical Engineering,*

11, 109-134.

[5] Wong, K. K., Wu, J., Liu, G., Huang, W., & Ghista, D. N. (2020). Coronary arteries hemodynamics: Effect of arterial geometry on hemodynamic parameters causing atherosclerosis. *Medical & Biological Engineering & Computing, 58*, 1831-1843.

[6] Berger, S. A., & Jou, L.-D. (2000). Flows in stenotic vessels. *Annual Review of Fluid Mechanics, 32*, 347-382.

[7] Dash, R. K., Jayaraman, G., & Mehta, K. N. (1999). Flow in a catheterized curved artery with stenosis. *Journal of Biomechanics, 32*(1), 49-61.

[8] Kim, J., Jin, D., Choi, H., Kweon, J., Yang, D. H., & Kim, Y. H. (2020). A zero-dimensional predictive model for the pressure drop in the stenotic coronary artery based on its geometric characteristics. *Journal of Biomechanics, 113*, 110076.

[9] Santamarina, A., Weydahl, E., Siegel, J. M., & Moore, J. E. (1998). Computational analysis of flow in a curved tube model of the coronary arteries: Effects of time-varying curvature. *Annals of Biomedical Engineering, 26*, 944-954.

[10] Hoque, M. M., Alam, M. M., & Ferdows, M. (2013). Numerical simulation of Dean number and curvature effects on magneto-biofluid flow through a curved conduit. *Proceedings of the Institution of Mechanical Engineers, Part H: Journal of Engineering in Medicine, 227*(11), 1155-1170.

[11] Chiang, C. H., Kao, R. H., Hung, T. K., & Bég, O. A. (2023). Computation of three-dimensional blood flow development in a 180° curved tube geometry. *Journal of Mechanics in Medicine and Biology.*

[12] Ali, N., Javid, K., Sajid, M., & Bég, O. A. (2016). Numerical simulation of peristaltic flow of a biorheological fluid with shear-dependent viscosity in a curved channel. *Computer Methods In Biomechanics and Biomedical Engineering, 19*(6), 614-627.

[13] Tripathi, D., Akbar, N. S., Khan, Z. H., & Bég, O. A. (2016). Peristaltic transport of bi-viscosity fluids through a curved tube: A mathematical model for intestinal flow. *Proceedings of the Institution of Mechanical Engineers, Part H: Journal of Engineering in Medicine, 230*(9), 817-828.

[14] Narla, V. K., Tripathi, D., & Bég, O. A. (2020). Electro-osmotic nanofluid flow in a curved microchannel. *Chinese Journal of Physics, 67*, 544-558.

[15] Khan, A. A., Akram, K., Zaman, A., & Bég, T. A. (2022). Electro-osmotic peristaltic flow and heat transfer in an ionic viscoelastic fluid through a curved micro-channel with viscous dissipation. *Proceedings of the Institution of Mechanical Engineers, Part H: Journal of Engineering in Medicine, 236*(8), 1080-1092.

[16] Bég, O. A., Hoque, M. M., Wahiduzzaman, M., Alam, M. M., & Ferdows, M. (2014). Spectral numerical simulation of magneto-physiological laminar dean flow. *Journal of Mechanics in Medicine and Biology, 14*(04), 1450047.

[17] Zaman, A., Ali, N., & Bég, O. A. (2016). Unsteady magnetohydrodynamic blood flow in a porous-saturated overlapping stenotic artery—Numerical modelling. *Journal of Mechanics in Medicine and Biology, 16*(04), 1650049.

[18] Wajihah, S. A., & Sankar, D. S. (2023). A review on non-Newtonian fluid models for multi-layered blood rheology in constricted arteries. *Archive of Applied Mechanics, 93*(5), 1771-1796.

[19] Sriyab, S. (2020). The effect of stenotic geometry and non-Newtonian property of blood flow through arterial stenosis. *Cardiovascular & Haematological Disorders-Drug Targets, 20*(1), 16-30.

[20] Lakzian, E., & Akbarzadeh, P. (2019). Numerical investigation of unsteady pulsatile Newtonian/non-Newtonian blood flow through curved stenosed arteries. *Bio-Medical Materials and Engineering, 30*(5-6), 525-540.

[21] Zaman, A., Ali, N., Anwar Bég, O., & Bég, T. A. (2016). Numerical simulation of unsteady micropolar hemodynamics in a tapered catheterized artery with a combination of stenosis and aneurysm. *Medical & Biological Engineering & Computing, 54*, 1423-1436.

[22] Vasu, B., Dubey, A., Bég, O. A., & Gorla, R. S. (2020). Micropolar pulsatile blood flow conveying nanoparticles in a stenotic tapered artery: Non-Newtonian pharmacodynamic simulation. *Computers in Biology and Medicine, 126*, 104025.

[23] Tripathi, J., Vasu, B., Bég, O. A., & Gorla, R. S. R. (2021). Unsteady hybrid nanoparticle-mediated magneto-hemodynamics and heat transfer through an overlapped stenotic artery: Biomedical drug delivery simulation. *Proceedings of the Institution of Mechanical Engineers, Part H: Journal of Engineering in Medicine, 235*(10), 1175-1196.

[24] Dubey, A., Vasu, B., Bég, O. A., & Gorla, R. S. R. (2020). Computational fluid dynamic simulation of two-fluid non-Newtonian nanohemodynamics through a diseased artery with a stenosis and aneurysm. *Computer Methods in Biomechanics and Biomedical Engineering, 23*(8), 345-371.

[25] Tripathi, J., Vasu, B., & Bég, O. A. (2021). Computational simulations of hybrid mediated nano-hemodynamics (Ag-Au/Blood) through an irregular symmetric stenosis. *Computers in Biology and Medicine, 130*, 104213.

[26] Roy, A. K., & Bég, O. A. (2021). Asymptotic study of unsteady mass transfer through a rigid artery with multiple irregular stenoses. *Applied Mathematics and Computation, 410*, 126485.

[27] Zaman, A., Ali, N., Bég, O. A., & Sajid, M. (2016). Heat and mass transfer to blood flowing through a tapered overlapping stenosed artery. *International Journal of Heat and Mass Transfer, 95*, 1084-1095.

[28] Zaman, A., Ali, N., Bég, O. A., & Sajid, M. (2016). Unsteady two-layered blood flow through an a-shaped stenosed artery using the generalized Oldroyd-B fluid model. *The ANZIAM Journal, 58*(1), 96-118.

[29] Akbar, N. S., Tripathi, D., & Bég, O. A. (2017). Variable-viscosity thermal hemodynamic slip flow conveying nanoparticles through a permeable-walled composite stenosed artery. *The European Physical Journal Plus, 132*, 1-11.

[30] Ali, N., Zaman, A., Sajid, M., Bég, O. A., Shamshuddin, M. D., & Kadir, A. (2018). Numerical simulation of time-dependent non-Newtonian nano-pharmacodynamic transport phenomena in a tapered overlapping stenosed artery. *Nanoscience and Technology: An International Journal, 9*(3).

[31] Bukač, M., Čanić, S., Tambača, J., & Wang, Y. (2019). Fluid–structure interaction between pulsatile blood flow and a curved stented coronary artery on a beating heart: A four stent computational study. *Computer Methods in Applied Mechanics and Engineering, 350*, 679-700.

[32] Bukač, M., Čanić, S., Glowinski, R., Tambača, J., & Quaini, A. (2013). Fluid–structure interaction in blood flow capturing non-zero longitudinal structure displacement. *Journal of Computational Physics, 235*, 515-541.

[33] Mendez, V., Di Giuseppe, M., & Pasta, S. (2018). Comparison of hemodynamic and structural indices of ascending thoracic aortic aneurysm as predicted by 2-way FSI, CFD rigid wall simulation and patient-specific displacement-based FEA. *Computers in Biology and Medicine, 100*, 221-229.

[34] Carvalho, V., Lopes, D., Silva, J., Puga, H., Lima, R. A., Teixeira, J. C., & Teixeira, S. (2022). Comparison of CFD and FSI simulations of blood flow in stenotic coronary arteries. In S. Bhattacharyya (Ed.), *Applications of Computational Fluid Dynamics Simulation and Modeling*. Intech Open Publishers.

[35] Luraghi, G., Wu, W., De Gaetano, F., Matas, J. F. R., Moggridge, G. D., Serrani, M., & Migliavacca, F. (2017). Evaluation of an aortic valve prosthesis: Fluid-structure interaction or structural simulation? *Journal of Biomechanics, 58*, 45-51.

[36] Failer, L., Minakowski, P., & Richter, T. (2021). On the impact of fluid structure interaction in blood flow simulations: Stenotic coronary artery benchmark. *Vietnam Journal of Mathematics, 49*, 169-187.

[37] Balzani, D., Heinlein, A., Klawonn, A., Rheinbach, O., & Schröder, J. (2023). Comparison of arterial wall models in fluid–structure interaction simulations. *Computational Mechanics, 2*, 1-7.

[38] Deparis, S., Forti, D., Heinlein, A., Klawonn, A., Quarteroni, A., & Rheinbach, O. (2015). A comparison of preconditioners for the Steklov–Poincaré formulation of the fluid-structure coupling in hemodynamics. *PAMM, 15*(1), 93-94.

[39] Gasser, T. C., Miller, C., Polzer, S., & Roy, J. (2023). A quarter of a century biomechanical rupture risk assessment of abdominal aortic aneurysms. Achievements, clinical relevance, and ongoing deve-

lopments. *International Journal of Numerical Methods in Biomedical Engineering, 39*(4), e3587.

[40] Turek, S., Hron, J., Madlik, M., Razzaq, M., Wobker, H., & Acker, J. F. (2010). Numerical simulation and benchmarking of a monolithic multigrid solver for fluid-structure interaction problems with application to hemodynamics. In H.-J. Bungartz et al. (Eds.), *Fluid Structure Interaction II*, Lecture Notes in Computational Science and Engineering (Vol. 73). Springer Berlin, Heidelberg.

[41] Bertaglia, G., Caleffi, V., & Valiani, A. (2020). Modeling blood flow in viscoelastic vessels: The 1D augmented fluid–structure interaction system. *Computer Methods in Applied Mechanics and Engineering, 360*, 112772.

[42] Charalambos, V., Michael, O., & Wilmer, W. N. (2012). *McDonald's blood flow in arteries: Theoretical, experimental and clinical principles* (6th ed.). CRC Press.

[43] Mamun, K., Akhter, M., & Ali, M. (2016). Physiological non-Newtonian blood flow through single stenosed artery. *Theoretical and Applied Mechanics, 43*, 99–115.

[44] Gendy, M. E., Bég, O. A., Kadir, A., Islam, M. N., & Tripathi, D. (2021). Computational fluid dynamics simulation and visualization of Newtonian and non-Newtonian transport in a peristaltic micro-pump. *Journal of Mechanics in Medicine and Biology, 21*(08), 2150058.

[45] Ali, N., Asghar, Z., Sajid, M., & Bég, O. A. (2020). Biological interactions between Carreau fluid and micro-swimmers in a complex wavy canal with MHD effects. *Journal of the Brazilian Society of Mechanical Sciences and Engineering, 41*, 446.

[46] Dubey, A., Vasu, B., Bég, O. A., & Gorla, R. S. R. (2021). Finite element computation of magneto-hemodynamic flow and heat transfer in a bifurcated artery with saccular aneurysm using the Carreau-Yasuda biorheological model. *Microvascular Research, 138*, 104221.

[47] Muhammed, R. K., Basha, H., Reddy, G. J., Shankar, U., & Bég, O. A. (2022). Influence of variable thermal conductivity and dissipation on magnetic Carreau fluid flow along a micro-cantilever sensor in a squeezing regime. *Waves in Random and Complex Media*, 1-30.

[48] Gambaruto, A., Janela, J., Moura, A., & Sequeira, A. (2013). Shear-thinning effects of hemodynamics in patient-specific cerebral aneurysms. *Mathematical Biosciences and Engineering, 10*, 649-667.

[49] Frolov, S. V., Sindeev, S. V., Liepsch, D., & Balasso, A. (2016). Experimental and CFD flow studies in an intracranial aneurysm model with Newtonian and non-Newtonian fluids. *Technology and Health Care, 24*, 317-333.

[50] Gijsen, F. J. H., van de Vosse, F. N., & Janssen, J. D. (1999). The influence of the non-Newtonian properties of blood on the flow in large arteries: Steady flow in a carotid bifurcation model. *Journal of Biomechanics, 32*, 601-608.

[51] ANSYS. (2021). *ANSYS FLUENT Theory Manual* (Version 21). Lebanon, NH: ANSYS, Inc.

[52] Ghigo, A. R., Wang, X. F., Armentano, R., Fullana, J. M., & Lagrée, P. Y. (2017). Linear and nonlinear viscoelastic arterial wall models: Application on animals. *Journal of Biomechanical Engineering, 139*(1), 011003.

EUROPEAN MECHANICAL SCIENCE

Research Article

e-ISSN: 2587-1110

Erosive-abrasive wear modeling of a water jet pump in a slurry medium

Ergin Kosa[1*], **Yaşar Mutlu**[1]

[1]Istanbul Beykent University, Faculty of Engineering and Architecture, Department of Mechanical Engineering, Istanbul, Türkiye

Abstract: In the study, water jet pump transfers the slurry in the well through pipe system to centrifugal pump. Sand-water mixture causes amount of material loss in the water jet pump structure computed by a software program. The purpose of the study is to determine the most critical part in the water jet pump. The wear amount is affected by many parameters such as sand particle diameter, mass flow rate of abrasive and inlet velocity. So, it is investigated that the wear amount on the jet pump is changed according to sand percentage in the well water, inlet velocity and erodent diameter. Mass flow rates of sand have a value of 0.097 kg/s for w.p. % 5, 0.194 kg/s for w.p. % 10, 0.291 kg/s for w.p. % 15 at an inlet velocity of 3.98 m/s. The maximum erosion wear rate is raised from $2.26x10^{-4}$ kg/(s m^2) to $6.84x10^{-8}$ kg/s^2m^2 for inlet velocities of 1.99 m/s, 3.98 and 7.96 m/s, respectively for the case of weight percentages of %15 in Finnie erosion wear model. Finnie, Mclaury, Generic and Oka erosion models have been compared. It is found that Mclaury's erosion model demonstrates the highest erosion value of $1.38x10^{-3}$ kg/(s m^2) for w.p. % 15 at 3.98 m/s inlet velocity for the erodent diameter of 0.0005m in all. It is claimed that erosive wear has been concentrated on the nozzle of the water jet pump. The wear rate can be predicted as straightforwardly for different conditions.

Keywords: Erosion-abrasive wear, Modeling, Water Jet Pump, Slurry, Flow

1. Introduction

Erosive-abrasive wear is caused by the solid particles carried by liquid [1-7]. It is prevalently formed in transportation systems such as pumps, pipes, turbines and valves [6,8-10]. Fine abrasive particles are transferred in the fluids in the field of industry such as oil [11,12], gas production [13] or in engineering applications such as dewatering and dredging [14]. These fine particles in the fluids are primary cause of wear in the transportation system components such as water jet pump providing simple structure without a movable part [15] or in a slurry mixed container [16,17] or in a turbine [18-20]. The water jet pump is used to transmit fluid at low speed from narrow deep wells when the water level is too low for a normal pump suction head to operate and a primary flow is named as motive flow diverged from the total volume flow in the pump [15,21-23]. The primary flow is recirculated to the jet pump which is mounted under the lowest water level [24].

Erosion wear is commonly investigated in pipe systems [11,12,25]. The researchers concentrated on the wear in pipe elbows because of the change in flow direction[11,12,25, 26]. The novelty of the research is that the study is focused on the erosive wear of water jet pump transferring slurry mixture in the well. The sand-water slurry mixture removes material on the parts of water jet pump such as nozzle, mixing part and diffuser because of continuous impingement of the abrasive sand particles. The effects of inlet speed, particle size and particle amount on the wear were studied in a software program and the results are discussed herein. The critical parts of this water jet pump such as nozzle, mixing and diffuser regions have not been discussed in terms of slurry erosion in the literature yet. Computational analysis of slurry erosion model is the straightforward method to provide the determination of critical points in the water jet pump, maintenance and protection of them.

Some researchers studied on erosion wear in literature. Kosinska et al studied on erosion of pipe elbow for different particle diameters from nano to micro size and fluid velocity. Although, the erosion rate for under the

*Corresponding author:
Email: erginkosa@beykent.edu.tr

Cite this article as:
Kosa, E., Mutlu, Y.(2024). Erosive-abrasive wear modeling of a water jet pump in a slurry medium.*European Mechanical Science*, 8(4):257-266.https://doi.org/10.26701/ems.1504033

History dates:
Received: 24.06.2024, *Revision Request*: 12.07.2024, *Last Revision Received*: 22.08.2024, *Accepted*: 22.08.2024

erodent diameter of 10^{-6}m decreases with particle size, nano particles cause clustering to form local erosion [27]. Doroshenko et al numerically analyzed worn-tee of the main gas pipeline withstanding additional stresses due to gas stream action. It is found that the maximum Mises equivalent stresses in the tee caused by the erosion wear of its line wall are formed on the outside of the tee line near the reinforcing lining located on the tee line [28]. Bai et al investigated erosion wear of helicopter rotor blades made up of titanium alloy, magnesium alloy, or aluminum alloy the construction material, respectively. It is found that Ti-4Al-1.5Mn alloy performs the highest erosion resistance. The erosion rates of the three materials remained nearly unchanged with changes in the angle of attack [29]. Yan et al (2020) modeled erosion wear in the hydraulic amplifier of the deflector jet servo valve influenced by abrasives in the oil. CFD simulation and Oka erosion model were used to emphasize the wear on the amplifier. It is claimed that the major erosion wear happens on the shunt wedge [30]. Yanan and Tingzhou numerically simulated computational fluid mechanics in 3 different types of elbows and experimentally tested the erosion wear performance of the elbows. Yanan and Tingzhou found that the elbow made up of 42CrMo material demonstrates the highest resistance to erosion wear in all [31]. Kannojiya and Kumar designed slurry pipe having a different bending angle to minimize the worn material on the pipe surface and focused on the velocity in the pipes having 150 mm diameter and 250 mm diameters. It is seen that increase in velocity can maximize wear amount and high bending angles provide to lower rate of erosion [32]. Kumar et al studied on effect of swirl vanes angle on erosion wear of AISI 316 pipe. Pipe model with vanes having different swirl angles and without a vane was compared in terms of erosion rate. Kumar *et al* claimed that placing a swirl vane enables reduce in the erosion rate on the pipe bend for all cases studied except when a 30° swirl vane was mounted at 360 mm from the inlet of the upstream pipe. Also, As the swirl angle is decreased, the erosion wear across bend is also decreasing [33]. Farokhipour et al. modeled sand particle erosion in gas-solid particle two phase flow at sharp bend, standard elbow, long elbow, and 180° pipe bend. Particle sizes of 150 and 300 μm were considered in the study of Farokhipour et al [34].

2. Mathematical Model of Flow

Pandhare and Pitale designed water jet pump parametrically. In the study, this water jet pump model [21] was modified and used in an irrigation system for transporting water and sand particles at low weight percentage as depicted in ▶**Figure 1**. The sand particles inside the water strike the inner surface of jet pumps during flow. The cyclic impact is the reason of material removal in the jet pump. Thus, action of the slurry mixture causes wear in the jet pump. The jet pump dimensions in units of mm have been illustrated in ▶**Figure 2**.

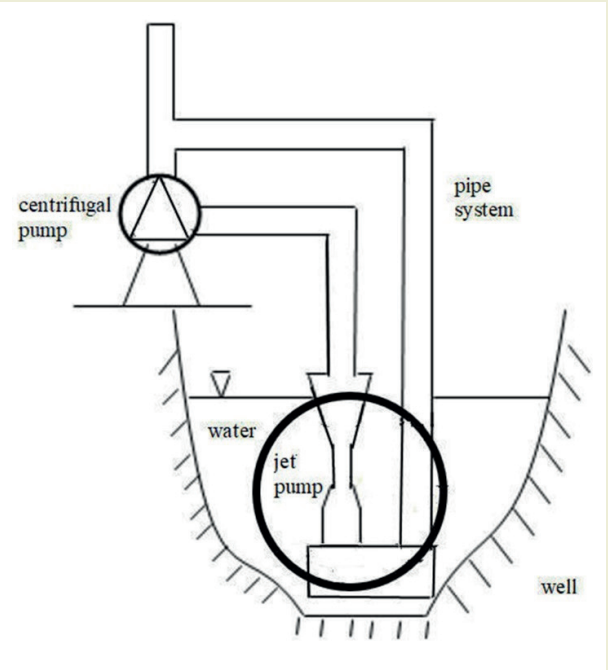

Figure 1. Irrigation system

2.1. Jet Pump Model

The water jet pump investigated for the current study consists of a diffuser and nozzle. RANS turbulence model was applied. The turbulent k-ω-SST was chosen as the flow model inside the water jet pump. Due to the

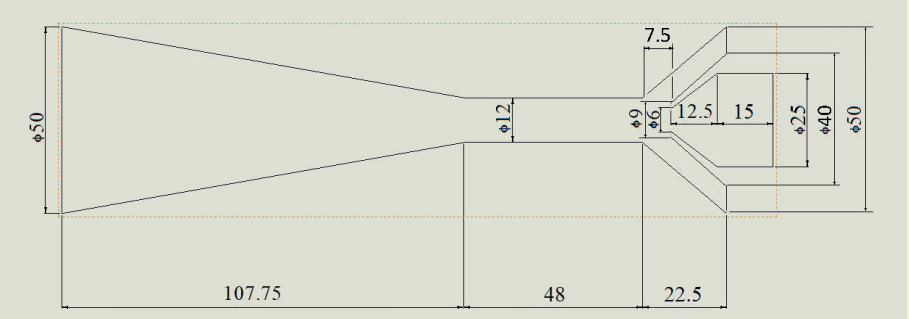

Figure 2. Water Jet Pump Dimensions

fact that the k-ω (SST) model utilizes both benefits of k-w and k-ε models. The k-w model demonstrates accurate results in the near wall, whereas k-ε models in the far-field region. So, the k-ω (SST) model can provides a wide range of accurate flow profiles [35].

The RANS momentum and continuity equations were used in computation. In physical model incompressible flow was activated. The flow analysis was realized at different velocities to emphasize the flow character inside the pump. It was performed at velocities of 1.99 m/s, 3.98 m/s and 7.96 m/s for representing low operating speeds, respectively. The other boundary conditions are given in ▶**Table 1**. On the other hand, the magnitude of velocity is one of the main effective parameters in erosion wear in slurry medium. In addition to turbulent flow model, particle tracing model for fluid flow was run to investigate erosion wear behavior of slurry mixture on the water jet pump design. The particle density of sand is specified as 2200 kg/m^3. The erosion rate on the surface of water jet pump was investigated and particle trajectory was simulated according to time. The model was run for 15s as illustrated in ▶**Figure 3** and Δt is set as 0.01 s.

2.2. CFD Model of Flow

Continuity equation in water jet pump is defined in Equations 1-3 as;

$$Q_{total} = Q_{pri} + Q_{\text{sec}} \tag{1}$$

$$A_{total}V_{total} = A_{pri}V_{pri} + A_{\text{sec}}V_{\text{sec}} \tag{2}$$

$$\pi\frac{(d_{total}^2)}{4}V_{total} = \pi\frac{(d_{pri}^2)}{4}V_{pri} + \pi\frac{(d_o^2-d_i^2)}{4}V_{\text{sec}} \tag{3}$$

Turbulent flow model [36]:

The mathematical expression of incompressible flow in steady state is defined in Equations 4-9 as;

$$\rho(u.\nabla)u = \nabla\left[-pl + (\mu+\mu_T)\left(\nabla u + (\nabla u)^T\right)\right] \tag{4}$$

$$\rho\nabla(u) = 0 \tag{5}$$

$$\rho(u.\nabla)k = \nabla\left[(\mu+\mu_T\sigma_k^*)\nabla k\right] + p_k - \beta_o^*\rho\omega k \tag{6}$$

Table 1. Boundary conditions for inlets

Parameters	Value
Particle density, ρ_p	2200 kg/m^3
Mass flow rate, $\dot{m}$	0.097 kg/s-0.388 kg/s
Initial particle diameter	0.0001 m-0.00025 m-0.0005m-0.00025m-0.001m
Normal inflow velocity, U	1.99-3.98-7.96 m/s

$$\rho(u.\nabla)k = \nabla[(\mu+\mu_T\sigma_\omega)\nabla\omega] + \alpha\frac{\omega}{k}p_k - \beta_0\rho\omega^2, \omega = om \tag{7}$$

and the turbulent viscosity are denoted as;

$$\mu_T = \rho\frac{k}{\omega} \tag{8}$$

the production term is expressed as;

$$p_k = \mu_T[\nabla u : (\nabla u + (\nabla u^T)]) \tag{9}$$

3. Mathematical Model of Erosion

3.1. Particle Tracing

The particle tracing for fluid flow was run to analyse particle trajectory in jet pump as illustrated in ▶**Figure 3**. The abrasive sand particles from different inlets are mixed at the end of nozzle part. The abrasive sand particles start to move along the jet pump and reach to outlet at the end. The inlet velocity of particles is 3.98 m/s along the jet pump axial direction. The computation according to time was run for the case of erodent size diameter of 500 µm and % 10 weight percentage slurry mixture.

3.2. Erosion Prediction

The mass flow rates of sand particles in slurry were varied from 0.097 kg/s to 0.388 kg/s. Those values are relatively low intensities. Thus, it is assumed that Newtonian flow is formed in water jet pump. The sand particles inside water jet pump cause an amount of material to be removed. The four erosion models are used to analyze the erosion behavior in the water jet pump. These are Finnie, Mclaury, Generic and Oka models that are selected in program. Mathematical expressions of these three erosion models are as follows;

3.2.1 Finnie Erosion Model [37]

Impact angle and velocity are principal factors affecting the wear in the Finnie model as expressed in Equation 10.

$$ER_{Finnie} = \sum_{p=1}^{N}\frac{\dot{m}_p L f(\alpha) v_p^{vel}}{A_{face}} \tag{10}$$

3.2.2 The Mclaury Model [38]

The McLaury erosion model computes the erosion rate of solid particles in slurry and is shown in Equations 11,12.

$$ER_{Mclaury} = GBh^j V^{vel} f(\gamma) \tag{11}$$

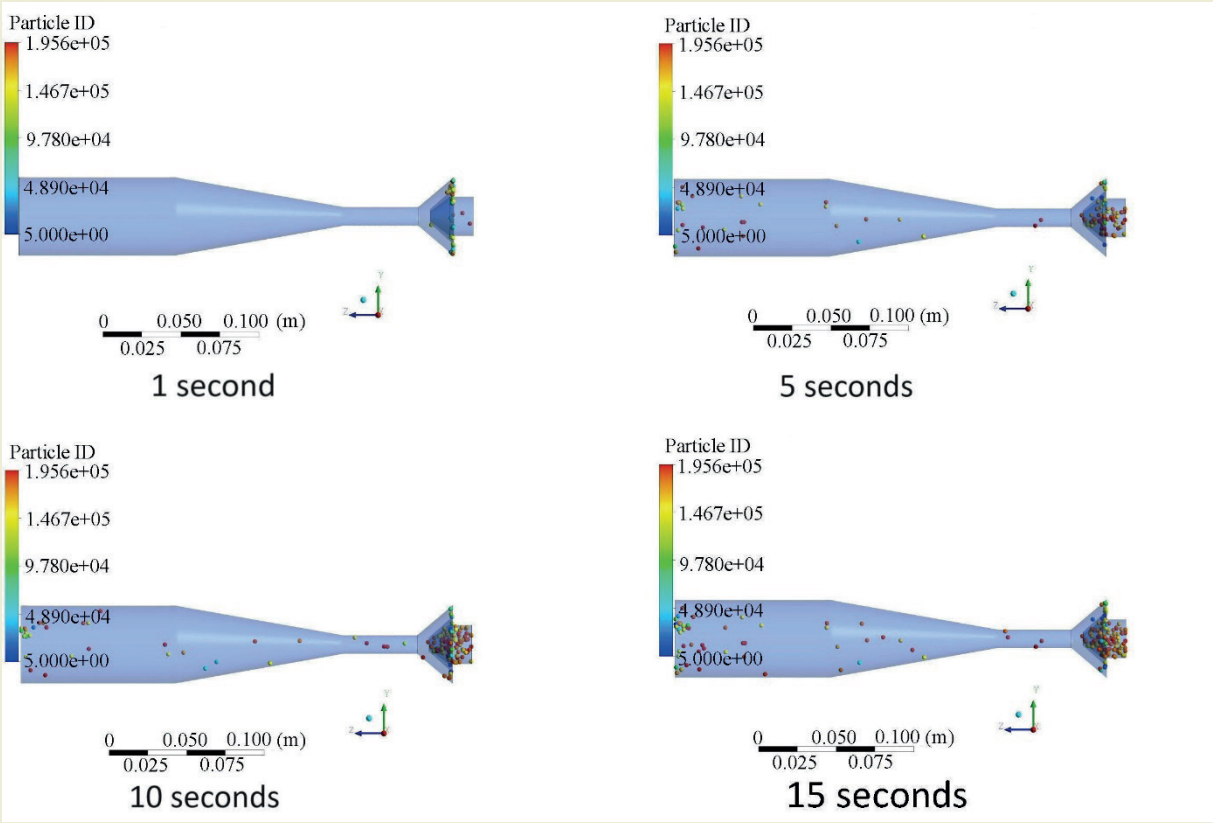

Figure 3. Particle trajectories in water jet pump-U=3.98 m/s After 1s, 5s, 10s, 15s.

$$f(\gamma) = \begin{cases} b\gamma^2 + c\gamma & \gamma \le \gamma_{\lim} \\ x\cos^2(\gamma)\sin(w\gamma) + y\sin^2\gamma + z & \gamma_{\lim} < \gamma \end{cases} \quad (12)$$

3.2.3 Oka Model [39, 40]

Oka model calculates erosion rate in Equations 13 as;

$$E_f = \frac{1}{A_f}\sum_i \dot{m}_d\,(sin\alpha)^{n_1}(1 + Hv(1-\sin\alpha))^{n_2} K\left(\frac{V_{rel}}{V_{ref}}\right)^{k_2}\left(\frac{D}{D_{ref}}\right)^{k_3} \quad (13)$$

3.2.4 Generic Model [41]

The generic model is developed by Hamed *et al* and is focused on the erodent's size, impact angle and impact velocity. The Generic model is expressed in Equation 14.

$$ER_{Generic} = \sum_{p=1}^{Ntrajct} \frac{m_{pfr} C(d_p) f(\alpha) v_p^{vel}}{A_{face}} \quad (14)$$

4. Results and Discussion

The investigated regions in the jet pump are illustrated in ▶**Figure 4**. The mixing region, diffuser and inlets of nozzle are depicted in ▶**Figure 4**. Outlet pressure is 100000 Pa. Pressure inlet is 0 Pa.

Mesh test was done for different number of mesh elements to determine the adequate number of elements to solve the model analysis and to get a much more accurate results as shown in ▶**Table 2**. The analysis resulted in magnitude of maximum Finnie wear rates in water jet pump and erosive wear values on water jet pump are changing approximately within 0.46 % deviation for 7070000 number of mesh elements and 44000000 number of mesh elements. Thus, it is determined that the 7070000 number of mesh elements is adequate to be used to solve 3-D erosion wear model. Inflation layer is 5. Infilation thickness is 0.005. Mesh size is 0.75.. Tetrahedral grid elements are adopted within the computational domain. Also, for capturing of near wall flow treatment, high gradient mesh structure is used along the walls. For this propose an inflation with first layer thickness of $5x10^{-3}$ mm and growth rate of 1.2 for 5 layers is applied to all walls. Accordingly, the enhanced

Table 2. Mesh dependence test

Number	Number of Mesh Elements	Finnie max. wear rates Velocity (m/s)
1	1100000	0.000320
2	3010000	0.000380
3	7070000	0.000430
4	23000000	0.000432
5	44000000	0.000432

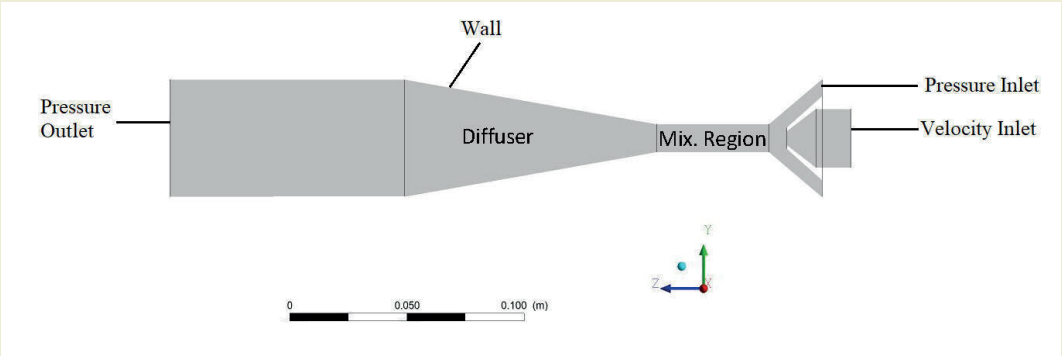

Figure 4. Regions on the water jet pump

wall treatment approach is implemented for turbulence modeling. The computational domain and the details of the mesh are shown in ▶**Figure 5**.

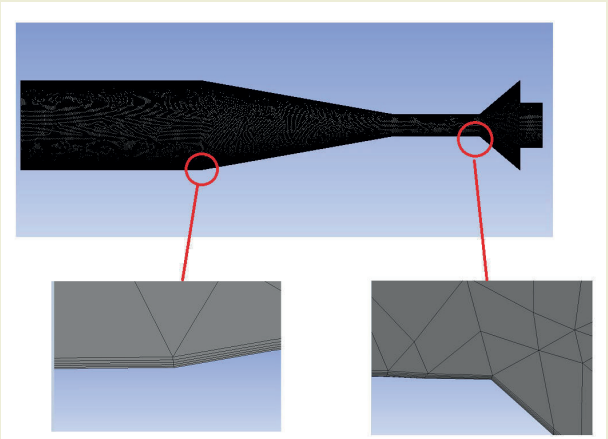

Figure 5. Mesh of model

4.1. Effect of Medium Parameters on Wear Rate

Erosive wear in jet pump depends on some parameters such as speed, slurry mass flow rate, diameter of abrasive particle. These parameters are called as medium conditions in jet pump. Thus, in the study, effect of these parameters inside the jet pump was investigated.

4.1.1 Influence of Sand Amount on Erosion Wear of Water Jet Pump

The weight percentages of sand in the slurry mixture were varied from % 5-%15 for all erosion wear models. The maximum erosion wear rate of Mclaury wear model increased from 4.54×10^{-4} kg/(s m^2) to 13.8×10^{-4} kg/(s m^2) for the wps from %5 - %15 as shown in ▶**Figure 6**. The maximum erosion wear rates in Finnie wear model were reached up to values of 6.84×10^{-4} kg/(s m^2), 4.30×10^{-4} kg/(s m^2), 2.26×10^{-4} kg/(s m^2) for the slurry mixtures of % 5, %10 and %15 weight percentages as illustrated in ▶**Figure 6**. Maximum wear rates in Oka models are 0.936×10^{-5} kg/(s m^2), 1.80×10^{-4} kg/(s m^2), 2.83×10^{-4} kg/(s m^2) for % 5, %10 and %15 weight percentages as depicted in ▶**Figure 6**. Generic models demonstrate the lowest wear rates in all erosion wear models. The maximum wear rates achieved to 11.3×10^{-4} kg/(s m^2), 7.5×10^{-4} kg/(s m^2), 3.75×10^{-4} kg/(s m^2) for % 5, %10 and %15 weight percentages of sand in slurry. The maximum erosion wear rates increase linearly according to weight percentages of sand in slurry in the water jet pump as illustrated in ▶**Figure 6**.

4.1.2 Influence of Abrasive Particle Diameters on Erosion Wear of Water Jet Pump

The effect of the erodent size on the erosion wear was studied in the work. As the particle size decreased from 0.0005 m to 0.001 m, the erosion wear rate increased as depicted in ▶**Figure 7**. In contrast, the wear rate increased from 4.30×10^{-4} kg/(s m^2) to 1.19×10^{-2} kg/(s m^2) for the case of Finnie wear model, from 7.50×10^{-4} kg/(s m^2) to 6.66×10^{-2} kg/(s m^2) for the case of Generic wear model, from 8.65×10^{-4} kg/(s m^2) to 1.66×10^{-2} kg/(s m^2) for the case of Mclaury wear model, from 1.80×10^{-4} kg/(s m^2) to 6.22×10^{-3} kg/(s m^2) for the case of Oka model. This demonstrates that the smaller abrasives were be-

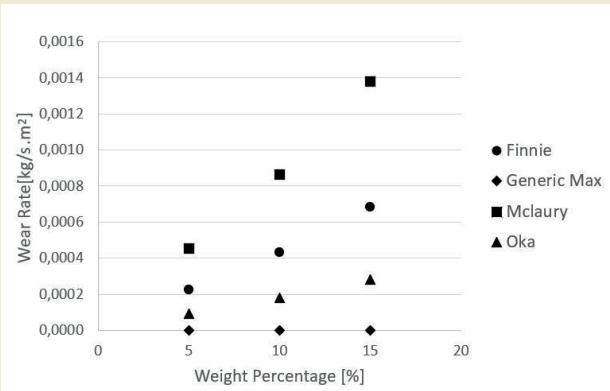

Figure 6. Wear rate for different weight percentages for each erosive wear model.

https://doi.org/10.26701/ems.1504033

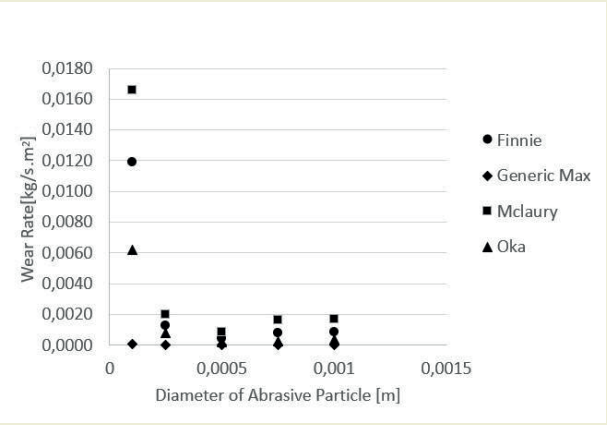

Figure 7. Wear rate under impacting of different abrasive diameter for different erosive wear models.

ing pulled towards the nozzle wall resulting in higher erosion wear.

The region for the case of smaller erodent diameter of 0.00025 m in ▶**Figure 8a** is greater than the case of 0.0005 m as depicted in ▶**Figure 8b**. The regions of higher erosion wear values were enlarged as the erodent diameter was increased from 0.0005 m to 0.001 m as shown in ▶**Figures** of **8b, 8c** and **8d**.

4.1.2 Influence of Flow Velocity on Erosion Wear of Water Jet Pump

The influence of inlet flow velocity on maximum erosion wear was investigated. The wear rate increases increasingly for all erosion wear models as shown in ▶**Figure 9**. The maximum wear rates on the nozzle of the water jet pump reached to $1.2x10^{-4}$ kg/(s m^2), $4.3x10^{-4}$ kg/(s m^2) and $3.92x10^{-3}$ kg/(s m^2) according to Finnie model for the inlet velocities of 1.99 m/s, 3.98 m/s, 7.96 m/s, respectively; $4.10x10^{-7}$ kg/(s m^2), $7.5x10^{-7}$ kg/(s m^2), $1.51x10^{-6}$ kg/(s m^2) according to the Generic model for the inlet velocities of 1.99 m/s, 3.98 m/s, 7.96 m/s, respectively; $2.3x10^{-4}$ kg/(s m^2), $8.65x10^{-4}$ kg/(s m^2), $6.78x10^{-3}$ kg/(s m^2) according to Mclaury model for the inlet velocities of 1.99 m/s, 3.98 m/s, 7.96 m/s, respectively; from $5.7x10^{-5}$ kg/(s m^2), $1.80\ x10^{-4}$ kg/(s m^2), $1.89x10^{-3}$ kg/(s m^2) according to Oka model for the inlet

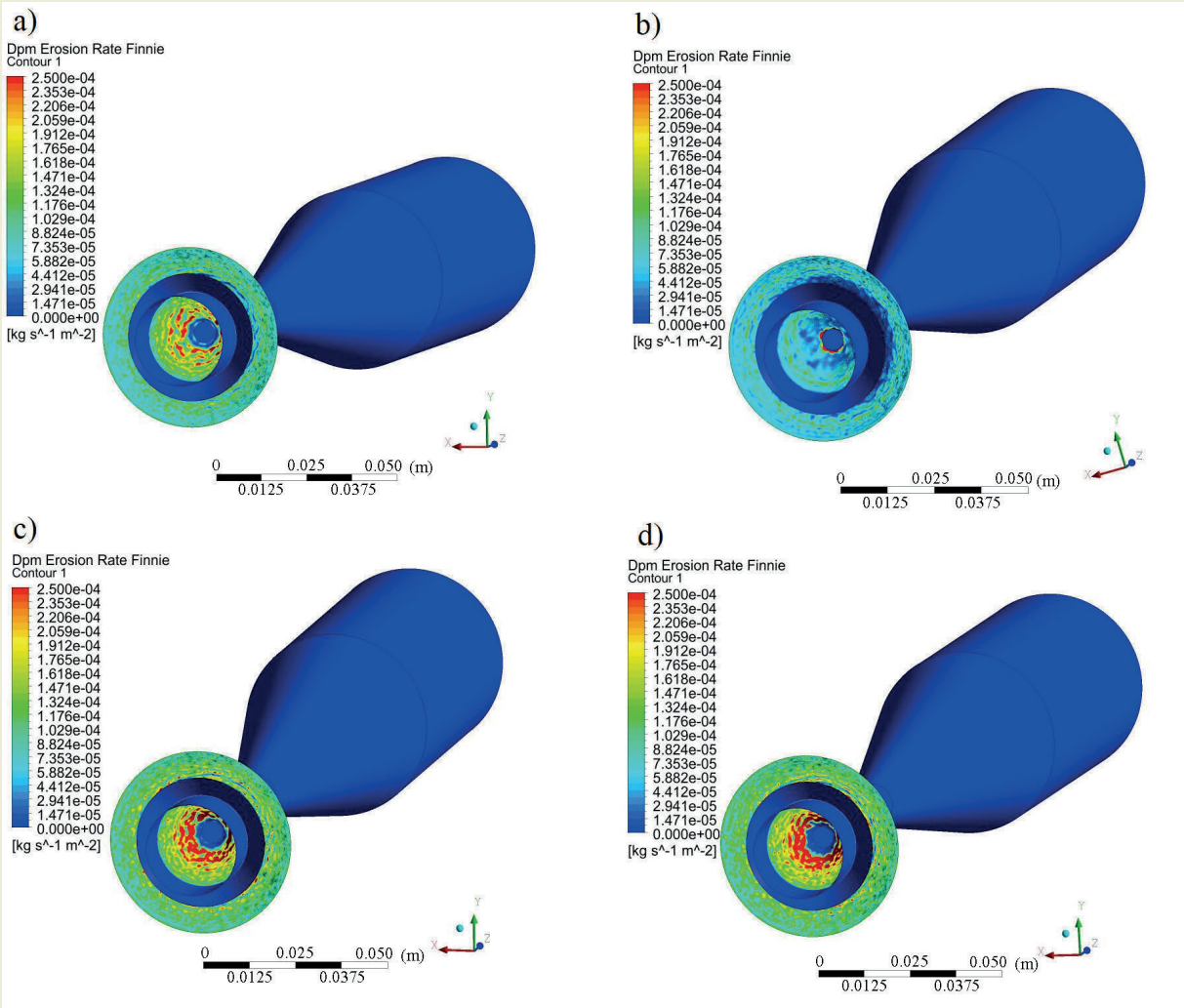

Figure 8. Erosion wear rates for different erodent diameters.

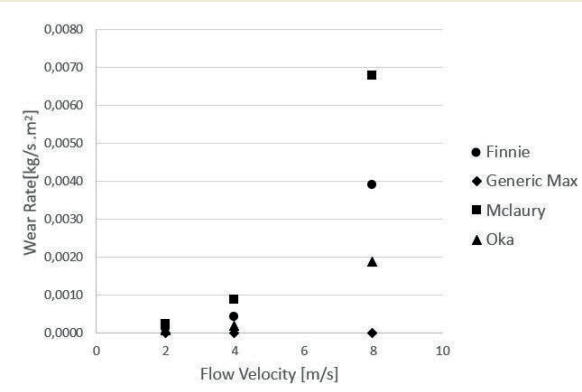

Figure 9. Wear rate at different flow velocities for different erosive wear models.

velocities of 1.99 m/s, 3.98 m/s, 7.96 m/s, respectively.

Erosion wear rate was focused on the lateral surface of the nozzle at velocity of 3.98 m/s as depicted in ▶**Figure 10b**. As the velocity increased from 3.98 m/s in ▶**Figure 10a** to 7.96 m/s in ▶**Figure 10c**, the higher values of erosion wear were concentrated around the nozzle exit as illustrated in ▶**Figure 10d**. In ▶**Figure 10a** and **c**, it is illustrated that flow is separated at certain point inside the diffuser part of water jet pump due to the turbulence.

4.2. Comparison of Erosion Wear Models

Erosion wear rates of four different wear models of Finnie, Mclaury, Oka and Generic were computed in the water jet pump as illustrated in ▶**Figure 11**. The maximum wear rates in Finnie, Oka and Mclaury have been evaluated inner part of the nozzle while the maximum wear rate has been achieved in outer part of the nozzle for Generic model.

5. Conclusion

The water jet pump was analyzed to identify the possible leakage locations due to impacting particles in slurry medium. The amount of sand particles affected the erosion rate inside the water jet pump directly. The wear rates were evaluated to determine maximum val-

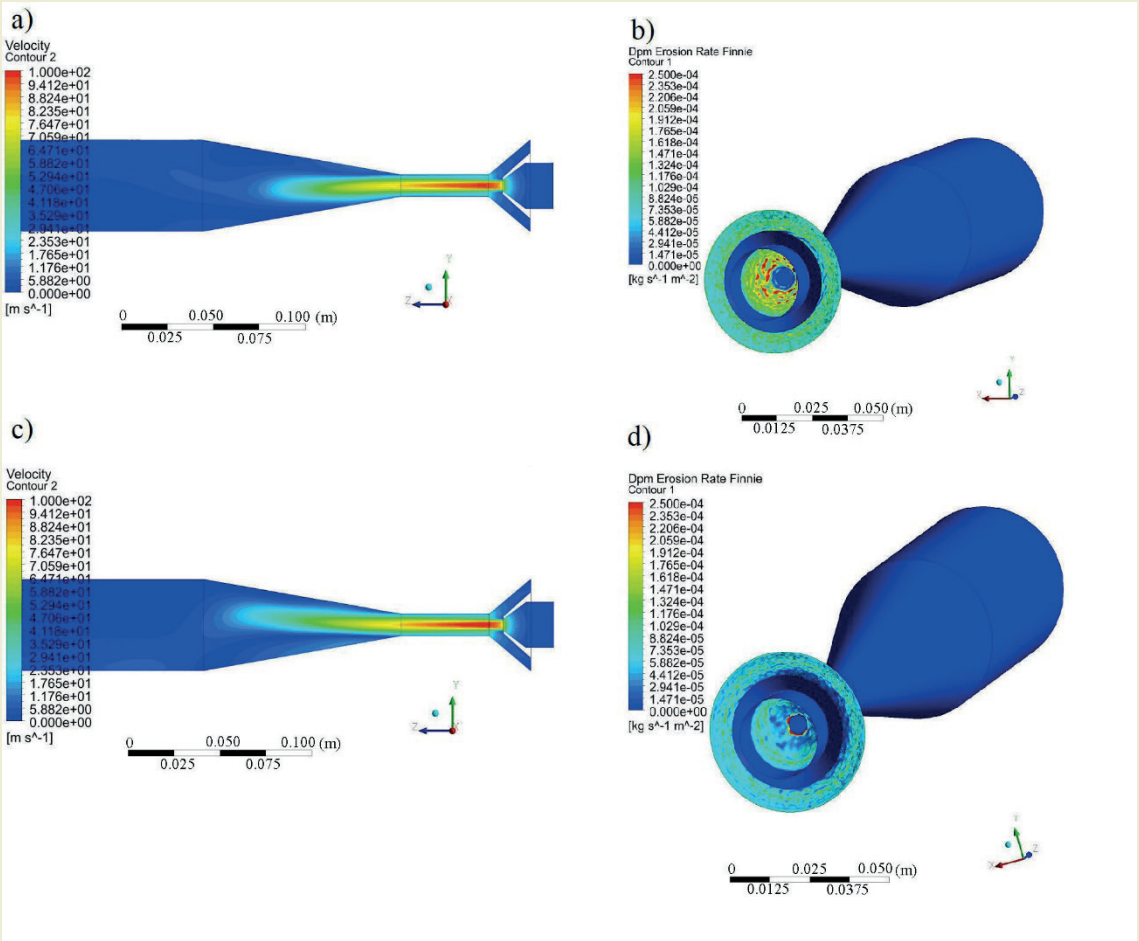

Figure 10. Erosion Wear Rate For Different Velocities.

https://doi.org/10.26701/ems.1504033

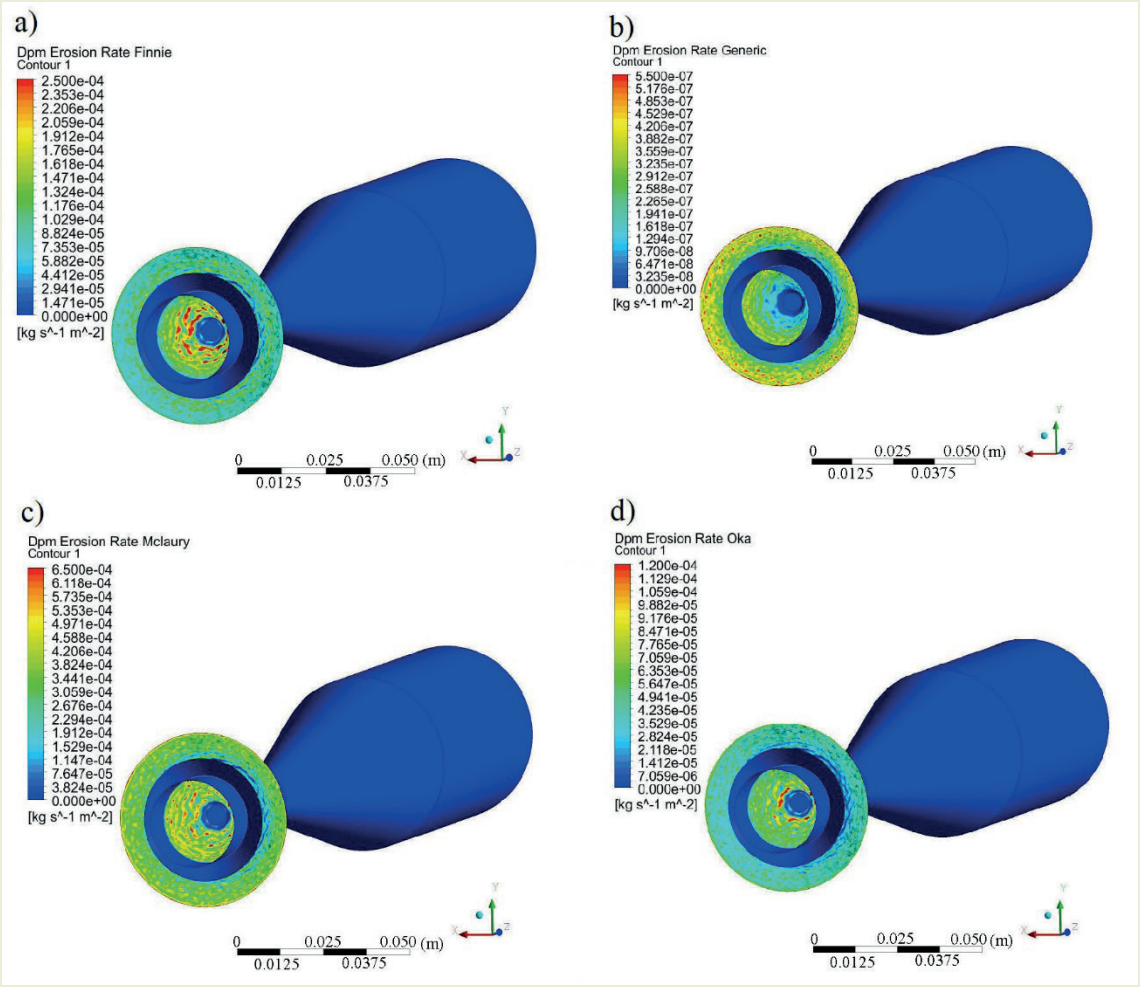

Figure 11. Finnie, Generic, Mclaury, OKA erosion rates in water jet slurry pump.

ues expressing the critical region of the water jet pump. The most affected area by the erosive wear is the nozzle of the water jet pump. This situation was approached with 4 erosive wear models.

It was concluded that all models showed that the wear rate increases when the slurry percentage in weight increases, and likewise for all modeling approaches the increase in erosion wear rate demonstrates similar tendency when the input speed and abrasive size increases. Mclaury Finnie, Oka and Generic erosive wear model values for the erodent diameter of 0.0001m results in the highest erosive rates of 1.66×10^{-2} kg/(s m^2), 1.19×10^{-2} kg/(s m^2), 6.22×10^{-3} kg/(s m^2), 6.66×10^{-5} kg/(s m^2) at the inlet velocity of 3.98 m/s in the % 10 w.p. slurry medium, respectively.

It has been also computed that increase in abrasive mass flow rate, abrasive size, particle speed increase the wear rate. Thus, the wear rate can be estimated as straightforwardly for various cases. It is significant, because gradually increase in wear amount in the water jet pump lowers the performance of water the jet pump. The indicated critical points on the nozzle can be coated as a material that are more resist to erosive wear to minimize wear rate.

Nomenclature

Q_{pri} : Primary flow (m^3 s^{-1})
Q_{sec} : Secondary flow (m^3 s^{-1})
Q_{total} : Total flow (m^3 s^{-1})
A_{pri} : Section area of primary flow (m^2)
A_{sec} : Section area of secondary flow (m^2)
V_{sec} : Velocity of secondary flow (m s^{-1})
V_{pri} : Velocity of primary flow (m s^{-1})
d_o : Outer diameter (m)
d_i : Inner diameter (m)
d_{pri} : Primary diameter (m)
d_{total} : Total diameter (m)
V_{total} : Total velocity (ms^{-1})
ρ : The fluid density (kg m^{-3})
ρ_p : *Density of particle (kg m^{-3})*

u: The fluid velocity (m s^{-1})
p: The fluid pressure (Pa)
$\dot{m}$: Mass flow rate (kg s−1)
μ_T : The modified eddy (or turbulent) viscosity (Pa s)
P_k : Rate of production of turbulent kinetic energy (m^2s^{-2})
H_v : Vickers hardness of material (HVN)
B_h : Brinell hardness of material
μ: Fluid viscosity (Pa s)
U: Inlet velocity (m s^{-1})
V: The velocity of the impacting particle (m s^{-1})
γ: The impact angle
ER_{Finnie} : The erosion rate (kg $s^{-1}m^2$)
$ER_{Mclaury}$: The erosion rate (kg $s^{-1}m^2$)
E_f: The erosion rate (kg $s^{-1}m^2$)
$ER_{Generic}$: The erosion rate (kg $s^{-1}m^2$)
f(γ): The function of the impact angle
γ_{lim} : The transition angle
b: Experimentally derived constant
c: Experimentally derived constant
w: Experimentally derived constant
x: Experimentally derived constant
y: Experimentally derived constant
z: Experimentally derived constant
m_{pfr} : Mass flow rate of the particles
$C(d_p)$: Concentration function in terms of the particle diameter
v_p : The particle impact velocity (m s^{-1})
vel: The velocity exponent
$\dot{m}_p$: The mass flow rate of the impact stream
f(α): An impact angle function
α: An impact angle (rad)
N: The number of particles
A_{face} : The impact area (m^2)
j: Constant
L: Constant
n_1 : Constant
n_2 : Constant
G : Constant
k_2 : Constant
k_3 : Constant
K : Constant
v_{rel} : The relative velocity of the particle with respect to the wall (m s^{-1})
v_{ref} : The reference value for velocity (m s^{-1})
D: Particle diameter (m)
D_{ref} : The reference value for diameter (m)
$\dot{m}d$: The mass flow rate of particles colliding with the surface (kg s^{-1})

Research Ethics

Ethical approval not required.

Author Contributions

The authors accept full responsibility for the content of this article and have approved its submission.

Competing Interests

The author(s) declare that there are no competing interests.

Research Funding

Not reported.

Data Availability

Not applicable.

Orcid

Ergin Kosa https://orcid.org/0000-0002-4607-4115
Yaşar Mutlu https://orcid.org/0000-0002-5460-5609

References

[1] Islam, M. A., & Farhat, Z. N. (2014). Effect of impact angle and velocity on erosion of API X42 pipeline steel under high abrasive feed rate. *Wear, 311,* 180–190. https://doi.org/10.1016/j.wear.2014.01.005

[2] Jerman, M., Zeleňák, M., Lebar, A., Foldyna, V., Foldyna, J., & Valentinčič, J. (2021). Observation of cryogenically cooled ice particles inside the high-speed water jet. *Journal of Material Processing Technology, 289,* 116947. https://doi.org/10.1016/j.jmatprotec.2020.116947

[3] Kosa, E., & Göksenli, A. (2015). Effect of impact angle on erosive abrasive wear of ductile and brittle materials. *International Journal of Mechanical, Aerospace, Industrial, Mechatronic and Manufacturing Engineering, 9,* 536-540. http://scholar.waset.org/1307-6892/10002428

[4] Sheng, M., Huang, Z. W., Tian, S. C., Zhang, Y., Gao, S-W., & Jia, J-P. (2020). CFD analysis and field observation of tool erosion caused by abrasive waterjet fracturing. *Petroleum Science, 17(3),* 701-711. https://doi.org/10.1007/s12182-020-00425-1

[5] Zhang, L., Ji, R., Fu, Y., Qi, H., Kong, F., Li, H., & Tangwarodomnukun, V. (2020). Investigation on particle motions and resultant impact erosion on quartz crystals by the micro-particle laden waterjet and airjet. *Powder Technology, 360,* 452-461. https://doi.org/10.1016/j.powtec.2019.10.032

[6] Zhang, R., Liu, H., & Zhao, C. A. (2013). Probability model for solid particle erosion in a straight pipe. *Wear, 308,* 1–9. https://doi.org/10.1016/j.wear.2013.09.011

[7] Zhao, Y. L., Tang, C. Y., Yao, J., Zeng, Z.-H., & Dong, S.-G. (2020). Investigation of erosion behavior of 304 stainless steel under solid–liquid jet flow impinging at 30°. *Petroleum Science, 17,* 1135–1150. https://doi.org/10.1007/s12182-020-00473-7

[8] Guo, B., Li, Y. H., Xiao, Y. X., Ahn, S. H., Wu, X., Zeng, C. J., & Wang, Z. W. (2021). Numerical analysis of sand erosion for a Pelton turbine injector at high concentration. *Earth and Environmental Science,* 627, 012022.

[9] Safaei, M. R., Mahian, O., Garoosi, F., Hooman, K., Karimipour, A., Kazi, S. N., & Gharehkhani, S. (2014). Investigation of micro- and nanosized particle erosion in a 90° pipe bend using a two-phase discrete phase model. *The Scientific World Journal.* https://doi.org/10.1155/2014/740578

[10] Vieira, R. E., Mansouri, A., McLaury, B. S., & Shirazi, S. A. (2016). Experimental and computational study of erosion in elbows due to sand particles in air flow. *Powder Technology, 288,* 339–353. https://doi.org/10.1016/j.powtec.2015.11.028

[11] Al-Baghdadi, M. A., Resan, K. K., & Al-Wail, M. (2017). CFD investigation of the erosion severity in 3D flow elbow during crude oil contaminated sand transportation. *Engineering and Technology Journal, 35,* 930–935. https://doi.org/10.30684/etj.35.9A.10

[12] Sanni, S. E., Olawale, A. S., & Adefila, S. S. (2015). Modeling of sand and crude oil flow in horizontal pipes during crude oil transportation. *Journal of Engineering,* 1–7. https://doi.org/10.1155/2015/457860

[13] Parsi, M., Najmi, K., & Najafifard, F. A. (2014). Comprehensive review of solid particle erosion modeling for oil and gas wells and pipelines applications. *Journal of Natural Gas Science and Engineering, 21,* 850–873. https://doi.org/10.1016/j.jngse.2014.10.001

[14] El-Sawaf, I. A., Halawa, M. A., Younes, M. A., & Teaima, I. R. (2011). Study of the different parameters that influence on the performance of water jet pump. *Fifteenth International Water Technology Conference,* Egypt.

[15] Song, X. G., Park, J. H., Kim, S. G., & Park, Y. C. (2013). Performance comparison and erosion prediction of jet pumps by using a numerical method. *Mathematical and Computer Modelling, 57,* 245–253. https://doi.org/10.1016/j.mcm.2011.06.040

[16] Jafari, A., & Abbasi, H. R. (2020). Investigation of parameters influencing erosive wear using DEM. *Friction, 8(1),* 136–150. https://doi.org/10.1007/s40544-018-0252-4

[17] Murugan, K., & Karthikeyan, S. (2018). CFD modelling, analysis and validation of slurry erosion setup with naval brass. *JAC: A Journal of Composition Theory, 11(10),* 63-72.

[18] Finn, J. R., & Doğan, Ö. N. (2019). Analyzing the potential for erosion in a supercritical CO2 turbine nozzle with large eddy simulation. *Turbomachinery Technical Conference and Exposition.* American Society of Mechanical Engineers Digital Collection. https://doi.org/10.1115/GT2019-91791

[19] Castorrini, A., Corsini, A., Rispoli, F., Venturini, P., Takizawa, K., & Tezduyar, T. E. (2019). Computational analysis of performance deterioration of a wind turbine blade strip subjected to environmental erosion. *Computational Mechanics, 64(4),* 1133-1153. https://doi.org/10.1007/s00466-019-01697-0

[20] Qian, Z., Zhao, Z., Guo, Z., Thapa, B. S., & Thapa, B. (2020). Erosion wear on runner of Francis turbine in Jhimruk Hydroelectric Center. *Journal of Fluids Engineering, 142(9).* https://doi.org/10.1115/1.4047230

[21] Pandhare, S. R., & Pitale, A. K. (2017). Study the performance of water jet pump by changing the angle of mixing nozzle. *International Journal of Scientific Research in Science and Technology, 3(3),* 538.

[22] Pitale, A. K., & Pandhare, S. R. (2017). Experimental investigation of jet pump at different nozzle-to-throat spacing to nozzle diameter ratio (X). *International Journal of Scientific Research in Science and Technology, 3(4),* 168-171.

[23] Sheha, A. A. A., Nasr, M., Hosien, M. A., & Wahba, E. (2018). Computational and experimental study on the water-jet pump performance. *Journal of Applied Fluid Mechanics, 11(4),* 1013-1020. https://doi.org/10.29252/jafm.11.04.28407

[24] Sakuragi, S., & Zhao, S. (2018). Operating characteristics of multi-injection type underwater jet pump. *American Journal of Mechanics and Applications, 6(3),* 68-77.

[25] Yam, K. S., Roy, S., Lee, V. C. C., & Law, M. C. (2020). Numerical analysis of erosion pattern on pipe elbow bend with swirling flows. *2nd International Conference on Materials Technology and Energy, IOP Conference Series: Materials Science and Engineering, 943,* 012037. https://doi.org/10.1088/1757-899X/943/1/012037

[26] Banakermani, M. R., Naderan, H., & Saffar-Avval, M. (2018). An investigation of erosion prediction for 15° to 90° elbows by numerical simulation of gas-solid flow. *Powder Technology, 334,* 9–26. https://doi.org/10.1016/j.powtec.2018.04.033

[27] Kosinska, A., Balakin, B. V., & Kosinski, P. (2020). Theoretical analysis of erosion in elbows due to flows with nano- and micro-size particles. *Powder Technology, 364,* 484–493. https://doi.org/10.1016/j.powtec.2020.02.002

[28] Doroshenko, Y., Zapukhliak, V., Grudz, Y., Poberezhny, L., Hrytsanchuk, A., & Popovych, P. (2020). Numerical simulation of the stress state of an erosion-worn tee of the main gas pipeline. *Archives of Material Science and Engineering, 101,* 63-78. https://doi.org/10.5604/01.3001.0014.1192

[29] Bai, X., Yao, Y., Han, Z., Zhang, J., & Zhang, S. (2020). Study of solid particle erosion on helicopter rotor blades surfaces. *Applied Sciences, 10(3),* 977. https://doi.org/10.3390/app10030977

[30] Yan, H., Li, J., Cai, C., & Ren, Y. (2020). Numerical investigation of erosion wear in the hydraulic amplifier of the deflector jet servo valve. *Applied Sciences, 10(4),* 1299. https://doi.org/10.3390/app10041299

[31] Yanan, G., & Tingzhou, N. (2020). Numerical simulation and experiment analysis on erosion law of fractured elbow pipe. *Academic Journal of Manufacturing Engineering, 18(2),* 109-115.

[32] Kannojiya, V., & Kumar, S. (2020). Assessment of optimum slurry pipe design for minimum erosion. *Scientia Iranica, 27(5),* 2409-2418. https://doi.org/10.24200/SCI.2019.52073.2519

[33] Kumar, K., Kumar, S., Singh, G., Singh, J. P., & Singh, J. (2017). Erosion wear investigation of HVOF sprayed WC-10Co4Cr coating on slurry pipeline materials. *Coatings, 7(4),* 54. https://doi.org/10.3390/coatings7040054

[34] Farokhipour, A., Mansoori, Z., Saffar-Avval, M., & Ahmadi, G. (2018). Numerical modeling of sand particle erosion at return bends in gas-particle two-phase flow. *Transactions B: Mechanical Engineering, Scientia Iranica B, 25(6),* 3231-3242. https://doi.org/10.24200/SCI.2018.50801.1871

[35] Pang, A. L. J., Skote, M., & Lim, S. Y. (2016). Modelling high Re flow around a 2D cylindrical bluff body using the k-ω (SST) turbulence model. *Progress in Computational Fluid Dynamics, An International Journal, 16(1),* 48-57. https://doi.org/10.1504/PCFD.2016.074225

[36] Al-Baghdadi, M. A. R. S. (2015). Applications of computational fluid dynamics and finite element methods in engineering education (Vol. 1). *International Energy and Environment Foundation.*

[37] Finnie, I. (1960). Erosion of surfaces by solid particles. *Wear, 3(2),* 87–103. https://doi.org/10.1016/0043-1648(60)90055-7

[38] McLaury, B. S., Shirazi, S. A., Shadley, J. R., & Rybicki, E. F. (1996). Modelling erosion in chokes. *Proceedings of the ASME Fluids Engineering Summer Meeting,* San Diego, California.

[39] Oka, Y. I., Okamura, K., & Yoshida, T. (2005). Practical estimation of erosion damage caused by solid particle impact. Part 1: Effects of impact parameters on a predictive equation. *Wear, 259,* 95–101. https://doi.org/10.1016/j.wear.2005.01.039

[40] Oka, Y. I., & Yoshida, T. (2005). Practical estimation of erosion damage caused by solid particle impact. Part 2: Mechanical properties of materials directly associated with erosion damage. *Wear, 259,* 102–109. https://doi.org/10.1016/j.wear.2005.01.040

[41] Hamed, A., & Tabakoff, W. (2006). Erosion and deposition in turbomachinery. *Journal of Propulsion and Power, 22(2),* 350-360. https://doi.org/10.2514/1.18462

EUROPEAN MECHANICAL SCIENCE

Research Article

e-ISSN: 2587-1110

Comparison of classical and heuristic methods for solving engineering design problems

Kürşat Tanrıver[1*], **Mustafa Ay**[2]

[1] Istanbul Health and Technology University, Faculty of Engineering and Natural Sciences, Dep. of Mechatronics Eng., Istanbul, Türkiye
[2] Marmara University, Faculty of Technology, Mechanical Engineering Department, Istanbul, Türkiye

Abstract: This paper presents an innovative application of the Ant Colony Optimization (ACO) algorithm to optimize engineering problems, specifically on welded beams and pressure vessels. A simulation study was conducted to evaluate the performance of the new ACO algorithm, comparing it with classical optimization techniques and other heuristic algorithms previously discussed in the literature. The algorithm was executed 20 times to obtain the most efficient results. The best performance outcome in the welded beam simulation was 1.7288, achieved after 540 iterations using 1000 ants, with a computation time of 6.27 seconds. Similarly, the best performance result in the pressure vessel simulation was 5947.1735, obtained after 735 iterations using 1000 ants and completed in 6.97 seconds. Compared to similar results reported in the literature, the new ACO algorithm demonstrated superior performance, offering an outstanding solution. Additionally, users can utilize this new ACO algorithm to quickly acquire information about welded beam design and prefabrication through simulation.

Keywords: Ant colony, engineering design, MATLAB, optimization, welded beam design, pressure vessel

1. Introduction

Optimization is generally used to achieve the best possible result within the determined goals and constraints. The optimization steps include creating basic configurations, defining design variables, formulating the objective function, and selecting and implementing suitable optimization problems [1].

Optimization techniques are often divided into two categories: mathematical and heuristic methods. Mathematical methods strive to find the most accurate analytical solution, while heuristic methods exhibit a more practical approach [2-3]. Some heuristic algorithms are used to solve engineering problems. These include ant colony optimization (ACO) [4], genetic algorithms (GA) [5], particle swarm optimization (PSO) [6], bat algorithms (BA) [7], firefly algorithms (FA) [8] and butterfly algorithms [9].

Studies can be conducted on the instinctual behaviors of animals like ants, bats, and fireflies using heuristic approaches. These instincts enable ants to search for food, birds to gather, and fish to move in schools, organizing these animals [10]. Scientists have studied insect behaviors and developed successful optimization algorithms in this context. These techniques have been successfully applied to many scientific fields and engineering problems. They possess a high level of flexibility in solving engineering problems [11].

Moreover, in recent years, many hybrid algorithms have been proposed by combining these algorithms to solve engineering problems [12]. Hybrid algorithms are created by taking the relatively better aspects of heuristic algorithms, depending on the characteristics and complexity of the problem being solved. One of the successful heuristic applications that can be modified and used in optimization problems is the ACO algorithm [13]. Solutions to optimization problems are also complex due to the high application areas and variability of engineering problems. To facilitate this, the computing power of computer programs is used [14]. One of the programs that

*Corresponding author:
Email: kursat.tanriver@istun.edu.tr

Cite this article as:
Tanrıver, K., Ay, M.(2024). Comparison of classical and heuristic methods for solving engineering design problems. *European Mechanical Science*, *8*(4):267-277. https://doi.org/10.26701/ems.1509881

History dates:
Received: 03.07.2024, *Revision Request*: 15.08.2024, *Last Revision Received*: 03.09.2024, *Accepted*: 04.09.2024

can be easily used to solve algorithms is MATLAB [15].

This study originated from the need to address specific engineering challenges in welded beam design and pressure vessel optimization, which are critical in ensuring structural integrity and cost-effectiveness in industrial applications. These design problems are characterized by complex constraints, such as minimizing material usage while maintaining structural strength and handling pressure conditions within safety limits. Traditional methods often struggle to navigate these challenges, leading to suboptimal designs efficiently. To overcome these issues, we employed Ant Colony Optimization (ACO) as a heuristic method and Sequential Quadratic Programming (SQP) as a classical optimization method. Recognizing the limitations of existing approaches, the ACO algorithm was modified to handle better the unique constraints and complexities of these design problems. The modifications include enhancements that leverage the advantageous aspects of ACO, making the algorithm more effective in exploring the solution space and avoiding local optima. The new ACO code was implemented in MATLAB, and its performance was compared against results obtained using other techniques reported in the literature. The enhanced ACO algorithm improves solution accuracy and provides valuable insights into welded beam design and pressure vessel optimization during pre-production. By offering a more robust solution framework, this study aims to contribute to cost and time savings for professionals and industries in these critical fields.

2. Literature View

Due to the challenging nature and extensive application areas of engineering problems in manufacturing and aerospace industries, numerous studies have been carried out to find solutions [16]. With the increased number of variables in problems, finding solutions using traditional methods has become difficult. Efforts have been made to simplify the solution and find the best one, leading to the development of metaheuristic algorithms. One such metaheuristic algorithm, ACO [17], has been used to solve many application problems in different areas of daily life [18]. ACO was analytically expressed first in 1930 and began to be frequently used after 1950. Since then, it has successfully solved various problems today [19].

A literature review was conducted on engineering problems, including welded beam design. The review found that previous studies had defined these problems, objective functions, constraints, variables, and solutions using various optimization techniques. These studies were examined to develop the solution further while considering the same definitions. The studies examined are given below.

Welded Beam has been described by Rao [20], Ray & Liew [21], Grković & Bulatović [22], and Cagnina *et al.* [23]. The design problems presented aim to determine the minimum cost due to shear stress, bending stress in the Beam, buckling load, and end deflection of the Beam. Pressure vessels have been previously described by Renato & Leandro Dos Santos [24], Zahara & Kao [25], He & Wang [26], and Huang *et al.* [27]. The design problem involves minimizing the weight of the spring while adhering to certain restraints on minimum deflection, shear stress, surge frequency, and limits on the outside diameter and design variables. Coelho & Mariani [28], Ray & Liew [21], Grković & Bulatović [22], Cagnina *et al.* [23], and Tanriver & Ay [29] have conducted ACO optimization studies on these problems.

Hasan *et al.* [30] studied optimal power flow analysis in power distribution networks, solved with the Sequential Quadratic Programming (SQP) algorithm. Wang *et al.* [31] studied optimization-based transient control of turbofan engines via a sequential quadratic programming approach.

While these studies have provided valuable contributions, the modified new ACO algorithm presented in this paper demonstrates improved efficiency and accuracy in solving these complex engineering problems by better navigating large solution spaces and avoiding local optima. In addition, unlike the literature, a classical optimization solution has been run and compared with the new ACO algorithm results so that the readers could better understand the algorithm's performance.

3. Methodology

Using the information accumulated in the form of pheromone trails laid by artificial colony ants, consecutively shorter feasible tours are formed. Thus, the best results are recorded at the end of the specified iteration to arrive at the problem solution. Computer simulations using programming languages have shown they can produce reasonable solutions to ACO examples [32].

This study combines these two methods to achieve a more effective and reliable solution. The primary ACO method's code has been modified to create a new algorithm for this goal. This new ACO algorithm's code has been tested for functionality and compared with results in the literature using MATLAB software.

3.1. Sequential Quadratic Programming (SQP)

Sequential Quadratic Programming (SQP) is among the classical methods used to solve optimization problems. SQP is used to solve nonlinear objective and constraint function problems [33, 34]. It is used in MATLAB with the fmincon code. SQP solves the optimization problem iteratively by solving a series of Quadratic Program-

ming (QP) subproblems. Each QP subproblem approximates the original problem at the current iterate. x_k.

Quadratic Approximation: The Lagrangian function using a quadratic model is below.

$$\mathcal{L}(x_k + \Delta x, \lambda_k, \mu_k) \approx \mathcal{L}(x_k, \lambda_k, \mu_k)$$

$$+ \nabla_x \mathcal{L}(x_k, \lambda_k, \mu_k)^T \Delta x + \frac{1}{2} \Delta x^T \nabla^2_{xx} \mathcal{L}(x_k, \lambda_k, \mu_k) \Delta \quad (1)$$

Linearize Constraints: Linearize the constraints around the current iterate x_k Is below.

$$c_i(x_k + \Delta x) \approx c_i(x_k) + \nabla c_i(x_k)^T \Delta x \leq 0,\ i = 1, \ldots, m \quad (2)$$

$$h_j(x_k + \Delta x) \approx h_j(x_k) + \nabla h_j(x_k)^T \Delta x = 0,\ j = 1, \ldots, p \quad (3)$$

Solve QP Subproblem: Solve the QP subproblem to find the search direction Δx below.

$$\min_{\Delta x}\ S(x)\ \nabla f(x_k)^T \Delta x + \frac{1}{2} \Delta x^T \nabla^2_{xx} \mathcal{L}(x_k, \lambda_k, \mu_k) \Delta x \quad (4)$$

$$\text{Subject to}\quad \nabla c_i(x_k)^T \Delta x + c_i(x_k) \leq 0,\ i = 1, \ldots, m$$

$$\nabla h_j(x_k)^T \Delta x + h_j(x_k) = 0,\ j = 1, \ldots, p$$

Update Iterates: The solution estimates are below.

$$x_{k+1} = x_k + \alpha_k \Delta x \quad (5)$$

where α_k Does a line search determine a step size?

3.2. ACO Max-Min Ant System

Wilson and Hölldobler [35] discovered that ants communicate via pheromone signals. It helps to understand how ants reach a food source upon their discovery and how they clear obstacles. Pheromones act as a communication medium among ants. The ant colony optimization algorithm is based on the natural behaviors of ants. The algorithm was first studied by Dorigo *et al.* [36] in a reference paper. The pheromones of ants enable information to be transmitted in the colony. Pheromones are the chemicals secreted by ants, and upon secretion, their trails survive for a short period. The more frequently ants visit the same place, the more pheromones they deposit on that path. In ant colony optimization, through a formulated decision mechanism, artificial ants inspired by real ants can communicate by depositing these trails on edges.

Besides their skills in finding the shortest way from food sources to anthills without using their sense of sight, they also can adapt. They can find the new shortest way if the current way they follow is not the shortest way anymore due to external factors. We can explain the behavior pattern of ants as they move casually until they find a pheromone trail. Then, based on the pheromone concentration on the trail, ants decide if they will follow the trail. Therefore, the more ants following a trail there are, the more likely other ants are following the trail [37].

Upon detecting pheromone trails, it becomes clear how ants find food and exhibit cooperative behavior. The classical ant colony algorithm is a meta-intuitive method based on an agent population aiming to solve intermittent optimization problems through behaviors emerging from swarm intelligence. Some additional features of the ant colony algorithm can be categorized as follows: Single artificial control architecture is the same for some units and has scalable characteristics. The solution to a given problem can be applied to other versions of the same problem, which is multifaceted. With minimum modification, it can be used in combinatorial optimizations such as second-degree assignment problems and the planning approach of mobile robots. As a multi-agent system, they can be used for general-purpose planning methods to handle ambiguity, including the noise of sensors and actuators of detection systems. As a search engine based on population, they sometimes tried to optimize positive feedback problems; however, as their goal is to optimize continuous functions, some modifications were made [38]. In the beginning, ants follow a straight line, and in the meantime, releasing the mentioned pheromones onto the path, they help the following ants find their way. The movements of ants, with the help of pheromones that they naturally release, and their path have been illustrated. As they cannot track pheromone trails when their path is blocked, ants primarily choose one of the two paths they can follow. As the transition from the short way for a unit of time will be longer, the amount of the dropped pheromone will also be more significant. Accordingly, in time, there will be a rise in the number of ants that prefer the shorter way. After a while, all ants will choose the shorter way. By checking trails, the ants that move randomly before will probably decide to take the direction of a more intense pheromone trail. As the algorithm was developed inspired by ant colonies, it is called the ACO algorithm.

In order to accelerate the ACO algorithm's speed, which is relatively complicated, various studies were tested successfully utilizing updating some parameters [39]. ACO algorithms have been studied in three categories: original ant system, maximum-minimum ant system and ant colony system. In addition to the pheromone update done in the optimization process, this algorithm initiates a local pheromone update. This update is also called an offline pheromone update. Following each iteration, all ants perform a local pheromone update, and each ant applies it only to the last edge covered. $\mathbf{T_{ij}}$ is shown below.

$$\tau_{ij} = \tau_{ij}.(1 - Q) + \ \tau_0 . Q \quad (6)$$

Q is the evaporation coefficient; its quantity is 0≤ Q ≤1. τ0 is the initiation value of the pheromone.

The primary purpose of the local pheromone update is to diversify the search performed by ants after each iteration. Decreasing pheromone concentration on traversed edges encourages subsequent ants to choose another edge and produce a different solution. Several ants' probability of producing an identical solution gets lower during iteration. The local pheromone update works similarly to the max and min in ant systems. It is also applied by a single ant at the end of each iteration. Likewise, the best update is considered at the end of each iteration, but the ACO algorithm is different, as shown below.

$$\tau_{ij} = \begin{cases} \tau_{ij}.(1-q) + \Delta\tau_{ij}.q, \\ if\ (i,j)belongs\ to\ best\ tour, \\ \tau_{ij}, \qquad otherwise, \end{cases} \tag{7}$$

An essential difference between the ant system and the ant colony system can be seen in the ants' decision rule in the solution process. In ACO, the rule below is employed.

The probability of an ant moving from city i to city j depends on a random variable q between the $0 \le q \le 1$ interval. If this Value is the new rate $q \le q0$, $j = argmax_{c_{il} \in N(s^p)}\{\tau_{il}\,\eta_{il}{}^{\beta}\}$, is employed. Otherwise, the following in below is employed.

$$P_{ij}^{k} = \begin{cases} \dfrac{\tau_{ij}^{\alpha}\ \eta_{ij}^{\beta}}{\sum_{c_{ij} \in N(s^P)} \tau_{ij}^{\alpha}\ \eta_{ij}^{\beta}}, & if\ C_{ij} \in N(S^P) \\ 0, & otherwise \end{cases} \tag{8}$$

3.3. Modified Ant Colony Optimization Algorithm

The algorithm we propose is a modification of the Ant Colony Optimization (ACO) algorithm. This modification is designed to enhance the adaptability of the algorithm and improve solution quality. The key points and how this new algorithm works is shown below.

Adaptive α and β Values: In each iteration of the algorithm, the importance of pheromone (α) and heuristic information (β) is dynamically adjusted. It makes the solution search process more flexible and may help avoid local minima.

Pheromone Update: All pheromone trails (τ) are updated in each iteration. The new pheromone value is increased based on the current pheromone value and the function value of the best solution in that iteration. That gives more weight to reasonable solutions.

Queen Ant (queen. Value): The best solution is stored as the "queen ant," and the Value of this solution influences the future search directions of other ants.

Status Check and Output: The algorithm checks the best solution in each iteration and if this solution is better than the previous best, it is accepted as the new best solution.

To integrate these proposed modifications into the existing ant optimization, it is necessary to update the functions to reflect the specified changes while maintaining the basic structure of the algorithm. This will include the pheromone update mechanism and the adaptive adjustment of α and β. Additionally, storing and updating the best solution ("queen ant") will be necessary. This approach can be practical in complex optimization problems, such as various engineering design problems. The parameter definition is given in ▶**Table 1**.

Table 1. New ACO Parameters Definition

max_iterations	The maximum number of iterations for the algorithm
ant_population	The size of the ant population
evaporation_rate (ρ)	The rate at which the pheromone evaporates
alpha (α)	The parameter that controls the importance of pheromone in the ant's decision-making process
beta (β)	The parameter that controls the importance of distance in the ant's decision-making process.
queen. Value	The best solution is stored as the "queen ant"

Only the solution obtained from the best ant pheromone trail is updated in the modified ant colony algorithm, and with determined modifications, the new ACO algorithm is obtained. In the first stage, m number of ants should be determined as a parameter. This parameter is based on the quality of the first solution and the I iteration number that represents the change number in the second loop. In the first loop, all ants randomly choose a location and take a value for each variable. Once each ant finds its location, through minval values optimized for variable values selected by ants, the Value of the function is determined. When the values of the function are obtained for each ant, it is evaluated which ant has chosen the best solution, and the Value of that solution is saved as minfunction. All ants obtain the best solution locally from first stage minfunction in the second loop. Pheromone update for the best Value is performed as shown in below.

$$\tau(i) = 0.1\left(1-\eta_{ij}\right).\tau(i) \tag{9}$$

αj and βj is given to correct the solution of each iteration. In the first iteration, this Value is given in a code, and this Value is selected depending on the intervals of possible solutions of variables in lower and upper band. Also, for each following iteration, correction values of α and β is done as in below.

$$\alpha_j = 0{,}05\,.\alpha_i \quad ; \quad \beta_j = 0{,}05\,.\beta_i \tag{10}$$

This procedure, explained in the second step, is an iter-

ation repetition in the second loop and is programmed to repeat to correct the solutions up to the maximum iteration number. Optionally, the best Value can be defined in the code. If a value is defined and a solution better than required cannot be obtained after a given iteration number, the entire loop can be repeated. Once the best solution values are obtained, these values are recorded, and their function values are defined. A simple optimization code of the new ACO algorithm is given in ▶**Figure 1**.

Algorithm MACO

```
for t = 1 : maxiteration
MACO= createMaco ( graph, colony , antnumber, τ, η, α
, β);
function [ graph ] = createGraph()
Update α and β;
α_j = 0,05 . α_i ; β_j = 0,05 . β_i

Determine optimun value and best function value
for i = 1 : antnumber
 τ(j) = τ(i) + 0,005. min_function

 if minfunction < bestfunction;
    function = new function;
   end

queen.value= bestvalue;
to update τ ;
τ = 0.1*( 1 - rho) .* τ;

output = [ 'MACO (Modified ACO) #' ,'Iteration #' ,
value1 ,
 ' optimum Function value = ' , value2];
disp(output)
```

Figure 1. Modified ant colony optimization code

4. Result

Optimization is a method of optimizing a system using mathematical operations to obtain the best possible result. It involves determining the basic configurations, defining the design variables, specifying the objective function, selecting the appropriate optimization algorithms, and applying the optimization procedures. These steps collectively define the optimization process. Optimization can be applied in various fields, such as bolt strength [40], drilling [41,42], cutting parameters [43, 44, 45], machinability of steels [46], and thermal performance [47]. This paper applies optimization to solve the welded Beam and pressure vessel engineering problem.

In the literature, the studies conducted with heuristic optimization methods are used to solve and compare engineering problems. Therefore, to measure the performance of this algorithm in other problems and to compare the results, the pressure vessel model was also included in the calculation in addition to the welded beam design. In addition, unlike the literature, a classical optimization solution was run and compared with the new ACO algorithm results so that the readers could better understand the algorithm performance.

4.1. Welded Beam Problem Definition

The objective is to design a beam subjected to some constraints fixed through the welding method with a minimum cost using the new ACO algorithm. Design variables are x_1, x_2, x_3, x_4 and constraints of shear stress, bending stress forming on the Beam, buckling load on the Beam and end deflection. Welded Beam is shown in ▶**Figure 2** [20],[21], [22], [23].

There are some constraints to optimizing welded beams at minimum cost. These are shear stress τ (g_1), bending stress on beam σ (g_2), buckling force PC (g_7), deflection δ (g_6) and other constraints that are stated below. Values are given as follows: the size of the weld h(x_1), the length of the welded part of the beam l(x_2), the width of the beam t(x_3) and the beam thickness b(x_4). The objective, constraint functions and coefficients are given by obtaining them from the literature [20],[21], [22], [23].

The objective function is shown in Equation 11.

$$f(x) = (1.10471\, x_1^2\, x_2 + 0.04811\, x_3\, x_4\, (14.0 + x_2) \quad (11)$$

Constraint conditions and design variables are shown in Equation 12-34

$$g_1(x) = \tau(x) - \tau_{max} \leq 0 \quad (12)$$

$$g_2(x) = \sigma(x) - \sigma_{max} \leq 0 \quad (13)$$

$$g_3(x) = x_1 - x_4 \leq 0 \quad (14)$$

$$g_4(x) = 0.10471\, x_1^2 + (0.04811\, x_3\, x_4\, (14.0 + x_2)) - 5 \leq 0 \quad (15)$$

$$g_5(x) = (0.125 - x_1) \leq 0 \quad (16)$$

$$g_6(x) = \delta(x) - \delta_{max} \leq 0 \quad (17)$$

$$g_7(x) = P - P_c(x) \leq 0 \quad (18)$$

$$0{,}125 \leq x_1 \leq 2 \quad (19)$$

$$0{,}1 \leq x_2 \leq 10 \quad (20)$$

$$0{,}1 \leq x_3 \leq 10 \quad (21)$$

$$0{,}1 \leq x_4 \leq 2 \quad (22)$$

Where:

$$\tau(x) = \sqrt{(\tau')^2 + 2\frac{\tau'\tau''}{2R}x_2 + (\tau'')^2} \quad (23)$$

$$\tau'' = M\frac{R}{J}, M = P\left(L + \frac{x_2}{2}\right) = 6000\left(14 + \frac{x_2}{2}\right), \tau' = \frac{P}{\sqrt{2}x_1 x_2} \quad (24)$$

$$\tau'' = M\frac{R}{J} \quad (25)$$

$$M = P\left(L + \frac{x_2}{2}\right) = 6000\,(14 + \frac{x_2}{2}) \quad (26)$$

$$R = \sqrt{\frac{{x_2}^2}{4} + \left(\frac{x_1 + x_3}{2}\right)^2} \quad (27)$$

$$J = 2\left\{\sqrt{2}x_1 x_2\left[\frac{{x_2}^2}{12} + \left(\frac{x_1 + x_3}{2}\right)^2\right]\right\} \quad (28)$$

$$\sigma(x) = \frac{6PL^3}{x_4 {x_3}^2} \quad (29)$$

$$\delta(x) = \frac{4PL}{E\,{x_3}^3\,x_4} \quad (30)$$

$$P_c(x) = \frac{4.013\sqrt{\frac{{x_3}^2 {x_4}^6}{36}}}{L^2}\left(1 - \frac{x_3}{2L}\sqrt{\frac{E}{4G}}\right) \quad (31)$$

4.2. Pressure Vessel Problem Definition

The new ACO algorithm was used to achieve minimum cost in pressure vessel design. The design variables are the thickness of the shell *Ts* (x_1), the thickness of the head (x_2), the inner radius R (x_3), and the length of the vessel L (x_4). Pressure Vessel is shown in ▶**Figure 3** [20], [21], [22], [23].

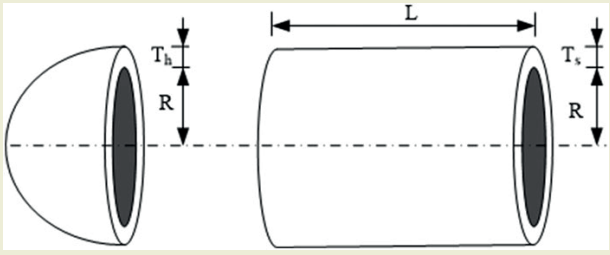

Figure 3. Schematic View of The Pressure Vessel [20], [21], [22], [23].

The objective, constraint functions and coefficients are given by obtaining them from the literature [20], [21], [22], [23].

The objective function is shown in Equation 35.

$$f(x) = 0.6224x_1x_3x_4 + 1.7781x_2x_3^2 + 3.1661x_1^2x_4 + 19.84x_1^2x_3 \quad (34)$$

Constraint conditions and design variables are shown in Equations 35-44.

$$g_1(x) = -x_1 + 0.0193x_3 \le 0 \quad (35)$$

$$g_2(x) = -x_2 + 0.00954x_3 \le 0 \quad (36)$$

$$g_3(x) = -\pi x_3^2 x_4 - \frac{4}{3}\pi x_3^3 + 1{,}296{,}000 \le 0 \quad (37)$$

$$g_4(x) = x_4 - 240 \le 0 \quad (38)$$

$$g_5(x) = 1.1 - x_1 \le 0 \quad (39)$$

$$g_6(x) = 0.6 - x_2 \le 0 \quad (40)$$

$$0 \le x_1 \le 100 \quad (41)$$

$$0.6 \le x_2 \le 0 \quad (42)$$

$$10 \le x_3 \le 200 \quad (43)$$

$$10 \le x_4 \le 200 \quad (44)$$

4.3. New ACO Algorithm and Sequential Quadratic Programming (SQP) Results Comparison

Considering the objective and constraint functions given for the welded beam design, it was run 20 times to obtain the best result. The best result in the new ACO algorithm is 1.7225, and the best result in the SQP algorithm was obtained at 1.9667. The MATLAB result screen is shown in ▶**Figure 4**.

Considering the objective and constraint functions given for the pressure vessel design, it was run 20 times to obtain the best result. The best result in the new ACO algorithm is 5947.1735, and the best result in the SQP algorithm was obtained at 5955.8184. The MATLAB result screen is shown in ▶**Figure 5**.

4.4. New ACO Algorithm and Literature Results Comparison

Considering the objective and constraint functions given for the welded beam design, it was run 20 times to get the best result. The best result was obtained with 540 iterations, 1000 ants and 6.27 seconds. In addition, the best result for the new ACO was compared with those obtained for the same problem in the literature. Result summaries are given in ▶**Table 2**.

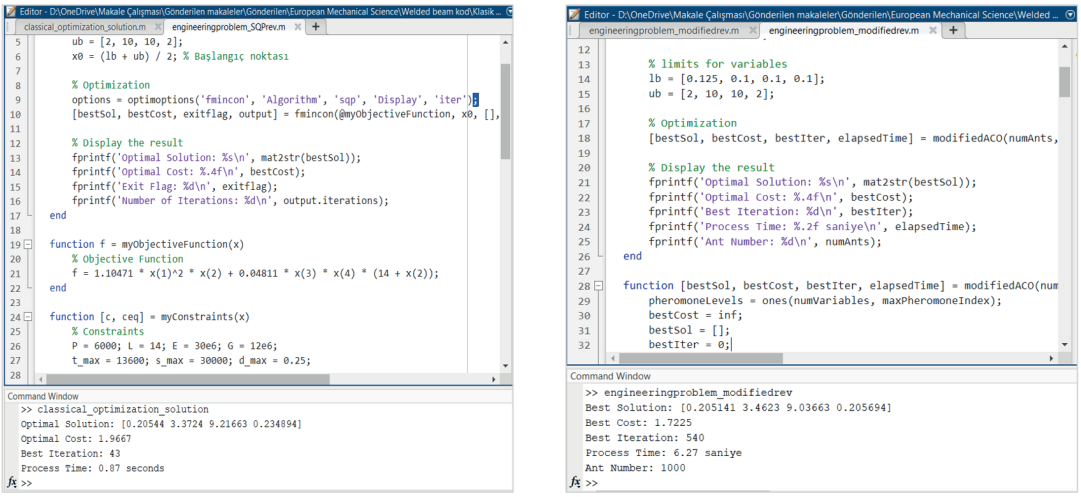

Figure 4. Welded Beam MATLAB Result Screen a) The new ACO b) SQP

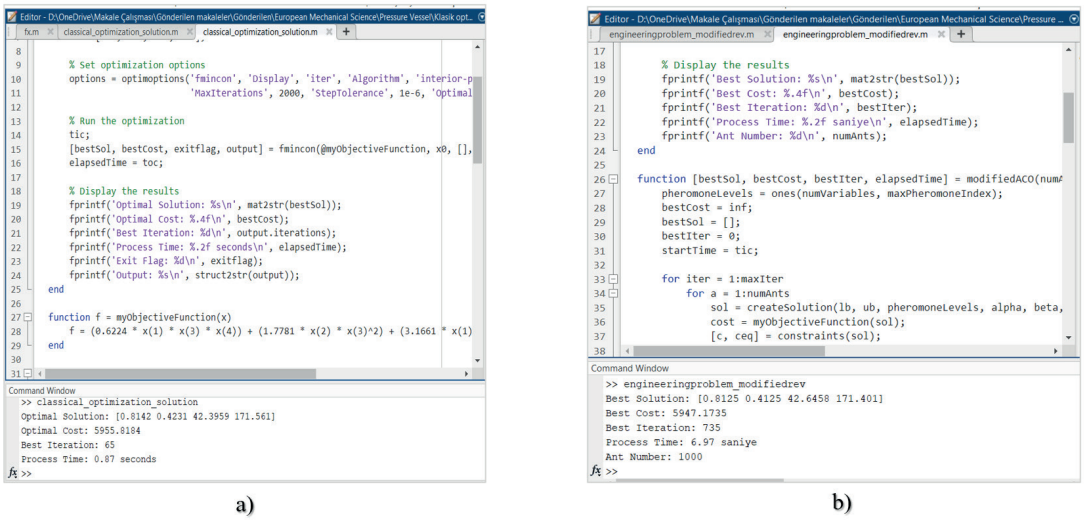

Figure 5. Pressure Vessel MATLAB Result Screen a) The new ACO b) SQP

Comparisons of welded beam design results with literature are as follows.

Eskandar *et al.* have conducted their research using the Water Cycle algorithm (WCA), Colelo with the Genetic Algorithm (GA), Zhao *et al.* with the Hybrid Genetic Algorithm with flexible allowance technique (GAFAT), and Grković & Bulatović have carried out their studies using a modified Ant Colony algorithm (MACA). When the new ACO algorithm was applied, the best solution was found to be 1.7225

The new ACO algorithm result is 0.13% better than Eskander *et al.*'s study (WCA) [48]. Although the algorithm solved with 540 iterations, WCA solved with 750 iterations. The new ACO algorithm result is 1.47 % better than Coello's study (CA) [49]. Although the algorithm solved with 540 iterations, GA solved with 11 iterations. The new ACO algorithm result is 0.13% better than Zhao *et al.* 's study (GAFAT) [50]. Although the algorithm solved with 540 iterations, SA solved with 3000 iterations. The new ACO algorithm result is 0.39 % higher than Grković & Bulatović's work (MACA) [22]. Although the algorithm solved with 1000 ants, MACA solved with 10000 ants. Considering the objective and constraint functions given for the pressure vessel design, it was run 20 times to get the best result. The best result was obtained with 735 iterations, 1000 ants and 6.97 seconds. In addition, the best result for the new ACO was compared with those obtained for the same problem in the literature. Result summaries are given in ▶**Table 3**.

Table 2. Comparison of The Results for Welded Beam Design

Definition	Eskandar et al. (WCA)	Colelo (GA)	Zhao et al. (GAFAT)	Grković & Bulatović (MACA)	This Paper
x_1	0.205728	0.2088	0.20572964	0.202611802838422	0.205141
x_2	3.470522	3.4205	3.47048867	3.538184790851369	3.462302
x_3	9.036620	8.9975	9.03662391	9.038385657692625	9.036633
x_4	0.205729	0.2100	0.020572964	0.205720941513918	0.205694
Best f(x)	1.724856	1.74830941	1.724852	1.729335567988	1.7225
Iteration	750	11	3000	-	540
Ant number	-	-	-	10000	1000
Process time (sec)	-	-	-	-	6.27

Table 3. Comparison of The Results of Pressure Vessel Design

Definition	Eskandar et al. (WCA)	Colelo (GA)	Zhao et al. (GAFAT)	Grković & Bulatović (MACA)	This Paper
x_1	0.7781	0.8125	0.8125	0.82217025865521	0.8125
x_2	0.3846	0.4375	0.4375	0.40638075763737	0.4125
x_3	40.3196	40.3239	42.0984455959	42.6028471508185	42.6458
x_4	_200.0000	200.0000	176.6365958424	170.484922696647	171.4015
Best f(x)	6288.7445	6288.7445	6059.7143	5964.5059570367	5947.1735
Iteration	1000	11	9000	-	735
Ant number	-	-	-	10000	1000
Process time	-	-	-		6.97

Comparisons of welded beam design results with literature are as follows.

Eskandar *et al.* have conducted their research using the Water Cycle algorithm (WCA), Colelo with the Genetic Algorithm (GA), Zhao *et al.* with the Hybrid Genetic Algorithm with flexible allowance technique (GAFAT), and Grković & Bulatović have carried out their studies using a modified Ant Colony algorithm (MACA). When the new ACO algorithm was applied, the best solution was 5947.1735. The new ACO algorithm result is 5.43 % better than Eskander *et al.*'s study (WCA) [48]. Although the algorithm solved with 735 iterations, WCA solved with 1000 iterations. The new ACO algorithm result is 5.43 % better than Coello's study (CA) [49]. Although the algorithm solved with 735 iterations, GA solved with 11 iterations. The new ACO algorithm result is 1.85% better than Zhao *et al.* 's study (GAFAT) [50]. Although the algorithm solved with 735 iterations, SA solved with 9000 iterations. The new ACO algorithm result is 0.29 % higher than Grković & Bulatović's work (MACA) [22]. Although the algorithm solved with 1000 ants, MACA solved with 10000 ants. From this, it is clear that new has achieved success among the results in the literature. Thus, it is clear that new ACO can be reliably used in bow design solutions.

5. Conclusions

This study presents a solution for welded Beam and pressure vessel design using a modified ant colony optimization (ACO) algorithm. The algorithm was enhanced to improve performance compared to previous techniques in the literature. The MATLAB-based implementation was tested 20 times for the new ACO and SQP methods.

The best result was achieved in welded beam design with 540 iterations, 1000 ants, and 6.27 seconds. When the algorithm was applied, the best solution was 1.7225 in the new ACO algorithm and 1.9667 in the SQP algorithm. The new ACO algorithm result is 0.13% better than Eskander *et al.*'s study (WCA). Although the algorithm solved with 540 iterations, WCA solved with 750 iterations. The new ACO algorithm result is 1.47 % better than Coello's study (CA). Although the algorithm solved with 540 iterations, GA solved with 11 iterations. The new ACO algorithm result is 0.13% better than Zhao *et al.* 's study (GAFAT). Although the algorithm solved with 540 iterations, SA solved with 3000 iterations. The new ACO algorithm result is 0.39 % higher than Grković Bulatović's work (MACA). Although the new ACO solved with 1000 ants, MACA solved with 10000 ants.

The best result was achieved in pressure vessel design with 735 iterations, 1000 ants, and 6.97 seconds. When the algorithm was applied, the best solution was

5947.173 in the new ACO algorithms and 5955.8184 in the SQP algorithm. The new ACO algorithm result is 5.43 % better than Eskander *et al.*'s study (WCA). Although the algorithm solved with 735 iterations, WCA solved with 1000 iterations. The new ACO algorithm result is 5.43 % better than that of Coello's study (CA). Although the algorithm solved with 735 iterations, GA solved with 11 iterations. The new ACO algorithm result is 1.85% better than Zhao *et al.* 's study (GAFAT). Although the algorithm solved with 735 iterations, SA solved with 9000 iterations. The new algorithm result is 0.29 % higher than Grković & Bulatović's work (MACA). Although the algorithm solved with 1000 ants, MACA solved with 10000 ants.

From this, it is clear that the new algorithm has succeeded among the results in the literature. Thus, the algorithm can be reliably used in welded beam design and pressure vessel solutions. Users can quickly learn about welded beam design, pressure vessel design and prefabrication through simulation using the new ACO algorithm. Therefore, the aim is to contribute to cost and time savings for Industry, professionals and users in this field. Further research and development of the algorithm is believed to yield more optimal results. Heuristic optimization methods such as particle swarm and other different classical optimization techniques can be used to measure the algorithm's applicability to other design problems. In addition, it is suggested that the algorithm be extended to other engineering design challenges, such as composite material design, to verify its versatility and effectiveness.

Research ethics

Ethical approval is not required.

Author contributions

Conceptualization: [Kursat Tanriver], Methodology: [Kursat Tanriver], Formal Analysis: [Kursat Tanriver], Investigation: [Kursat Tanriver], Resources: [Kursat Tanriver], Data Curation: [Kursat Tanriver], Writing - Original Draft Preparation: [Kursat Tanriver], Writing - Review & Editing: [Mustafa Ay], Visualization: [Mustafa Ay], Supervision: [Mustafa Ay], Project Administration: [Mustafa Ay]

Competing interests

The authors declare that there is no competing financial interest or personal relationship.

Research funding

There is no funding for this study

Data availability

Data may be made available on request.

Orcid

Kürşat Tanrıver https://orcid.org/0000-0002-1723-4108
Mustafa Ay https://orcid.org/0000-0002-7672-1846

References

[1] Akcay, O. (2023). Structural optimization of the brake pedal using artificial intelligence. *International Journal of Automotive Science and Technology, 7*(3), 187–195. https://doi.org/10.30939/ijastech..1330096

[2] Tanriver, K., & Ay, M. (2023). Experimental software and topological optimization study of unpredictable forces in bolted connections. *Tehnički Vjesnik - Technical Gazette, 30*(4). https://doi.org/10.17559/TV-20221113121639

[3] Zhao, W., Liu, Y., Li, Y., Hu, C., & Rui, S. (2023). Multi-robot coverage path planning for dimensional inspection of large free-form surfaces based on hierarchical optimization. *The International Journal of Advanced Manufacturing Technology, 127*(11–12), 5471–5486. https://doi.org/10.1007/s00170-023-11788-1

[4] Harikrishnan, V. K., Sivakumar, A. I., Sampath, S., & Paramasivam, S. (2023). A time-performance improvement model with optimal ergonomic risk level using genetic algorithm. *Transactions of FAMENA, 47*(4), 109–128. https://doi.org/10.21278/TOF.474049022

[5] Avci, I., & Yildirim, M. N. (2023). Solving weapon-target assignment problem with Salp swarm algorithm. *Tehnički Vjesnik - Technical Gazette, 30*(1), 17–23. https://doi.org/10.17559/TV-20220113192727

[6] Katiyar, S., & Dutta, A. (2022). Comparative analysis on path planning of ATR using RRT*, PSO and modified APF in CG-Space. *Proceedings of the Institution of Mechanical Engineers, Part C: Journal of Mechanical Engineering Science, 236*(10), 5663–5677. https://doi.org/10.1177/09544062211062435

[7] Essiz, E. S., Kilic, V. N., & Oturakci, M. (2023). Firefly-based feature selection algorithm method for air pollution analysis for Zonguldak region in Turkey. *Turkish Journal of Engineering, 7*(1), 17–24. https://doi.org/10.31127/tuje.1005514

[8] Irmak, B., & Gülcü, Ş. (2021). Training of the feed-forward artificial neural networks using butterfly optimization algorithm. *MANAS Journal of Engineering, 9*(2), 160–168. https://doi.org/10.51354/mjen.91783

[9] Tian, T., Liang, Z., Wei, Y., Luo, Q., & Zhou, Y. (2024). Hybrid whale optimization with a firefly algorithm for function optimization and mobile robot path planning. *Biomimetics, 9*(1), 39. https://doi.org/10.3390/biomimetics9010039

[10] Tuncer, A. (2023). Path planning of autonomous mobile robots based on Voronoi diagram and ant colony optimization. *Journal of Innovative Engineering and Natural Science, 4*(1), 138–146. https://doi.org/10.61112/jiens.1365282

[11] Zhang, D., Luo, R., Yin, Y.-B., & Zou, S. (2023). Multi-objective path planning for mobile robot in nuclear accident environment based on improved ant colony optimization with modified A*. *Nuclear Engineering and Technology, 55*(5), 1838–1854. https://doi.org/10.1016/j.net.2023.02.005

[12] Sun, L., Chen, Y. S., Ding, W., & Xu, J. (2023). LEFSA: Label enhancement-based feature selection with adaptive neighborhood via ant colony optimization for multilabel learning. *International Journal of Machine Learning and Cybernetics, 15*, 533–558. https://doi.org/10.1007/s13042-023-01924-4

[13] Zhou, X., Gui, W., Heidari, A. A., Cai, Z., Liang, G., & Chen, H. (2023).

Random following ant colony optimization: Continuous and binary variants for global optimization and feature selection. *Applied Soft Computing, 144*, 110513. https://doi.org/10.1016/j.asoc.2023.110513

[14] Hizaroğlu, O., & Akkurt, A. (2023). Simulating gait profile in MATLAB Simulink environment. *Gazi Journal of Engineering Sciences, 9*(3), 622–633. https://doi.org/10.30855/gmbd.0705093

[15] Hashemi, M., Joodaki, N. Z., & Dowlatshahi, M. B. (2022). Ant colony optimization equipped with an ensemble of heuristics through multi-criteria decision making: A case study in ensemble feature selection. *Applied Soft Computing, 124*, 109046. https://doi.org/10.1016/j.asoc.2022.109046

[16] Maniezzo, V., Gambardella, L. M., & De Luigi, F. (2004). Ant colony optimization. In: *New Optimization Techniques in Engineering*. Studies in Fuzziness and Soft Computing, 141, 101–121. https://doi.org/10.1007/978-3-540-39930-8_5

[17] Zheng, X., Wang, Z., Liu, D., & Wang, H. (2021). A path planning algorithm for PCB surface quality automatic inspection. *Journal of Intelligent Manufacturing, 33*(6), 1829–1841. https://doi.org/10.1007/s10845-021-01766-3

[18] Das, M., Roy, A., Maity, S., & Kar, S. (2023). A quantum-inspired ant colony optimization for solving a sustainable four-dimensional traveling salesman problem under type-2 fuzzy variable. *Advanced Engineering Informatics, 55*, 101816. https://doi.org/10.1016/j.aei.2022.101816

[19] Heins, J., Bossek, J., Pohl, J., Seiler, M., Trautmann, H., & Kerschke, P. (2022). A study on the effects of normalized TSP features for automated algorithm selection. *Theoretical Computer Science, 940*, 123–145. https://doi.org/10.1016/j.tcs.2022.10.019

[20] Rao, S. S. (1996). *Engineering optimization: Theory and practice*. John Wiley & Sons. https://doi.org/10.1002/9781119454816

[21] Ray, T., & Liew, K. M. (2003). Society and civilization: An optimization algorithm based on the simulation of social behavior. *IEEE Transactions on Evolutionary Computation, 7*(4), 386–396. https://doi.org/10.1109/TEVC.2003.814902

[22] Grković, V., & Bulatović, R. (2012). Modified ant colony algorithm for solving engineering optimization problems. *IMK-14 - Research & Development, 18*(4), EN115-122.

[23] Cagnina, L., Esquivel, S. C., & Coello, C. A. C. (2008). Solving engineering optimization problems with the simple constrained particle swarm optimizer. *Informatica, 32*(3), 319–326.

[24] Renato, A. K., & Leandro, D. S. C. (2006). Coevolutionary particle swarm optimization using Gaussian distribution for solving constrained optimization problems. *IEEE Transactions on Systems, Man, and Cybernetics, Part B: Cybernetics, 36*, 1407–1416. https://doi.org/10.1109/tsmcb.2006.873185

[25] Zahara, E., & Kao, Y. T. (2009). Hybrid Nelder–Mead simplex search and particle swarm optimization for constrained engineering design problems. *Expert Systems with Applications, 36*(2), 3880–3886. https://doi.org/10.1016/j.eswa.2008.02.039

[26] He, Q., & Wang, L. (2007). A hybrid particle swarm optimization with a feasibility-based rule for constrained optimization. *Applied Mathematics and Computation, 186*, 1407–1422. https://doi.org/10.1016/j.amc.2006.07.134

[27] Huang, F. Z., Wang, L., & He, Q. (2007). An effective co-evolutionary differential evolution for constrained optimization. *Applied Mathematics and Computation, 186*(1), 340–356. https://doi.org/10.1016/j.amc.2006.07.105

[28] Coelho, L. D. S., & Mariani, V. C. (2008). Use of chaotic sequences in a biologically inspired algorithm for engineering design optimization. *Expert Systems with Applications, 34*(3), 1905–1913. https://doi.org/10.1016/j.eswa.2007.02.002

[29] Tanriver, K., & Ay, M. (2024). Simulation of speed reducer design with the modified ant colony optimization algorithm. *The Journal of Engineering Sciences and Research, 6*(1), 53–64. https://doi.org/10.46387/bjesr.1435356

[30] Hasan, M. S., Chowdhury, M. M.-U.-T., & Kamalasadan, S. (2024). Sequential quadratic programming (SQP) based optimal power flow methodologies for electric distribution system with high penetration of DERs. *IEEE Transactions on Industry Applications, 60*(3), 4810–4820. https://doi.org/10.1109/TIA.2024.3371428

[31] Wang, J., Hu, H., Zhang, W., & Hu, Z. (2023). Optimization-based transient control of turbofan engines: A sequential quadratic programming approach. *International Journal of Turbo & Jet-Engines, 40*(s1), s119–s128. https://doi.org/10.1515/tji-2021-0072

[32] Alhaji, H. S., Celik, Y., & Goel, S. (2024). An approach to deepfake video detection based on ACO-PSO features and deep learning. *Electronics, 13*(2), 2398. https://doi.org/10.3390/electronics13122398

[33] Sabir, Z., Raja, M. A. Z., Wahab, H. A., Shoaib, M., & Aguilar, J. F. G. (2024). Integrated neuro-evolution heuristic with sequential quadratic programming for second-order prediction differential models. *Numerical Methods for Partial Differential Equations, 40*, e22692. https://doi.org/10.1002/num.22692

[34] Ji, W., Li, G., Wei, L., & Yi, Z. (2024). An improved sequential quadratic programming method for identifying the total heat exchange factor of reheating furnace. *International Journal of Thermal Sciences, 204*, 109238. https://doi.org/10.1016/j.ijthermalsci.2024.109238

[35] Wilson, E. O., & Hölldobler, B. (1988). Dense hierarchies and mass communication as the basis of organization in ant colonies. *Trends in Ecology & Evolution, 3*(3), 65–68. https://doi.org/10.1016/0169-5347(88)90018-3

[36] Dorigo, M., Maniezzo, V., & Colorni, A. (1996). The ant system: Optimization by a colony of cooperating agents. *IEEE Transactions on Systems, Man, and Cybernetics, Part B: Cybernetics, 26*(1), 29–41. https://doi.org/10.1109/3477.484436

[37] Hashemi, A., & Dowlatshahi, M. B. (2024). Exploring ant colony optimization for feature selection: A comprehensive review. In N. Dey (Ed.), *Applications of ant colony optimization and its variants* (pp. 101–121). Springer. https://doi.org/10.1007/978-981-99-7227-2_3

[38] Benhala, B., Ahaitouf, A., Mechaqrane, A., Benlahbib, B., Abdi, F., Hossain Abarkan, E. H., & Fakhfakh, M. (2011). Sizing of current conveyors by means of an ant colony optimization technique. In *Proceedings of the International Conference on Multimedia Computing and Systems* (pp. 1–6). Ouarzazate, Morocco. https://doi.org/10.1109/ICMCS.2011.5945669

[39] Shen, Q., Jiang, J., Tao, G., Shen, J., & Yu, R. (2005). Modified ant colony optimization algorithm for variable selection in QSAR modeling: QSAR studies of cyclooxygenase inhibitors. *Journal of Chemical Information and Modeling, 45*(4), 1024–1029. https://doi.org/10.1021/ci049610z

[40] Tanriver, K., & Ay, M. (2020). Topology optimization of a steel construction bolt under boundary conditions. *Euroasia Journal of Mathematics, Engineering, Natural & Medical Sciences, 7*(12), 31–47. https://doi.org/10.38065/euroasiaorg.272

[41] Ay, M., Altunpak, Y., & Hartomacioglu, S. (2017). The grey-based Taguchi method: Optimization of drilling of hybrid aluminum matrix composites. *Acta Physica Polonica A, 131*(3), 551–554. https://doi.org/10.12693/APhysPolA.131.551

[42] Tanriver, K., & Ay, M. (2024). Efficient path planning for drilling processes: The hybrid approach of a genetic algorithm and ant colony optimization. *Transactions of FAMENA, 48*(3), 125–140. https://doi.org/10.21278/TOF.483062023

[43] Basmaci, G., Kurt, M., Ay, M., & Barkin, B. (2018). Optimization of the effects of machining parameters in turning on Hastelloy C22 composition through Taguchi response surface methodology. *Acta Physica Polonica A, 134*(1), 28–31. https://doi.org/10.12693/APhysPolA.134.28

[44] Yüksel, S., Şirin, T. B., Ay, M., & Kurt, M. (2024). A study on end mill tool geometry parameters for end milling of 316L: Finite element analysis and response surface methodology optimization based on resultant cutting force. *Journal of the Brazilian Society of Mechanical Sciences and Engineering, 46*(8), 452. https://doi.org/10.1007/s40430-024-05027-1

[45] Basmaci, G., Kayacan, M. Y., Ay, M., & Etyemez, A. (2023). Optimization of cutting forces and surface roughness via ANOVA and grey relational analysis in machining of In718. *Open Chemistry, 21*(1). https://doi.org/10.1515/chem-2022-0273

[46] Erman, B., & Kalyon, A. (2022). Multi-objective optimization of parameters in EDM of Mirrax steel. *Materials and Manufacturing Processes, 38*(7), 848–858.

[47] Tanriver, K., & Ay, M. (2024). Investigation of flue gas temperature effects in natural gas-fueled systems: Experimental thermal performance and structural optimization. *International Journal of Heat and Fluid Flow, 107*, 109428. https://doi.org/10.1016/j.ijheatfluidflow.2024.109428

[48] Eskandar, H., Sadollah, A., Bahreininejad, A., & Hamdi, M. (2012). Water cycle algorithm: A novel metaheuristic optimization method for solving constrained engineering optimization problems. *Computers & Structures, 110–111*, 151–166. https://doi.org/10.1016/j.compstruc.2012.07.010

[49] Coello, C. A. C. (2000). Use of a self-adaptive penalty approach for engineering optimization problems. *Computers in Industry, 41*(2), 113–127. https://doi.org/10.1016/S0166-3615(99)00046-9

[50] Zhao, J. G., Wang, L., Zeng, P., & Fan, W. H. (2012). An effective hybrid genetic algorithm with flexible allowance technique for constrained engineering design optimization. *Expert Systems with Applications, 39*(5), 6041–6051. https://doi.org/10.1016/j.eswa.2011.12.012

EUROPEAN MECHANICAL SCIENCE

Research Article

e-ISSN: 2587-1110

The effect of impactor shape on low velocity impact behavior of cylindrical sandwich structures with trapeozidal core

Ilyas Bozkurt[1*]

[1]Department of Mechanical Engineering, Architecture and Engineering Faculty, Mus Alparslan University, 49250 Mus, Türkiye

Abstract: The aim of this study is to investigate the impact performance of a cylindrical sandwich structure with Trapeozidal core under different geometries of impactors using the finite element method. The effects of impactor shape, facesheets thickness and impact point on peak contact force, absorbed energy efficiency, maximum displacement and damage deformation are investigated. *Progressive damage analysis* based on the *Hashin damage criterion* was performed using *MAT 54* material model in *LS DYNA* finite element program for low velocity simulations. The impact behavior was investigated by creating a *Cohesive Zone Model (CZM)* based on *bilinear traction-separation law* while providing the connection between the core structure and its surfaces. At the end of the study, it was determined that the contact force values at P2 were higher than P1. Peak force variation values for cylinder, cone and sphere tipped impactors at P1 and P2 points were 43.5%, 132.3% and 62.2%, respectively. Core support has a significant effect on the contact force. The peak force value and energy absorption efficiency value obtained with the Cone impactor are higher than the others. For all three impactors, it was determined that the largest and dominant damage type was matrix damage.

Keywords: impactor shape; cylindrical sandwich composite; Impact test; Progressive damage analysis; Finite element method; cohesive zone model (CZM).

1. Introduction

Composite structures are effectively used in many sectors, especially in the aerospace industry, due to their high strength-to-weight ratio [1]. Especially with the recent technological developments and the development of production machines and production methods, composite structures have started to be used in many areas in our daily lives, from bicycle bodies to car steering wheels, from laptop cases to shoe fabrics. In addition, the rate of use of composite structures in airplanes and cars carrying life and property is increasing day by day. However, their performance decreases due to the loads they are exposed to in application areas and during service [2]. These structures used in different areas can be subjected to loads and impacts of very different types and magnitudes. Due to these loads, the service life of the damaged structure decreases. This can cause major disasters and huge cost losses during service. Therefore, researchers and engineers working in this field should determine the type of impact and the type of impactor that composite structures will be exposed to, and make appropriate material selection and structure selection by predicting the reaction of the structure to it.

Sandwich structures are structures formed by the combination of core and facesheet structures and are widely used in the field of engineering. These structures, which are usually produced flat, can be produced in many different shapes, curved or cylindrical, with the advancement of technological developments and production techniques. These structures are used in many areas of our lives, such as airplane tips or new generation lightweight bicycle bodies, without even realizing it.

*Corresponding author:
Email: i.bozkurt@alparslan.edu.tr

Cite this article as:
Bozkurt, I.(2024). The effect of impactor shape on low velocity impact behavior of cylindrical sandwich structures with trapeozidal core. *European Mechanical Science*, *8*(4): 278-292. https://doi.org/10.26701/ems.1522846

History dates:
Received: 26.07.2024, ***Revision Request***: 07.09.2024, ***Last Revision Received***: 10.09.2024, ***Accepted***: 09.10.2024

In general, when metal materials are subjected to impact, the material behavior can be predicted due to the linearity in their structure. However, in composite structures, it is more difficult to make this prediction due to the complexity of the micro-mechanical structure of the material. Because in these structures, there are many factors affecting the material strength such as fiber type, matrix type, fiber and matrix ratio, fiber and matrix compatibility. All of these have an effect on material mechanics to some extent. Therefore, it is very difficult to predict all these possibilities in advance. For this reason, researchers conduct research on the mechanical performance of composite structures in laboratory environments or with the help of numerical analysis.

Many specialized machines and devices have been developed for the manufacturing of composite structures and the determination of their mechanical properties. Many special devices must be used for the mechanical properties of composite structures produced using high-cost consumables. In institutions where laboratory facilities are limited and financial support is limited, researchers cannot carry out healthy studies in this field. To overcome this problem, researchers have been able to investigate the mechanical behavior of composite structures with the finite element method. In addition, even some complex and difficult experiments can be applied with high accuracy precision with the finite element method.

There are many studies investigating the behavior of sandwich composite structures with high impact absorption potential under impact [2-12]. Li et al. [13] experimentally and numerically investigated the effects of impactor in corrugated sandwich structures with carbon fiber reinforced polymer (CFRP) facesheets and aluminum cores. Low-velocity impact tests were carried out to study the impact resistance when impacted by conical, hemispherical and flat impactors. They applied a progressive damage model based on Hashin fracture criteria and Yeh delamination fracture criteria in *ABAQUS/Explicit*. Khalkhali et al. [14] investigated the nonlinear low-velocity impact response of a sandwich plate subjected to impacts with different geometric shapes. The sandwich plate is assumed to consist of two face layers reinforced with CNTs graded as X profile along their thickness and a homogeneous core. They experimentally carried out impact tests using three different impactors: spherical impactor, conical impactor, and cylindrical impactor. Shirbhate et al. [15] examined the explosion response of a hexagonal honeycomb sandwich structure with holes along the cell height of the core compared to conventional honeycomb cores. Yalkın et al. [16] numerically investigated the low-velocity impact properties of E-glass fiber/epoxy and PVC foam core sandwich composite configurations. Damghani et al. [17] simulated the impact behavior of aluminum foam core sandwich structures with *LS-DYNA* software.

In this study, unlike the literature, the impact performance of cylindrical sandwich CFRP composite structure with Trapeozidal core was investigated by the finite element method. The effects of impactor shape and facesheets thickness on peak contact force, absorbed energy efficiency, maximum displacement and damage deformation were investigated. Progressive damage analysis based on the Progressive damage analysis based on the *Hashin damage criterion* was performed using *MAT 54* material model in *LS DYNA* finite element program for low velocity simulations.

2. Materials and Methods

2.1. Finite Element Model

The dimensional details of the cylindrical sandwich structure with Trapeozidal core are given in ▶**Figure 1**. Impact tests will be applied to the sandwich structure with different geometry impactors. The specimens, which were drawn as a flat plate, were twisted with the Flex command in Solidworks and brought to a cylindrical shape. In this structure with diameter x length dimensions of 100 x 140 mm, impact performances were also examined by using two different facesheets with thicknesses of 2 mm and 4 mm. Low velocity impact simulation was modeled as shown in ▶**Figure 2**. All impact tests were applied to the center of the specimens. The top and bottom holders were fixed. The impactor was limited to displacements in the x and y directions and could only move in the direction of the impactor (z-axis). Although the run time of the analysis with the shell element was fast, an eight-node solid element (*ELFORM1*) was used to show the damage structures more clearly and realistically.

This element structure is given in ▶**Figure 3** for the impactors used in the study. A mesh element size of 2x2 mm was chosen by mesh convergence and considering the processing time. In total, 30197 nodes and 26750 solid elements were used. The CONTACT ERODING SURFACE TO SURFACE contact card was used to define the contact between the impactor and the cylindrical sandwich structure. The CONTACT AUTOMATIC SURFACE TO SURFACE contact card was used to ensure that the specimen between the grippers does not move during impact and is held stationary by the gripper. The static and dynamic friction coefficients were entered as 0.2 and 0.3 respectively [18].

Since the core structure used in the study is corrugated, it does not contact everywhere in the specimen in the same way. Therefore, while there is core support at some points where the impactor is applied, there is core support in some places. Impact tests were performed at two different points in the study. Impact points are given in ▶**Figure 4**. The impact performances of these points were also compared.

2.2. Modeling of adhesive layer

Sandwich composite structures are composed of top and bottom surfaces and the core structure between them. To model the adhesive behavior between these two elements, the CZM model with a bilinear traction-separation law has been developed. This law is based on the application of 3 independent parameters. The traction t_0, between the layers when the force is applied, the separation distance δ_0 when the damage starts and G_C under this curve. After the impact occurs, the separation between the layers occurs according to this principle (▶**Figure 5**)

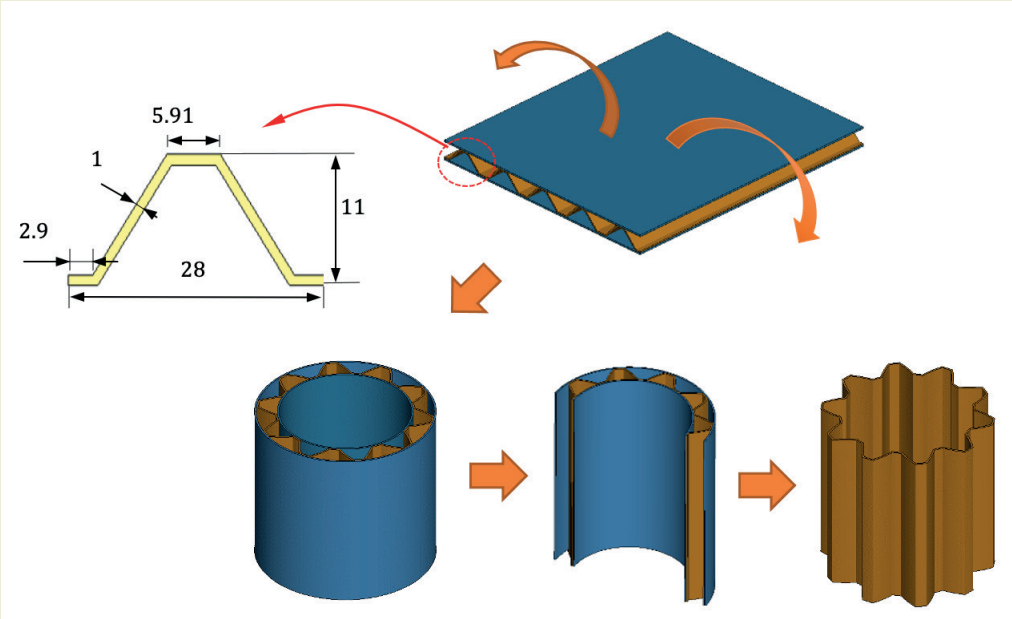

Figure 1. Specimen dimensions.

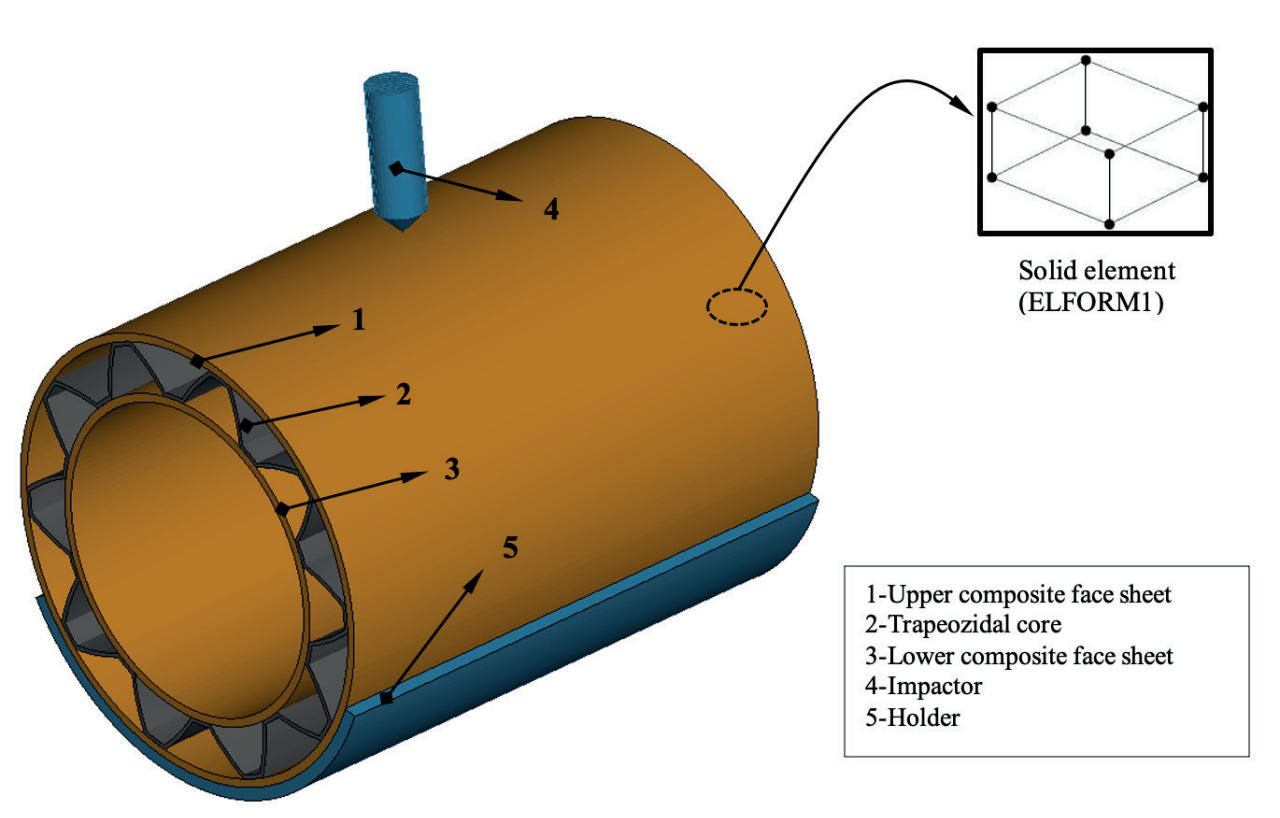

Figure 2. Finite element model of low velocity impact test.

Adhesion here can be achieved in two ways. First, it can be achieved by defining a thin interfacial material between the top cover and the core in the middle. Or it can be achieved by using an adhesion surface that performs the same task. Dogan et al. [19] found this method to be effective instead of using an intermediate material. In this study, The CONTACT_AUTOMATIC SURFACE TO SURFACE TIEBREAK contact board was used to adhere the top and bottom cover to the core material in between. While adhesion is achieved here, separations occur based on the bilinear traction-separation law. With this contact card, the nodes making contact in the beginning connect with each other according to the following criterion.

$$\left(\frac{|\sigma_n|}{NFLS}\right)^2 + \left(\frac{|\sigma_s|}{SFLS}\right)^2 \geq 1 \quad (1)$$

Here, while σ_n and σ_s are the current normal and shear stresses, NFLS and SFLS are respectively the interface and shear strength. When the condition of Equation (1) is met, interface node stress is decreased to zero and the connection between the nodes is released. The contact parameters for Araldite 2015, which was used as the adhesive material in this research, are provided in ▶**Table 1**.

2.3. MAT_54-55: Enhanced Composite Damage Model

The mechanical properties of the CFRP material used in the study are given in ▶**Table 2-3**. The most commonly used model in the analysis of composite structures is the *MAT 54-55* material model. In the material model, it is assumed that the material is orthotropic and linearly elastic in the absence of any damage. In this model, *MAT 54* damage criterion was proposed by Chang and *MAT 55* damage criterion was proposed by *Tsai-Wu*. The working principle of this material model and

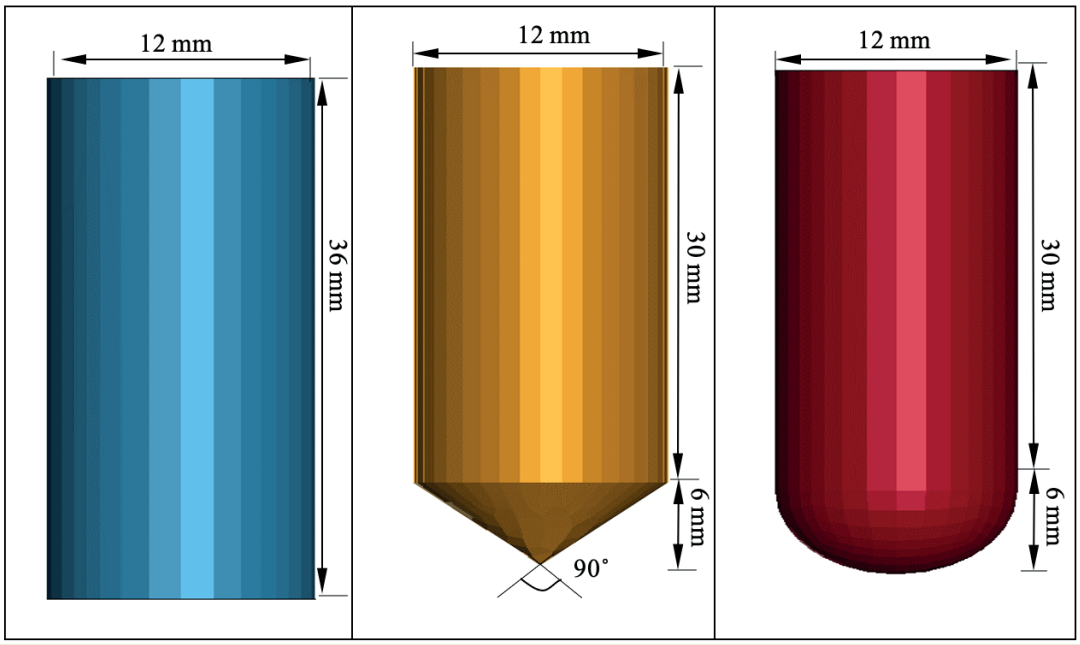

Figure 3. Impactor's dimensions.

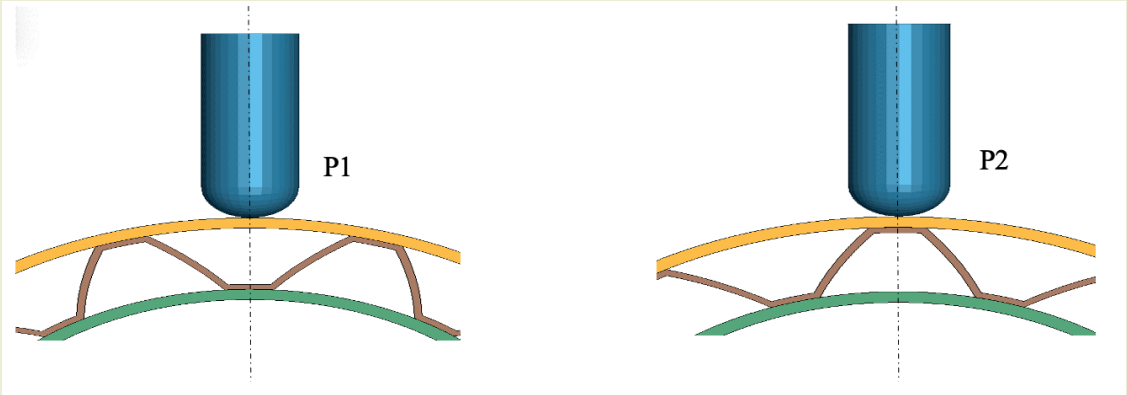

Figure 4. Impact points.

Table 1. Cohesive parameters of delamination between core and face sheets interfaces [4].

Contact Tiebreak Variable	Value	Units
NFLS	21.63x10⁹	Pa
SFLS	17.9x10⁹	Pa
PARAM	1	-
ERATEN	430	N/m
ERATES	4700	N/m
CT2CN	1	-
CN	8080	Pa/m

MAT 22 model is the same, but additionally includes compression damage mode. The *Chang–Chang criterion* (*MAT 54*) is given below;

Tensile fibre ($\sigma_{11} > 0$).

$$\left(\frac{\sigma_{11}}{S_1}\right)^2 + \bar{\tau} = 1 \quad (2)$$

All moduli and Poisson's ratios are set to zero when the tensile fibre failure criteria are met, that is $E_1 = E_2 = G_{12} = \upsilon_{12} = \upsilon_{21} = 0$ All the stresses in the elements are reduced to zero, and the element layer has failed.

Failure mode for compressive fibre ($\sigma_{11} > 0$),

$$\left(\frac{\sigma_{11}}{S_{12}}\right)^2 = 1 \quad (3)$$

Failure mode for tensile matrix ($\sigma_{11} > 0$),

Table 2. Mechanical parameters of the twill CFRP composite [18].

Symbol	Value	Unit
ρ	1500	kg/m³
E_a, E_b	43.7	GPa
E_c	14.57	GPa
υ_{ab}	0.21	-
υ_{bc}	0.21	-
υ_{ca}	0.21	-
G_{ab}	14.18	GPa
G_{bc}	14.65	GPa
G_{ca}	14.65	GPa
S_{aT}	0.589	GPa
S_{aC}	0.1096	GPa
S_{bT}	0.589	GPa
S_{bC}	0.1096	GPa
S_{ab}	0.1082	GPa

$$\left(\frac{\sigma_{22}}{S_2}\right)^2 + \bar{\tau} = 1 \quad (4)$$

Failure mode for compressive matrix

$$\left(\frac{\sigma_{22}}{2S_{12}}\right)^2 + \left[\left(\frac{C_2}{2S_{12}}\right) - 1\right]\frac{\sigma_{22}}{C_2} + \bar{\tau} = 1 \quad (5)$$

Where E_1 and E_2 are the longitudinal and transverse

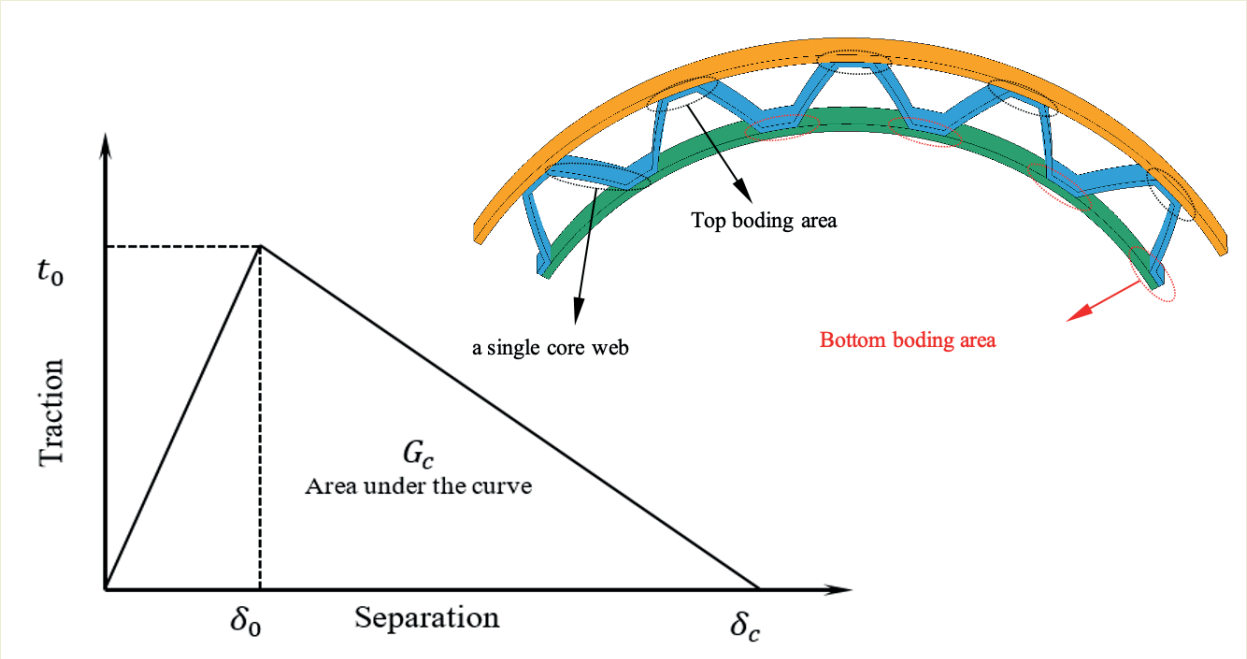

Figure 5. Bilinear traction-separation law

elastic moduli, respectively, G_{12} is the shear modulus, υ_{12} and υ_{21} are the in-plane Poisson's ratios.

Table 3. Failure parameters of the CFRP composite.

Symbol	Unit
DFAILM	0.0
DFAILS	0.0
DFAILT	0.0
DFAILC	0.0
TFAIL	0.16
Alpha	0.0
Soft	0.7
FBRT	1
YCFAC	3
EFS	0.90

3. Results and Discussion

Low-velocity impact tests are usually applied to determine the behavior of the material under impact load. These tests provide information about the mechanical performance of the material. The most important graphs obtained as a result of impact tests are given in ▶**Figure 6**. These results contain important information for researchers about material mechanics. For example, in the Contact force-time graph in ▶**Figure 6a**, after the impactor contacted the specimen, the force increased to the maximum point (peak force, PF) and then returned. Fluctuations occurred at the peak point, where changes in the force value occurred due to damage to the layers at the point of contact. We can see this reversal in ▶**Figure 6b** from the displacement movements of the impactor. ▶**Figure 6c** shows the absorbed energy (AE) value of the difference between the initial energy of the impactor and the probe energy. The impactor bounced back from the specimen surface. Because it continues, its energy at a certain speed after the contact is broken. With these graphs, appropriate material and structure selection can be made by evaluating the mechanical conditions experienced in the impact scenario.

Contact force-time, absorbed energy-time, contact force-displacement and velocity-time graphs for different impactors of circular sandwich structure with Trapeozidal core are given in ▶**Figure 7**. The impact test here was applied at point P1. In the contact force-time graph in ▶**Figure 7a**, the force reaches a maximum point due to the impactor contacting the specimen surface and then returns back to zero point with the energy discharge. The same scenario was observed for all three impactors. With 5 J impact energy, impact simulation

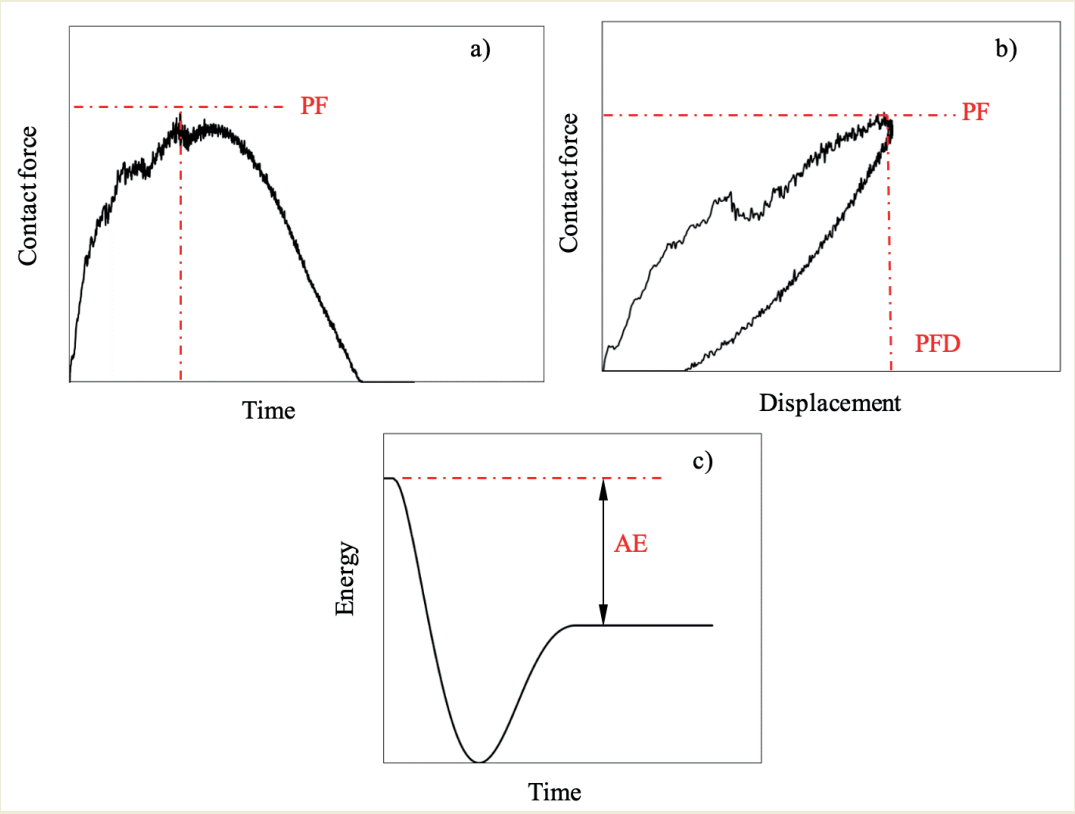

Figure 6. Composite cylinder structures under impact load a) Contact force-time, b) Contact force -displacement and c) Energy-time graphs.

was performed with cylindrical, conical and spherical impactors. The peak contact forces for cylindrical, conical and spherical impactors are 1.55, 1.58 and 1.16 kN respectively. Accordingly, the highest peak force value among these three impactors was obtained in the sphere impactor [13]. When the graph is examined in detail, it is determined that the force increases and decreases linearly to the peak point in the impact with the cylinder. However, in the cone and sphere impactor, the force increased up to a point and then dropped

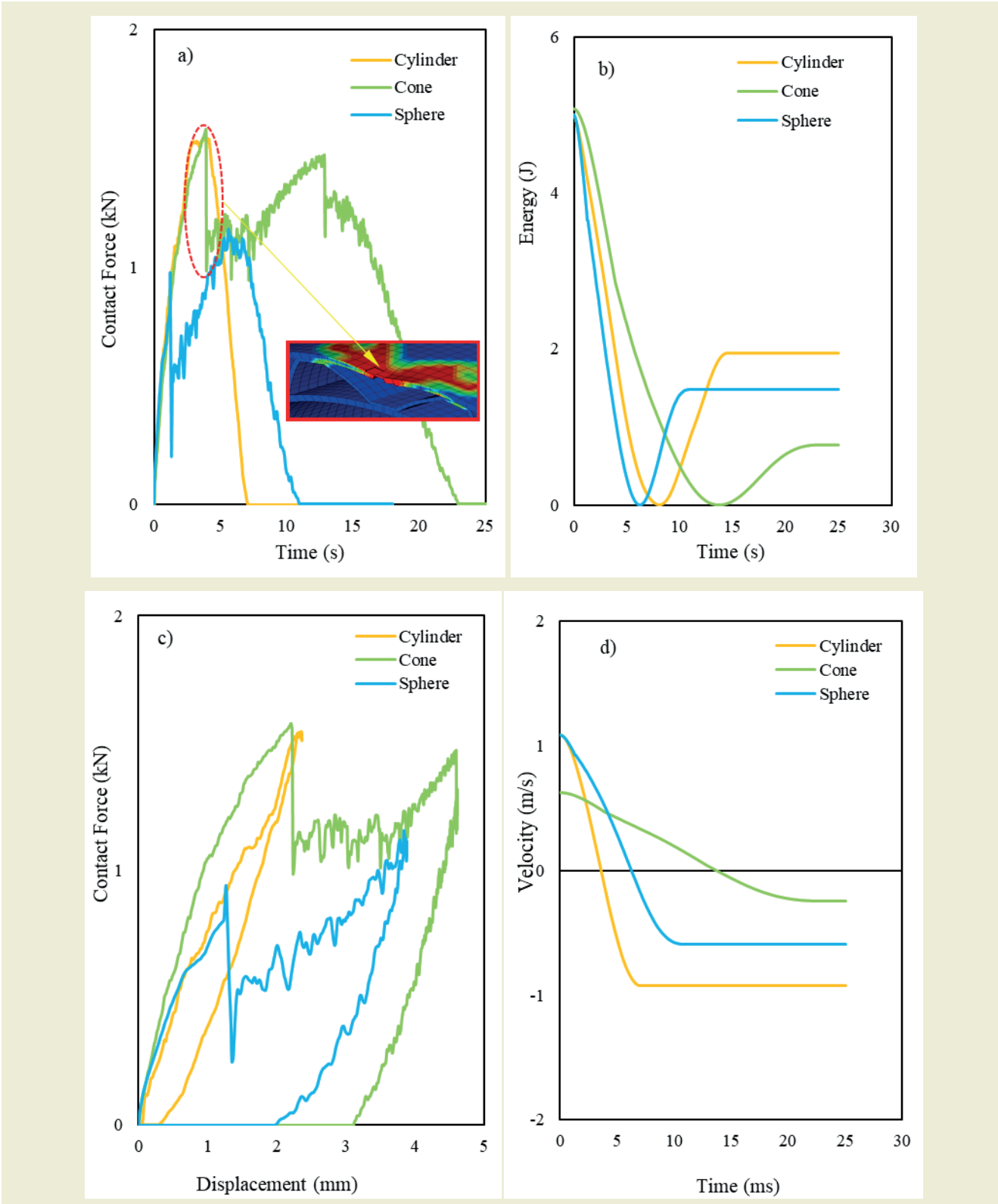

Figure 7. Variation of a) Contact force-Time, b) Energy-Time, c) Contact force-Displacement and d) Velocity-Time graphs with impactor geometry (P1).

sharply. It is understood that damage to the top layer occurred here. Therefore, the point of contact of the impactor at the moment when this force fell is shown on the graph. In ▶**Figure 7b**, the initial energy is 5 J for all three impactors in the energy-time graph. But at the end of the impact, the remaining energies for the cylinder, cone and sphere impactor are 3.16 J, 0.77 J and 1.48 J respectively. To calculate the energy absorption efficiency, we divide this energy difference (final energy - initial energy) by the initial energy. Therefore, the energy absorption efficiency (η) for cylinder, cone and sphere impactor is 0.28, 0.92 and 0.70 respectively. The highest energy absorption was obtained in the impact simulation with the cone impactor. When the displace-

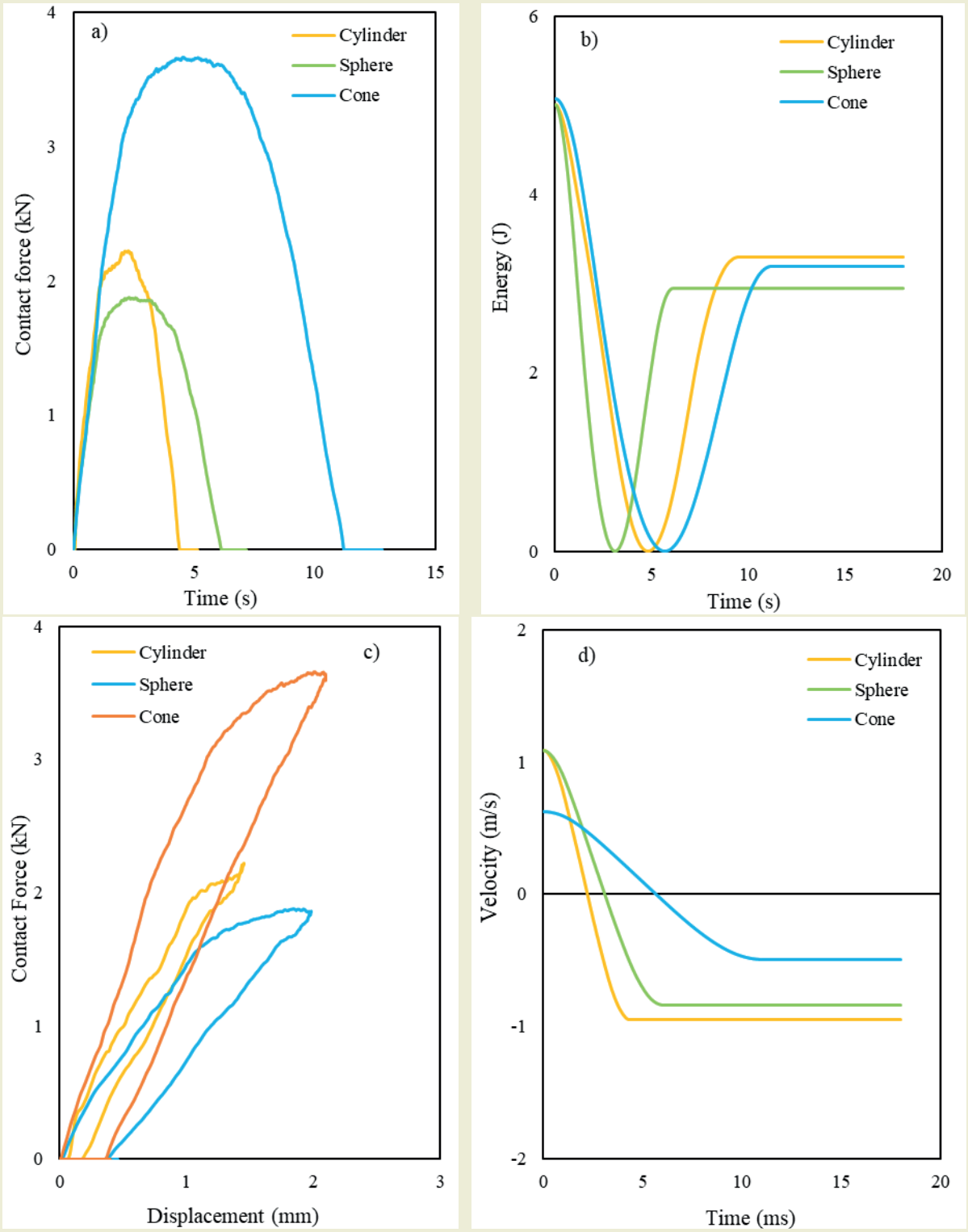

Figure 8. Variation of a) Contact force-Time, b) Energy-Time, c) Contact force-Displacement and d) Velocity-Time graphs with impactor geometry (P2).

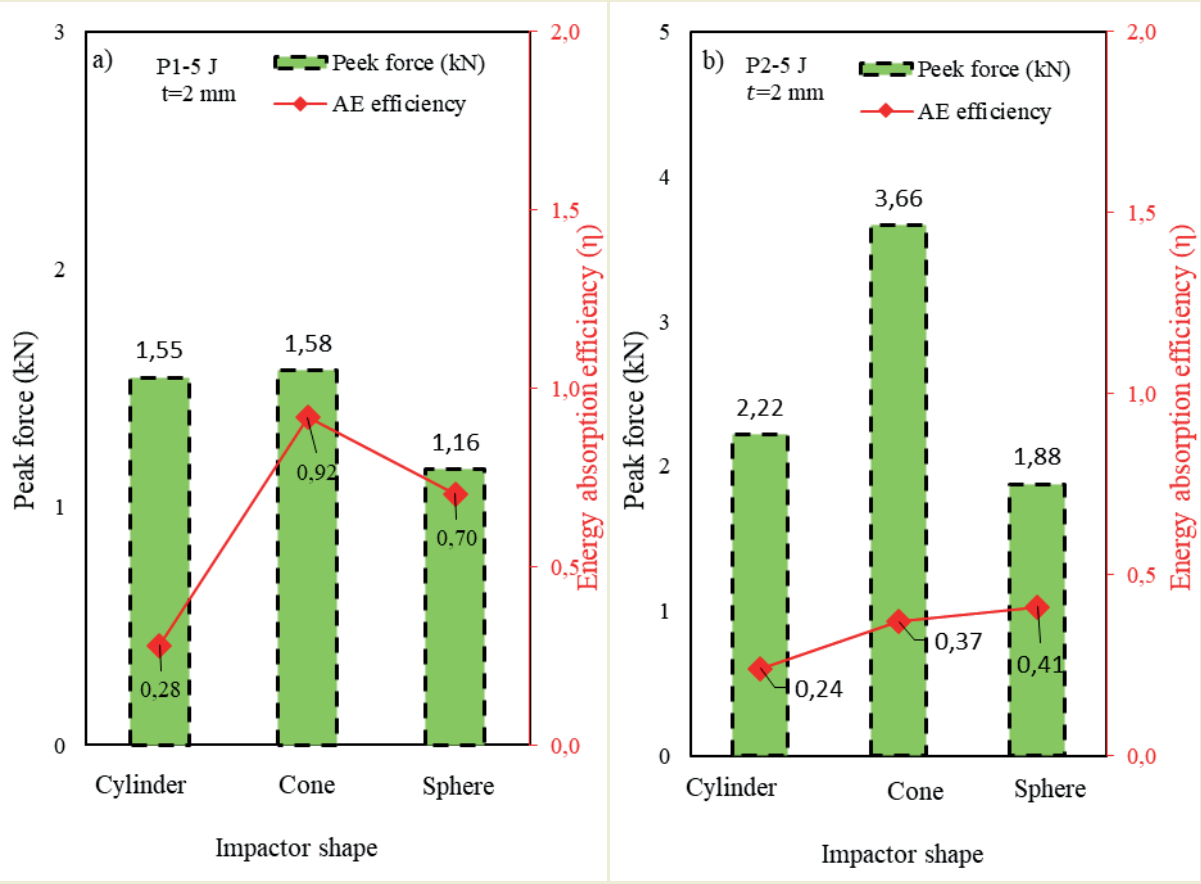

Figure 9. Variation of Contact force, Absorbed energy efficiency values for a) P1, b) P2 impact points (Facesheets thickness *t*= 2 mm).

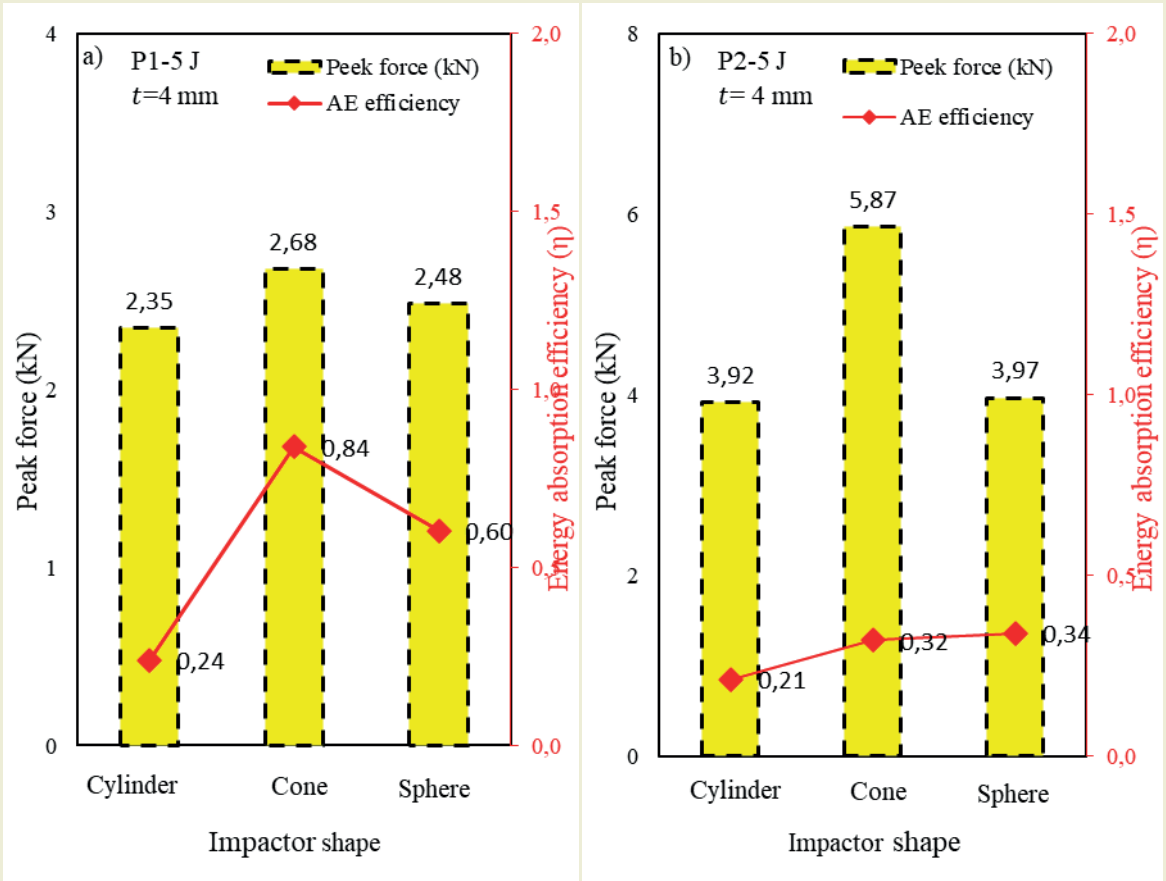

Figure 10. Variation of Contact force, Absorbed energy efficiency values for a) P1, b) P2 impact points (Facesheets thickness *t*= 4 mm).

ments are analyzed in the contact force-displacement graph in ▶**Figure 7c**, 2.82, 4.62 and 3.88 mm displacement occurred for the cylinder, cone and sphere impactor, respectively. ▶**Figure 7d** shows the changes in the velocity-time graph. When the graph is analyzed, it is seen that the velocity decreases to 0 and then moves in the negative direction. This indicates that the velocity decreases to zero after the impactor makes contact and then moves in the opposite direction. In ▶**Figure 8**, similar graphs are given for point P2. In ▶**Figure 8a**, in the contact force-time graph, the force goes up and down to the peak point without oscillation. Therefore, it is understood that a large deformation does not occur here, i.e. at point P2, like point P1. This is because this point is supported by the core structure [16]. In the energy-time graph in ▶**Figure 8b**, it is seen that the final output energy values are close to the initial energy values. Therefore, it is determined that there is less energy absorbed from P1. In the contact force-displacement graph in ▶**Figure 8c**, it is more clearly seen that the force goes to the peak point and returns back again. In ▶**Figure 8d**, the changes in the velocity-time graph are similar.

▶**Figure 9** shows the peak force and energy absorption efficiency values of the Trapeozidal sandwich structure under different impactors. In ▶**Figure 9a**, the peak force value for impact point P1 is the highest with 1.58 kN with cone impactor. Energy absorption efficiency value was also obtained with cone impactor. In ▶**Figure 9b**, for impact point P2, the cone impactor has the highest contact force value with 3.66 kN. The energy absorption efficiency of 0.41, i.e. 40%, was obtained with the sphere impactor. ▶**Figure 10** shows the peak force and energy absorption efficiency values under different impactors for facesheet thickness t=4 mm. It was observed that the maximum contact force increased for all three specimens when the facesheets thickness t was increased from 2 mm to 4 mm [21]. On the other hand, the energy absorbed value also decreased. The peak contact force value and the highest energy absorption efficiency value were obtained with cone impactor.

In ▶**Table 4** and ▶**Table 5**, Tensile fiber mode, Compressive fiber mode, Tensile matrix mode and Compressive matrix mode damages are shown separately for different impact points (P1 and P2). The damages in the core structure for 5 J impact for different impactors are compared. Here, the regions shown in red color represent the damaged areas and the regions shown in blue represent the areas where no damage occurred [22]. First of all, it is seen that the deformation at point P1 is large because it is not supported by the core [13]. However, it was determined that the effect of the damage spread over a wider area. It was mentioned in the previous section that this effect causes large fluctuations in the graphic structures. At P2, the damage was more stable and localized compared to P1 since it was supported by the core structure [18]. It is seen that the Cone impactor has a more destructive effect. It is understood that the core structure is a very important parameter against impact [4], [23], [24]. However, it is seen that matrix damage is the most dominant damage type.

One of the most important conveniences offered by the finite element method is to see the deformations at the desired point during the impact simulation [25]. ▶**Figure 11** shows the Contact force-time result obtained as a result of the impact at point P1 for the cone impactor. When the graph is examined, the force value increased to the peak point with the contact of the impactor to the specimen. Then a sharp decrease in the force value occurred here. While the force continued to fluctuate, the second sharp drop occurred. In the last part, it is seen that the force value reaches zero point by making certain oscillations and fluctuations. In general, when the graph is analyzed, a more fluctuating and oscillating contact force value is obtained than other graphs due to the destructive effect of the cone tip [2], [26]. Each movement mentioned here provides valuable information about material mechanics to researchers and engineers working in this field. Therefore, each point should be analyzed very carefully [27]. Shortly after the impactor contacts the cylindrical sandwich specimen, the damage starts (Phase 1). As the force increased, the stresses on the elements here increased. Then the damage occurred with element deletion (Phase 2). As the force increased, the damage area, i.e. the area of the red zone, increased (Phase 3). Since the elements were deleted due to the force and therefore stresses, there was a sharp decrease in the contact force value (Phase 4). The final state of the damage in the contact area as the impactor breaks contact is given below (Phase 5-6).

4. Conclusions

In this study, the impact performance of cylindrical sandwich structure with Trapeozidal core under different geometries of impactors was investigated by the finite element method. The effects of impactor shape, facesheets thickness and the impact point on Peak contact force, absorbed energy efficiency, maximum displacement and damage deformation were investigated. Low velocity impact simulations were performed in *LS DYNA* finite element program. The results obtained at the end of the study can be listed as follows;

- In general, the contact force values at P2 are higher than P1. Core support has a significant effect on the contact force.
- Peak force variation values for cylinder, cone and sphere tipped impactors at P1 and P2 points were 43.5%, 132.3% and 62.2%, respectively. The biggest change at P1 and P2 points occurred in the cone impactor.

Table 4. Deformation images under different impactor force (P1).

E (J)		Tensile fiber mode	Compressive fiber mode	Tensile matrix mode	Compressive matrix mode
Cylinder, 5 J	Top face	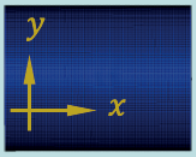	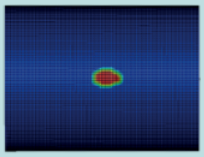	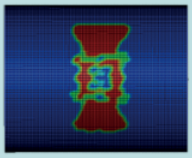	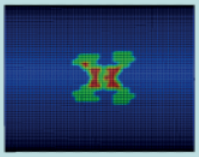
	Section view	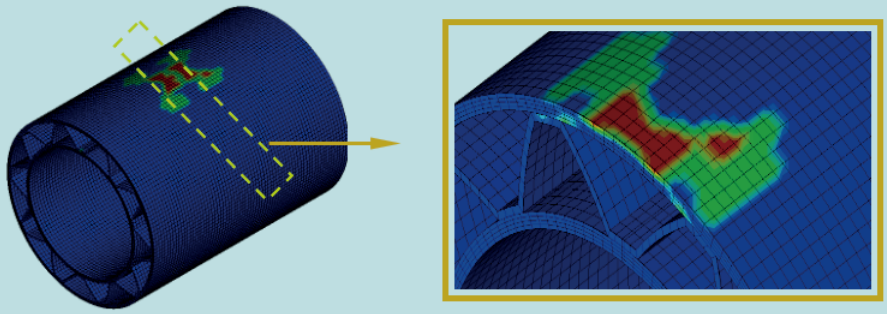			
Cone 5 J	Top face	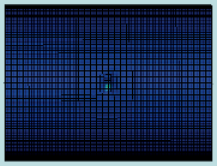	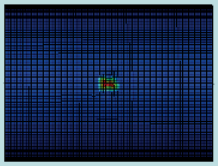	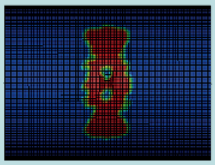	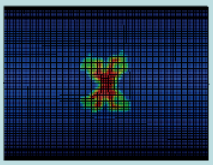
	Isometric	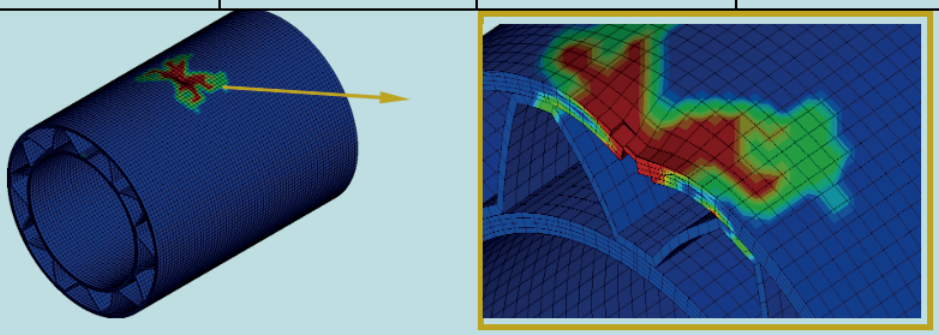			
Sphere 5 J	Top face	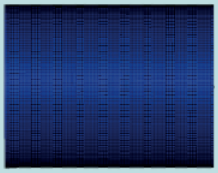	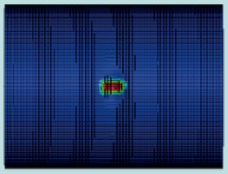	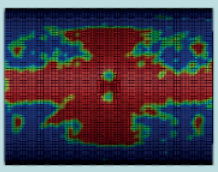	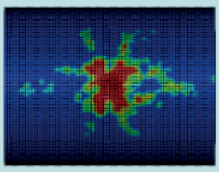
	Isometric	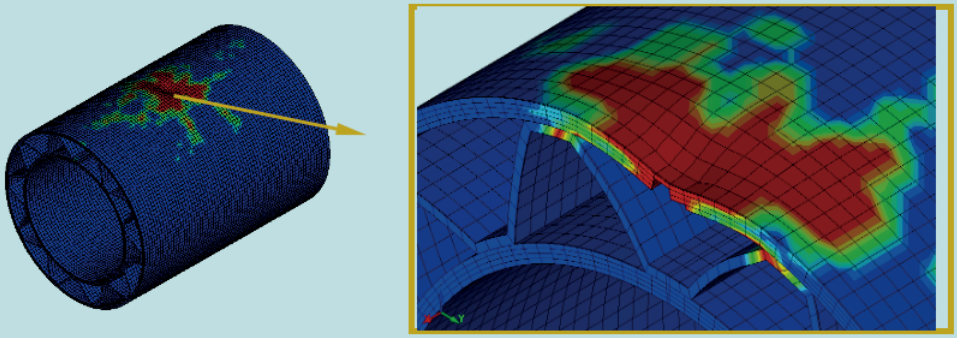			

Table 5. Deformation images under different impactor force (P2).

E (J)		Tensile fiber mode	Compressive fiber mode	Tensile matrix mode	Compressive matrix mode
Cylinder, 5 J	Top face	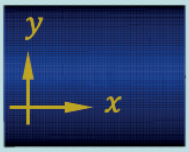	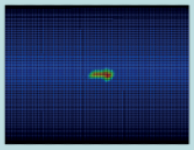	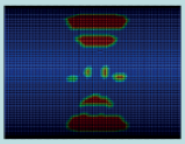	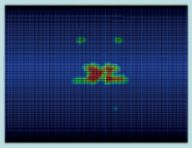
	Section view	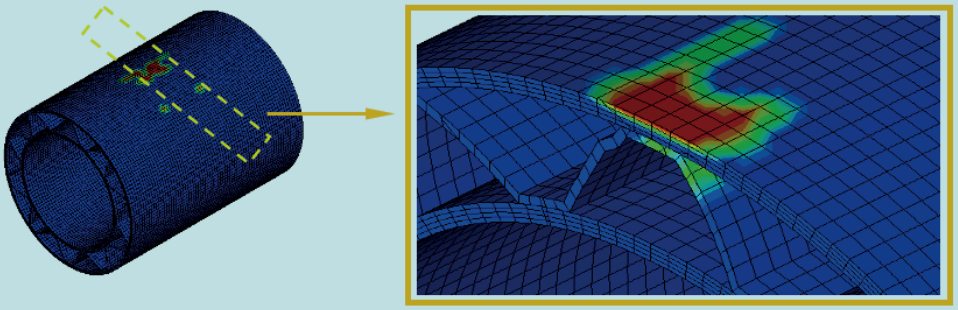			
Cone 5 J	Top face	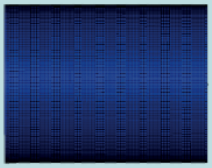	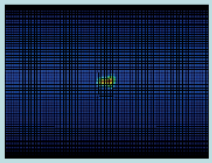	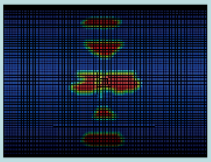	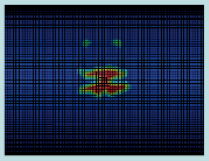
	Isometric	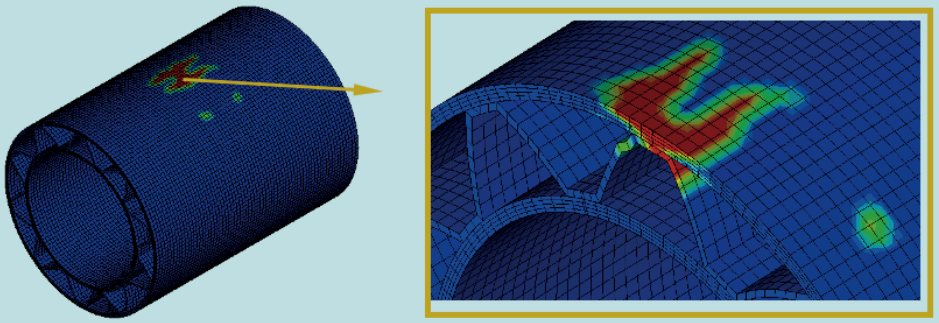			
Sphere 5 J	Top face	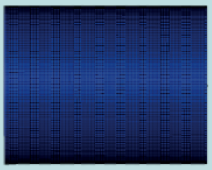	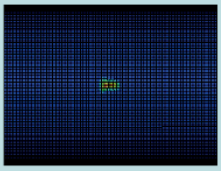	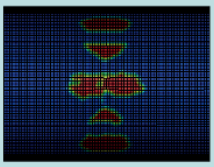	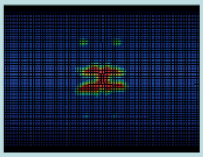
	Isometric	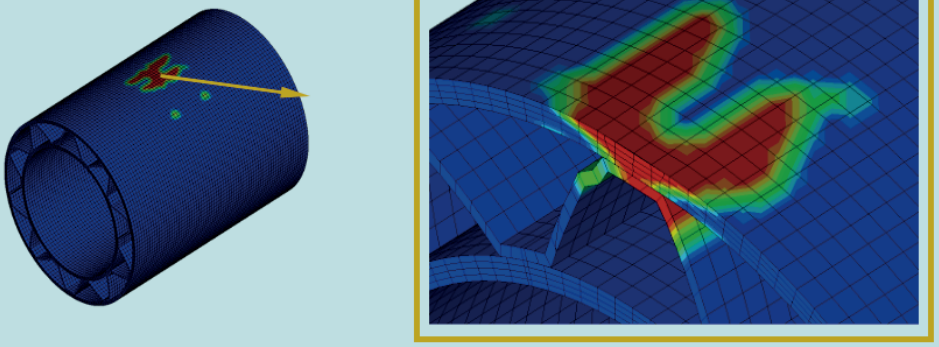			

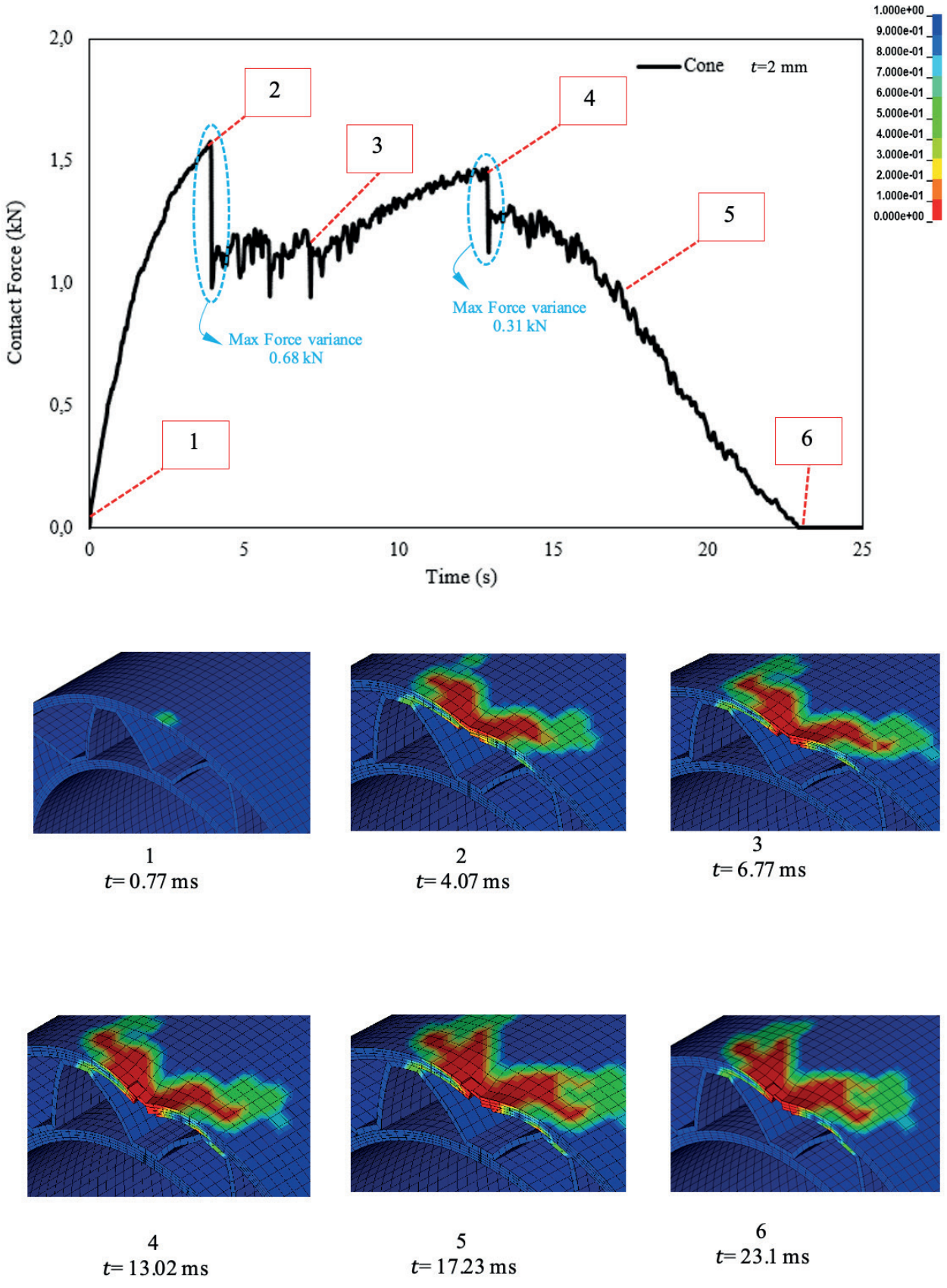

Figure 11. Matrix damage progress for cone impactor (P1).

- The peak force value and energy absorption efficiency value obtained with the Cone impactor are higher than the others. This is due to the fact that the contact area of the impactor with the specimen is small and destructive.
- The largest displacement as a result of the impact occurred with the cone impactor.
- The impactor geometry was found to have a significant effect on the energy absorption efficiency.
- For all three impactors, the largest and dominant damage type was matrix damage.
- This study has the potential to contribute to the literature if it is supported by an experimental study in future research.

Research ethics

Not applicable.

Author contributions

The author has accepted responsibility for the entire content of this manuscript and approved its submission.

Competing interests

The author states no conflict of interest.

Research funding

None declared.

Data availability

Not applicable.

Peer-review

Externally peer-reviewed.

References

[1] Crupi, V., Kara, E., Epasto, G., Guglielmino, E., & Aykul, H. (2015). Prediction model for the impact response of glass fibre reinforced aluminium foam sandwiches. *International Journal of Impact Engineering, 77*, 97–107. https://doi.org/10.1016/j.ijimpeng.2014.11.012

[2] Kazemianfar, B., Esmaeeli, M., & Nami, M. R. (2020). Response of 3D woven composites under low velocity impact with different impactor geometries. *Aerospace Science and Technology, 102*. https://doi.org/10.1016/j.ast.2020.105849

[3] Solmaz, M. Y., & Topkaya, T. (2020). The flexural fatigue behavior of honeycomb sandwich composites following low velocity impacts. *Applied Sciences (Switzerland), 10*(20), 1–14. https://doi.org/10.3390/app10207262

[4] Bozkurt, I., Kaman, M. O., & Albayrak, M. (2024). Experimental and numerical impact behavior of fully carbon fiber sandwiches for different core types. *Journal of the Brazilian Society of Mechanical Sciences and Engineering, 46*(5), 318. https://doi.org/10.1007/s40430-024-04865-3

[5] He, W., Lu, S., Yi, K., Wang, S., Sun, G., & Hu, Z. (2019). Residual flexural properties of CFRP sandwich structures with aluminum honeycomb cores after low-velocity impact. *International Journal of Mechanical Sciences, 161–162*, 105026. https://doi.org/10.1016/j.ijmecsci.2019.105026

[6] He, W., Liu, J., Tao, B., Xie, D., Liu, J., & Zhang, M. (2016). Experimental and numerical research on the low velocity impact behavior of hybrid corrugated core sandwich structures. *Composite Structures, 158*, 30–43. https://doi.org/10.1016/j.compstruct.2016.09.009

[7] Chen, Y., Fu, K., Hou, S., Han, X., & Ye, L. (2018). Multi-objective optimization for designing a composite sandwich structure under normal and 45° impact loadings. *Composites Part B: Engineering, 142*, 159–170. https://doi.org/10.1016/j.compositesb.2018.01.020

[8] Zhang, X., Xu, F., Zang, Y., & Feng, W. (2020). Experimental and numerical investigation on damage behavior of honeycomb sandwich panel subjected to low-velocity impact. *Composite Structures, 236*, 111882. https://doi.org/10.1016/j.compstruct.2020.111882

[9] He, W., Liu, J., Wang, S., & Xie, D. (2018). Low-velocity impact behavior of X-Frame core sandwich structures – Experimental and numerical investigation. *Thin-Walled Structures, 131*, 718–735. https://doi.org/10.1016/j.tws.2018.07.042

[10] Demircioğlu, T. K., Balıkoğlu, F., İnal, O., Arslan, N., & Ataş, A. (2018). Experimental investigation on low-velocity impact response of wood skinned sandwich composites with different core configurations. *Materials Today Communications, 17*, 31–39. https://doi.org/10.1016/j.mtcomm.2018.08.003

[11] Wang, J., Waas, A. M., & Wang, H. (2013). Experimental and numerical study on the low-velocity impact behavior of foam-core sandwich panels. *Composite Structures, 96*, 298–311. https://doi.org/10.1016/j.compstruct.2012.09.002

[12] Rong, Y., Liu, J., Luo, W., & He, W. (2018). Effects of geometric configurations of corrugated cores on the local impact and planar compression of sandwich panels. *Composites Part B: Engineering, 152*, 324–335. https://doi.org/10.1016/j.compositesb.2018.08.130

[13] Liu, J., He, W., Xie, D., & Tao, B. (2017). The effect of impactor shape on the low-velocity impact behavior of hybrid corrugated core sandwich structures. *Composites Part B: Engineering, 111*, 315–331. https://doi.org/10.1016/j.compositesb.2016.11.060

[14] Khalkhali, A., Geran Malek, N., & Bozorgi Nejad, M. (2020). Effects of the impactor geometrical shape on the non-linear low-velocity impact response of sandwich plate with CNTRC face sheets. *Journal of Sandwich Structures and Materials, 22*(4), 962–990. https://doi.org/10.1177/1099636218778998

[15] Shirbhate, P. A., & Goel, M. D. (2023). Investigation of effect of perforations in honeycomb sandwich structure for enhanced blast load mitigation. *Mechanics of Advanced Materials and Structures, 30*(17), 3463–3478. https://doi.org/10.1080/15376494.2022.2076958

[16] Yalkın, H. E., Karakuzu, R., & Alpyıldız, T. (2023). Low-velocity impact behaviors of sandwich composites with different structural configurations of foam core: Numerical study and experimental validation. *Physica Scripta, 98*(11). https://doi.org/10.1088/1402-4896/ad008f

[17] Nouri Damghani, M., & Mohammadzadeh Gonabadi, A. (2019). Numerical study of energy absorption in aluminum foam sandwich panel structures using drop hammer test. *Journal of Sandwich Structures and Materials, 21*(1), 3–18. https://doi.org/10.1177/1099636216685315

[18] Bozkurt, I., Kaman, M. O., & Albayrak, M. (2023). Low-velocity impact behaviours of sandwiches manufactured from fully carbon fiber

composite for different cell types and compression behaviours for different core types. *Materialprüfung/Materials Testing, 65*(9), 1349–1372. https://doi.org/10.1515/mt-2023-0024

[19] Dogan, F., Hadavinia, H., Donchev, T., & Bhonge, P. S. (2012). Delamination of impacted composite structures by cohesive zone interface elements and tiebreak contact. *Central European Journal of Engineering, 2*(4), 612–626. https://doi.org/10.2478/S13531-012-0018-0

[20] Albayrak, M., & Kaman, M. O. (2021). Production of curved surface composites reinforced with rubber layer. *European Journal of Technic, 11*(1), 19–22. https://doi.org/10.36222/ejt.824761

[21] Atas, C., Icten, B. M., & Küçük, M. (2013). Thickness effect on repeated impact response of woven fabric composite plates. *Composites Part B: Engineering, 49*, 80–85. https://doi.org/10.1016/j.compositesb.2013.01.019

[22] Bozkurt, I., & Kaman, M. O. (2022). LS-DYNA MAT162 finding material inputs and investigation of impact damage in carbon composite plates. In *XVI International Research Conference 2022*.

[23] Zhao, T., et al. (2020). An experimental investigation on low-velocity impact response of a novel corrugated sandwiched composite structure. *Composite Structures, 252*, 112676. https://doi.org/10.1016/j.compstruct.2020.112676

[24] Kaman, M. O., Solmaz, M. Y., & Turan, K. (2010). Experimental and numerical analysis of critical buckling load of honeycomb sandwich panels. *Journal of Composite Materials, 44*(24), 2819–2831. https://doi.org/10.1177/0021998310371541

[25] Gama, B. A., Bogetti, T. A., & Gillespie, J. W. Jr. (2009). Progressive damage modeling of plain-weave composites using LS-DYNA composite damage model MAT162. In *7th European LS-DYNA Conference*.

[26] Icten, B. M., Kiral, B. G., & Deniz, M. E. (2013). Impactor diameter effect on low velocity impact response of woven glass epoxy composite plates. *Composites Part B: Engineering, 50*, 325–332. https://doi.org/10.1016/j.compositesb.2013.02.024

[27] Albayrak, M., Kaman, M. O., & Bozkurt, I. (2023). The effect of lamina configuration on low-velocity impact behaviour for glass fiber/rubber curved composites. *Journal of Composite Materials, 57*(11), 1875–1908. https://doi.org/10.1177/00219983231164950

EUROPEAN MECHANICAL SCIENCE

Research Article

e-ISSN: 2587-1110

Fuel consumption analysis and cost overview of mechanical vehicles in petroleum drilling rig

Muhammed İkbal Yıldız[1], **Adem Yılmaz**[2]

[1] Batman University, Faculty of Engineering and Architecture, Türkiye
[2] Batman University, Faculty of Technology, Batman, Türkiye

Abstract: During the drilling activities carried out before the use of Petroleum and Geothermal Energy resources, daily fuel consumption occurs depending on the operational diversity of the mechanical components of different types of rigs in our country. In this study, a time-dependent financial analysis of the preferred operating procedure and fuel consumption during drilling operations was performed, both in engineering studies and in order to reach a predictable level in terms of cost, oil drilling operations were mentioned by drilling rig type today, and comparisons of mechanical evenings were made to provide an economically predictable earning environment for daily fuel consumption. As a result of the research and findings, Group Motors/Drawworks, Pump Motor and Generators were actively used during the idling of mechanical evenings, and the average daily diesel consumption of 23.61 lt/h, 45.8 lt/h and 33.3 lt/h was reached, respectively. Maneuver Opr. the average daily diesel consumption of 37.5 lt/h, 0 lt/h and 39.58 lt/h was reached based on the active use of Group Motors/Drawworks, Pump Motors and Generators during the operation. Drilling Opr. the average diesel consumption of 26.24 lt/h, 129 lt/h, 33.3 lt/h and 83 lt/h respectively was reached based on the active use of Group Motors/Drawworks, Pump Motor, Generators and Top Drive.

Keywords: Petroleum, Drilling, Fuel, Cost.

1. Intorduction

Petroleum, neft or ground oil, a naturally combustible mineral oil composed of hydrocarbons, denser than water, dark in color, unrefined, with a distinctive odor, extracted from the ground. It is formed from the Latin words “petra” meaning stone and “oleum” meaning oil. Although petroleum is popularly known only as a specific fuel, the word petroleum actually means unprocessed crude oil that occurs naturally and is extracted from the ground. Petroleum is a mixture of hydrocarbons and does not always have a fixed chemical composition. Crude oil, which is a natural fuel, has different compositions depending on the countries where it is found. There are many types of petroleum with different chemical compositions which are formed by combining hydrocarbons with different chemical contents. Hundreds of millions of years ago, the remains of animals and plants living in the seas or washed into the seas by the waters formed kerogen, similar to crude oil, in an anaerobic environment under the necessary conditions (heat, pressure and the action of microorganisms). Kerogen then gradually changed during its migration to the upper layers and formed crude oil [1]. In this context, oil and natural gas exploration is of great importance in the world. The most basic of the processes carried out before production is drilling operations and these operations are diesel engine or electric drilling rigs. The cost analysis of diesel-powered drilling rigs, which are actively used in our country, and the related income/expense regulation are also important for today’s companies.

2. Overview of Mechanical Vehicles

The production of oil and gas underground is possible by drilling wells into reservoir rocks. The development of a reservoir or field also requires the drilling of a certain number of wells. Drilling is carried out onshore

*Corresponding author:
Email: adem.yilmaz@batman.edu.tr

Cite this article as:
Yıldız, M. İ, Yılmaz, A.(2024). Fuel consumption analysis and cost overview of mechanical vehicles in petroleum drilling rig. *European Mechanical Science, 8*(4): 293-302. https://doi.org/10.26701/ems.1404250

History dates:
Received: 13.12.2023, *Revision Request*: 21.04.2024, *Last Revision Received*: 09.10.2024, *Accepted*: 09.10.2024

and offshore for Exploration, Development, Production and Injection (▶Figure 1).

There are 2 drilling methods that have been used since the beginning.

1. Cable-Tool Drilling

2. Rotary Drilling

The first of these was widely used in the early years of oil discovery. In this method, drilling was achieved by successively striking the formation with a steel drill attached to the end of a steel cable. This method has been completely replaced by Rotary Drilling for the last 60 years.

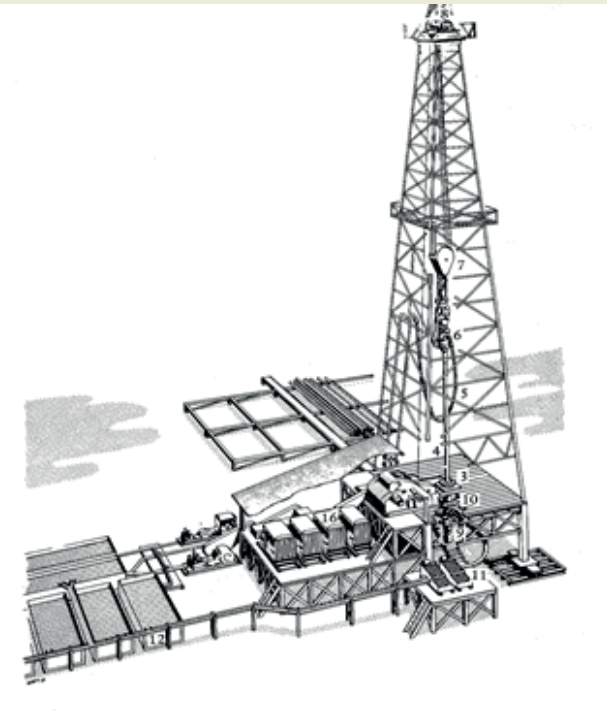

Figure 1. Rotary Drilling Rig [2]

The main components that can be included in the diesel expenses/expenditure category in diesel engine drilling rigs are Drawworks and Transmission (Group Engines), Generators and Pump Engines. Since the kelly system was used in primitive towers, this component, which was not included in the main category most of the time, has been replaced by the Top Drive system in today's technology. Accordingly, Top Drive and the engine to which it is connected can also be included in the fuel expenditure category (▶Table 1).

3. Mechanical Vehicles for Drilling Rigs

3.1. Drawworks and Transmission

Drawworks, which is the leading basic equipment in drilling rigs, is the component that determines the basic load capacity of the rig. It lifts and tilts the right and left mast of the rig or carries the drill string and transfers it to the rotary table drive unit with the power it receives from the transmission. Drawworks has 5 main sub-equipment. The conventional process of mechanical power transmission system of existing rotary drive system of deep drillingis complicated, involves different mechanisms, consume lot of input power due to various transmission losses in the systems [3]. The band brake system in its structure is used and the brake system is mechanically operated and the brake is a pneumatic system that works in the form of on/off. This system will not be able to apply sufficient force when it is below 7.5 bar. For this reason, in fast maneuvers, the belt brake system has a negative effect on expansion and braking due to wear (▶Figure 2). Pneumatic systems use compressed air to operate the brakes. In pneumatic brakes, there are three different braking systems: service brake (primary brake), secondary brake and parking brake. In recent years, electronically controlled brake systems (EBS) have begun to be used in new model heavy vehicles. EBS has been developed specially to improve brake safety in the latest model heavy-duty vehicles [4].

1. Drawworks Boiler: There is a water reservoir connected to the hydromatic brake. Thanks to the water centrifuge in its structure, it is a boiler system used to provide braking with water in the opposite direction of the rotation direction of the blades [4].

2. Overrunning Clutch: It is located between the drawworks and brake systrem and when it is desired to be pulled in the opposite direction (up), it disables the Hydromatic brake system and allows it to move. It ensures

Table 1. Rig Types and Mechanical Components Number of Charging Stations

Number	Rig Types	Motors	Drawworks
1	F320	2 x CAT398 Group Motors & 2 x FD1600 Mud Pumps & CAT3512 Generation	TF-38 (200 HP)
2	F200	2 x CAT512 Group Motors & 2 x PN700 Mud Pumps & CAT3512 Generation	TF-35 (1350 HP)
3	F125	2 x CAT398 Group Motors & 2 x PN700 Mud Pumps & CAT3512 Generation	TF-20 (1100 HP)
4	NAT80	2 x CAT398 Group Motors & 2 x 8P80 Mud Pumps & CAT408 Generation	TF-20 (1000 HP)

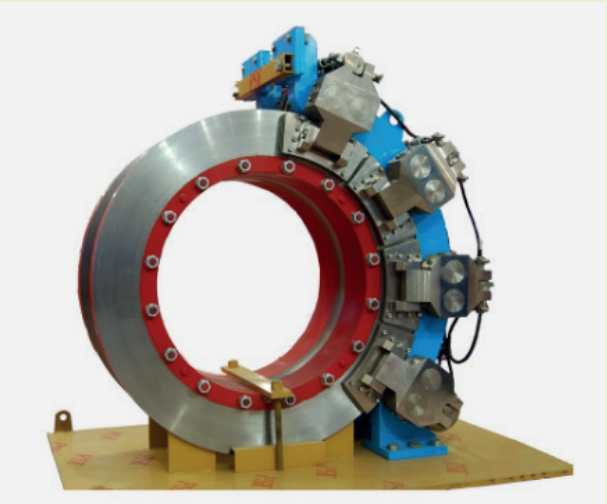

Figure 2. Drawworks and Brake System [5]

Figure 3. Drawworks Transmission System [6]

that the hyromatic brake is activated when the moving pulley goes down [4].

3. Hydromatic Brake Systtem: Drawworks' band brake system is used. The brake system is mechanically moved by means of a pneumatic system (▶**Figure 3**). There is also a water boiler connected to the hydromatic brake and the water centrifuge works. It provides braking with water against the direction of rotation with the blades inside [4].

4. Hook Block Limiting Device (Crown-o-matic): It is a safety system used to prevent the moving spool from hitting the crown spool. It is an automatic braking system that works with pneumatic system [4].

5. It provides communication between Drawworks and Group Engines: It collects the power from the group motors and transmits it to the drawworks, which provides maneuvering and drilling. In addition, it also helps to provide movement to the mechanical compressor and pumps [4].

3.2. Generations

Generators used in drilling rigs are machines that convert rotational force into electrical energy. They work with diesel (diesel) fuel types. They are generally used as a continuous energy source. The cost spent for the formation of energy in generators is higher than the cost of energy. The types of generators used vary according to the installed power and real needs of the towers. Diesel generator systems and batteries automatically supply electricity to maintain the cooling system of the reactors and the spent fuel pools of each unit [7].

Generators, 1750 KVA (1400 kW) Power, Voltage 600 V AC, Phase Number 3P, Speed 1500 rpm. In addition, for the C18 Generator used as backup, 700 KVA (560 kW), Voltage 400 V AC, Phase Number 3P and Speed 1500 rpm (▶**Figure 4**).

The total installed power values of the Drilling Rigs used in Average Oil and Geothermal Drilling are shown as follows.

1. Hopper Motors: 2x75 kW
2. Mud Cleaner: 1 x 75 kW
3. Degasser: 1 x 55 kW
4. Compressors: 2 x 55 kW
5. Closing Unit: 1 x 37 kW
6. Trip Tank: 1 x 22 kW
7 Hydromatic System: 1 x 7.5 kW
8. Screen Motors: 4 x 2.5 kW
9. Mixer Motors: 10 x 7.5 kW
10. Sheds: 12 x 5 kW
11. Lighting System: 10 kW
12. Other: 10 kW

Total installed power is 622 kW (777.2 kVA). Installed power value according to generator power is 1110 kV.

Figure 4. Generation for Drilling Rigs [8]

3.3. Mud Pumps

The selected mud pump should be capable of providing mud flow rates that are high enough to transport drill cuttings to the surface at all stages of drilling. Mud properties that influence the type of pump include mud weight and rheological properties. For Newtonian fluids, viscosity is the only parameter describing fluid rheological characteristics. Plastic viscosity and yield point are the two parameters used to describe the rheological characteristics of Bingham plastic fluids. The minimum required mud flow rate from the mud pump is equal to the minimum required mud velocity times the maximum possible cross-sectional area of annular space during drilling. The minimum required mud flow rate demanded by the borehole geometry from the mud pump is estimated based on the minimum required mud velocity, which should be higher than the drill cuttings slip velocity (▶**Figure 5**). The selected mud pump should also be capable of providing pressure that is strong enough to overcome the total pressure loss and pressure drop at the bit in the circulating system at the total hole depth [7].

Figure 5. Mud Pumps [9]

3.4. Drilling Rig's Engines (Group Motors)

Excepting the early usage of steam-powered engines, diesel engines have long been the engine of choice for powering drilling rigs. Sturdiness, reliability, and efficiency are synonymous with diesel engines. Located onsite at well pads and platforms, they typically range from 400 – 3,000 hp. As the sole source of power generation at many production sites, these engines are essential to all drilling operations. Renowned for their steadfast performance, diesel engines maintain their status as the dependable internal combustion engine for drilling rigs [10]. The group engines used in the drilling rigs are diesel/motorized and the power they generate enables the operation of the mechanical parts between the drawworks and transmission (▶**Figure 6**). CAT3512 or CAT398 (1014 HP) type group engines are used in mechanical rigs. In this type of diesel engines, the air is compressed in the cylinder to reach high pressure and temperature and the engine power is the result of the combustion of the fuel sprayed into the compressed air.

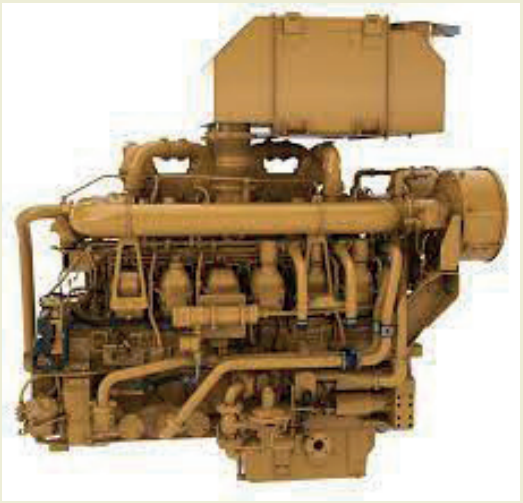

Figure 6. Drilling Rig's Engines [11]

4. Effect of Fuel Consumption

4.1. Idle Fuel Analysis of Consumption

Within the scope of operational-based fuel consumption in Oil and Geothermal Drilling rigs, the average fuel consumption as a result of idling without any load in the evening, such as the preparation phase before the operation or when the rig is on standby with the crew. Before the components work under load, they should be idled for 1-2 hours as a standard before drilling operations (▶**Table 2**). The data obtained in the appendix are prepared according to the catalog values of the manufacturers of the specified evenings and the comparison of on-site (lt/h) measurements made in the field (▶**Table 3**).

Table 2. Idle Fuel Analysis of Fuel Consumption

Number	Mechanical Vehicle Types	Avarage Fuel Consumption
1	Drawworks & Rig Engines (C398)	3 x C398 Rig Engines at 520 ROM for 24 hours (total fuel consumption of 1400 liters) – 23.61 lt/h
2	Mud Pumps	3 x C3516 Mud Pumps Motor for 24 hours at 430 RPM (total fuel consumption of 2200 liters) – 45.8 lt/h
3	Generations	1 x C3512 Generation for 24 hours at 390 RPM (total fuel consumption of 800 liters) – 33.3 lt/h

4.2. Fuel Consumption during Wiper Trip Operation

Wiper trips can be short or long for cleaning purpose or for making the wall smoother and more stable. Ashort trip is an action or some operation for tripping out / or in the drill string to a certain planned depth inside the open hole section. Performing a short trip helps to remove the cutting bed and to improve the smoothness of the wall. Sometimes a short trip can be done when there is a long sliding section via a mud motor. It is beneficial to do sobecause sliding with the mud motor creates a lot of cutting beds that are not effectively removed [12]. Although it consists of the integrity of different types of operations in Oil and Geothermal Drilling Rigs, the first type and basic wiper trip operation can be taken as the basis in order to minimize fuel consumption (▶**Table 4**). Travelling Block is the basic type of operation that covers the descent and ascent maneuvers of the string elements by means of the Crown Block wrapped with the drill string. However, in case of an ascent or descent maneuver with circulation, the Pump and Engine also operate. In this study, average fuel consumption is calculated in case of full ascent and circulation (pump and engine are not active) is not performed (▶**Figure 7**).

Figure 7. Wiper Trip Operation Fuel Analysis of Fuel Consumption (2023)

4.3. Fuel Consumption during Drilling

It is a type of operation that is defined as the basic operation in Oil and Geothermal Drilling rigs and must be

Table 3. Idle Fuel Analysis of Fuel Consumption (lt/h)

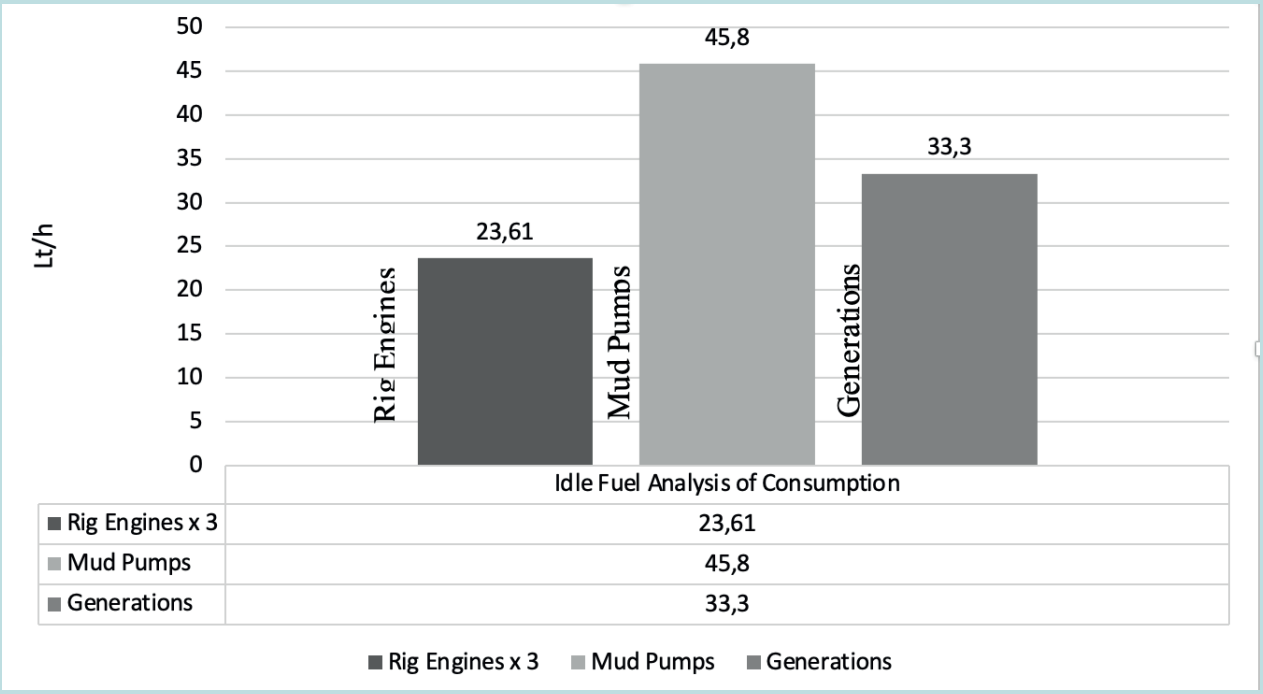

Table 4. Wiper Trip Operation Fuel Analysis of Fuel Consumption

Number	Mechanical Vehicle Types	Average Fuel Consumption
1	Drawworks & Rig Engines (C398)	It runs at 1000 RPM for 24 hours with 3 x C398 Engines (total fuel consumption of 2700 liters) – 37.5 lt/h
2	Mud Pumps	Wiper Trip is realized by deactivating the mud pumps during operation
3	Generations	2 x C3512 Generations for 24 hours at 1300 RPM (total fuel consumption of 1900 liters) – 39.58 lt/h

https://doi.org/10.26701/ems.1404250

performed to reach the target depth. There are many parameters that affect and differentiate the drilling operation (▶Table 5). These parameters are WOB (Weight on Bit), Rotary (Speed), SPP (Pressure), Torque, Mud

Weight and Viscosity, Drill Type and Flow Rate (Q). According to the change of these parameters, there will be load and power differences on the mechanical evenings and the parameter values based on the study are shown below. Drawworks (Rig Engines), Pumps and Engines, Generators are actively working during the Drilling Operation. Parameters of Drilling are WOB: 10-13 Tones, Rotary: 110 RPM, Q: 375 gpm, SPP: 900 psi, Torque: 3-4 klb-ft, MW: 65 ppcf (Table 6).

It is observed that the ROP value between 1281-1385 meters is 4.5 m/h at the end of the 24-hour period in which drilling activities actively continued in the parameters stated in the ▶Table 6. Considering that the Top Drive system is also actively working in the tower assembly, it is also observed that the TD engine consumed 1985 liters of diesel fuel at the end of 24 hours (▶Table 7). In this context, it is also observed that the Generator, Group Engines and Pump Engines consumed a total of 10041 liters of diesel fuel (Total 12241 liters) (▶Figure 8).

Figure 8. Drilling Operation Fuel Analysis of Fuel Consumption (2023)

Considering the different parameters and quantity ranges of the drilling operation, with the activation of the double mud pump, it was observed that the highest

Table 5. Wiper Trip Operation Fuel Analysis of Fuel Consumption (lt/h)

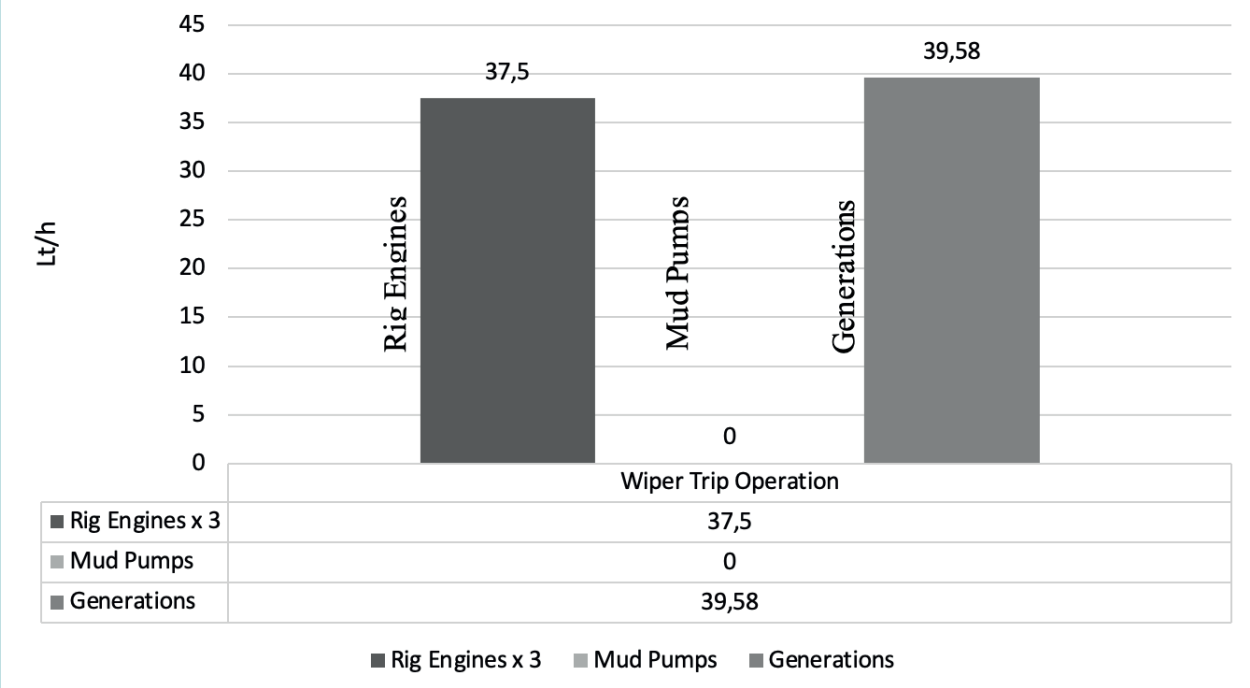

Table 6. Wiper Trip Operation Fuel Analysis of Fuel Consumption

Number	Mechanical Vehicle Types	Avarage Fuel Consumption
1	Drawworks & Rig Engines (C398)	It runs at 1000 RPM for 24 hours with 3 x C398 Engines (total fuel consumption of 2700 liters) – 37.5 lt/h
2	Mud Pumps	Wiper Trip is realized by deactivating the mud pumps during operation
3	Generations	2 x C3512 Generations for 24 hours at 1300 RPM (total fuel consumption of 1900 liters) – 39.58 lt/h

fuel consumption was observed in the pump and motor, while the lowest fuel consumption was observed in the group motors and Drawworks system. In this context, it is understood that unlike the wiper trip operation, less group motors provide labor to the drawworks through transmission. In addition, in the rigs with TD connection, it was observed that TD and its Engine burned the most fuel in the second place due to the power that the torque, wob and rotary functions brought by the drilling, wob and rotary functions received from the engine itself. Considering the different parameters and quantity ranges of the drilling operation, with the activation of the double mud pump, it was observed that the highest fuel consumption was observed in the pump and motor, while the lowest fuel consumption was observed in the group motors and rig engines system.

In the most of the drilling operations it is obvious that a considerable amount of money is spent for drilling related problems; including stuck pipe, lost circulation, and excessive mud cost. In order to decrease the percentage of non-productive time (NPT) caused by these kinds of problems, the aim is to control annular frictional pressure losses especially in the fields where pore pressure and fracture pressure gradient is too close which is called narrow drilling window.his context, it is understood that unlike the wiper trip operation, less group motors provide labor to the drawworks through transmission. In addition, in the rigs with TD connection, it was observed that TD and its Engine burned the most fuel in the second place due to the power that the torque, wob and rotary functions brought by the drilling, wob and rotary functions received from the engine itself [10].

5. Effect of Cost

5.1. Fuel Cost of Consumption

Unlike electric towers, roman towers have daily consumption and stock amounts depending on the diesel fuel. According to the amount of stock calculated on a daily basis, the next diesel supply is made and accordingly, daily costs are formed. Correct analysis of daily diesel cost tables on operational basis (idling, maneuvering and drilling) is important in the oil drilling sector. (*The exchange rate is calculated so that 1 dollar is equivalent to 28 Turkish liras, 12.08.2023*)

The global economy has changed in significant ways during the past several decades, and these changes are rooted in how the global economy is organized and governed [12]. For this reason, cost management is important.

When the idle cost analysis of the oil drilling rigs was calculated, it was observed that the cost of the group engines, generator and pump engines and circulation was calculated on the basis that the generators were 33.3 liters, the pump and engine 45.8 liters and the group engines 23.61 liters per hour. In this context, according to the current diesel prices, when a financial analysis is made specifically for each mechanical component, the hourly cost of the generators is calculated as 25$, the pump and motor as 34$ and the rig engines as 17,6$ (▶**Table 8**).

Table 7. Drilling Operation Fuel Analysis of Fuel Consumption (lt/h)

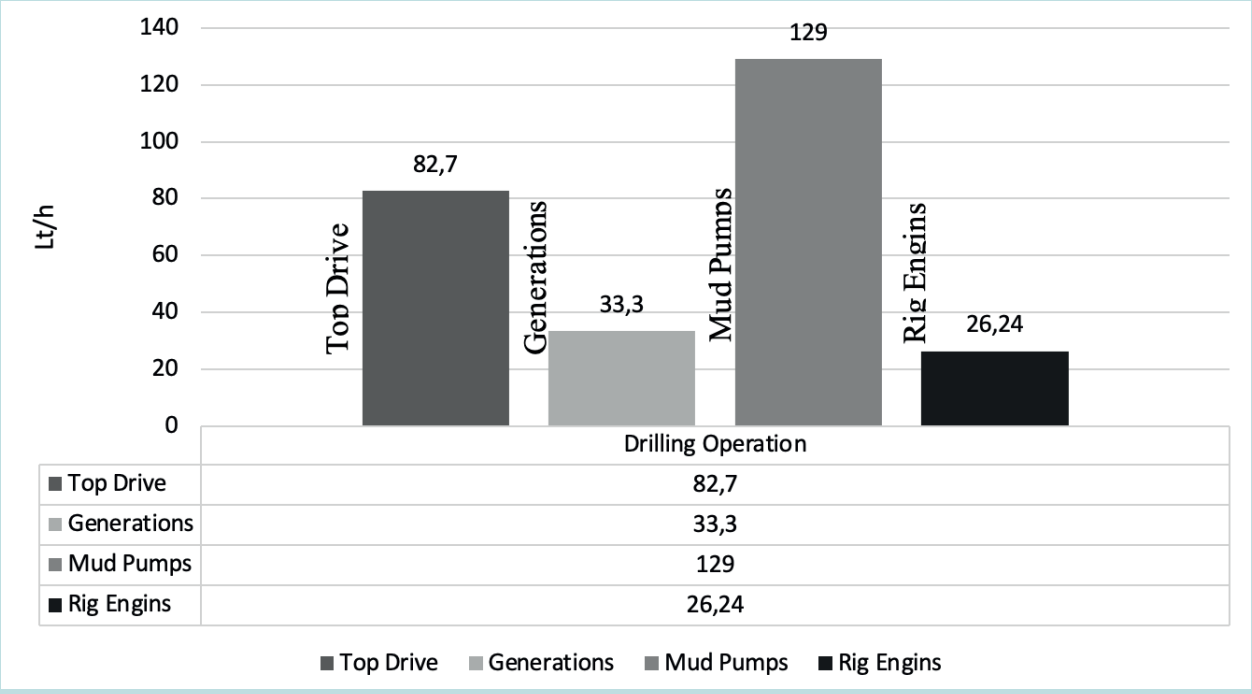

When the cost analysis was calculated during the maneuvering operation of the oil drilling rigs, it was observed that the generators were calculated as 39.58 liters, the pump and motor as 0 liters and the group motors as 37.5 liters per hour when the cost was calculated on the basis that the group motors, generator and pump motors were not circulated. In this context, according to the current diesel prices, when a financial analysis is made specifically for each mechanical component, the hourly cost of the generators is calculated as 29,67$, the pump and motor as 0 $ and the rig engines as 28,10$ (▶Table 9).

When the cost analysis of the cost of oil drilling rigs during the drilling operation is calculated on the basis of group engines, generator and pump engines and circulation, it is observed that the generators are calculated as 33.3 liters, the pump and motor 129 liters and the group engines 26.24 liters per hour. In this context,

Table 8. Idle Fuel Cost of Consumption (l/h and $)

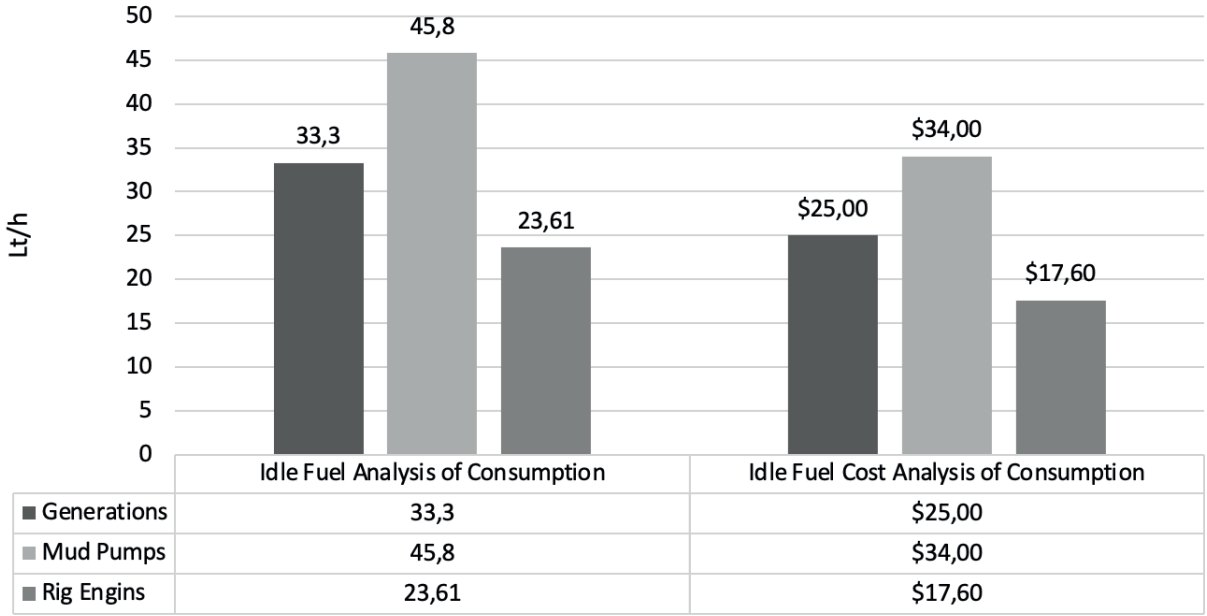

	Idle Fuel Analysis of Consumption	Idle Fuel Cost Analysis of Consumption
Generations	33,3	$25,00
Mud Pumps	45,8	$34,00
Rig Engins	23,61	$17,60

Table 9. Wiper Trip Operation and Fuel Cost of Consumption (l/h and $)

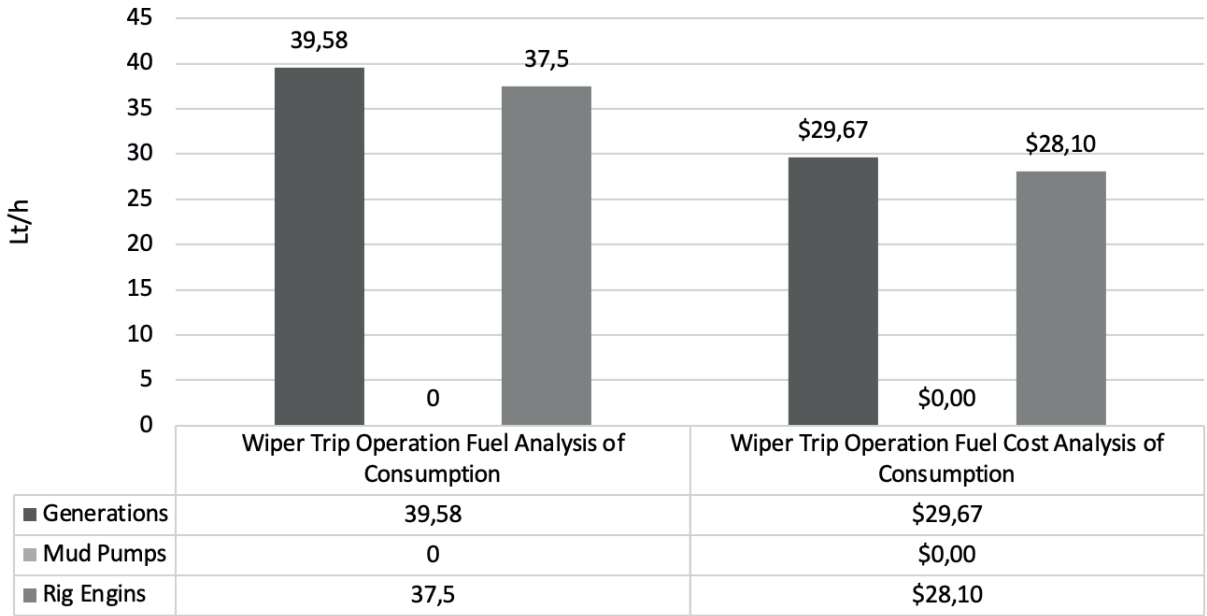

	Wiper Trip Operation Fuel Analysis of Consumption	Wiper Trip Operation Fuel Cost Analysis of Consumption
Generations	39,58	$29,67
Mud Pumps	0	$0,00
Rig Engins	37,5	$28,10

Table 10. Drilling Operation and Fuel Cost of Consumption (l/h and $)

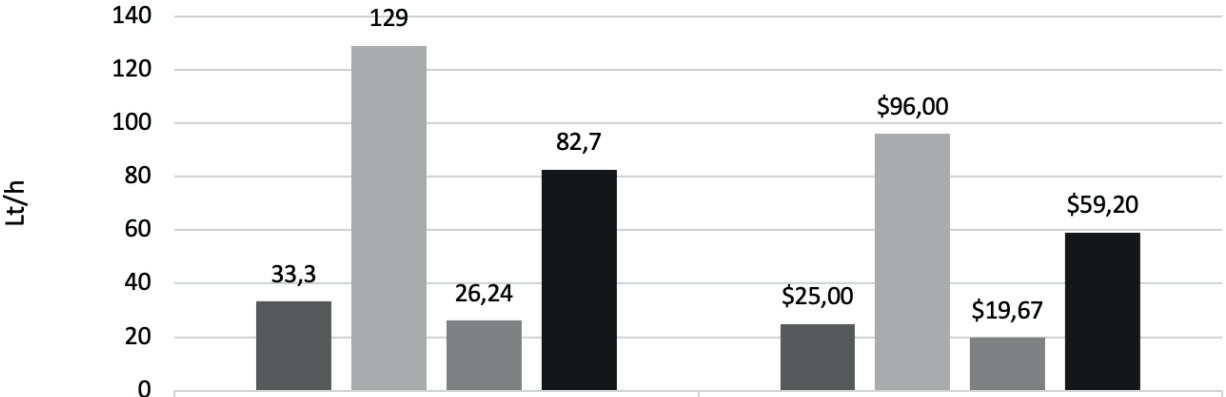

	Drilling Operation Fuel Analysis of Consumption	Drilling Operation Fuel Cost Analysis of Consumption
Generations	33,3	$25,00
Mud Pumps	129	$96,00
Rig Engins	26,24	$19,67
Top Drive	82,7	$59,20

according to the current diesel prices, when a financial analysis is made specifically for each mechanical component, the hourly cost of the generators is calculated as 25$, the pump and motor as 96$ and the rig engines as 19,67$. 38.24 tl-28 TL/dollars. *(The unit liter price of diesel is 38.24 Turkish liras and 38.24 Turkish liras is equal to 0.73 dollars, 12.08.2023)* (▶**Table 10**).

As a result of these analysis, petroleum is the most important resource for global energy production, far exceeding the role of coal and natural gas, the role of river energy and wind energy, and also the role of nuclear fuel [13]. And also, it is found all over the earth, usually in places where oceans were once present, because petrol produces a lot of energy, people have been using it to fuel their cars and generate electricity [14].

6. Conclusion

Cost analysis is of great importance in the Oil and Geothermal Drilling sector. Different operational techniques are used until the well program created according to the planned drilling depth and reaching the target depth/reserve, and depending on these techniques, the daily fuel amount and cost of diesel/motorine-based mechanical evenings are formed. In accordance with standard practices, the daily fuel amount is calculated as a result of sometimes manual and sometimes digital measurements. Regardless of the measurement method, the main goal is to ensure the integration of minimum consumption and maximum gain. The aim of this study is to determine the average daily fuel amount according to different operational variations of oil rigs with diesel-based mechanical nights and to present a predictable cost analysis accordingly. As a result of the research and findings, the average daily diesel fuel consumption of 23.61 l/h, 45.8 l/h and 33.3 l/h were obtained based on the active use of rig engines, pump engine and generators when the mechanical nights were idling. During the wiper trip operation, rig engines, pump engine and generators are used actively and average daily diesel fuel consumption is 37.5 l/h, 0 l/h and 39.58 l/h respectively. During the drilling operation, rig engines, pump engine, generators and top drive were used actively and the average diesel consumption was 26.24 lt/h, 129 lt/h, 33.3 lt/h and 83 lt/h respectively.

Due to the high-cost results of the petroleum drilling exploration sector, it has always been aimed to keep the failure hours at a minimum level and accordingly to realize the type of operation in a minimum time. In line with this goal, it is of great importance that the cost analysis based on the average fuel consumption and the official working in the field can deduce the average cost as a foresight. In this study, it is aimed to prevent possible problems that may occur in line with the data to be obtained. For example, it is to reveal the possibility of theft as a result of the detection of high fuel amount or the possibility that the operation has not been carried out correctly/efficiently as a result of the detection of low fuel consumption amount.

Acknowledgments

I would like to thank Mr. Adem Yılmaz who my valuable advisor and also Turkish Petroleum Cooperation with support and preliminary information and opportunities in this research.

Research Ethics

Ethical approval not required.

Author Contributions

Conceptualization: [Muhammed İkbal Yıldız], Methodology: [Adem Yılmaz], Formal Analysis: [Muhammed İkbal Yıldız], Investigation: [Muhammed İkbal Yıldız], Resources: [Muhammed İkbal Yıldız], Data Curation: [Adem Yılmaz], Writing – Original Draft Preparation: [Muhammed İkbal Yıldız], Writing – Review & Editing: [Adem Yılmaz], Visualization: [Muhammed İkbal Yıldız], Supervision: [Adem Yılmaz], Project Administration: [Adem Yılmaz]

Competing Interests

The author(s) declare that there are no competing interests.

Research Funding

Not reported.

Data Availability

Not applicable.

Peer-review

Externally peer-reviewed.

Orcid

Muhammed İkbal Yıldız https://orcid.org/0000-0003-1590-0952
Adem Yılmaz https://orcid.org/0000-0001-7266-0866

References

[1] Maden Yönetmeliği. (2024, June 10). *Maden Yönetmelikleri*. https://www.mapeg.gov.tr/Sayfa/Genel/maden-yonetmelikleri

[2] Fuel Theft Prevention. (2024, April 15). *Digital Drilling*. https://jv-technoton.com/solutions/digital-drilling

[3] Nazer, M. A. (2017). Design modification of drawworks transmission system of oil well drilling rigs. *International Journal of Engineering Science and Computing (IJSCE, 7)*(4), 9982–9984.

[4] Bali, E. (2018). Design of on-off type solenoid valve for electropneumatic brake systems and investigation of its static characteristics. *International Journal of Advances on Automotive and Technology, 3*(4), 175–184.

[5] Drawworks brake system in drilling rigs. (2024, June 17). *Drilling Manual*. https://www.drillingmanual.com/drawworks-brake-system-in-drilling-rigs/#google_vignette

[6] Three speed chain transmission. (2024, January 15). *DeepL Translator*. https://www.deepl.com/tr/translator#tr/en-us/ocak

[7] Group Engines and Independent Engines. (2014). *Training Presentation*. Türkiye Petrolleri Anonim Ortaklığı (TPAO).

[8] All drive modes explained. (2024, February 24). *Sovonex*. https://www.sovonex.com/drilling-equipment/api-land-drilling-rigs/electric-mechanical-drilling-rigs/

[9] Mechanical drilling rig equipment. (2024, January 8). *Bentec*. https://www.bentec.com/equipment/mechanical-drilling-rig-equipment/mud-pumps/mud-pumps.html

[10] Hochgraf, C. (2009). Fuel control, applications – Transportation electric vehicles: Fuel cells. *Science Direct, 5*(3), 83–75.

[11] Drilling rigs, engines, and fuels. (2024, June 15). *EPCM Holdings*. https://epcmholdings.com/rigs_engines_fuels/

[12] Boyun, G. (2011). Mud pumps. In *Applied Drilling Circulation System* (pp. 47–63). https://doi.org/10.1016/B978-0-12-381957-4.00003-6

[13] Rasmussen, T. M. (2018). Wiper trips effect on wellbore instability using net rising velocity methods. *The Open Petroleum Engineering Journal, 11*, 14-28. https://doi.org/10.2174/1874834101811010014

[14] Kök, V. M. (2010). Managed pressure drilling techniques, equipment, and applications (Master's thesis). Middle East Technical University, Graduate School of Natural and Applied Sciences.

EUROPEAN MECHANICAL SCIENCE

Research Article

e-ISSN: 2587-1110

Numerical investigation of electrocoalescence-induced fluid demixing between parallel plates

Aslı Tiktaş[1*]

[1]Kırşehir Ahievran University, Faculty of Engineering-Architecture, Department of Mechanical Engineering, Kırşehir, Türkiye

Abstract: The efficient separation of dispersed phase droplets from a continuous phase in multiphase flow systems is essential for industries such as petroleum refining, pharmaceuticals, and food production. Conventional methods, relying on gravitational and buoyancy forces, are often inadequate for small droplets due to their weak influence. Electrocoalescence, utilizing electrical forces to enhance droplet coalescence, has gained attention as a promising alternative. However, most studies have focused on simplified models, limited electrical potentials, or axis-symmetric configurations, overlooking the effects of varying electrical potentials on droplet behavior in complex flows. This study bridges that gap by developing a numerical solver that couples the phase-field method with the Navier-Stokes equations to simulate electrocoalescence of two-dimensional droplets in laminar phase flow between parallel plates. The solver provides detailed insights into multiphase flow dynamics, including contact line behavior and interface tracking under different electrical potentials. The novelty of this work lies in its systematic evaluation of how varying electrical potentials affect droplet deformation, separation time, and interface dynamics, which are often not fully addressed by standard commercial solvers. The findings indicated that increasing electrical potentials from 50 kV to 100 kV leads to droplet deformation, with the droplet deformation index (DDI) increasing from 0.35 to 0.52. Additionally, phase separation time decreases by 20%, from 0.15 seconds to 0.12 seconds, as electrical potential increases. The increasing electrical potentials lead to asymmetric droplet shapes and instability, accelerating separation by disrupting the formation of stable liquid bridges. These findings offer valuable insights into optimizing electrocoalescence processes for industrial applications. In this study, a multi-objective optimization process was conducted using the Non-dominated Sorting Genetic Algorithm II (NSGA-II), with the aim of minimizing droplet deformation and phase separation time. The optimization results revealed that the ideal initial contact angle for minimizing deformation was 123.45°, while the optimal contact angle for minimizing separation time was 145.67°. These results highlight the potential of optimizing system parameters to improve the efficiency and stability of electrocoalescence processes in various industrial applications.The current study provides a deeper understanding of the interaction between electrical forces and multiphase flow dynamics, laying the groundwork for advancements in phase separation technologies across various industries.

Keywords: Multiphase flow, Electrocoalescence, Phase separation, Numerical modelling, Phase field method.

1. Introduction

The separation of the disperse phase from the continuous phase in multiphase flow systems is a common process in various industries, such as petroleum, pharmaceuticals, food, and paint, where emulsions are frequently used. A conventional method to achieve separation is through the coalescence of dispersed phase droplets within the continuous phase, driven by gravitational, buoyant, or electrical forces. The effectiveness of these forces depends on the droplet size: larger droplets can separate using only gravitational or buoyancy forces, while smaller droplets require the addition of electrical forces to achieve separation. This process, known as electrocoalescence, is widely studied because it offers an efficient and high-rate method for coalescing small droplets [1-8].

*Corresponding author:
Email: asli.tiktas@ahievran.edu.tr

Cite this article as:
Tiktaş, A.(2024). Numerical investigation of electrocoalescence-induced fluid demixing between parallel plates. *European Mechanical Science, 8*(4): 303-318. https://doi.org/10.26701/ems.1545084

History dates:
Received: 07.09.2024, *Revision Request*: 03.10.2024, *Last Revision Received*: 13.10.2024, *Accepted*: 29.10.2024

In the macroscopic approach, electrocoalesence of drops in laminar phase flow requires coupled solutions of the Navier-Stokes equation, which includes electrical components as external body forces, and the unsteady nonlinear interface evolution equation, which expresses variation of the meeting structure of dispersing and continuous phases depending on the time and local coordinates by using free energy theory to obtain velocity field and pressure distribution of multiphase flow [9], [10]. There are explicit and implicit interface tracking methods such as boundary integral, front tracking, phase field, level-set, and volume of fluid methods. Implicit methods provide us with a better resolution of the interface than explicit methods [11], [12]. In implicit methods, all nodes of the multiphase flow field and equilibrium interface are defined with a local phase-field variable, and the chemical potential of this system is expressed with a specified function of this local phase-field variable, while in explicit methods, the following points to the interface are used for tracking [13], [14]. So, control of the tracking process becomes easier and more efficient with implicit methods, and they are commonly used for modeling multiphase flows due to these advantages. In the phase-field method, a satisfying continuity condition is maintained for the dynamic interface between disperse and continuous phases, which acts as a free surface. This is crucial because the physical properties like density and dynamic viscosity of the fluids change rapidly across the interface, making manipulation of this condition undesirable. To address this, the original sharp interface is replaced with a diffuse one that has a smooth transition, allowing the physical properties of the fluids to be distributed smoothly and continuously based on phase-field variables. This approach simplifies tracking the equilibrium interface. Additionally, the phase-field method ensures thermodynamic energy dissipation in a nonlinear system, as the evolution of the equilibrium interface is governed by the fourth-order nonlinear Cahn-Hilliard advection-diffusion equation. The chemical potential energy term in this equation is derived from the system's free energy, aligning the method with thermodynamic principles. Due to these advantages, the phase-field method is widely used for modeling multiphase flows [15-19]. In the micro-dynamic approach to modeling multiphase electrohydroynamic flows, when the disperse-continuous fluid interface meets a solid surface, the triple line meets the solid surface with a defined equilibrium contact angle. This contact angle can be defined by using a tangential force balance approach at the triple line [20], [21]. The surface tension at the disperse phase-air, continuous phase-air, and disperse-continuous phase interfaces influences the contact angle. Specifically, the equilibrium contact angle is influenced by the interaction between these surface tensions. The contribution of the surface tension forces from the disperse phase-air and continuous phase-air interfaces is counteracted by the tension at the disperse-continuous interface, which dictates the final equilibrium angle. The contact angle between the fluid phases deviates from its equilibrium value when electrical potential is applied between the electrodes. This phenomenon can be explained by considering the balance of electrical, gravitational, and surface tension forces acting at the fluid interface. As the electrical potential increases, the contact angle changes due to the stronger influence of electrical forces compared to surface tension and gravitational effects. This situation was given by Young and Lippmann [20]. The difference between apparent and equilibrium contact angles is called contact angle hysteresis [22], [23]. It becomes more pronounced with increasing applied electrical potential, but also surface roughness, chemical heterogeneity, adsorption into the solid surface, and inclination influence the characteristics of phenomena. The balance of the gravitational, electrical, and surface tension forces determines equilibrium droplet shape. Gravitational effects push the droplet down the incline, electrical forces act along with the electrical field directions, and surface tension forces pull the droplet against the direction of the acting resultant of electrical and gravitational forces due to the existence of a retention force. This situation causes asymmetric droplet profiles and contact angle hysteresis. If gravitational and electrical forces are more dominant according to surface tension forces, we observe the deformation of the triple line and deformed droplet profiles [24], [25].

Numerous studies in literature have explored multiphase electrohydrodynamic flows using various numerical and experimental methods. Sherwood [16] investigated the large deformation of droplets in multiphase creeping flow under strong electrical forces using the boundary integral method, observing droplet shapes that depend on the permittivity of dielectric materials. Fernández et al. [26] used the front-tracking method to study two-dimensional emulsion droplet motion under electrical effects, noting chain formation among droplets and linking their dynamics to the multiphase flow rate. Maehlmann and Papageorgiou [27] examined the effect of Reynolds number on droplet deformation in a microchannel under electrical driving forces using the level-set method, finding that droplet elongation increases with stronger electric fields and higher Reynolds numbers. Lin et al. [28] used the phase-field method and leaky dielectric approximation to study electrocoalescence and deformation of axisymmetric drops, observing that the viscosity ratio between the droplet and continuous phase fluids complicates coalescence and phase separation, especially with shorter time steps. Hadidi et al. [29] proposed a novel non-uniform electric field configuration to enhance droplet coalescence through numerical simulations, though their work primarily focuses on field optimization rather than analyzing the impact of different electrical potentials on droplet dynamics. Utiugov et al. [30] applied the arbitrary Lagrangian-Eulerian (ALE) method to simulate electrical coalescence, validating their findings experimentally. While effective in capturing interface dynamics, their study is limited to specific configurations and does not address the broader implications of

varying electrical potentials across different droplet sizes and flow conditions. In more recent studies, Sun et al. [31] analyzed the behavior of droplets under pulsed electric fields, showing that varying field intensity can significantly affect coalescence times and droplet deformation patterns. Zhang et al. [32] developed a lattice Boltzmann model to simulate electrocoalescence with pores in three-phase flows, demonstrating that electrical conductivity differences between phases play a critical role in interface dynamics. Majd et al. [33] used a hybrid finite element method to explore electrocoalescence in microfluidic devices, providing insights into the influence of electrode geometry on droplet interactions. Lastly, Ou et al. [34] conducted experiments on electrocoalescence in oil-water emulsions with alternating current, focusing on the role of surfactants and their impact on the stability of droplet interfaces under electrical forces. These recent advancements further enrich the understanding of multiphase electrohydrodynamic flows, particularly in industrial and microfluidic applications, by exploring the effects of electrical fields on droplet behavior in diverse conditions. Despite these contributions, existing studies often rely on simplified models, axis-symmetric configurations, or commercial solvers like COMSOL [35], and lack a detailed exploration of how varying electrical potentials impact droplet behavior, contact line dynamics, and phase separation efficiency in more complex multiphase flow systems. This gap in literature highlights the need for a more nuanced approach. Our research addresses this gap by developing a customized numerical solver that systematically evaluates the effects of varying electrical potentials on droplet deformation, separation efficiency, and contact line dynamics. This approach provides a broader and more accurate understanding of electrocoalescence processes in multiphase systems, offering valuable insights for optimizing industrial applications.

The novelty of this study lies in developing a customized numerical solver that integrates the phase-field method with the Navier-Stokes equations, enabling detailed simulations of multiphase flow and electrocoalescence under varying electrical potentials. Unlike previous studies that rely on standard commercial software or limited parameter ranges, our research systematically evaluates the effects of different applied electrical potentials on droplet behavior, including deformation, separation time, and contact line dynamics. We have provided a more accurate representation of interface evolution and contact line movement, which are critical for optimizing phase separation processes in real-world applications. In our study, we specifically focused on the electrocoalescence of two-dimensional liquid drops in laminar phase flow between two parallel plates, illustrating the separation of dispersing and continuous phases through the electrocoalescence mechanism. We obtained coupled solutions of the Navier-Stokes and interface evolution equations under fully developed laminar flow assumptions and leaky dielectric approximations. By tracking the interface between the dispersed and continuous fluids using the phase-field method, we demonstrated how increasing electrical potential leads to asymmetric, unstable droplet shapes, and faster separation due to strong, unbalanced electrical forces. Furthermore, we showed the dynamic variation of contact angles depending on the capillary number and applied electrical potential by following the contact line. Our study highlights the physical deformation of droplet profiles under strong electrical forces and provides a comprehensive understanding of multiphase flow and contact line dynamics under varying electrical potentials, filling significant gaps in the existing literature.

2. Model Problem

The electrocoalescence of two drops in laminar phase flow between two parallel plates was modeled, as shown in ▶**Figure 1**. The Cartesian coordinate system was fixed on the bottom plate. In this configuration, H is the distance between plates, r_1 and r_2 are the initial radius of drops, respectively, and V0 is the applied voltage on the top plate.

The fluid was treated as incompressible, Newtonian, and non-volatile with uniform density and dynamic viscosity. Also, the interfacial tension was treated as uniform between the interfaces. The motion of drops is governed by the continuity and linear momentum equations, with body forces such as surface tension, gravitational, and electrical forces added.

$$\nabla.u = 0 \tag{1}$$

$$\rho\left(\frac{\partial u}{\partial t} + u.\nabla u\right) = -\nabla p + \eta\nabla^2 u + \rho g + F_s + F_e \tag{2}$$

Here ∇ is divergence operator, ∇^2 is Laplacian operator, and u is the velocity vector defined in-plane as, $u = ui + vj$, where p is the pressure and t is the time. η, g, F_s, and F_e are dynamic viscosity, gravitational accelaration, surface tension force and electrical force, respectively. Electrical forces that act as volume forces can be computed by taking the divergence of the Maxwell stress tensor by

$$F_e = \nabla.T,\ T = ED^T - \frac{1}{2}(E.D)I \tag{3}$$

where T is the Maxwell stress tensor, E is the electric field, D is the electric displacement field, and I is the identity matrix. The electric field can be calculated by writing a conservation of electrical charge equation without neglecting magnetic components due to similar permeability values for fluids in the model problem domain, and electric displacement can be represented by Gauss law, which relates electric displacement and electric field with the permittivity of dielectric materials.

$$E = -\nabla V \tag{4}$$

$$D = \epsilon_0 \epsilon_r E \tag{5}$$

where V is the electric potential, ∇V is the gradient of electric potential, D is the electric displacement field, ϵ_0 is the permittivity of the space, and ϵ_r is the relative permittivity, which is the ratio of the permittivity of dielectric material to space.

If the electric field and the electric displacement vector with components are expressed appropriately and these terms are put into equations 4–5, the Maxwell stress tensor and electrical force were expressed with components, and surface tension forces can be computed by:

$$F_s = \gamma \delta \kappa n \tag{6}$$

where $\gamma, \kappa, \delta, n$ are the surface tension coefficient between the fluid phases, curvature of the fluid-fluid interface, the Dirac delta function, and the outward unit normal vector to this interface, respectively. Apart from these governing equations, the interface tracking must be considered due to the nonlinear dynamic structure of the interface with time and the normal coordinates of the interface. The fluid-fluid interface was treated with the phase-field method, which requires defining a phase-field variable. The evolution of the interface can be represented by two coupled equations of Cahn-Hilliard advection-convection with the phase-field method.

$$\frac{\partial \phi}{\partial t} + u.\nabla\phi = \nabla.(M\nabla\mu) \tag{7}$$

$$\mu = -K\nabla^2\phi + \frac{K}{\epsilon^2}\phi(\phi^2 - 1) \tag{8}$$

where ϕ, K, ϵ, M and μ are phase-field variables, mixing energy density, control parameters of interface thickness, which affect the stability condition, mobility parameter, and chemical potential of the system, respectively. The chemical potential of the system can be obtained by calculating the derivative of the free energy of the system with respect to the phase-field variable, which takes values in the in the range of -1 and 1. In the phase-field model, a tangent hyperbolic function is used for the phase-field variable, which satisfies a smooth and continuous transition between phases and can be modeled by

$$\phi = -tanh\left(\frac{n}{\sqrt{2}W}\right) \tag{9}$$

Where n is the normal coordinate to the interface, defining the position along which the phase-field variable transitions between phases and W is the width of the hyperbolic tangent function, and this term can be considered a control parameter of the interface thickness for this model problem. As mentioned earlier, the den-

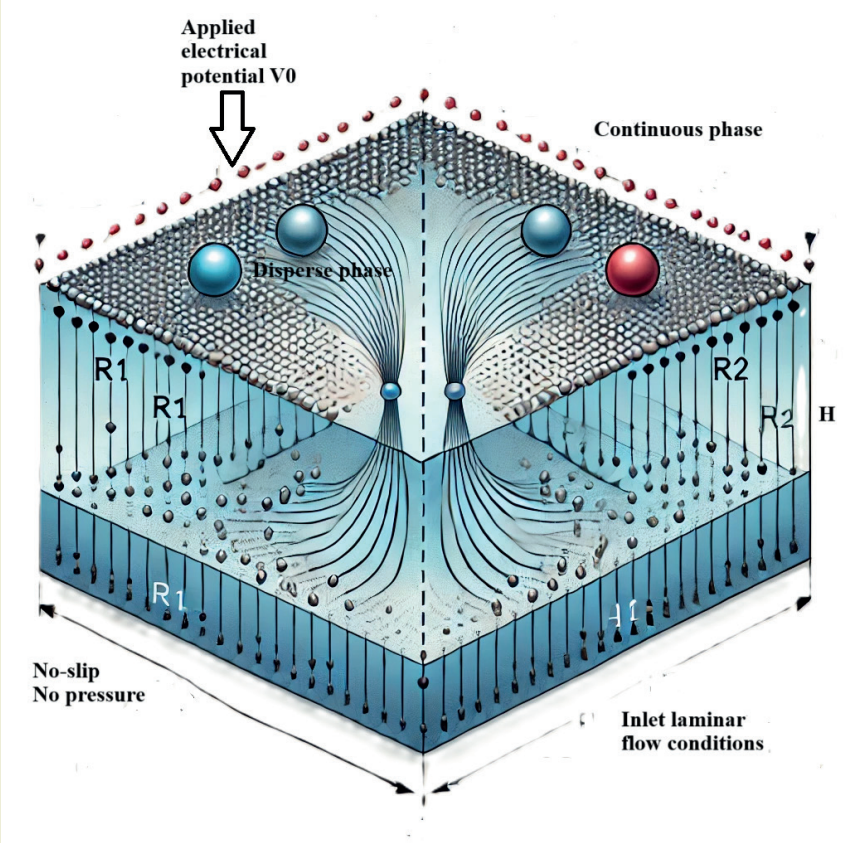

Figure 1. Schematics of our model problem.

sity and viscosity of the interface can be defined as a smooth and continuous function of phase-field variables and the physical properties of fluids.

$$\rho(\phi) = \frac{1}{2}[(1-\phi)\rho_1 + (1+\phi)\rho_2] \tag{10}$$

$$\eta(\phi) = \frac{1}{2}[(1-\phi)\eta_1 + (1+\phi)\eta_2] \tag{11}$$

where $\rho(\phi)$ and $\eta(\phi)$ are the density and viscosity as a function of the phase-field variable, script 1 and 2 are disperse and continuous-phase fluids, respectively. Also, surface tension forces can be modeled $\nabla\phi$ by using the divergence theorem on the free energy of the system [36].

$$F_s(\phi) = \left(-K\nabla^2\phi + \frac{K}{\epsilon^2}\phi(\phi^2-1)\right)\nabla\phi \tag{12}$$

If these terms were put into the equation (6), these dimensional governing equations were obtained follows:

$$\nabla.u = 0 \tag{13}$$

$$\rho(\phi)\left(\frac{\partial u}{\partial t} + u.\nabla u\right) = -\nabla p + \eta(\phi)\nabla^2 u + \rho g + F_s + F_e \tag{14}$$

$$\frac{\partial\phi}{\partial t} + u.\nabla\phi = \frac{MK}{\epsilon^2}\nabla^2(-\epsilon^2\nabla^2\phi + \phi(\phi^2-1)) \tag{15}$$

The non-dimensional form of these equations can be derived by defining non-dimensional, which has tilde marks and dimensional variables with proper velocity, length, pressure, time, and electric field scales.

$$\nabla = \frac{1}{H}\tilde{\nabla},\ u = U\tilde{u},\ t = \frac{H}{U}\tilde{t},\ p = \rho(\phi)U^2\tilde{p},\ E = E_s\tilde{E} \tag{16}$$

where H, U, E_s are characteristic length scale, reference velocity scale, reference electric field, and tilted variables indicated dimensionless parameters. So, the dimensionless governing equations are:

$$\frac{\partial\tilde{\phi}}{\partial t} + \tilde{u}.\nabla\tilde{\phi} = \frac{3}{2\sqrt{2}}\frac{1}{Pe}\nabla^2\left(-Cn^2\nabla^2\tilde{\phi} + \tilde{\phi}\left(\tilde{\phi}^2-1\right)\right) \tag{17}$$

$$\frac{\partial\tilde{u}}{\partial t} + \tilde{u}.\tilde{\nabla}\tilde{u} = -\tilde{\nabla}\tilde{p} + \frac{1}{Re}\tilde{\nabla}^2\tilde{u}$$

$$+\frac{3}{2\sqrt{2}}\frac{1}{ReCnCa}\left(-Cn^2\tilde{\nabla}^2\widetilde{\phi} + \tilde{\phi}\left(\tilde{\phi}^2-1\right)\widetilde{\nabla\tilde{\phi}}\right)$$

$$+2\frac{WeRe}{Ca}\tilde{E}^2 + \frac{Bo}{CaRe} \tag{18}$$

where

$$Pe = \frac{\epsilon HU}{M\gamma},\ Cn = \frac{\epsilon}{H},\ Ca = \frac{\eta U}{\gamma},\ .$$

$$Bo = \frac{\rho g H^2}{\gamma},\ We_{el} = \frac{\epsilon_0\epsilon_r E_s^2 H}{\gamma},\ Re = \frac{\rho UH}{\eta} \tag{19}$$

where $Pe, Cn, Ca, Bo, We_{el}, Re$ are Peclet, Cahn, Capillary, Bond, electrical Weber, and Reynolds numbers. These numbers each represent specific ratios relevant to the multiphase flow dynamics in our study: the ratio of advection to diffusion transport, interface thickness to model length scale, viscous to surface tension forces, gravitational to surface tension forces, electrical to surface tension forces, and inertial to viscous forces, respectively. Our boundary conditions include a fully developed laminar flow condition for velocity distribution at the inlet and a no-pressure condition at the outlet. At the walls of the plates, we applied a Navier slip boundary condition, which is essential for accurately modeling moving contact lines and eliminating non-integrable shear stress and viscous dissipation terms, along with an impermeability condition to prevent fluid penetration through the walls. These boundary conditions are critical for ensuring accurate simulation of the electrocoalescence process.

$$\beta(\phi)\tilde{u}_{slip} = -\frac{\partial\tilde{u}}{\partial\tilde{n}}.\tilde{n} + \tau L\left(\tilde{\phi}\right) \quad \text{at the walls} \tag{20}$$

$$\frac{\partial\tilde{\phi}}{\partial\tilde{t}} + \tilde{u}\widetilde{\nabla\tilde{\phi}} = -\tau L\left(\tilde{\phi}\right) \quad \text{at the walls} \tag{21}$$

$$\frac{\partial}{\partial\tilde{n}}\left(-Cn^2\tilde{\nabla}^2\widetilde{\phi} + \tilde{\phi}\left(\tilde{\phi}^2-1\right)\widetilde{\nabla\tilde{\phi}}\right) \quad \text{at the walls} \tag{22}$$

$$\tilde{u}.\tilde{n} = 0,\ \tilde{\nabla}\tilde{u}.\tilde{n} = 0 \quad \text{at the walls} \tag{23}$$

$$\tilde{p} = 0 \tag{24}$$

$$\frac{\partial\tilde{u}}{\partial\tilde{n}}.\tilde{n} = 0 \quad \text{at the walls} \tag{25}$$

Where $\tilde{u}_{slip}$ is the slip velocity, $L\left(\tilde{\phi}\right) = K\frac{\partial\tilde{\phi}}{\partial\tilde{n}} + \frac{\partial\gamma}{\partial\tilde{\phi}}$, τ is the phenomenological parameter, $\tilde{n}$ is the normal vector to the surface, and β is the slip coefficient. The Navier slip boundary condition indicates that slip velocity causes static and dynamic components of tangential stress on the fluid-wall interfacial region, and the summation of these stresses is given by $L\left(\tilde{\phi}\right)$. The static component of the tangential stress on the fluid-wall interfacial region is known as Young stress and is defined by $K\frac{\partial\tilde{\phi}}{\partial\tilde{n}}$. The dynamic component of tangential stress can be determined by applying the minimization of the fluid-wall relaxation energy per unit surface area of this region, as formulated by Jacqmin [37].

3. Materials and Methods

The mentioned numerical solver was developed using a finite element framework to integrate the phase-field method with the Navier-Stokes equations, ensuring

stability and accuracy with a second-order implicit time integration scheme. Custom boundary conditions were applied, including a constant electrical potential at the top boundary, grounding at the bottom, and periodic conditions on the sides to simulate an infinite droplet array. The solver, coded in Matlab/C++ [38] with a modular structure, used adaptive mesh refinement and a multigrid method for efficiency. Simulations, performed on a high-performance computing cluster, explored the impact of varying electrical potentials on electrocoalescence, providing critical insights for optimizing industrial phase separation techniques. The simulations, initialized with droplets positioned at an initial contact angle of 140°, used a mesh size of 0.01 mm and a time step of 0.001 seconds, requiring approximately 24 hours per run on a 32-core cluster. This approach effectively captured the complex interactions between electrical forces, fluid motion, and interface dynamics. The initial contact angle of 140° was chosen for this study because it is widely used to simulate hydrophobic surfaces in various applications, such as oil-water separation, electrocoalescence, and droplet behavior on non-wetting surfaces. Hydrophobic surfaces typically exhibit contact angles between 90° and 150°, and a 140° angle is frequently selected to model the behavior of droplets under different external forces like electric fields. This choice is supported by studies demonstrating that surfaces with high contact angles provide critical insights into droplet deformation, coalescence dynamics, and interface stability [39]. Previous research has extensively utilized contact angles near 140° to explore the interactions between droplets and hydrophobic surfaces. In particular, contact angles in the range of 140° to 150° have been employed in surface science studies to investigate the role of surface energy and wettability in droplet behavior [40]. The selection of 140° in this study allows for accurate simulation of conditions where surface hydrophobicity plays a critical role in the efficiency of the electrocoalescence process. The assumptions made before the simulation were presented as follows:

- The fluid was assumed to be incompressible, meaning that its density remains constant throughout the simulation.
- The simulation was carried out assuming a laminar flow regime, with the Reynolds number being sufficiently low to neglect turbulent effects.
- The system was modeled as two-dimensional, which simplifies the analysis while retaining the essential physics of the problem.
- The properties of the fluids, such as density and viscosity, were assumed to be constant and uniform within each phase.
- Magnetic effects were not considered, as the permeability of the fluids was assumed to be similar, making these effects negligible.
- Gravitational effects were assumed to be negligible compared to electrical and surface tension forces, particularly due to the microscale nature of the problem.
- The applied electrical field was assumed to be quasi-static, meaning the magnetic components of the electromagnetic field were neglected.
- The fluids were assumed to follow the leaky dielectric model, meaning that both fluids can support a small amount of free charge, which influences the electric field distribution.
- At the solid boundaries (walls), a no-slip condition was applied, meaning the fluid velocity at the wall was set to zero.
- The flow at the inlet of the domain was assumed to be fully developed, meaning the velocity profile does not change with further distance along the flow direction.

4. Validation of Numerical Method

To validate the correctness of the mesh structure used in the simulations, a mesh convergence study was conducted. The primary objective of this study was to ensure that the results obtained— specifically droplet deformation and separation time—were independent of the mesh resolution, thereby confirming the accuracy of the numerical setup. Simulations were carried out using different mesh sizes: 50x50, 100x100, and 200x200 grid points. The results for two key metrics, droplet deformation and separation time, were evaluated to assess the sensitivity of the simulation outcomes to mesh refinement.

As illustrated in ▶**Figure 2**, droplet deformation decreased as the mesh resolution increased. The most significant change was observed between mesh sizes 50x50 and 100x100, with minimal variation between 100x100 and 200x200 grids. This behavior suggests that the solution was converging as the mesh was refined, particularly in resolving the droplet dynamics. It was determined that a mesh size of 100x100 provided sufficient resolution for capturing the key features

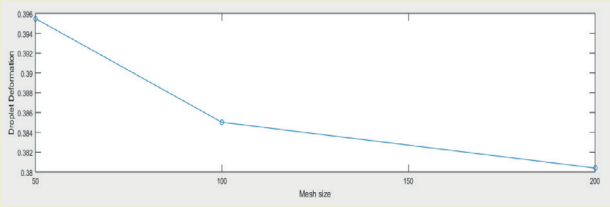

Figure 2. Convergence of droplet deformation with mesh refinement.

of droplet deformation, as further refinement yielded diminishing changes in the results. This indicates that the chosen mesh size of 0.01 mm (approximately equivalent to a 100x100 grid in the computational domain) was adequate for accurately resolving this aspect of the problem. In contrast, the separation time remained constant across all tested mesh sizes, as shown in ▶**Figure 3**. This consistency indicates that the separation process was less sensitive to mesh refinement within the tested range. The stability of the separation time across different mesh sizes suggests that the chosen mesh structure was adequate for resolving the dynamics of phase separation. Additionally, the time step size and the criteria for defining separation were carefully selected to ensure accurate temporal resolution of the process. Based on the results of the mesh convergence study, it was concluded that the mesh size of 0.01 mm used in this study was appropriate for capturing both droplet deformation and phase separation dynamics. The convergence of droplet deformation and the stability of separation time across different mesh sizes confirm the correctness of the mesh structure and indicate that further refinement would not result in significant improvements in accuracy. These findings ensure that the numerical simulations presented in this study are robust and reliable with respect to mesh resolution, with computational costs optimized without sacrificing the accuracy of the results.

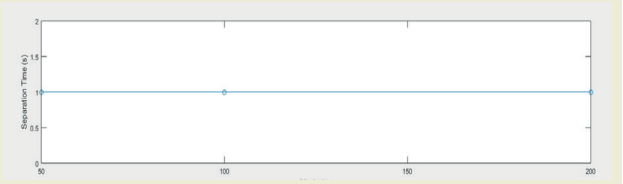

Figure 3. Convergence of separation time with mesh refinement.

5. Results and Discussions

The electrocoalescence process in laminar multiphase flow involves the interaction of viscous, surface tension, and electrical forces. Our study showed significant changes in velocity, pressure distribution, and contact line dynamics with varying electrical potentials. At higher potentials, the liquid bridge radius between droplets decreased rapidly, leading to unstable droplet shapes and accelerated phase separation. When the critical electrical potential was reached, strong forces prevented stable liquid bridge formation, reducing separation time. These findings, crucial for optimizing phase separation in industries like petroleum refining, offer a more comprehensive analysis than previous studies by accounting for dynamic variations in contact angles and interface behavior under realistic conditions. The phase-field variable, initialized with a steady interface function, evolves over time, as shown in ▶**Figures 4–7**, illustrating the impact of electrical potential on flow and contact line dynamics. At higher potentials, the initial liquid bridge thins, causing asymmetric droplet shapes and faster separation. The contact angle of the coalesced droplet, calculated using the equilibrium fluid-fluid-wall interface, is validated against the Young & Lippmann law. ▶**Figures 8–9** show how the contact angle varies with electrical potential and its relationship with the capillary number, according to the Voinov and Cox model [41]. To gain further insight into how varying the initial contact angle affects the electrocoalescence process, additional simulations were performed with contact angles of 120°, 130°, and 150°. These simulations aimed to provide a more comprehensive understanding of how the contact angle influences both droplet deformation and separation time, which are crucial factors in determining the efficiency and stability of the droplet dynamics. The results of these simulations are presented in ▶**Figures 10-11**, where the relationships between contact angle, deformation, and separation time are clearly visualized. Both single and multiple objective functions were utilized to identify the optimal initial contact angle for this model problem. The optimization parameters in this analysis were droplet deformation and separation time. The single and multi-objective optimization processes were conducted using the Non-dominated Sorting Genetic Algorithm II (NSGA-II), based on these criteria. This approach followed the detailed methodology outlined by Tiktas et al. [42]. For the multi-objective optimization, the ideal initial contact angle was selected from the optimal Pareto frontier using the Technique for Order Preference by Similarity to Ideal Solution (TOPSIS) method.

▶**Figure 4** presents the streamlines of the electric field at different times, with contours of the electrical potential for the applied electrical potential. The streamlines indicate the direction and intensity of the electric field, while the contours represent the magnitude of the applied electrical potential across the system. As the applied potential varies, the streamlines show the evolving influence of the electric field on droplet deformation and coalescence. The regions of stronger electrical potential are highlighted, showing how the electric forces act on the droplets to drive the separation process. ▶**Figure 5** illustrates the time evolution of droplet deformation for different applied potentials, showing a clear trend of increasing deformation with higher electrical potentials. ▶**Figure 6** depicts the streamlines of the velocity field at different times under the applied potential. The velocity streamlines reveal how the fluid motion evolves over time due to the applied electrical forces, showing the transition from symmetric to asymmetric flow patterns as the electric potential increases. Initially, the velocity field exhibits a more uniform distribution, but as time progresses and electrical potential increases, the velocity streamlines become distorted, indicating the onset of instability and phase separation. ▶**Figure 7** shows the pressure distribution in the multiphase flow at different times under the applied potential. The con-

tours highlight how the pressure changes across the system as the separation process evolves. Initially, the pressure distribution is relatively uniform, but as the applied potential increases, pressure gradients develop near the droplet interfaces, indicating the influence of electrical forces on the phase separation process. ▶**Figure 8** illustrates the dynamic variation of the contact angle against the applied electrical potential. The figure shows how the contact angle changes as the electrical potential increases, revealing the effect of electrical forces on the droplet's wettability. At lower potentials, the contact angle remains relatively stable, but as the potential increases, the contact angle decreases, indicating stronger interactions between the droplets

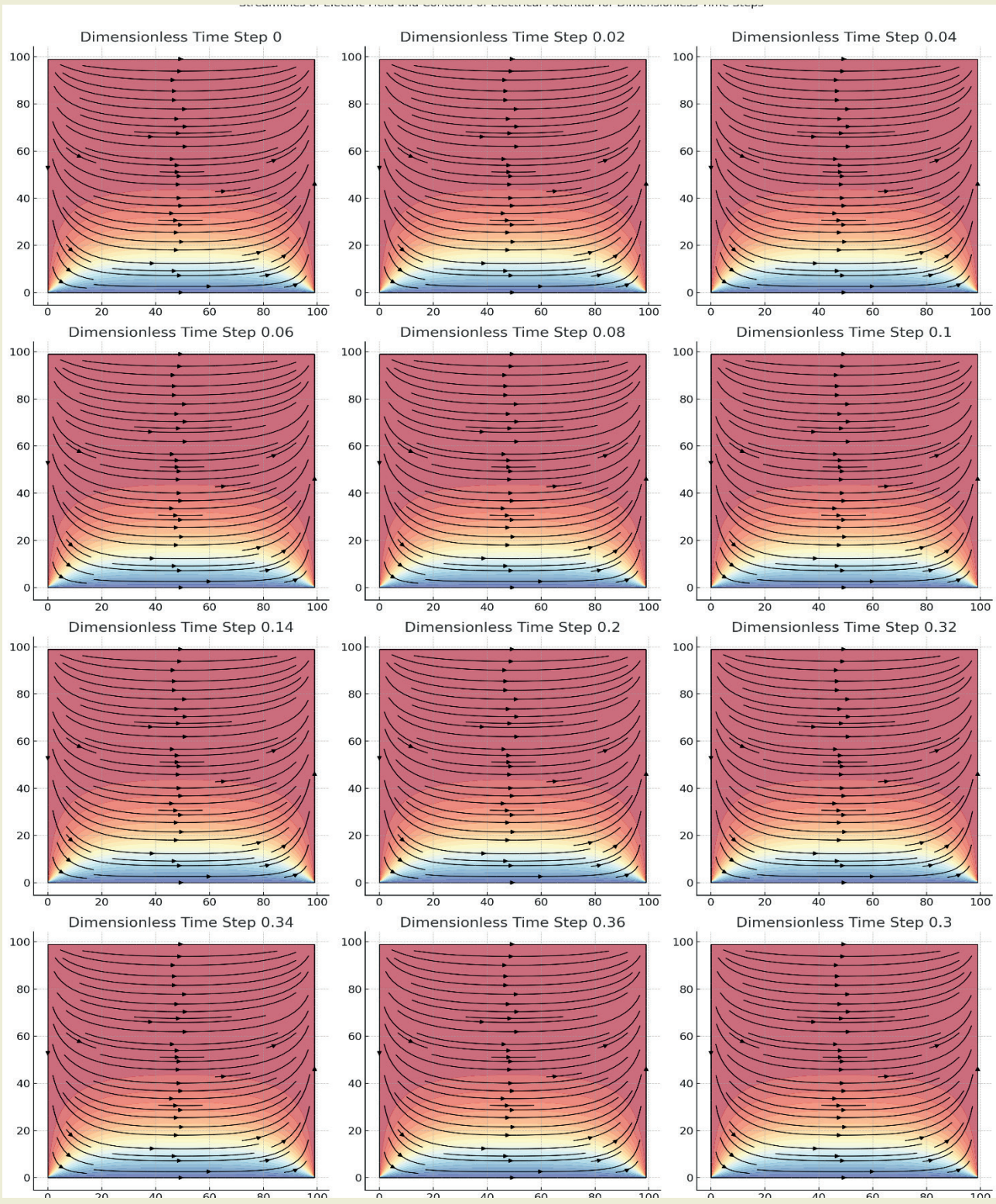

Figure 4. Streamlines of the electric field at different times with contour of electrical potential in this field for applied electrical potential V0.

and the surface. ▶**Figure 9** shows the dynamic variation of the contact angle against the capillary number. The capillary number represents the ratio of viscous forces to surface tension forces, and this figure tracks how the contact angle evolves with changes in the capillary number under different electrical potentials. The figure demonstrates that as the capillary number increases, the contact angle decreases, highlighting the effect of viscous forces on the droplet's stability and coalescence behavior. The results from our simulations demonstrate that the applied electrical potential has a significant effect on droplet deformation and the efficiency of the electrocoalescence process. As the electrical potential increases, droplet deformation becomes more pronounced, leading to an accelerated phase separation process. Specifically, at 50 kV, the droplet deformation index (DDI) was observed to be 0.35, indicating a mild asymmetry in droplet shapes. When the potential was increased to 100 kV, the DDI rose to 0.52, showing a substantial increase in droplet asymmetry. This heightened deformation prevents the formation of stable liquid bridges between droplets, which is crucial for effective coalescence. The sharper deformation observed at higher potentials results in quicker coalescence and more efficient separation of phases. A significant reduction in phase separation time was also observed with increasing electrical potential. At 50 kV, the time required for complete separation was 0.15 seconds. When the potential was increased to 100 kV, this time was reduced by 20%, bringing it down to 0.12 seconds. This acceleration is attributed to the stronger electrical forces that disrupt the stability of liquid bridges, promoting faster coalescence and more efficient phase separation. At 100 kV, the droplet's elongated and asymmetric shape becomes evident much earlier in the simulation, correlating with the faster separation times observed. Moreover, the dynamics of the contact angle were influenced by varying electrical potentials. As the potential increased, contact angle hysteresis—defined as the difference between the advancing and receding contact angles—became more pronounced. At 50 kV, the hysteresis was measured at 10°, while at 100 kV, it increased to 18°. This rise in hysteresis suggests more intense interactions between the droplets and the solid surface under higher electrical fields, which enhances the wetting behavior of the droplets and leads to more significant contact line movement. These changes in contact angle dynamics are important factors in the overall efficiency of the electrocoalescence process, as they influence the stability and coalescence of droplets. Our findings extend the results reported in previous studies. For example, Hadidi et al. [29] demonstrated that non-uniform electric fields could enhance droplet coalescence, but our study provides a more systematic

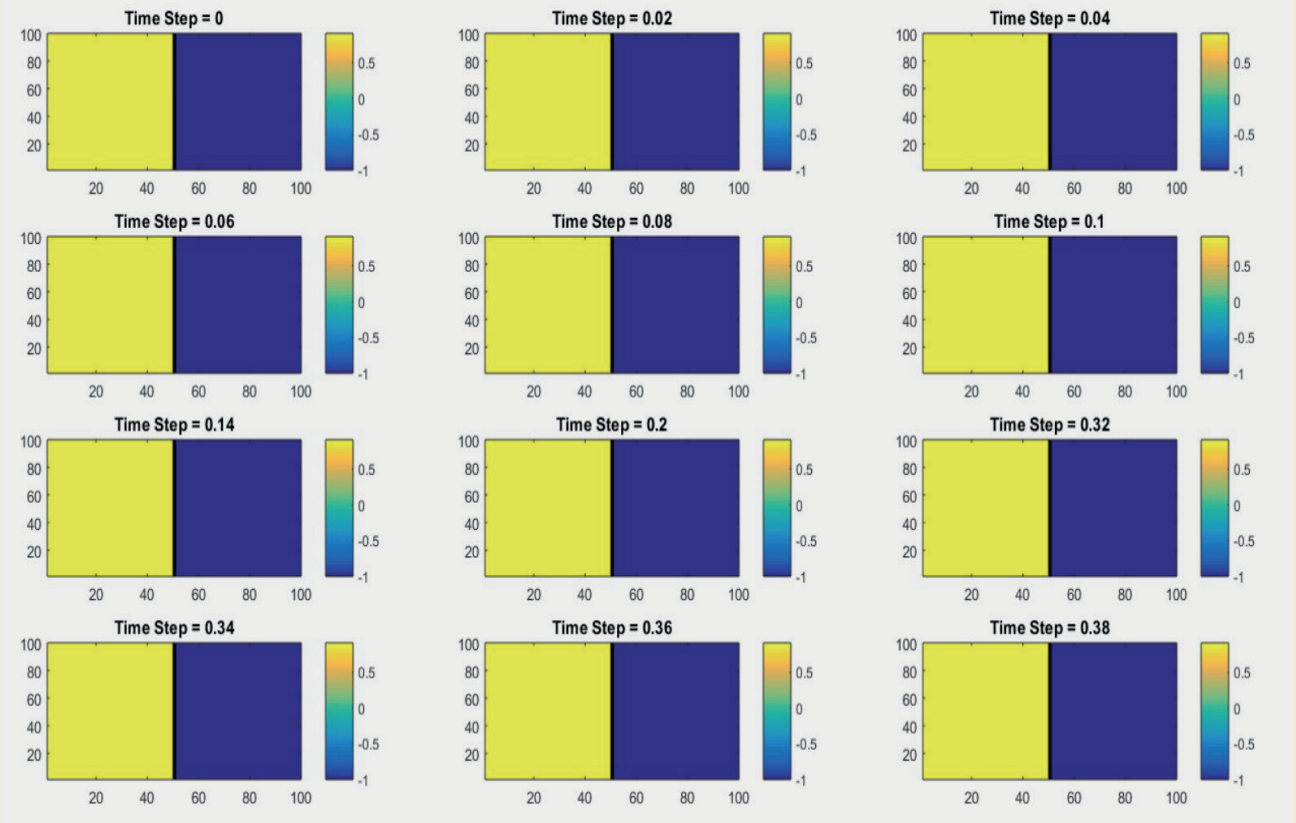

Figure 5. Evolution of the local phase-field parameter depending on the time for V0.

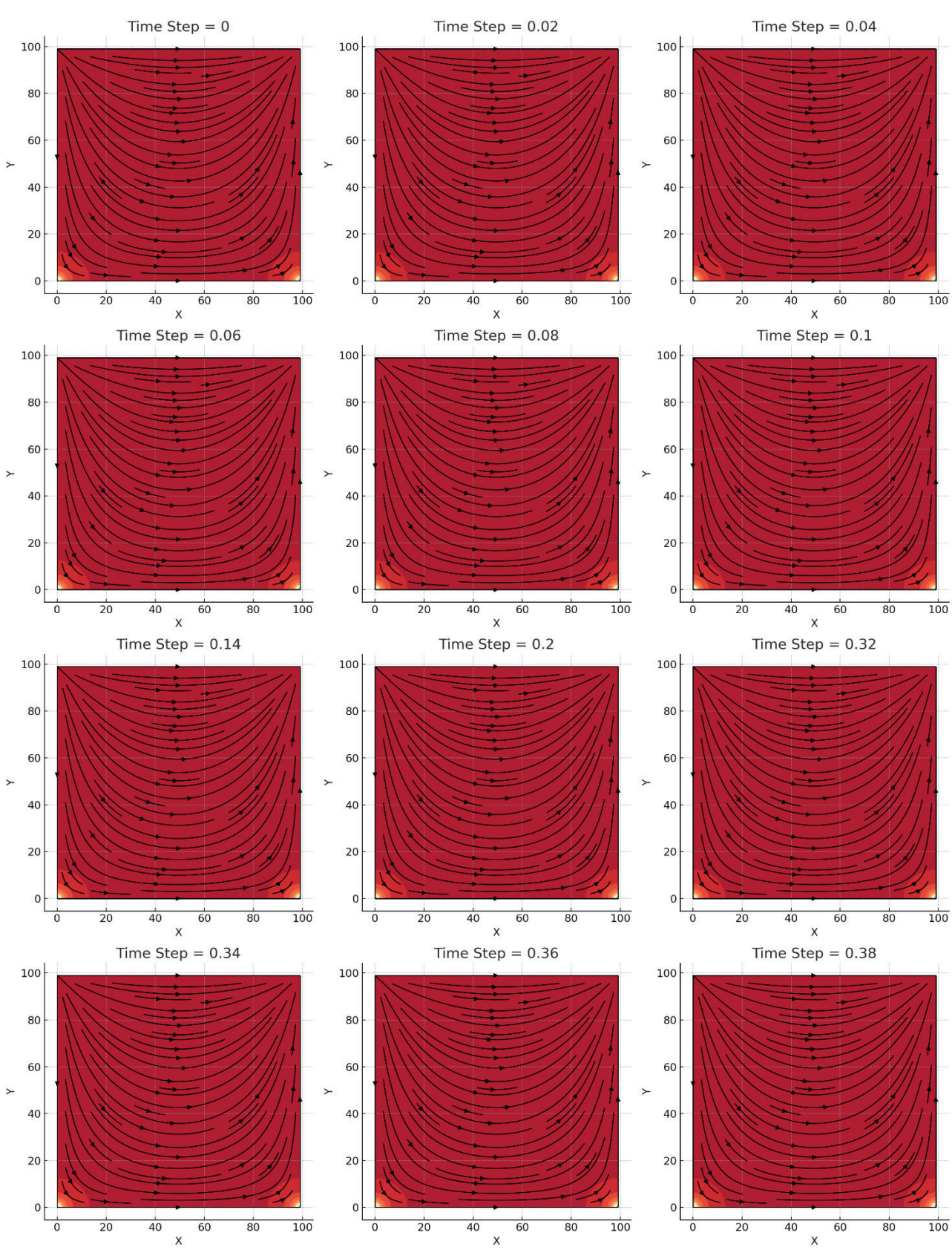

Figure 6. Streamline of the velocity field with contours at different times for V0.

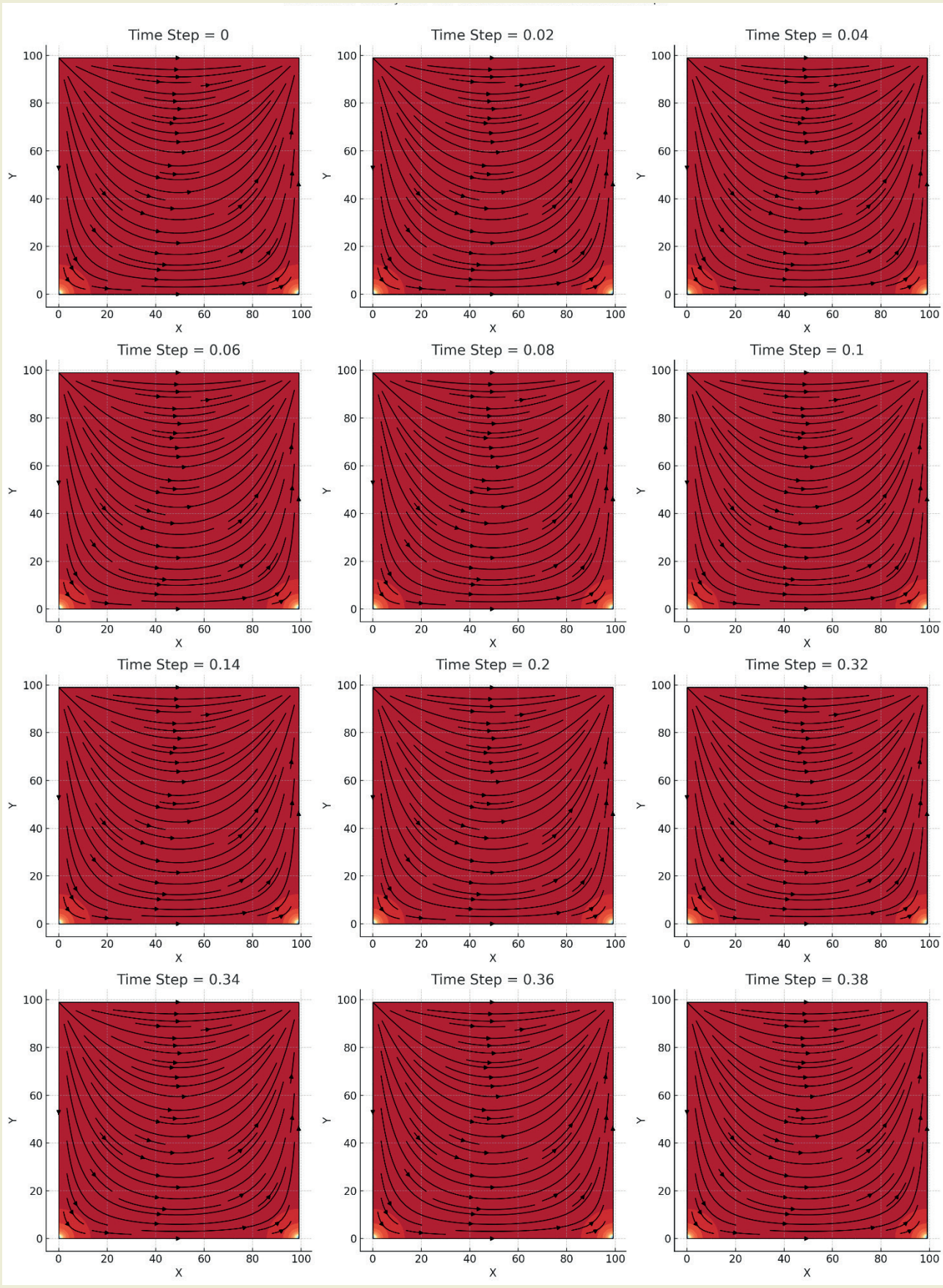

Figure 7. Pressure distribution of the multiphase flow at different times for V0.

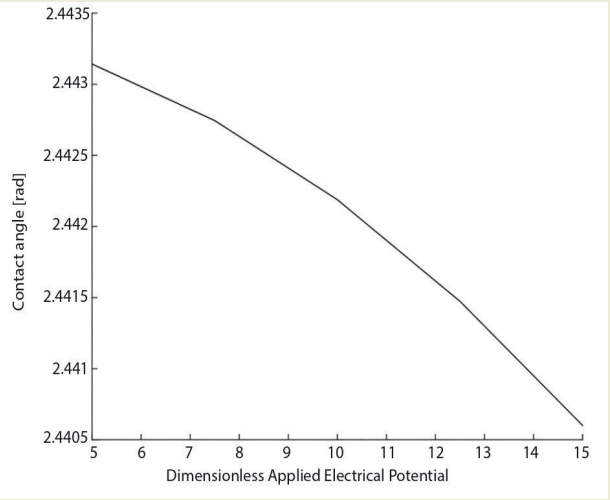

Figure 8. Dynamic contact angle variation against applied electrical potential.

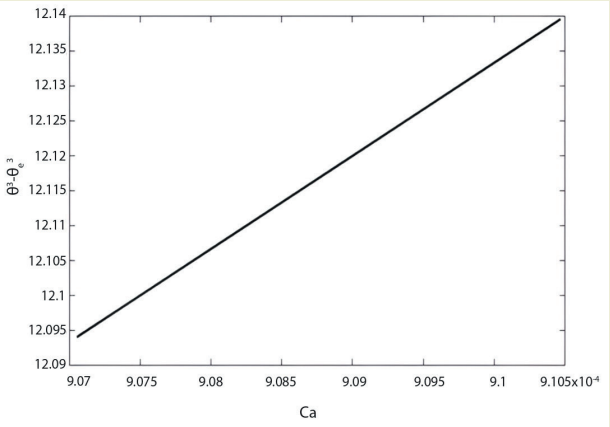

Figure 9. Dynamic contact angle variation against Ca.

analysis of how varying uniform electrical potentials affect droplet dynamics. Additionally, the numerical results from Utiugov et al. [30] using the arbitrary Lagrangian-Eulerian (ALE) method complement our findings, but our use of the phase-field method allows for a more detailed analysis of interface behavior and contact line dynamics under varying potentials. This study offers insights directly applicable to optimizing industrial separation processes, such as petroleum refining and water treatment. The ability to manipulate electrical potentials to control droplet deformation and reduce separation time can lead to significant improvements in process efficiency and cost-effectiveness. Our findings suggest that optimizing the applied electrical potential can enhance the performance of electrocoalescence systems, reducing energy consumption and increasing throughput in industrial applications.

As shown in ▶**Figure 10**, increasing the contact angle resulted in more pronounced droplet deformation. This effect can be attributed to the fact that as the contact angle increases, the surface becomes more hydrophobic, resisting wetting and encouraging the droplet to maintain a more spherical shape. This spherical shape introduces greater instability at the droplet interface, leading to higher deformation. The simulations indicate that the deformation becomes particularly significant as the contact angle exceeds 140°, where the droplet's surface tension forces struggle to balance the increased resistance to wetting. Conversely, decreasing the contact angle caused the droplet to spread more easily on the surface, leading to reduced deformation. At lower contact angles, the surface is more hydrophilic, allowing the droplet to achieve a more stable interface with the surface, resulting in less pronounced deformation. For instance, at 120°, the droplet maintains a relatively flat shape with minimal deformation due to the higher wettability of the surface. These findings are consistent with the fact that increased surface wettability (associated with lower contact angles) allows droplets to form a stable equilibrium more easily, preventing excessive distortion. ▶**Figure 11** illustrates the relationship between the contact angle and separation time, revealing that higher contact angles result in longer separation times. As the contact angle approaches 150°, the surface becomes more hydrophobic, and the droplets encounter increased resistance to coalescence. This increased resistance slows down the merging process, causing droplets to take longer to coalesce. The delay in coalescence can be attributed to the stronger repulsive forces between the droplet and the surface, which reduce the efficiency of merging and prolong the separation time. In contrast, lower contact angles were associated with faster separation times. As the surface becomes more hydrophilic (with contact angles closer to 120°), the increased wettability facilitates quicker droplet coalescence, resulting in shorter separation times. This phenomenon can be explained by the reduced resistance to interface merging at lower contact angles, which promotes faster droplet interactions and accelerates the separation process. As observed in the simulations, droplets on more hydrophilic surfaces have less resistance to forming a common interface, allowing for more efficient coalescence. The results of the single-objective optimization, based on different objective functions to determine the optimal initial contact angle for the model problem, are summarized in ▶**Table 1**. In this table, the objectives of minimizing droplet deformation and minimizing separation time are evaluated separately. Reducing separation time enhances efficiency, conserves energy, improves stability, and boosts performance across numerous engineering, industrial, and scientific fields. In systems where droplet dynamics play a critical role, achieving shorter separation times often leads to significant improvements in overall system performance. Conversely, minimizing droplet deformation is vital for maintaining the stability, efficiency, and accuracy of processes involving droplets. It allows for greater control over droplet behavior, resulting in more energy-efficient systems and better outcomes in applications ranging from microfluidics to printing technol-

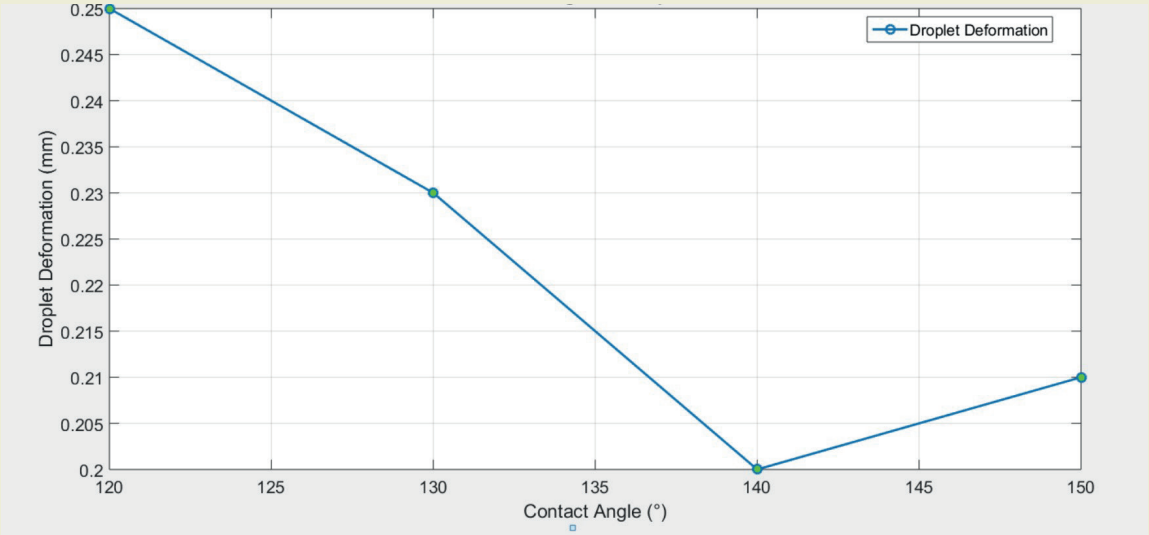

Figure 10. Effect of initial contact angle on droplet deformation.

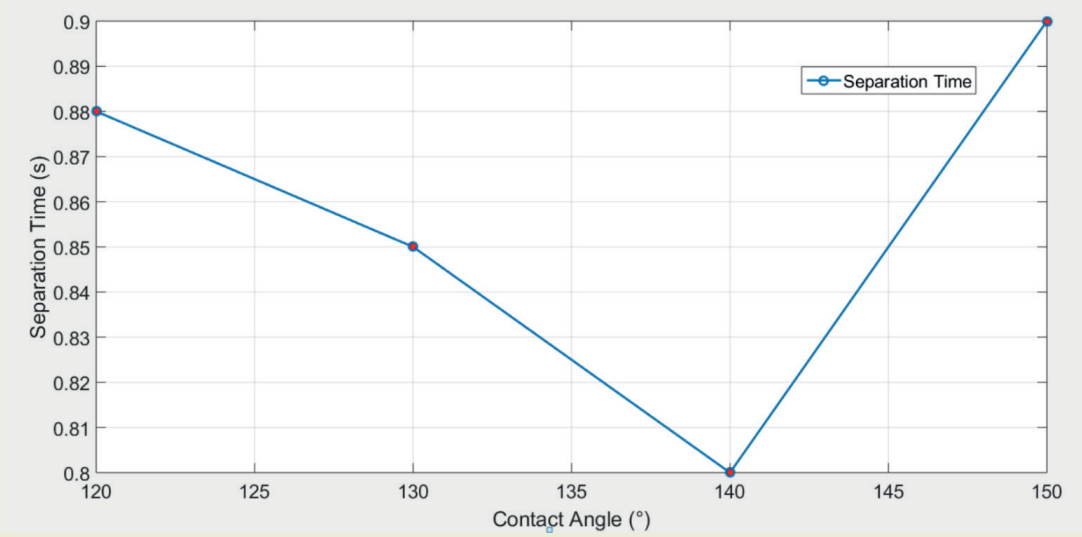

Figure 11. Effect of initial contact angle on droplet separation time.

ogies. By minimizing deformation, the droplet retains stability, structural integrity, and predictable responses to external forces, making it easier to manage and achieve desired results in various applications. For the objective of minimizing droplet deformation, the optimal initial contact angle was found to be 123.45° with a deformation value of 0.345 mm. This suggests that at this angle, the surface tension forces within the droplet are sufficient to counterbalance external forces, such as gravity or applied fields, that could otherwise deform it. This angle represents a stable equilibrium where the droplet maintains its shape, which is essential for ensuring proper functionality in applications such as material transport, micro-reactors in microfluidic systems, or precise deposition in printing and coating processes. For the objective of minimizing separation time, the optimal initial contact angle was determined to be 145.67° with a separation time of 1.23 seconds. This angle represents the point where the interaction between the droplet and the surface (or another droplet) is most conducive to rapid detachment. At this angle, surface tension forces are optimized for quick separation, and contact line dynamics favor rapid detachment. External forces, such as gravity or electric fields, are also more effective at facilitating separation at this contact

Table 1. Single objective optimization results for determination of optimum initial contact angle.

Objective function	Optimum initial contact angle (°)
Minimization of droplet deformation	123.45
Minimization of droplet separation time	145.67

angle. The optimization of droplet deformation and separation time revealed two competing objectives in this analysis. The multi-objective optimization, which focused on determining the ideal initial contact angle to balance these objectives, was conducted using the NSGA-II method. The resulting optimal Pareto frontier is shown in ▶**Figure 12**. To determine the best initial contact angle, equal weights (0.5) were assigned to both objective functions, and the TOPSIS method was applied. The results of the TOPSIS analysis are presented indicating that the optimal initial contact angle was 148°. Based on these optimization results, we conclude that if precision is the priority, as in printing technologies, biological experiments, or coating processes, the optimal contact angle of 123.45° should be selected for minimizing droplet deformation, as it maintains droplet shape with minimal distortion. If speed is the primary concern, as in spray drying, high-speed cooling, or large-scale manufacturing, the result focused on minimizing separation time (145.67°) will be more suitable, enabling faster droplet detachment and increased throughput. In systems that require a balance between these two objectives, such as biomedical applications, microfluidics, or complex multi-phase systems, the multi-objective optimization result of 148° offers a practical solution that balances both speed and precision, ensuring neither objective is overly compromised.

6. Conclusions

The contact angle was calculated for coalesced drop by following the contact line depending on time and plotting the contact angle variation against the applied electrical potential, which is compatible with Young-Lippmann law, and the dynamic variation of the contact angle against the Capillary number, which holds Cox-Voinov law, to check our solver with these two laws by choosing the proper applied electrical potential values. A comprehensive evaluation of the role of electrical forces in driving phase separation through electrocoalescence in laminar multiphase flows is provided in this study. The influence of varying electrical potentials on droplet behavior, interface dynamics, and separation efficiency was examined using a customized numerical solver that integrates the phase-field method with the Navier-Stokes equations. It was revealed through simulations that increasing the applied electrical potential from 50 kV to 100 kV significantly enhances phase separation efficiency, with the time required for complete separation being reduced by approximately 20%, from 0.15 seconds to 0.12 seconds. This improvement is attributed primarily to the stronger electrical forces, which induce greater droplet deformation, prevent the formation of stable liquid bridges, and promote quicker coalescence. Droplet deformation was quantified using the droplet deformation index (DDI), which was found to increase from 0.35 to 0.52 as the electrical potential was raised from 50 kV to 100 kV. This increase indicates a more pronounced asymmetric deformation of droplets, correlating with the observed acceleration in phase separation. A critical point was identified at an electrical potential of 80 kV, where droplet coalescence became more irregular, leading to the breakup of larger droplets into smaller ones, thereby further accelerating the separation process. Additionally, contact angle dynamics were monitored, and it was observed that contact angle hysteresis increased from 10° to 18° as the electrical potential was increased from 50 kV to 100 kV. This increase in hysteresis is indicative of more intense interactions between droplets and the solid surface under higher electrical fields, contributing to the observed changes in droplet behavior. The effectiveness of the numerical solver was validated through the quantitative data obtained from these simulations, which also provided new insights into the complex interactions between electrical forces and multiphase flow dynamics. These findings have significant implications for optimizing electrocoalescence processes in various industrial applications, such as oil-water separation, where precise control of phase separation is critical for operational efficiency. Future work will focus on the experimental validation of these numerical results and the exploration of the effects of non-uniform electric fields and more complex droplet configurations, with the aim of enhancing understanding and refining the numerical models used in electrocoalescence studies. In this study, the effects of varying the initial contact angle on the electrocoalescence process were investigated, with a focus on understanding how the contact angle influenced both droplet deformation and separation time. Additional simulations were conducted at contact angles of 120°, 130°, and 150° to provide a more comprehensive understanding of the relationship between surface wettability and droplet behavior. It was observed that increasing the contact angle led to more pronounced droplet deformation due to the increased hydrophobicity of the surface. This effect

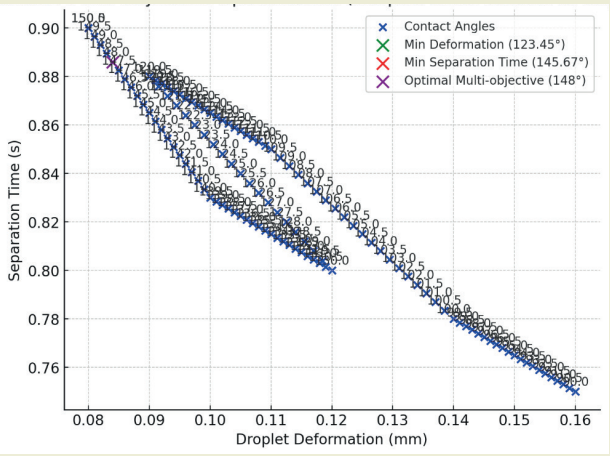

Figure 12. Pareto Frontier for multiobjective optimization of droplet deformation and separation time.

became more significant at contact angles above 140°, where the droplet exhibited greater instability at the interface. Lower contact angles promoted faster droplet coalescence, with shorter separation times observed at angles closer to 120°. The increased wettability at lower angles facilitated quicker droplet interactions and reduced resistance to merging. Through single and multi-objective optimizations, the ideal initial contact angles were determined based on the minimization of droplet deformation and separation time. The optimal initial contact angle was calculated to be 123.45°, with a deformation value of 0.345 mm. This angle represents the point where surface tension forces are sufficient to counter external forces, ensuring droplet stability and minimal deformation. The optimal initial contact angle was determined as 145.67°, with a separation time of 1.23 seconds, where the interaction between the droplet and surface optimizes rapid detachment. In balancing these conflicting objectives, a multi-objective optimization process using the NSGA-II method followed by the TOPSIS technique resulted in an optimal initial contact angle of 148°. This result offers a practical compromise between minimizing deformation and achieving efficient separation, making it suitable for applications where both speed and precision are necessary.

Nomenclature

Symbol	Description
Bo	Bond number
Ca	Capillary number
Cn	Cahn number
DDI	Droplet Deformation Index
E	Electric field (V/m)
F_e	Electrical force (N)
F_s	Surface tension force (N)
H	Distance between plates (m)
κ	Curvature of the fluid-fluid interface (m^{-1})
μ	Dynamic viscosity (Pa·s)
p	Pressure (Pa)
Pe	Peclet number
ϕ	Phase-field variable
ρ	Density ($\mathrm{kg/m}^3$)
Re	Reynolds number
σ	Surface tension (N/m)
t	Time (s)
u	Velocity vector (m/s)
V_0	Applied voltage (V)
∇	Gradient operator
∇^2	Laplacian operator
We_{el}	Electrical Weber number
ϵ_0	Permittivity of free space (F/m)
ϵ_r	Relative permittivity of dielectric material

Research ethics

The study complies with research and publication ethics.

Author contributions

The author have accepted responsibility for the entire content of this manuscript and approved its submission.

Competing interests

The author states no conflict of interest.

Research funding

This research did not receive any specific grant from funding agencies in the public, commercial, or not-for-profit sectors.

Data availability

The raw data can be obtained on request from the corresponding author.

Peer-review

Externally peer-reviewed.

Orcid

Aslı Tiktaş https://orcid.org/0000-0003-3685-5134

References

[1] Eow, J. S., Ghadiri, M., & Sharif, A. O. (2002). Electrostatic and hydrodynamic separation of aqueous drops in a flowing viscous oil. *Chemical Engineering and Processing: Process Intensification, 41*(8), 649–657.

[2] Wu, J., Xu, Y., Dabros, T., & Hamza, H. (2003). Effect of demulsifier properties on destabilization of water-in-oil emulsion. *Energy & Fuels, 17*(6), 1554–1559.

[3] Dezhi, S., Chung, J. S., Xiaodong, D., & Ding, Z. (1999). Demulsification of water-in-oil emulsion by wetting coalescence materials in stirred-and packed-columns. *Colloids and Surfaces A: Physicochemical and Engineering Aspects, 150*(1–3), 69–75.

[4] Klasson, K. T., Taylor, P. A., Walker, J. F., Jr, Jones, S. A., Cummins, R. L., & Richardson, S. A. (2005). Modification of a centrifugal separator for in-well oil-water separation. *Separation Science and Technology, 40*(1–3), 453–462.

[5] Scalarone, D., & Chiantore, O. (2004). Separation techniques for the analysis of artists' acrylic emulsion paints. *Journal of Separation Science, 27*(4), 263–274.

[6] Pouliot, Y., Conway, V., & Leclerc, P. (2014). Separation and concent-

ration technologies in food processing. In *Food processing: Principles and applications* (pp. 33–60).

[7] Yesair, D. W., & Coutinho, C. B. (1970). Method for extraction and separation of drugs and metabolites from biological tissue. *Biochemical Pharmacology, 19*(5), 1569–1578.

[8] Abeynaike, A., Sederman, A. J., Khan, Y., Johns, M. L., Davidson, J. F., & Mackley, M. R. (2012). The experimental measurement and modelling of sedimentation and creaming for glycerol/biodiesel droplet dispersions. *Chemical Engineering Science, 79*, 125–137.

[9] Narváez-Muñoz, C., Hashemi, A. R., Hashemi, M. R., Segura, L. J., & Ryzhakov, P. B. (2024). Computational electrohydrodynamics in microsystems: A review of challenges and applications. *Archives of Computational Methods in Engineering*.

[10] Santra, S., Mandal, S., & Chakraborty, S. (2021). Phase-field modeling of multicomponent and multiphase flows in microfluidic systems: A review. *International Journal of Numerical Methods for Heat & Fluid Flow, 31*(10), 3089–3131.

[11] Li, J., Zheng, D., & Zhang, W. (2023). Advances of phase-field model in the numerical simulation of multiphase flows: A review. *Atmosphere, 14*(8), 1311.

[12] Abbasi, M. S., Song, R., Cho, S., & Lee, J. (2020). Electro-hydrodynamics of emulsion droplets: Physical insights to applications. *Micromachines, 11*(10), 942.

[13] Chen, L.-Q., & Zhao, Y. (2022). From classical thermodynamics to phase-field method. *Progress in Materials Science, 124*, 100868.

[14] Jain, S. S. (2022). Accurate conservative phase-field method for simulation of two-phase flows. *Journal of Computational Physics, 469*, 111529.

[15] Brenner, H. (2013). *Interfacial transport processes and rheology*. Elsevier.

[16] Sherwood, J. D. (1988). Breakup of fluid droplets in electric and magnetic fields. *Journal of Fluid Mechanics, 188*, 133–146.

[17] Cahn, J. W., & Hilliard, J. E. (1958). Free energy of a nonuniform system. I. Interfacial free energy. *Journal of Chemical Physics, 28*(2), 258–267.

[18] Probstein, R. F. (2005). *Physicochemical hydrodynamics: An introduction*. John Wiley & Sons.

[19] Krotov, V. V., & Rusanov, A. I. (1999). *Physicochemical hydrodynamics of capillary systems*. World Scientific.

[20] Lippmann, G. (1875). Démonstration élémentaire de la formule de Laplace. *Journal de Physique Théorique et Appliquée, 4*(1), 332–333.

[21] Dupré, A., & Dupre, P. (1969). *Théorie mécanique de la chaleur*. Gauthier-Villars.

[22] Li, X., Bodziony, F., Yin, M., Marschall, H., Berger, R., & Butt, H.-J. (2023). Kinetic drop friction. *Nature Communications, 14*(1), 4571.

[23] Butt, H.-J., et al. (2022). Contact angle hysteresis. *Current Opinion in Colloid & Interface Science, 59*, 101574.

[24] López-Herrera, J. M., Popinet, S., & Herrada, M. (2011). A charge-conservative approach for simulating electrohydrodynamic two-phase flows using volume-of-fluid. *Journal of Computational Physics, 230*(5), 1939–1955.

[25] Yang, Q., Li, B. Q., & Ding, Y. (2013). 3D phase field modeling of electrohydrodynamic multiphase flows. *International Journal of Multiphase Flow, 57*, 1–9.

[26] Fernandez, A., Tryggvason, G., Che, J., & Ceccio, S. L. (2005). The effects of electrostatic forces on the distribution of drops in a channel flow: Two-dimensional oblate drops. *Physics of Fluids, 17*(9).

[27] Maehlmann, S., & Papageorgiou, D. T. (2009). Numerical study of electric field effects on the deformation of two-dimensional liquid drops in simple shear flow at arbitrary Reynolds number. *Journal of Fluid Mechanics, 626*, 367–393.

[28] Lin, Y., Skjetne, P., & Carlson, A. (2012). A phase field model for multiphase electro-hydrodynamic flow. *International Journal of Multiphase Flow, 45*, 1–11.

[29] Hadidi, H., Kamali, R., & Manshadi, M. K. D. (2020). Numerical simulation of a novel non-uniform electric field design to enhance the electrocoalescence of droplets. *European Journal of Mechanics-B/Fluids, 80*, 206–215.

[30] Utiugov, G., Chirkov, V., & Reznikova, M. (2021). Application of the arbitrary Lagrangian-Eulerian method to simulate electrical coalescence and its experimental verification. *International Journal of Plasma Environmental Science & Technology, 15*.

[31] Sun, Z., Li, N., Li, W., Weng, S., Liu, T., & Wang, Z. (2024). Effect of droplet angle on droplet coalescence under high-frequency pulsed electric fields: Experiments and molecular dynamics simulations. *Chemical Engineering Science, 295*, 120195.

[32] Zhang, Z., Gao, M., Zhou, W., Wang, D., & Wang, Y. (2023). The numerical simulation of behaviors of oil-water-emulsion flow in pores by using phase field method. *Petroleum Science and Technology*.

[33] Alizadeh Majd, S., Moghimi Zand, M., Javidi, R., & Rahimian, M. H. (2023). Numerical investigation of electrohydrodynamic effect for size-tunable droplet formation in a flow-focusing microfluidic device. *Soft Materials, 21*(2), 174–190.

[34] Ou, G., Li, J., Jin, Y., & Chen, M. (2023). Droplet coalescence of W/O emulsions under an alternating current electric field. *Industrial & Engineering Chemistry Research, 62*(17), 6723–6733.

[35] Comsol. (2023). *IEEE Microwave Magazine, 24*(2). https://doi.org/10.1109/mmm.2022.3229860

[36] Kim, J. (2012). Phase-field models for multi-component fluid flows. *Communications in Computational Physics, 12*(3), 613–661.

[37] Jacqmin, D. (2000). Contact-line dynamics of a diffuse fluid interface. *Journal of Fluid Mechanics, 402*, 57–88.

[38] MathWorks. (2022). MATLAB (R2022a). The MathWorks Inc.

[39] Danish, M. (2022). Contact angle studies of hydrophobic and hydrophilic surfaces. In *Handbook of Magnetic Hybrid Nanoalloys and their Nanocomposites* (pp. 1–22). Springer.

[40] Zhu, Y., et al. (2023). Prediction of contact angle for oriented hydrophobic surface and experimental verification by micro-milling. *Coatings, 13*(8), 1305.

[41] Voinov, O. V. (1976). Hydrodynamics of wetting. *Fluid Dynamics, 11*(5), 714–721.

[42] Tiktaş, A., Gunerhan, H., & Hepbasli, A. (2023). Exergy and sustainability-based optimisation of flat plate solar collectors by using a novel mathematical model. *International Journal of Exergy, 42*(2), 192–215.

EUROPEAN MECHANICAL SCIENCE

Research Article

e-ISSN: 2587-1110

Investigation of cutting qualities of AISI304 stainless steel using plasma arc cutting method

Şerafettin Hırtıslı[1], **Oğuz Erdem**[1*]

[1]Kırıkkale University, Faculty of Engineering and Natural Sciences, Mechanical Engineering Department, 71450, Kırıkkale, Türkiye

Abstract: Since cutting stainless steels with non-traditional manufacturing processes such as laser beam cutting or water jet cutting is quite costly, machining with the plasma arc cutting (PAC) method, which is generally more economical, has been preferred more frequently in recent years. In this context, the use of PAC method in manufacturing of machine parts, especially in the construction and manufacturing industries, as well as in other industries such as food, automotive and petrochemicals, is increasing day by day. In these sectors, where high corrosion resistance and resistance to acidic environments are required, AISI304 stainless steel is generally preferred as the raw material. In this study, comprehensive literature research on PAC was conducted and the cutting qualities of AISI304 stainless steel plates with 4 and 8 mm thickness were investigated. Nine different types of experiment conditions (E1-E9) were created by the machining parameters (gas pressure: 0.6, 0.7 and 0.8 MPa – cutting speed: 151, 215 and 217 mm/min) determined from other experimental studies in the literature. The lowest average kerf taper value (0.32°) was obtained on the 4 mm thick plate with a gas pressure of 0.6 MPa and a cutting speed of 151 mm/min, whereas the highest average kerf taper value (2.59°) was obtained on the 8 mm thick plate where the gas pressure was 0.8 MPa and the cutting speed was 217 mm/min. The results revealed that for both plates, as the cutting speed increases at constant pressure values, the cutting surface roughness values increase. On the other hand, as the cutting speed is constant, the surface roughness decreases as the gas pressure value increases. The plates were cut into 100 mm long straight lines and the bottom surface burr formations and the top surface spatter formations in the PAC method were also examined.

Keywords: Plasma arc cutting, plasma cutting speed, plasma gas pressure, cutting width taper, kerf taper angle, cutting surface roughness

1. Introduction

Plasma arc cutting (PAC), a non-traditional manufacturing process, begins with the creation of a plasma arc by constricting a high-temperature, partially ionized gas (plasma) through a torch. It involves transferring the high energy released by the plasma arc to the electrically conductive workpiece surface to be processed, melting the material and removing the melted parts from the cutting environment [1]. For the plasma arc to form, the electrode (cathode) and the workpiece (anode) must be polarized with direct current, as seen in ▶**Figure 1**. Therefore, electrically conductive materials such as stainless steels, alloy steels, aluminium and copper can be machined with PAC [2-4]. The consumables and processing parameters (gas pressure, cutting speed, workpiece thickness, torch-to-workpiece distance, arc voltage, arc current, plasma and shielding gas type) used in the method directly affect the cutting quality [5, 6].

Austenitic stainless steels are the most widely used stainless steel class in the world, and the 304-grade stainless steel in this class is a steel quality containing high amounts of Cr and Ni. Due to their properties such as high hardness, corrosion resistance, high melting point and good weldability, AISI304 stainless steels are widely used in food, automotive, petrochemical, painting etc. industries [7]. In these industries, it is very dif-

*Corresponding author:
Email: oguz.erdem@kku.edu.tr

Cite this article as:
Hırtıslı, Ş., Erdem, O. (2024). Investigation of cutting qualities of AISI304 stainless steel using plasma arc cutting method. *European Mechanical Science, 8*(4): 319-330. https://doi.org/10.26701/ems.1573836

History dates:
Received: 25.10.2024, *Revision Request*: 12.11.2024, *Last Revision Received*: 22.11.2024, *Accepted*: 04.12.2024

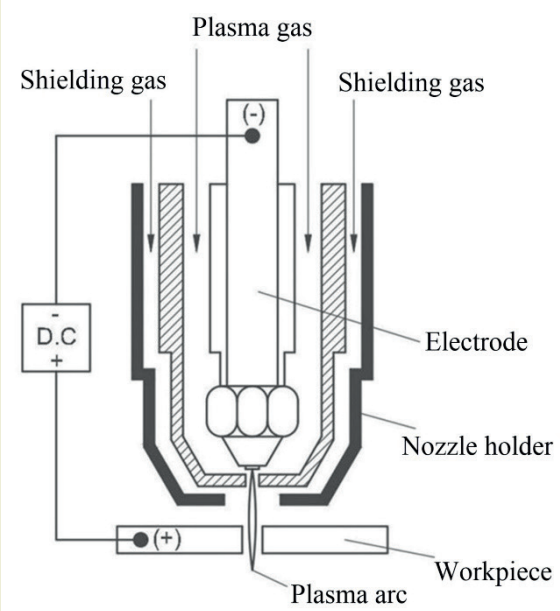

Figure 1. The schematic representation of the PAC process

ficult to cut and drill the hard-to-machine and thick sheet materials with the desired surface properties and geometric tolerances. At this point, the PAC offers more economical and faster production opportunities compared to other non-traditional manufacturing methods.

A considerable amount of literature has been published on the machining of stainless steels with the PAC. Numerous studies have argued that effects of machining parameters on cutting quality of PAC. For example, Bhowmick et al. [8] investigated the workpiece removable rate (WRR) and surface roughness by machining AISI304 stainless steel sheets with thicknesses of 4, 6 and 8 mm in the PAC method at different gas pressures (0.6, 0.7 and 0.8 MPa) and cutting speeds (151, 214 and 217 mm/min). They found that the cutting speed and plate thickness had a greater effect on the WRR value, while the gas pressure had a more significant effect on the surface roughness. They observed that WRR value increased in three different experiments by increasing the plate thickness at 0.6 MPa gas pressure and 151 mm/min cutting speed. They also found that the average surface roughness (R_a) decreased as the gas pressure value increased on the 6 mm thick plate at a cutting speed of 217 mm/min. Çelik and Özek [9] subjected the S235JR plate material to the PAC process to obtain standard tensile samples using different machining parameters. In their experiments for 80 A current, they found that the R_a value decreased with increasing arc voltage, and for 130 A current, the R_a value increased with increasing arc voltage. Likewise, Tsiolikas et al. [10] investigated the surface roughness of St37 steel in the PAC by cutting rectangular samples with dimensions of 30x40 mm at different cutting speeds (2000, 2600 and 3200 mm/min), different torch-to-workpiece distances (3, 3.6 and 4.2 mm) and different arc voltages (145, 150 and 155 V). They determined the best machining parameters in terms of surface roughness as follows: cutting speed 2000 mm/min, torch-to-workpiece distance 3.6 mm and arc voltage 155 V. For the surfaces cutting with these machining parameters, the R_a value was determined as 0.835 µm and the R_z value was determined as 7.7 µm. Similarly, Patel et al. [11] concluded that cutting speed has a significant effect on surface roughness in machining AISI D2 steel by PAC method. Bhuvenesh et al. [12] reported that the relationship between the WRR and R_a values in the PAC is inversely proportional and the lowest R_a value was obtained in the machining that they performed at 6.0 bar gas pressure, 80 A cutting current, 600 mm/min cutting speed and 4.0 mm torch-to-workpiece distance.

Improving the cutting quality of stainless steel by controlling the machining parameters during PAC is a very difficult task. Recent developments in the field of PAC have led to a renewed interest in kerf width and kerf taper. For example, Parthiban et al. [13] determined the top surface kerf width, bottom surface kerf width and kerf taper by cutting 2 mm thickness AISI316L stainless steel with different parameters and determined the best processing parameters as 40 A cutting current, 5000 mm/min cutting speed and 2 mm torch-to-workpiece distance. Guatam and Gupta [14] obtained the lowest R_a value (2.635 µm) in a 30x30 mm square cutting process at 6 bar gas pressure, 150 A cutting current, 400 mm/min cutting speed and 2 mm torch-to-workpiece distance. Ilii et al. [15] detected burr (beard) formation at the bottom of the cut surface depending on the cutting speed and material thickness. The machining parameters that did not cause burr formation in the cutting of a 4 mm thick plate (AISI304) were determined as 130 A cutting current and 1000 mm/min cutting speed. Rana et al. [16] observed that the current value has more than 65% effect on the kerf, the cutting speed has about 34% effect and the gas pressure have less than 1% effect. Hamid et al. [17] conducted research using Taguchi and GRA methods for surface roughness and kerf taper angles by experimenting with different machining parameters in PAC. They discovered that the cutting current primarily affects the surface roughness and taper angle values by 79.42%, while the cutting speed affects the value secondarily by 11.03%. Similarly, Das et al. [18] reported that gas pressure significantly affects WRR and surface roughness as a result of their study. Chamarthi et al. [19] investigated the surface roughness by cutting Hardox-400 material with different machining parameters using a water-cooled torch at PAC. They stated that the cutting speed should be reduced to decreased surface roughness. They also mentioned that the required machining parameters (cutting speed 2100 mm/min, arc voltage 125 V and plasma gas flow rate 70 l/h) must be to obtain the minimum surface roughness. Skoczylas et al. [20] encountered rougher and more curved surfaces with increasing cutting speed and cutting current in their study. However, they reported that the smoothest sur-

face (R_a = 1.27 μm) and less directional curvature were obtained in the machining where the cutting speed was 1200 mm/min, the cutting current was 60 A, and the gas pressure was 10 bar. Hatala et al. [21] determined from their experiments that the most important parameter affecting the surface roughness is the cutting speed and the least affecting parameter is the nozzle diameter. Chiarelli et al. [22] have conducted studies to investigate the fatigue properties of 8 mm thick Fe510D1 steel sheet by cutting it with both PAC and milling methods to obtain 40 mm wide fatigue test specimens. When milled and PAC cut samples were compared, it was observed that the fatigue strengths of PAC cut samples were almost equal to the milled samples.

A theoretical issue that has dominated the field for many years is artificial neural network (ANN). Radovanovic and Madic [23] conducted experimental studies for PAC modelling using ANN. For modelling, cutting operations were performed using different cutting speeds (0.33 and 2.8 m/min), different cutting currents (45 and 130 A) and workpieces of different thicknesses (4 and 15 mm). They determined from experimental studies that the surface roughness increases with the decrease in cutting current and increase in cutting speed and confirmed it with the ANN model. Hoult et al. [24] investigated the cutting performances of aluminium-based metal matrix composite sheet by cutting in the rolling direction. They concluded that the surface roughness increased by 25% in the right region, and the left side of the cut was twice as bad as the right side in terms of heat affected zone (HAZ) width and kerf angle. Similarly, Gostimirović et al. [25] found that the increase in cutting speed resulted in a larger kerf angle, a smaller kerf width, and a HAZ width of approximately 1 mm for all machining conditions. Also, Singh et al. [26] obtained the minimum kerf angle value (2.52 °) by machining 10 mm thick mild steel material with PAC at 1600 mm/min cutting speed and 7 mm torch-to-workpiece distance. Suresh and Diwakar [27] found that arc voltage had the greatest effect on WRR and surface roughness, while cutting speed had the smallest effect. Iida et al. [28] investigated the slag formed after cutting steel material with PAC at 125 A cutting current, 1000 mm/s cutting speed and 1.6 mm diameter nozzle. They used a high-speed video camera to observe the slag that formed during melting and the metal that adhered to the other side of the cutting zone. From video recordings, they determined that cutting speed is a more effective parameter than cutting current in slag formation. Naik and Maity [29] investigated the cutting performances of 10 mm thick Hardox-400 steel by machining it with PAC under the influence of four different plasma gases (air, argon, oxygen and nitrogen). In their experiments conducted at a plasma gas flow rate of 12 g/min, they determined that nitrogen, argon and air created sharper surfaces. Ferreira et al. [30] cut 15 mm thick QstE-380 alloy steel with PAC under different machining conditions to increase productivity and make cost analysis in PAC with response surface methodology. They stated that in order to increase productivity and surface quality, the cutting speed should generally be above 1800 mm/min, and the arc voltage should be kept as low as possible to keep the cost low. Masoudi et al. [31] found that increasing the cutting current increases the HAZ width, while high gas pressure and cutting speed decrease the HAZ width. Sharma et al. [32] determined that with the increase in gas pressure in PAC, the WRR initially decreases but increases after a certain value (68 psi). Sandeep et al. [33] found in their study that the cutting current and torch-to-workpiece distance values in the PAC affect the surface roughness in direct proportion. Muhamedagic et al. [34] stated that cutting speed is a more important parameter than plasma gas pressure for cutting quality and the best machining parameter values is 2500 mm/min for cutting speed - 6 bar for plasma gas pressure.

Hamood and Najm [35] discovered that although the machining parameters have direct effects on dimensional accuracy and machining time, the most affecting machining parameter is the cutting current. Adalarasan et al. [36] stated that in order to increase the surface quality, the cutting current should be reduced, the distance between the torch-to-workpiece should be reduced and the gas pressure should be increased. Kim and Kim [37] observed that the surface roughness increased with increasing cutting speed, and the surface roughness decreased with increasing cutting current, but the HAZ width increased. Begic et al. [38] observed that the top surface kerf width increased with increasing cutting speed, and the top surface kerf width and surface roughness decreased with increasing plasma gas pressure while the cutting speed was constant. Peko et al. [39] discovered that the cutting current has the most significant effect on the kerf width. Kountouras et al. [40] calculated the kerf angle by drilling 20 mm diameter holes in 6.5 mm thick St37 steel with PAC at variable parameters. They concluded that the kerf angle was affected by cutting speed, arc current and torch-to-workpiece distance by 19%, 59% and 16%, respectively. Zajac and Pfeifer [41] found that the cutting speed affects the surface quality, the cutting speed affects the kerf angle more than the cutting current, and the kerf angle value increases as the cutting speed increases.

Mentioning current applications of the PAC method, many old oil production facilities are currently being decommissioned. Removing underground pipes from abandoned oil wells and shutting down facilities is very important in terms of protecting the environment. In this conjecture, PAC has been preferred in cutting steel structures in oil facilities in recent years due to its low cost and high-speed precision cutting performance. Liu et al. [42] experimentally investigated the cutting of oil pipes by underwater plasma arc method. They used a workpiece composed of a steel plate and a cement block to simulate the oil casing pipe during the cutting process. Their experimental results revealed that optimizing the side air flow at constant cutting speed improved

the slag emissions but reduced the kerf depth. They also stated that underwater plasma arc cutting could be a suitable method for extracting oil pipes.

In PAC, the characteristics of the plasma gas flow existing from the nozzle significantly affect the cutting quality. The high-pressure jet in the PAC creates complex shock wave structures as it is incident on the metal surface to be cut. In this area, Tuladhar et al. [43] used a computational fluid dynamics simulation model to analyse the effects of a curved cutting front on the gas flow behaviour during the PAC process. They observed that the curvature of the cutting fronts creates oblique shock wave structures that significantly reduce the flow velocity. Recently, studies on the effects of polarization have also been encountered in the PAC. Sidorov et al. [44] examined the phase compositions on the near-surface layers of Al-Mg, Al-Cu-Mg alloys and commercially pure titanium samples obtained by plasma cutting using direct current forward polarity (DCSP) and direct current reverse polarity (DCRP). They discovered that the "water mist" formed around the plasma jet during cutting of all types of materials with DCRP, results in more intense oxidation of the metal, less thermal impact on the material and reduced roughness of the cutting surface. Similarly, Grinenko et al. [45] investigated the structure and properties of the surface layers of AA5056 and AA2024 aluminium alloy plates with a thickness of 35 to 40 mm after DRCP plasma cutting. They stated that the alloy plate could not be cut to its full thickness under the reduced heat input condition with DCRP.

It is a fact that plasma flows under the workpiece are affected by machining parameters. Various variance analyses are performed to determine the significance of independent variables affecting the kerf geometry in the PAC process. For example, Tuladhar et al. [46] proved that the variables selected for PAC significantly affect the kerf length difference and the upper surface kerf width using the regression model they developed. The existing research fail to explain the magnetic effect on PAC. Especially, studies on magnetic re-limiting of plasma cutting arc particularly remain limited in the literature. To fill this gap in the literature, Liu et al. [47] comprehensively investigated the distribution of longitudinal magnetic field (LMF) for PAC with a combined simulation approach using Maxwell and ANSYS. They stated that the application of LMF can significantly increase the current density, temperature and uniformity of the plasma cutting arc and thus improve the cutting performance. Another research area for PAC is statistical data analysis. Hussain et al [48] used Taguchi orthogonal array design to investigate and optimize the PAC parameters. They stated that their current work can contribute to industrial practitioners by providing high efficiency, minimum material waste and reduction of stubborn resolidified metal buildup. They also reported that it can help them to select, to control and optimize PAC machining parameters to achieve excellent cutting quality.

In this study, comprehensive literature review on PAC was conducted and the cutting qualities of PAC were investigated using nine different types of experiment conditions (E1-E9) created with different cutting speeds (151, 214 and 217 mm/min) and different gas pressures (0.6, 0.7 and 0.8 MPa) on AISI304 stainless steel plates with thicknesses of 4 and 8 mm with the machining parameters determined from the experimental studies in literature. Kerf taper was determined by cutting AISI304 sheets into 30 mm long straight lines and cutting them into 30x50 mm rectangles to determine the cutting surface roughness values. Moreover, the plates were cut into straight lines of 100 mm length and the bottom surface burr formations and the top surface spatter formations were also examined.

2. Materials and Methods

Experimental studies were carried out on the AJAN brand CNC Plasma Arc Cutting machine, which is capable of cutting materials with a maximum size of 2000x12000 mm and a thickness of 40 mm, as shown in ▶**Figure 2**, at a maximum current of 260 A and an arc voltage of 171 V. AISI304 stainless steel sheets with dimensions of 950x730 mm and thicknesses of 4 and 8 mm were used as workpieces. Air was chosen as the plasma gas and nitrogen was chosen as the shielding gas. The torch was held in a perpendicular position relative to the workpiece and the distance between the two was set as 1 mm for each experiment. The nozzle diameter used is 1.2 mm. The equipment used in the torch is selected as follows: electrode E1, swirl ring SW2, nozzle N5, gas ring G1 and shield cup S3, depending on the type of material to be cut, the plasma gas used and the current at which the cutting process will be performed (▶**Figure 3**) [49].

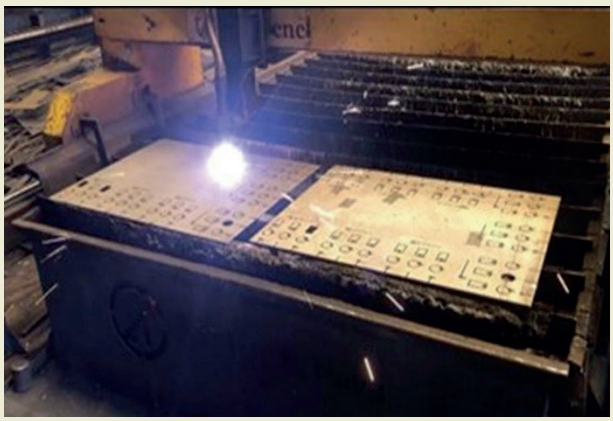

Figure 2. AJAN brand PAC machine (during cutting of AISI304 sheets with thicknesses of 4 and 8 mm) [49]

In literature, because AISI304 steel plates were cut by the PAC method in the study of Bhowmick et al. [8], it was preferred the same machining parameters for our

study. Three gas pressures (0.6, 0.7 and 0.8 MPa) were directly taken as reference from the study of Bhowmick et al. However, instead of the maximum cutting speed value (417 mm/min) used in Bhowmick et al. study's, the cutting speed value of 217 mm/min, which is closer to the cutting speed value of 214 mm/min, was preferred for our study. It can be said that the reason for this preference is to investigate the possible cutting quality results in cutting speed ranges closer to each other in our study. Because it is also known that surface quality will be negatively affected in thick plates at high cutting speeds. In addition, it is very difficult to observe the change in the kerf angle at very high cutting speed values. For each experiment, the current value was kept constant at 80 A and the arc voltage was kept constant at 120 V. As seen in ▶**Table 1**, nine different experiment conditions (E1-E9) created from machining parameters, 18 experiments were applied to 4- and 8-mm thick plates, and a total of 54 cuts were performed, with each experiment being repeated 3 times. ▶**Figure 4** shows the geometries and machined forms of the test samples prepared for experimental studies. As seen in ▶**Figure 4**.b, circles cut with a diameter of 40 mm were used in another study conducted by the authors of this study on circularity tolerance in PAC [49].

Table 1. Nine different experiment conditions created with machining parameters [8, 49]

Experiment No.	Cutting speed (mm/min)	Gas pressure (MPa)
E1	151	0.6
E2	214	0.6
E3	217	0.6
E4	151	0.7
E5	214	0.7
E6	217	0.7
E7	151	0.8
E8	214	0.8
E9	217	0.8

Figure 3. The equipment used inside the torch [49]

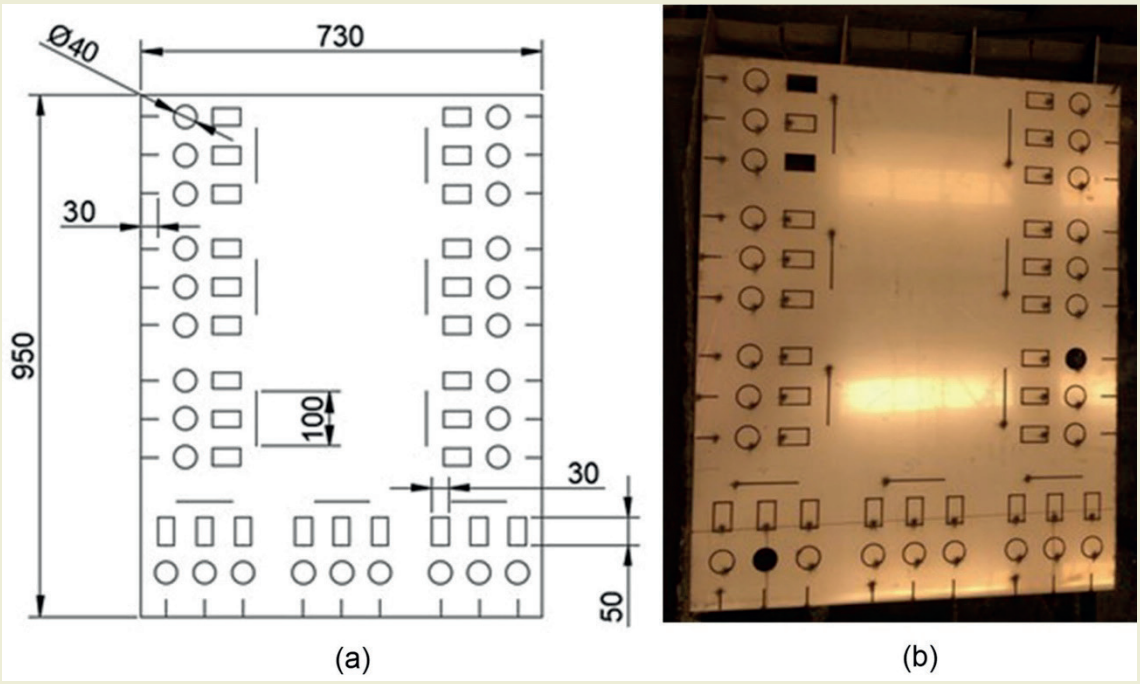

Figure 4. Geometries of the test samples: a) technical drawing and b) processed state with PAC [49]

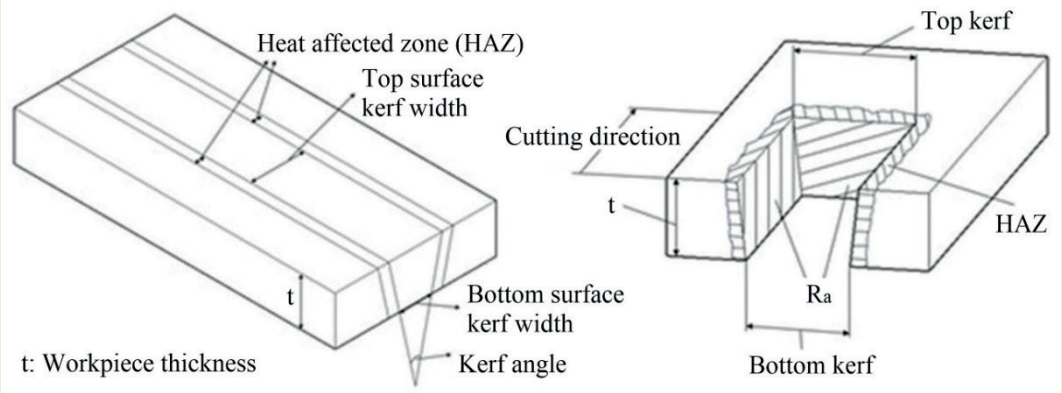

Figure 5. The schematic representation of the kerf taper angle

2.1. Calculation of Average Cutting Width (Kerf) Taper Angle

After cutting AISI304 sheets with thicknesses of 4 and 8 mm with PAC to create 54 straight lines of 30 mm length (▶**Figure 5**) using different experiment conditions (E1-E9), measurements were taken from 3 different areas (start-middle-end) of the lower and upper edges of the straight lines with the help of a digital calliper (GFB brand, 1/100 precision). The average cutting width taper angles were calculated by taking the arithmetic averages of the measurements with the help of E.1 [11].

$$The\ avg.kerf\ taper\ angle = \frac{(Avg.top\ margin - Avg.bottom\ margin) \times 180}{Workpiece\ thickness \times 2\pi} \quad (E.1)$$

2.2. Cutting Surface Roughness Measurements

AISI304 sheets with thicknesses of 4 and 8 mm were cut into rectangular shapes of 30x50 mm dimensions with PAC with different experiment conditions (E1-E9). Then, with the help of the MarSurf PS1 surface roughness measuring device shown in ▶**Figure 6**, measurements were taken from three different points from the 4 side cutting surfaces of each sample (a total of 12 different measurements for each sample) and the average R_a values were found by calculating the arithmetic mean. The measuring needle of the device used has a diameter of 2 µm, the pressure force is 0.7 mN and the measurement scan length is 5.6 mm. In surface roughness measurements, the sampling length was selected as 0.8 mm and the measurement length as 2.5 mm, taking Bozdemir's work [50] as reference.

2.3. Investigation of the Bottom Surface Burr Formation and the Top Surface Spatter Formation

100 mm length cutting was performed on 4 and 8 mm thick AISI304 sheets using experiment conditions (E1-E9) created with different machining parameters. During the cutting process (18 lines in total), burr and spatter formations on the bottom and top surfaces of the lines were visually examined and interpreted.

3. Results and Discussions

3.1. Kerf Taper Angle Measurement Results

It was observed that the upper and lower edges of the 30 mm long lines cut with different experiment conditions had different widths compared to each other. This situation is an inevitable result of the PAC method. In the PAC method, if the cutting speed is not adjusted to the appropriate value according to the material thickness, the desired tolerance for the kerf taper cannot be achieved. A total of 54 lines of 30 mm length cut from the plate of both thicknesses were used to calculate the average kerf taper angles using Equation 1. As seen in the graph in ▶**Figure 7**, the kerf taper angle increases as the cutting speed increases at constant pressure values in the machining of both 4 mm and 8 mm plates. When the cutting speed is constant, as the gas pressure value increases, the kerf taper angle value increases similarly. When the processes carried out under the same experimental conditions (E1-E9) were compared, it was determined that the kerf taper was greater in the 8 mm thick plate. Considering Equation 1, under normal

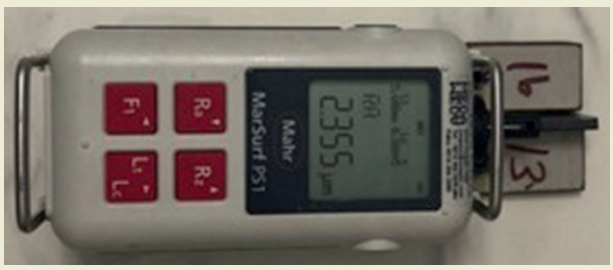

Figure 6. MarSurf PS1 surface roughness measuring device

conditions, the kerf taper angles in 8 mm thick plates should be smaller due to the thicker material, but larger values were obtained. This finding was unexpected, and it was concluded that the reason for this situation was the fixed torch-to-workpiece distance (1 mm). Also, this constant parameter was thought to be insufficient for cutting an 8 mm plate. With this determination, it was concluded that the amount of thermal energy generated with the initially determined machining parameters was insufficient for the 8 mm plate and therefore the taper tolerance control could not be provided during cutting. In the cutting process (E1) performed with a gas pressure of 0.6 MPa and a cutting speed of 151 mm/min, the lowest average kerf taper value (0.32 °) was obtained on the 4 mm thick plate. In the E9 experiment condition where the gas pressure was 0.8 MPa and the cutting speed was 217 mm/min, the highest average kerf taper value (2.59 °) was obtained on the 8 mm thick plate. When the PAC experiments carried out with the experiment conditions of E1-E4-E7, E2-E5-E8 and E3-E6-E9 in both thicknesses were compared, it was concluded that the cutting speed is a more effective machining parameter than the gas pressure for the average kerf taper.

In the study of Gostimirovic et al. [25], a larger kerf angle and a smaller kerf width were obtained by increasing the cutting speed while the gas pressure was constant. This determination obtained for the cutting speed when the gas pressure is constant from the study of Gostimirovic et al. is parallel to our experimental study. When ▶**Figure 7** is examined again, the kerf angle values increase when the cutting speed increases at constant gas pressure in both thicknesses of the plate. In the study of Begic et al. [38], it was concluded that the kerf angle decreased in experiments where the cutting speed was constant, and the gas pressure increased. In this context, the result of the kerf angle decreasing with the increase in gas pressure when the cutting speed is constant in the study of Begic et al. contrasts with this study. Also, as seen in ▶**Figure 7**, kerf taper angles increase with increasing gas pressure while the cutting speed is constant.

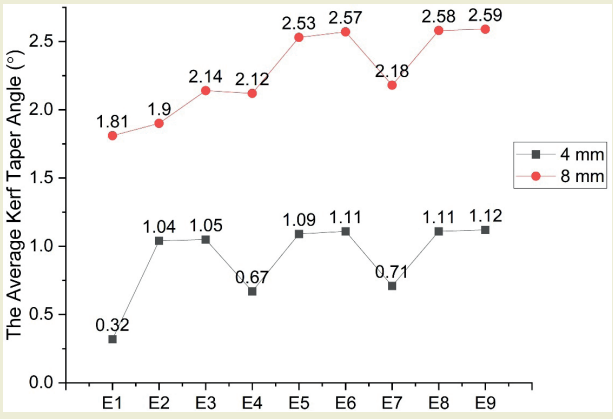

Figure 7. The average kerf taper angle values of lines cut on 4- and 8-mm thick plates

3.2. Roughness Measurement Results of Cutting Surfaces

In the machining of both plates, as the cutting speed increases at constant pressure values, the cutting surface roughness values increase (▶**Figure 8**). When the cutting speed is constant, R_a decreases as the gas pressure value increases. As the experiments carried out under the same experiment conditions on 4- and 8-mm thick plates were compared, rougher surfaces were observed on the 8 mm thick plate. As clearly seen in ▶**Figure 8**, the lowest surface roughness value (R_a = 24.12 µm) was obtained on the 4 mm thick plate in the cutting operation (E7) performed at a gas pressure of 0.8 MPa and a cutting speed of 217 mm/min. Moreover, in the E3 experiment condition where the gas pressure was 0.6 MPa and the cutting speed was 217 mm/min, the roughest surface was encountered on the 8 mm thick plate and the surface roughness value was obtained as (R_a = 31.65µm). As the PAC tests performed on the plates of both thicknesses in the E1-E4-E7, E2-E5-E8 and E3-E6-E9 experiment conditions were compared, it was concluded that gas pressure is a more effective parameter for R_a than cutting speed.

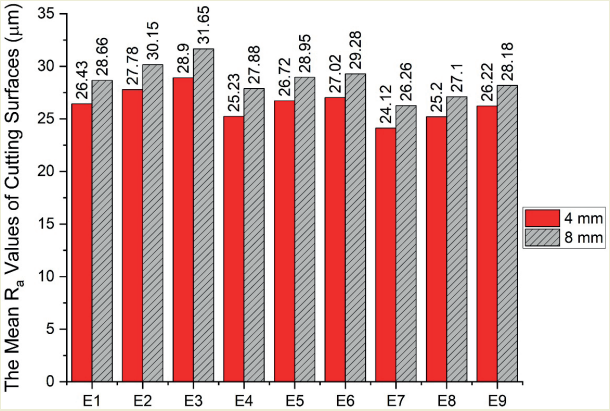

Figure 8. The mean R_a values of cutting surfaces of samples cut from 4 and 8 mm thick plates

With this study, many studies in the literature were identified in which similar results were obtained in terms of surface roughness values. For example, Bhowmick et al [8]. reported that gas pressure is the most effective parameter in terms of surface roughness. They concluded that with the increase of gas pressure, less roughness is encountered on the cutting surface. So, this finding is parallel to our experimental study. While the nozzle diameter used in the study conducted by Bhowmick et al. was 1.4 mm, the nozzle diameter used in our study was preferred as 1.2 mm. Since the nozzle diameter is narrower, the plasma arc is focused in a smaller area, which causes the melting process to occur relatively less. For this reason, although the same workpiece and the same machining parameters were used in both studies, larger surface roughness values were obtained in our study. In addition, it was concluded that another effect causing the difference between these two studies in terms of surface

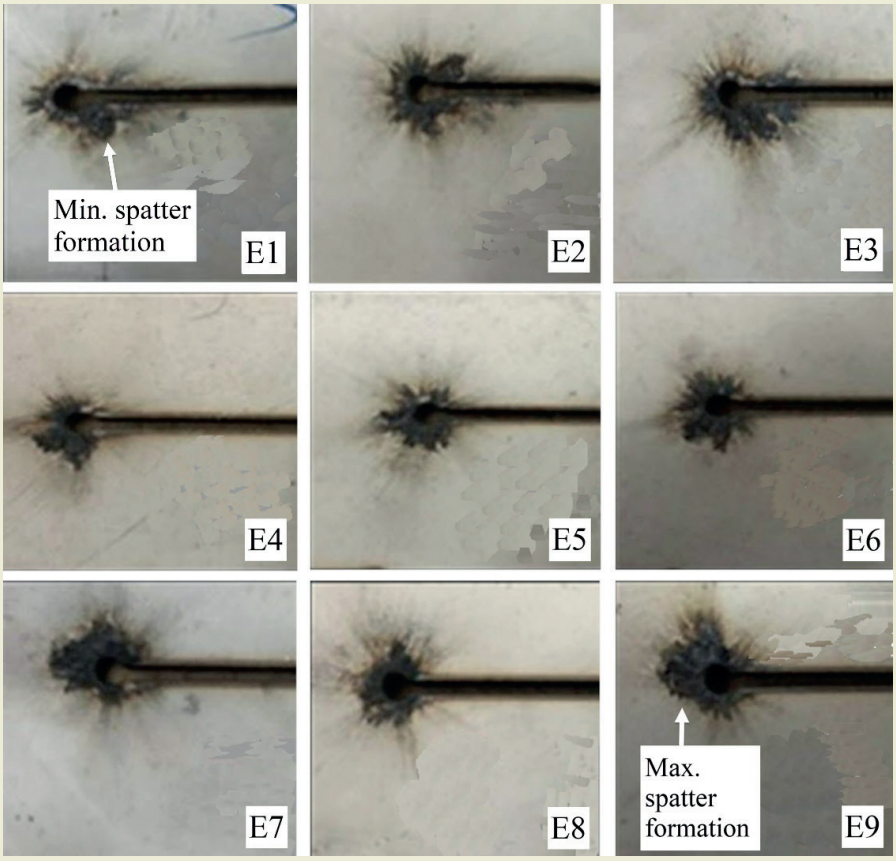

Figure 9. Top surface spatter formation after cutting on a 4 mm thick plate

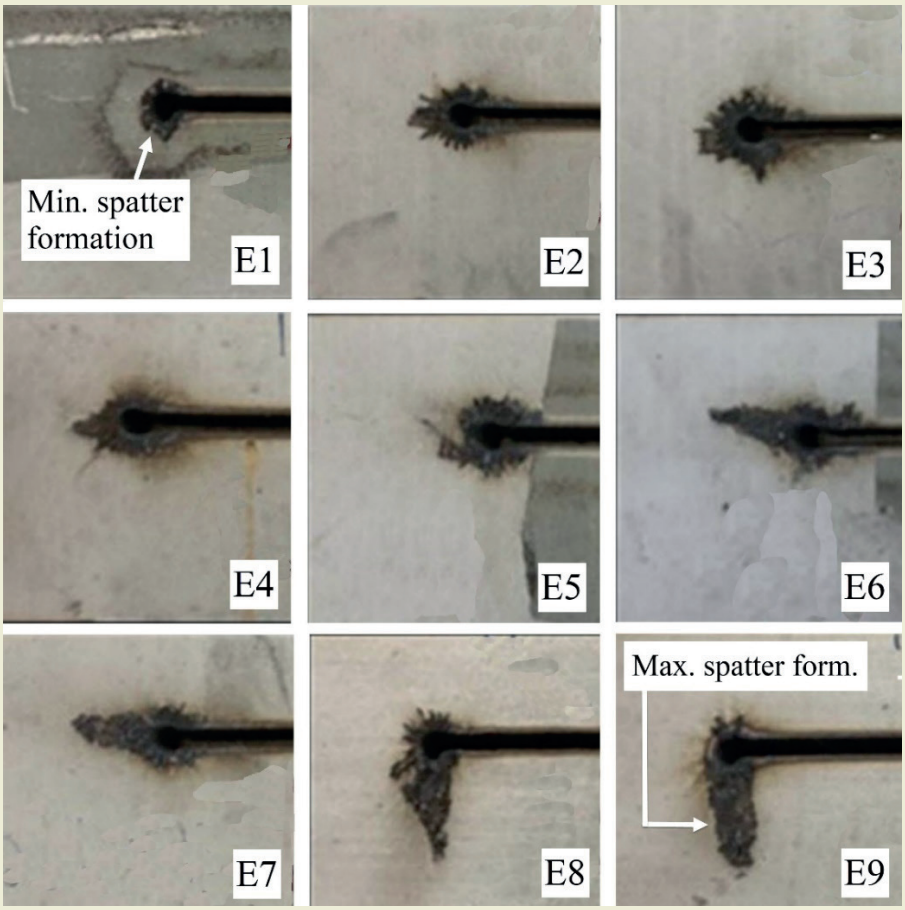

Figure 10. Top surface spatter formation after cutting on 8 mm thick plate

roughness was the electrical parameters. In our study, 80 A cutting current and 120 V open circuit voltage were used, while in the study of Bhowmick et al., 100 A cutting current and 300 V voltage were used. As can be understood from this point, Bhowmicks et al. obtained cutting surfaces with relatively lower rough surfaces than our surfaces by using high energy input (100 A and 300 V) at high cutting speed (417 mm/min). Because, with high energy input at high cutting speed, the molten metal was not allowed to solidify on the surface again. Thus, it is thought that by this mechanism they obtain lower surface roughness values.

Guatam et al. [14] reported that they obtained fewer rough surfaces at high gas pressure and low cutting speed. However, our study is fundamentally in contrast to the results of Das et al.'s study [18], which showed that a smoother and less rough surface was obtained in the experiment conducted at low gas pressure. Chamarthi et al. [19] also reported that they obtained smoother surfaces by reducing the cutting speed. Skoczylas et al. [20] observed that the roughness would increase with increasing cutting speed and decrease with increasing gas pressure. Both of their findings are clearly parallel to this study. Hatala et al. [21] stated that gas pressure has the greatest effect on surface roughness, considering this result, it can be said that their study is parallel to this study. Similarly, Gostimirovic et al. [25] reported that surface roughness increased with increasing cutting speed. Masoudi et al. [31] reported that they encountered the smoothest surface at low cutting speed and average gas pressure. In common, Adalarsan et al. [36] concluded that surface roughness decreases with increasing gas pressure. Likewise, Kim et al. [37] observed that surface roughness increased with increasing cutting speed.

Our study and the vast majority of studies in the literature show that surface roughness decreases as gas pressure increases and also that surface roughness increases as cutting speed increases. It is evaluated that when the plasma gas pressure increases at a constant cutting speed, shock waves will be formed due to the increase in the amount of gas transferred to the cutting zone per unit time, and the surface roughness will decrease because the resulting shock waves increase the molten metal flow rate and move away from the machining zone rapidly without allowing it to resolidify on the surface. Surface roughness increases when the cutting speed increases at constant plasma gas pressure. It is thought that the reason for this situation is the molten metal cools rapidly and resolidifies irregularly on the surface before the spraying operation is completed due to the fast movement of the torch.

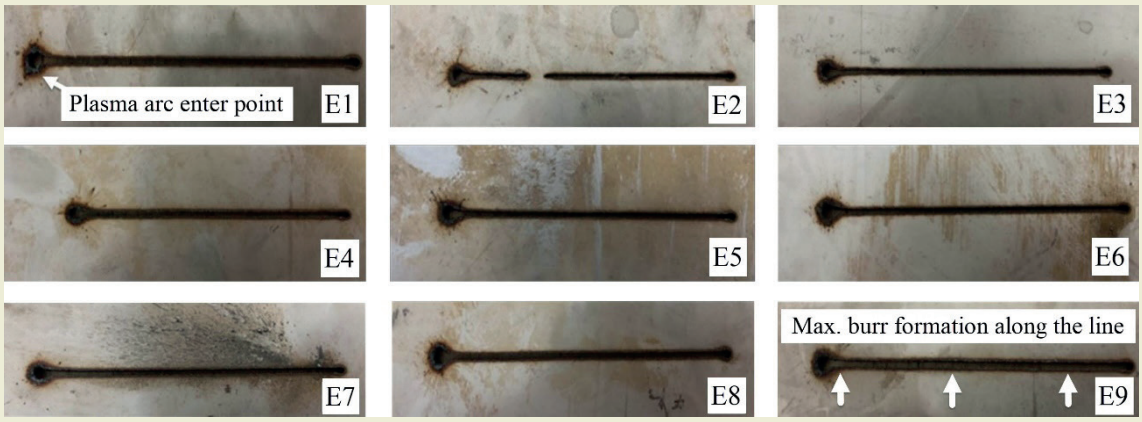

Figure 11. Bottom surface burr formation after cutting on a 4 mm thick plate

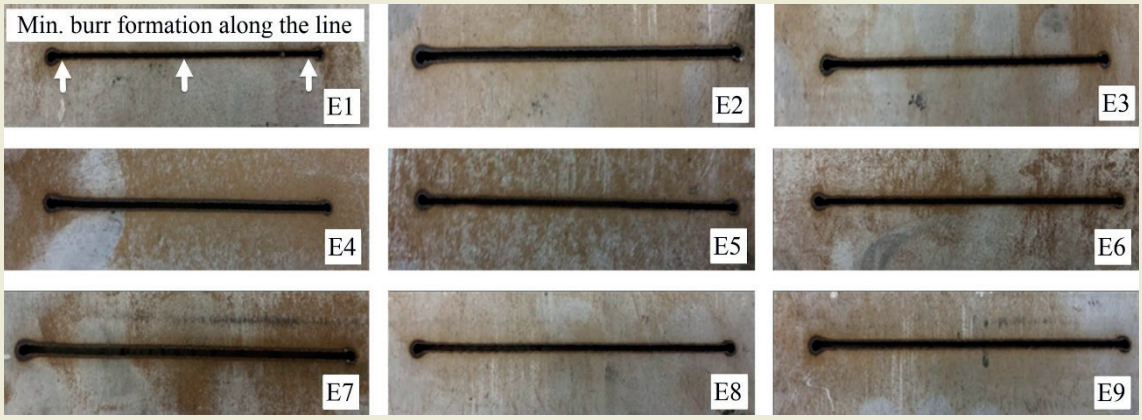

Figure 12. Bottom surface burr formation after cutting on a 8 mm thick plate

3.3. Results of Investigation of Bottom Surface Burr Formation and Top Surface Spatter Formation

When ▶Figure 9 and ▶Figure 10 are examined separately for both plate thicknesses, it is seen that top surface spatter formation relatively increases as the gas pressure is kept constant and the cutting speed increases (E1-E2-E3), (E4-E5-E6), (E7-E8-E9) and as the cutting speed is kept constant and the gas pressure increases (E1-E4-E7), (E2-E5-E8), (E3-E6-E9). The highest surface spatter formation in both plates was observed in the E9 processing type, which has the highest cutting speed and highest gas pressure. When the plates were compared with each other for the same experiment conditions, it was determined that the top surface spatter formation in the plates with 8 mm thickness was more and thicker.

When ▶Figure 11 and ▶Figure 12 are examined, it can be said that the bottom surface burr formation increases relatively as the gas pressure is kept constant and the cutting speed increases in 4 mm thick plates. It was found that when the cutting speed was kept constant and the gas pressure was increased, the bottom surface burr formation increased similarly to the top surface spatter formation. As the plates with both thicknesses were compared in the same experiment conditions, very small and less bottom surface burr formation was observed in the plate with 8 mm thickness compared to the plate with 4 mm thickness (▶Figure 12). According to the visual inspection for burr and spatter formations, it was concluded that the cutting lines in PAC processes were at an acceptable level in terms of burr and spatter formations. In this context, it was determined that lines along the cutting line were generally smooth in each experiment condition, except for the first entry and exit points of the plasma in the PAC process.

In the study of Ilii et al. [15], like our study, it was found that more intense burr and spatter formation occurred when the cutting speed was increased in the machining of plates of the same thickness with PAC. In addition, in the study of Ilii et al., it was determined that burr and spatter formations increased with increasing workpiece thickness in experiments carried out on workpieces with different thickness values at the same cutting speed. The increase in burr and spatter formation with increasing material thickness is not consistent with the results of our study.

4. Conclusions

This study has the feature of shedding light on industrial applications with the experimental data obtained. As a result of comprehensive research on key parameters (gas pressure and cutting speed), it can provide a reference for cutting austenitic steels used in industry with PAC. As a general result, it was found that machining parameters such as cutting speed, gas pressure, torch-to-workpiece distance and electrical parameters (voltage and current) directly affect output performances such as kerf taper and cutting surface roughness.

According to our experimental results, in the machining of both 4- and 8-mm AISI304 plates, the kerf taper increases as the cutting speed increases at constant pressure values. When the cutting speed is constant, as the gas pressure value increases, the cutting gap taper value increases similarly. In the machining of both plates, as the cutting speed increases at constant pressure values, the cutting surface roughness values increase. While the cutting speed is constant, the surface roughness decreases as the gas pressure value increases. For both plate thicknesses, it was observed that top surface spatter formation increased relatively as the gas pressure was kept constant and the cutting speed increased, and the cutting speed was kept constant and the gas pressure increased. As the plates with both thicknesses were compared in the same experiment conditions, very small and less bottom surface burr formation was observed in the plate with 8 mm thickness compared to the plate with 4 mm thickness. These findings emphasize the importance of considering the machining parameters before PAC operation and the appropriate machining parameters should be considered together according to the desired output performance.

Research Ethics

Ethical approval not required.

Author Contributions

Conceptualization: [Şerafettin Hırtıslı and Oğuz Erdem], Methodology: [Şerafettin Hırtıslı and Oğuz Erdem], Formal Analysis: [Şerafettin Hırtıslı and Oğuz Erdem], Investigation: [Şerafettin Hırtıslı and Oğuz Erdem], Resources: [Şerafettin Hırtıslı and Oğuz Erdem], Data Curation: [Şerafettin Hırtıslı and Oğuz Erdem], Writing – Original Draft Preparation: [Şerafettin Hırtıslı and Oğuz Erdem], Writing – Review & Editing: [Oğuz Erdem], Visualization: [Oğuz Erdem], Supervision: [Oğuz Erdem].

Competing Interests

The authors declare that there is no conflict of interest regarding the publication of this paper.

Research Funding

Not reported.

Data Availability

Not applicable.

Orcid

Şerafettin Hırtıslı https://orcid.org/0000-0001-6924-2583
Oğuz Erdem https://orcid.org/0000-0002-8094-3222

5. References

[1] Bini, R., Colosimo, B. M., Kutlu, A. E., & Monno, M. (2008). Experimental study of the features of the kerf generated by a 200 A high tolerance plasma arc cutting system. *Journal of Materials Processing Technology, 196*(1-3): 345-355. https://doi.org/10.1016/j.jmatprotec.2007.05.061

[2] Kavka, T., Chumak, O., Šonský, J., Heinrich, M., Stehrer, T., & Pauser, H. (2013). Experimental study of anode processes in plasma arc cutting. *Journal of Physics D: Applied Physics, 46*(6): 1-11. doi:10.1088/0022-3727/46/6/065202

[3] Colombo, V., Concetti, A., Ghedini, E., Rotundo, F., Sanibondi, P., Boselli, M., Dallavalle, S., Nemchinsky, V. & Vancini, M. (2012). Advances in plasma arc cutting technology: the experimental part of an integrated approach. *Plasma Chemistry and Plasma Processing*, 32: 411-426. doi:10.1007/s11090-011-9338-8

[4] Cinar, Z., Asmael, M., & Zeeshan, Q. (2018). Developments in plasma arc cutting (PAC) of steel alloys: a review. *Jurnal Kejuruteraan, 30*(1): 1-6. https://doi.org/10.17576/jkukm-2018-30(1)

[5] Silvia, F. P., Bogdan-Ciprian, P., & Cornel, C. (2012). Plasma arc cutting-overview. 2nd International Conference on Quality and Innovation in Engineering and Management, 357-360.

[6] Kutlu, A. E., Monno, M., & Bini, R. (2005). Plazma ile kesme metoduna genel bir bakış. *Mühendis ve Makina, 46*(541): 21-29.

[7] Yalçın, H. & Gürü, M. (2002). *Malzeme Bilgisi*. Palme Yayıncılık, Ankara.

[8] Bhowmick, S., Basu, J., Majumdar, G., & Bandyopadhyay, A. (2018). Experimental study of plasma arc cutting of AISI 304 stainless steel. *Materials Today: Proceedings, 5*(2): 4541-4550. https://doi.org/10.1016/j.matpr.2017.12.024

[9] Çelik, Y. H., & Özek, C. (2011). CNC Plazma ile kesmede işleme parametrelerinin kesme kalitesine etkisinin araştırılması. 6th International Advanced Technologies Symposium (IATS'11), 65-70.

[10] Tsiolikas, A., Kechagias, J., Salonitis, K., & Mastorakis, N. (2016). Optimization of cut surface quality during CNC Plasma Arc Cutting process. *International Journal of Systems Applications, Engineering & Development*, 10: 305-308.

[11] Patel, P., Nakum, B., Abhishek, K., Kumar, V. R., & Kumar, A. (2018). Optimization of surface roughness in plasma arc cutting of AISID2 steel using TLBO. *Materials Today: Proceedings, 5*(9): 18927-18932. https://doi.org/10.1016/j.matpr.2018.06.242

[12] Bhuvenesh, R., Norizaman, M. H., & Manan, M. S. (2012). Surface roughness and MRR effect on manual plasma arc cutting machining. *International Journal of Industrial and Manufacturing Engineering*, 6: 131-134.

[13] Parthiban, A., Prasath, J. P., Vivek, P., & Pugazhenthi, R. (2018). Experimental investigation of plasma arc cutting for stainless steel sheet. *International Journal of Mechanical and Production Engineering Research and Development, 8*(1): 907-914.

[14] Gautam, P. K. & Gupta, V. (2019). Analysis of process parameters of plasma arc cutting using design of experiment. *International Research Journal of Engineering and Technology (IRJET)*, 6: 2733-2742.

[15] Ilii, S. M., Coteata, M., & Munteanu, A. (2010). Experimental results concerning the variation of surface roughness parameter (Ra) at plasma arc cutting of a stainless steel workpiece. *International Journal of Modern Manufacturing Technologies, 2*(1): 31-36.

[16] Rana, K., Kaushik, P., & Chaudhary, S. (2013). Optimization of plasma arc cutting by applying Taguchi Method. *International Journal of Enhanced Research in Science Technology & Engineering, 2*(7): 106-110.

[17] Hamid, A., Novareza, O., & Widodo, T. D. (2019). Optimization of process parameters and quality results using plasma arc cutting in aluminum alloy. *Journal of Engineering and Management in Industrial System (JEMIS), 7*(1): 7-14. doi:ub.jemis.2019.007.01.2

[18] Das, M. K., Kumar, K., Barman, T. K., & Sahoo, P. (2014). Optimization of MRR and surface roughness in PAC of EN 31 steel using weighted principal component analysis. *Procedia Technology, 14*: 211-218. https://doi.org/10.1016/j.protcy.2014.08.028

[19] Chamarthi, S., Reddy, N. S., Elipey, M. K., & Reddy, D. R. (2013). Investigation analysis of plasma arc cutting parameters on the unevenness surface of Hardox-400 material. *Procedia Engineering, 64*: 854-861. https://doi.org/10.1016/j.proeng.2013.09.161

[20] Skoczylas, A. & Zaleski, K. (2015). Effect of plasma cutting parameters upon shapes of bearing curve of C45 steel surface. *Advances in Science and Technology Research Journal, 9*(27): 78-82. https://doi.org/10.12913/22998624/59088

[21] Hatala, M., Zajac, J., Čep, R., & Orlovský, I. (2012). Research of the technological parameters importance for plasma arc thermal cutting. *Applied Mechanics and Materials, 110*: 3742-3749. https://doi.org/10.4028/www.scientific.net/AMM.110-116.3742

[22] Chiarelli, M., Lanciotti, A., & Sacchi, M. (2000). Effect of plasma cutting on the fatigue resistance of Fe510 D1 steel. *Journal of Engineering Materials and Technology, 122*(1): 141-145. https://doi.org/10.1115/1.482778

[23] Radovanovic, M. & Madic, M. (2011). Modeling the plasma arc cutting process using ANN. *Nonconventional Technologies Review, 4*: 43-48.

[24] Hoult, A. P., Pashby, I. R., & Chan, K. (1995). Fine plasma cutting of advanced aerospace materials. *Journal of Materials Processing Technology, 48*(1-4): 825-831. https://doi.org/10.1016/0924-0136(94)01727-I

[25] Gostimirović, M., Rodić, D., Sekulić, M., & Aleksić, A. (2020). An experimental analysis of cutting quality in plasma arc machining. *Advanced Technologies and Materials, 45*(1): 1-8. doi:10.24867/ATM-2020-1-001

[26] Singh, G. & Akhai, S. (2015). Experimental study and optimisation of MRR in CNC plasma arc cutting. *International Journal of Engineering Research and Applications, 5*(6): 96-99.

[27] Suresh, A. & Diwakar, G. (2021). Optimization of process parameters in plasma arc cutting for TWIP steel plates. *Materials Today: Proceedings, 38*(5): 2417-2424. https://doi.org/10.1016/j.matpr.2020.07.383

[28] Iida, K., Takenaka, Y., Uesugi, Y., Tanaka, Y., Ishijima, T., Nakano, Y., Yamaguchi, Y., & Takata, N. (2020). Observation system of molten steel behavior on plasma arc cutting surface. *IEEJ Transactions on Electrical and Electronic Engineering, 15*(5): 796-801. https://doi.org/10.1002/tee.23119

[29] Naik, D. K. & Maity, K. (2020). Experimental analysis of the effect of gas flow rate and nature on plasma arc cutting of hardox-400. *Welding in the World, 64*: 345-352. https://doi.org/10.1007/s40194-019-00836-8

[30] Ferreira, P., Melo, I., Coelho, A. G., & Mourão, A. (2009). Plasma cutting optimization by using the response surface methodology. International Conference NEWTECH 2009-Annals of "Dunarea de Jos" University of Galati, Fascicle V, Technologies in machine building, 213-218.

[31] Masoudi, S., Mirabdolahi, M., Dayyani, M., Jafarian, F., Vafadar, A., & Dorali, M. R. (2019). Development of an intelligent model to optimize heat-affected zone, kerf, and roughness in 309 stainless steel plasma cutting by using experimental results. *Materials and Manufacturing Processes, 34*(3): 345-356. https://doi.org/10.1080/10426914.2018.1532579

[32] Sharma, S., Gupta, M., Kumar, R., & Bindra, N. S. (2017). Experimental analysis and optimization of process parameters in plasma arc cutting machine of EN-45A material using Taguchi and ANOVA method. *International Journal of Mechanical and Industrial Engineering, 11*(7): 1387-1391.

[33] Sandeep, R., Sudhakara, D., & Sreenivasulu, B. (2015). Multi objective optimization of process parameters in plasma arc cutting of SS 420 using Grey-Taguchi analysis. *International Journal of Advanced Engineering Research and Science (IJAERS), 2*: 46-52.

[34] Muhamedagic, K., Begic-Hajdarevic, D., Pasic, M., & Cekic, A. (2018). Optimization of process parameters in plasma arc cutting using TOPSIS method. 29th DAAAM International Symposium on Intelligent Manufacturing and Automation, 202-209.

[35] Hamood, S. A. & Najm, V. N. (2020). Optimization of plasma cutting parameters on dimensional accuracy and machining time for low carbon steel. *Engineering and Technology Journal*, *38*(8A): 1160-1168. https://doi.org/10.30684/etj.v38i8A.1151

[36] Adalarasan, R., Santhanakumar, M., & Rajmohan, M. (2015). Application of Grey Taguchi-based response surface methodology (GT-RSM) for optimizing the plasma arc cutting parameters of 304L stainless steel. *The International Journal of Advanced Manufacturing Technology*, *78*: 1161-1170. doi: 10.1007/s00170-014-6744-0

[37] Kim, S. I. & Kim, M. H. (2013). Evaluation of cutting characterization in plasma cutting of thick steel ship plates. *International Journal of Precision Engineering and Manufacturing*, *14*: 1571-1575. doi: 10.1007/s12541-013-0212-x

[38] Begic, D., Kulenovic, M., Cekic, A., & Dedic, E. (2012). Some experimental studies on plasma cutting quality of low alloy steel. 23rd International DAAAM Symposium, 183-186.

[39] Peko, I., Nedić, B., Đorđević, A., & Veža, I. (2018). Modelling of kerf width in plasma jet metal cutting process using ANN approach. *Tehnički vjesnik*, *25*(2): 401-406. https://doi.org/10.17559/TV-20161024093323

[40] Kountouras, D., Papanikolaou, S., Intzevidou, P., Kechagias, J., & Maropoulos, S. (2014). The Influence of micro structural aspects on a parameter design of carbon steel plate CNC plasma arc-cutting. *Scientific Works of University of Food Technologies*, *61*: 790-796.

[41] Zajac, A. & Pfeifer, T. (2006). Restricting the heat-affected zone during the plasma cutting of high-alloy steels. *Welding international*, *20*(1): 5-9. https://doi.org/10.1533/wint.2006.3534

[42] Liu, P., Liu, Y., Zheng, C., Wang, Q., & Qin, Z. (2024). Underwater plasma arc cutting process of oil casing in shallow. *Applied Ocean Research*, *153*: 1-16. https://doi.org/10.1016/j.apor.2024.104302

[43] Tuladhar, U., Ahn, S. H., Jeong, G. H., Bae, J., Kim, S., Kang, J., Cho, D. W., & Ahn, S. (2024). Numerical analysis and Schlieren visualization of gas flow dynamics inside the plasma arc cut kerf with curved cutting fronts. *International Communications in Heat and Mass Transfer*, *159*: 1-14. https://doi.org/10.1016/j.icheatmasstransfer.2024.108075

[44] Sidorov, E. A., Grinenko, A. V., Chumaevskii, A. V., Rubtsov, V. E., Nikolaeva, A. V., Panfilov, A. O., Knyazhev, E. O., Cheremnov, A. M., Utyaganova, V. R., Osipovich, K. S., Gurianov, D. A., & Kolubaev, E. A. (2024). Surface structure formation in plasma cutting of aluminum and titanium alloys using direct current straight and reverse polarity. *Physical Mesomechanics*, *27*(5): 518-528. doi: 10.1134/S1029959924050023.

[45] Grinenko, A. V., Chumaevskii, A. V., Knjazhev, E. O., Gurianov, D. A., Sidorov, E. A., & Kolubaev, E. A. (2024). Reverse-polarity plasma cutting of thick aluminum alloy plates. *Russian Physics Journal*, *67*(9): 1309-1315. doi: 10.1007/s11182-024-03249-3.

[46] Tuladhar, U., Ahn, S. H., Cho, D. W., Ahn, S., Kim, D. H., Bae, S. H., Kim, S., Park, T. K., & Kang, J. (2024). Experimental investigation of plasma arc cutting process to evaluate the characteristics of kerf geometry using ANOVA. *Journal of Mechanical Science and Technology*, *38*(7): 3641-3655. doi: 10.1007/s12206-024-0637-4.

[47] Liu, X., Wang, Z., Wu, J., & Tian, J. (2024). Three-dimensional numerical simulation of magnetically confined plasma cutting arc. *The International Journal of Advanced Manufacturing Technology*, *133*: 2419-2433. https://doi.org/10.1007/s00170-024-13828-w

[48] Hussain, S., Qazi, M. I., & Abas, M. (2024). Investigation and optimization of plasma arc cutting process parameters for AISI 304 by integrating principal component analysis and composite desirability method. *Journal of the Brazilian Society of Mechanical Sciences and Engineering*, *46*(33): 1-16. https://doi.org/10.1007/s40430-023-04614-y

[49] Hirtisli, S., Erdem, O. (2023). The effects of machining parameters on circularity tolerance in plasma arc cutting method. 7th International Symposium on Multidisciplinary Studies and Innovative Technologies (ISMSIT), 1-6.

[50] Bozdemir, M. (2018). Prediction of surface roughness considering cutting parameters and humidity condition in end milling of polyamide materials. *Computational Intelligence and Neuroscience*, *1*: 1-7. doi:10.1155/2018/5850432

EUROPEAN MECHANICAL SCIENCE

Research Article

e-ISSN: 2587-1110

Hydraulic fault detection of wind turbine generators using artificial neural networks

Tacettin Ahmet Döndüren[1], **Mustafa Yağcı**[2*]

[1]Institute of Science, Necmettin Erbakan University, Konya, Türkiye
[2]Department of Electrical and Electronics Engineering, Necmettin Erbakan University, Konya, Türkiye

Abstract: In the current context where fossil resources are diminishing globally, and carbon emissions are increasing daily, the importance of green energy, particularly wind energy, is growing significantly. The increasing of wind turbines will not only reduce the carbon footprint but also decrease dependence on external resources. To increase the installed capacity of wind turbines, it is crucial to reduce not only installation costs but also operational costs. The largest proportion of operational costs is service, and maintenance costs. One of the most critical approaches to reducing service, and maintenance costs is preventive maintenance activities. The objective of preventive maintenance activities is to minimize or ideally eliminate production losses through scheduled turbine shutdowns before failures occur. In this study, artificial neural network-based algorithms that predict potential hydraulic failures during the operational period were utilized. For this purpose, data from the turbine SCADA system over a period of two years, considering the equipment, and sensors connected to hydraulic systems, were compiled. The study was conducted using the WEKA program, comparing Multilayer Perceptron (MLP), Radial Basis Function Classifier (RBF Classifier), SMOreg (Support Vector Machines for Regression) algorithms. Result of the study, the MLP algorithm was applied with a percentage split of 66% for training, and 33% for testing, achieving a prediction accuracy of 96.32%

Keywords: Artificial Neural Networks, Faults Detection, Predictive Maintenance, WEKA, Wind Turbine

1. Introduction

Since wind energy is one of the most important sources of clean energy, it has gained global support in recent years. Renewable resources are utilized to reduce the carbon footprint, and achieve carbon neutrality. Wind turbines are often exposed to harsh environmental conditions because they are typically installed in remote areas, far from residential zones. Consequently, wind turbines frequently experience malfunctions. The most common malfunctions include electrical failures, control system issues, and sensor defects. Under these conditions, fault diagnosis in wind turbines is crucial in terms of operational, and maintenance costs. Moreover, timely fault diagnosis, and maintenance can significantly reduce major financial losses. To minimize turbine downtime, lower operational, and maintenance expenses, and extend service life, machine learning-based fault diagnosis is recommended.

In this study, the hydraulic failures of a wind power plant located in Konya between 2020, and 2022 were analyzed. The variables considered for failure included hydraulic oil temperature, wind speed, hydraulic unit pressure, yaw brake pressure, internal ambient temperature, external ambient temperature, active power data, and blade angles. Additionally, the fundamental characteristics of artificial neural networks (ANN) were discussed, and a model capable of predicting hydraulic failures using ANN was developed, and its performance evaluated.

1.1. Fundamental Components and Failures of Wind Turbines

Wind turbines primarily consist of a gearbox, generator, converter, yaw systems, pitch systems, hydraulic systems, control systems, and auxiliary systems. Experts, and researchers recommend conducting failure analysis

*Corresponding author:
Email: myagci@erbakan.edu.tr

Cite this article as:
Döndüren, A. T., Yağcı, M. (2024). Hydraulic fault detection of wind turbine generators using artificial neural networks. *European Mechanical Science*, *8*(4): 331-340. https://doi.org/10.26701/ems.1577643

History dates:
Received: 04.11.2024, *Revision Request*: 27.11.2024, *Last Revision Received*: 03.12.2024, *Accepted*: 19.12.2024

on various components such as power systems, mechanical systems, drive systems, generators, and gearboxes, as these are the most studied for efficient fault diagnosis. Data-driven real-time fault diagnosis is performed using data mining technologies in wind turbines. By observing useful data, and classifying the system as either faulty or normal conditions. The SCADA system contains both real-time data, and recorded historical [1].

Real-time monitoring of wind turbine conditions allows for overcoming these defects. Through turbine condition monitoring technology, parameters such as vibration, temperature, pressure, and electrical data tracks. Comparing these results with predefined optimal values enables the early detection of electrical, and mechanical failures [2].

1.2. Artificial Neural Networks and Their General Characteristics

Artificial Neural Networks (ANN) were first developed by Rosenblatt under the name "perception." The purpose of ANN is to ensure accurate classification of data by determining optimal parameter values. After each iteration (epoch), the error rate is updated, and these rates are distributed across the weight parameters, allowing the values assigned to each node to be refreshed [3].

ANN is a machine learning method inspired by the structure of biological neurons. In the input layer of the network, the input values are defined, and the data then passes through multiple layers. The data moves through various nodes, referred to as neurons, in each layer, where its numerical value is calculated, and compared with the previous value. The goal of this comparison is to minimize the difference, aiming to bring the error closer to zero, thereby enabling the network to learn. The performance of the network is measured using accuracy functions. Structurally, the network consists of three fundamental layers: an input layer, hidden layer, and an output layer.

Artificial neural networks (ANN) are mathematically composed of inputs, weights, a summation function, an activation function, and output layers. Inputs are the data provided for the network to learn. The weight value represents the multiplication of the input data by a factor. The magnitude of the weight does not indicate the importance of the data. The summation function is used to combine information from the inputs for computation. The activation function aids in determining the outputs. Activation functions such as Linear, Step, and Sigmoid are commonly used [4].

The Sigmoid function is the most widely used activation function, limiting the data between 0, and 1. The Tanh function, which restricts data between -1, and 1, often provides better performance than the Sigmoid function due to its directional change in processing [5].

By multiplying the inputs with the weights, the NET inputs are obtained. The term "NET" is an abbreviation for "Network." Various methods exist for calculating the NET value. The calculation using the summation method can be seen in the following equation [6].

$$NET = \sum_{i=1}^{n} x_i . w_i \tag{1}$$

From this, it can be understood that the data from the first to the nth value are multiplied by their respective weights, and summed to obtain the NET inputs. The X values represent the inputs, while w represents the weights. The same calculation method does not need to use throughout the entire ANN model. The NET value obtained in artificial neurons is then passed through the activation function. The activation function processes the NET value, and converts it into the output. Increasing the number of neurons in the hidden layer may make the ANN system more complex, but it also leads to better outputs [6].

Prediction studies using artificial neural networks have been applied across various fields in literature. One study, which aimed to predict solar radiation data using artificial neural networks, and machine learning, employed daily/hourly solar radiation data from the provinces of Bursa, and Çanakkale for the years 2015-2019. The study involved prediction using artificial neural networks, and classification analysis using a machine learning algorithm [4].

In a study aimed at predicting the production data of a solar power plant, the goal was to develop the plant's feasibility software. This study developed the Solar Power Plant Feasibility Software by predicting the production data of solar, and wind power plants, both renewable energy sources, based on meteorological, and geological data. To achieve production forecasting, advanced feed forward back propagation Artificial Neural Networks (ANN), the Adaptive Neuro-Fuzzy Inference System (ANFIS), and the deep learning model Long Short-Term Memory (LSTM) were employed, due to their success in predicting with nonlinear models, a key application of artificial intelligence [7].

Aiming to forecast wind speed, and guide planned operations, various artificial neural networks, and models were compared. In the study, short-term wind speed forecasting was performed using ANN methods with data obtained from a station in Yalova, Turkey. The analysis aimed to predict wind speed one hour ahead, allowing for interventions in sudden failures, and maintenance planning [8].

Additionally, a study was conducted on identifying, detecting, and locating faults in power transmission lines using ANN. In this study, feed forward neural networks, convolutional neural networks, and generalized regression neural networks were employed [9].

A comprehensive fault detection system for wind turbines is presented, utilizing sensors in the process. Specifically, the model is designed with a lightweight, highly efficient structure, and employs ensemble-based artificial neural networks, achieving a fault detection rate of 96.5%. The robustness of this model has been validated through various numerical simulations. Additionally, it has been compared with other methods,

and the operating model has been found to exhibit higher accuracy [10].

They have worked on artificial neural network-supported early fault detection for bearing failures in wind turbine generators. It is noted that gearbox failures cause significant downtime in wind turbines, and a large portion of these failures originate from gearbox bearings. Detecting wear, and degradation in gearbox bearings early would enable effective preventive maintenance, which in turn would reduce overall maintenance costs. In this study, a neural network-based monitoring system is proposed using data from the control, and data acquisition system. This application was implemented on 2 MW onshore turbines located in southern Sweden. The results demonstrate that the proposed neural network-based condition monitoring system is capable of detecting severe damage [11].

2. Materials and Methods

In this study, artificial neural network-based algorithms were used to predict potential hydraulic failures that may occur during operation. In this way, possible failures will be addressed during non-windy periods through preventive actions. The aim of preventive maintenance activities is to minimize or, if possible, eliminate production losses by performing turbine shutdowns before a failure occurs.

For this purpose, data from a two-year period was collected through the turbine SCADA system, taking into account the equipment, and sensors connected to the hydraulic systems. Sensors located in relevant areas on the turbine transmit data to the SCADA system via various communication protocols. Data related to the topic has been analyzed, and compiled in the SCADA system. The date, and time of hydraulic failures are recorded as fault logs in the SCADA system. The approach here involves creating datasets based on the assumption that the first 60 seconds before a failure is considered faulty, while the subsequent 60-second interval is considered fault-free.

2.1. Data Sources

Data from hydraulic failures occurring between 2020, and 2022 were used in the models. The variables considered include hydraulic oil temperature, wind speed, hydraulic unit pressure, yaw brake pressure, internal temperature, external temperature, production data, and blade angles. ▶**Table 1** provides a summary of the data included in the study, and their respective units.

2.2. Correctly Classified Examples and Confusion Matrix

Correctly classified examples: This is the percentage of the total number of examples that the model classifies correctly relative to the total dataset. It reflects the overall performance of the classification [12].

$$\text{Accuracy } (\%) = \frac{\text{TN} + \text{TP}}{\text{TN} + \text{TP} + \text{FN} + \text{FP}} \text{x100} \quad (2)$$

Confusion Matrix: A matrix that compiles information about actual, and predicted classifications. This can be seen following ▶**Table 2**.

Correctly classified data refers to the TN (True Negative), and TP (True Positive) components. The performance of the model is proportional to the number of correctly classified data, and indicates the effectiveness of the classification [13]. The terms used in the confusion matrix are defined as follows:

TN (True Negative): The number of correct predictions where an example is truly negative.

FP (False Positive): The number of incorrect predictions where an example is predicted to be positive.

FN (False Negative): The number of incorrect predictions where an example is predicted to be negative.

TP (True Positive): The number of correct predictions where an example is truly positive.

2.3. Classification Accuracy, Sensitivity, Specificity, and F-Measure

Sensitivity, and specificity are commonly used statistical methods for interpreting, and explaining the results of data testing. Classification sensitivity, and specificity are determined using the equations shown below.

$$Sensitivity\ (\%) = \frac{TP}{TP + FN} x100 \quad (3)$$

Table 1. Variables of Data

Variables	Unit
Hydraulic Oil Temperature	Degree Celsius
Wind speed	m/sec
Hydraulic Unit Pressure	bar
Yaw Brake Pressure	bar
Temperature	Degree Celsius
Ambient Temperature	Degree Celsius
Production	kW
Blade Degree-1	Degree
Blade Degree-2	Degree
Blade Degree-3	Degree

Table 2. Confusion Matrix

		Predicted Values	
		Negative	Positive
Actual Values	Negative	TN (True Negative)	FP (False Positive)
	Positive	FN (False Negative)	TP (True Positive)

https://doi.org/10.26701/ems.1577643

$$\text{Specificity } (\%) = \frac{TN}{TN + FP} x100 \quad (4)$$

$$Error\ Rate\ (\%) = \frac{FN + FP}{TN + TP + FN + FP} x100 \quad (5)$$

Sensitivity: The ratio of true positives to all data predicted as positive. It measures the model's ability to correctly classify positive examples. A high sensitivity ratio indicates that there are few false negatives [13].

Specificity: The ratio of true negatives to all data predicted as negative. It measures the model's ability to correctly classify negative examples. A high specificity ratio indicates that there are few false positives [13].

F-Measure: To provide more meaningful comparative results, the F-Measure combines both sensitivity, and specificity. The F-Measure is the harmonic mean of sensitivity, and specificity [13].

$$F\ Measure = \frac{2\ x\ Sensitivity\ x\ Specificity}{Sensitivity + Specificity} \quad (6)$$

2.4. Kappa Statistics

Kappa statistics is a statistical method used to measure the agreement between classifications based on the same category. It is a more reliable measure than a simple percentage calculation. It is a robust method used to test inter-rater or intra-rater reliability. The values can range from -1 to 1, where 0 represents agreement occurring by chance, and 1 indicates perfect agreement. Details are provided in ▶Table 3 [14].

Kappa adjusts for the agreement that could have occurred randomly among similar responses.

$$\varkappa = \frac{P_0 - P_e}{1 - P_e} \quad (7)$$

P_0: The percentage of agreement between observers

P_e: The percentage of agreement between observers due to chance

Table 3. Kappa Coefficient Values Interpretation

Kappa Value	Interpretation
< 0.00	Poor
0.01 – 0.02	Slight
0.21 – 0.40	Fair
0.41 – 0.60	Moderate
0.61 – 0.80	Substantial
0.81 – 1.00	Almost Perfect

2.5. Other Approaches

Mean Absolute Error (MAE): This can be expressed as the average of the absolute differences between the actual values, and the predicted values. A low mean absolute error indicates good performance of the model [13].

$$A = \frac{1}{n}\sum_{i=1}^{n}|x_i - x'_i| \quad (8)$$

Relative Absolute Error (RAE): This is a metric used to measure the performance of a model. It is the ratio of the sum of the model's absolute errors to the sum of the deviations of the actual values from their mean. A low relative absolute error indicates good performance of the model.

$$RAE = \frac{\sum_{i=1}^{n}|x_i - x'_i|}{\sum_{i=1}^{n}|x_i - \bar{x}|} \quad (9)$$

$\bar{x}$: The mean of the actual values

x_i: The actual values

x'_i: The predicted values

n: The number of samples in the data

Root Mean Square Error (RMSE): This is a metric used to measure the performance of a model. It is the square root of the average of the squared differences between the predicted values, and the actual values [13].

$$RMSE = \sqrt{\frac{1}{n}\sum_{i=1}^{n}(x_i - x'_i)^2} \quad (10)$$

A small RMSE indicates that the model's predictions are accurate.

Root Relative Squared Error (RRSE): This metric is the square root of the ratio of the sum of the squared differences between the actual values, and the predicted values to the sum of the squared differences between the actual values, and their mean [13].

$$RRSE = \sqrt{\frac{\sum_{i=1}^{n}(x_i - x'_i)^2}{\sum_{i=1}^{n}(x_i - \bar{x}_i)^2}} \quad (11)$$

A small RRSE indicates that the model's predictions are accurate.

2.6. Model Features and Methods Implemented on WEKA

The algorithms used on the datasets include Multilayer Perceptron (MLP), Radial Basis Function Classifier (RBF Classifier), and SMOreg (Support Vector Machines for Regression). The parameter settings in the software are the default settings.

2.7. Multilayer Perceptron

The Multilayer Perceptron (MLP) identifies the relationship between linear or non-linear data. The input layers, output layers, and hidden layers form the core of the MLP classifier. In most cases, a single hidden layer is sufficient for solving the problem. However, additional hidden layers may be added to improve the results, although this will increase data processing time[12].

The input layer processes the input data, while tasks

such as prediction, and classification are handled by the output layer. In MLP, a feed-forward structure is established from input to output [15].

All nodes in the network utilize the sigmoid function, which ensures that the data remains within the range of 0 to 1.

$$sigmoid\ (x) = \frac{1}{1+e^{-x}} \tag{12}$$

2.7.1. Parameter settings in MLP

Learning Rate: Determines the speed at which the weights are updated. A high learning rate can lead to instability in the model, while a low learning rate may result in slower learning.

Momentum: Ensures more stable weight updates, and helps the model avoid local minima. A high momentum can accelerate the learning process, but it also increases the risk of instability. On the other hand, a low momentum slows down the learning process but allows for more control over the model.

Hidden Layers: Refers to the number of hidden layers, and the number of neurons in each layer. Fewer hidden layers make the model more interpretable, and reduce the risk of overfitting. However, with fewer hidden layers, the model may be insufficient for capturing non-linear relationships, making it less capable of detecting complex patterns, and reducing the likelihood of accurate predictions.

Training Time: Specifies the number of iterations required to train the model. A short training time may prevent the model from fully learning the data, while a long training time can lead to overfitting.

2.8. Radial Basis Function Classifier

The Radial Basis Function Classifier (RBFC) is a feed-forward model used in artificial neural networks. The structure of the RBFC consists of an input layer, a hidden layer, and an output layer. The input layer is where the data is collected, and the calculations take place in the hidden layer [16]. The connection weights between the hidden layer, and the output layer can be determined more quickly, and independently of local minima compared to the Multilayer Perceptron (MLP). The hidden layer utilizes a Gaussian function, and the distance between the input vector, and the center vector of the hidden layer is calculated using this function [17].

$$\varphi(x) = \exp\left(-\frac{\|x-c\|^2}{2\sigma^2}\right) \tag{13}$$

φ(x): Output

x: Input vector

c: Center vector of the RBF

σ: Standard deviation

$\|x-c\|^2$: Represents the Euclidean distance

2.8.1. Parameter settings in RBFC

Number of Functions: This parameter determines the number of Gaussian functions in the model. As the number increases, the complexity of the model also increases, which may lead to overfitting.

Scale Optimization Option: Specifies the scale optimization option. Option 1 sets a single factor for the entire model, while Option 2 assigns a separate scale for each Gaussian function.

2.9. Sequential Minimal Optimization

SMO is a machine learning algorithm associated with Support Vector Machines (SVM) available in WEKA. SVMs are used for classification, and regression problems.

2.9.1. Parameter settings in SMO

C (Complexity Parameter): Balances model flexibility, and error rate. A high C value offers a more flexible model but increases the risk of overfitting, whereas a low C value reduces the risk of overfitting but may result in more errors.

Kernel Type: Used to determine the relationship between data points. Various options are available in WEKA.

Epsilon Parameter: Represents the tolerance value between the actual value, and the predicted value. The smaller the epsilon, the more precise the model becomes.

Tolerance: Defines the tolerance used during the optimization process.

2.10. K-Fold Cross Validation in MLP, RBFC, and SMO

The dataset is divided into K parts. K-1 parts are used for training, while the remaining part is used for testing. The test set is rotated each time, ensuring that the model is trained K times [4].

The evaluations of K-fold cross-validation in this study for K=4, 10, and 24 can be seen in ▶Table 4.

2.11. Percentage-Based Data Splitting in MLP, RBFC, and SMO

The program allows the data was split into training, and test sets based on percentages. Different scenarios where 50%, 66%, and 80% of the data are allocated to the training set have been compared can be seen in ▶Table 5.

Table descriptions can be seen ▶Table 4.

3. Research Findings and Discussion

A comprehensive comparison of the program results has been conducted, and the top 3 most important pa-

rameters of the best-performing algorithm, based on the J48 decision tree, have been identified. The points where the algorithm made errors are presented as part of the program output.

The hydraulic unit oil temperature, hydraulic unit pressure, and yaw brake pressure are identified as the most important criteria, as shown in ▶**Figure 1** based on the J48 decision tree classification method.

▶**Figure 2** illustrates that the classification errors in the WEKA program indicate approximately 38 degrees, and 60 degrees as the range where predicted data for the hydraulic unit oil temperature generates errors.

▶**Figure 3** shows that the classification errors in the WEKA program indicate that the predicted data for hydraulic unit pressure generates errors within the range of approximately 162 bar to 220 bar.

▶**Figure 4** demonstrates that the yaw brake pressure predictions generate errors within the range of approximately 223 bar to 228 bar, as indicated by the classification error outputs from the WEKA program.

4. Results and Discussions

Data from the turbine SCADA system, collected between 2020, and 2022, were evaluated using artificial neural networks, and other algorithms. The algorithms employed include Multilayer Perceptron (MLP), Radial Basis Function Classifier (RBF Classifier), and SMOreg (Support Vector Machines for Regression). The parameters of the algorithms were processed using their default settings in the WEKA program. The algorithms were executed with a percentage-based data split, and K-fold cross-validation approaches. For the percentage-based data splitting, ratios of 50%, 60%, and 80% were selected, while K values of 4, 10, and 24 were chosen for the K-fold cross-validation approach, with results recorded accordingly. The results were evaluated, and compared using statistical measures such as Kappa Statistic, Mean Absolute Error, Root Mean Square Error, Relative Mean Absolute Error, and Root Relative Square Error, as well as criteria including Sensitivity, Specificity, Error Rate, and F-measure. The findings

Table 4. K-fold cross-validation in this study for K=4, 10, and 24 with MLP, RBFC, SMO

Algorithm / K Fold	Kappa	MAE	RMSE	RAE [%]	RRSE [%]	Accuracy [%]	Sensitivity [%]	Specificity [%]	Error Rate [%]	F Score [%]
MLP / K=24	0,812	0,117	0,240	23	48	90,63	91,85	89,47	9,38	90,64
MLP / K=10	0,875	0,100	0,222	20	44	93,75	94,49	93,03	6,25	93,76
MLP / K=4	0,775	0,149	0,285	29	57	88,75	88,43	89,08	11,25	88,75
RBFC / K=24	0,45	0,36	0,41	74	82	72,50	70,93	74,32	27,50	72,59
RBFC / K=10	0,51	0,36	0,4	73	81	75,63	72,36	80,00	24,38	75,99
RBFC / K=4	0,475	0,36	0,4	73	81	73,75	70,21	78,79	26,25	74,25
SMO / K=24	0,008	0,495	0,704	99	140	50,42	50,65	50,31	49,58	50,48
SMO / K=10	0,016	0,491	0,701	98	140	50,83	51,02	50,70	49,17	50,86
SMO / K=4	0,079	0,460	0,678	92	135	53,96	53,85	54,08	46,04	53,96

Kappa: Kappa statistics are a statistical method
MAE: Mean Absolute Error
RMSE: Root Mean Square Error
RAE: Relative Absolute Error
RRSE: Root Relative Squared Error
Accuracy: Correctly classified examples
Sensitivity: Measures the model's ability to correctly classify positive examples
Specificity: Measures the model's ability to correctly classify negative examples
Error Rate: Incorrectly classified examples
F-Score: Harmonic mean of sensitivity, and specificity

Table 5. Training Set Ratio in this study for 80%, 66%, and 50% with MLP, RBFC, SMO

Algorithm / Training Set Ratio	Kappa	MAE	RMSE	RAE [%]	RRSE [%]	Accuracy [%]	Sensitivity [%]	Specificity [%]	Error Rate [%]	F Score [%]
MLP / 80%	0,89	0,116	0,225	23	45	94,79	92,31	97,73	5,21	94,94
MLP / 66%	0,925	0,087	0,168	17	33	96,32	96,67	95,89	3,68	96,28
MLP / 50%	0,749	0,163	0,287	33	57	87,50	86,51	88,60	12,50	87,54
RBFC / 80%	0,62	0,343	0,383	69	77	81,25	82,98	79,59	18,75	81,25
RBFC / 66%	0,452	0,356	0,392	71	78	72,39	80,00	65,91	27,61	72,27
RBFC / 50%	0,442	0,392	0,422	78	84	72,08	73,91	70,40	27,92	72,11
SMO / 80%	0,012	0,5	0,707	99	141	50,00	52,63	49,35	50,00	50,94
SMO / 66%	0,185	0,43	0,66	86	131	56,44	85,19	50,74	43,56	63,59
SMO / 50%	0,151	0,43	0,66	85	130	57,08	73,17	53,77	42,92	61,99

https://doi.org/10.26701/ems.1577643

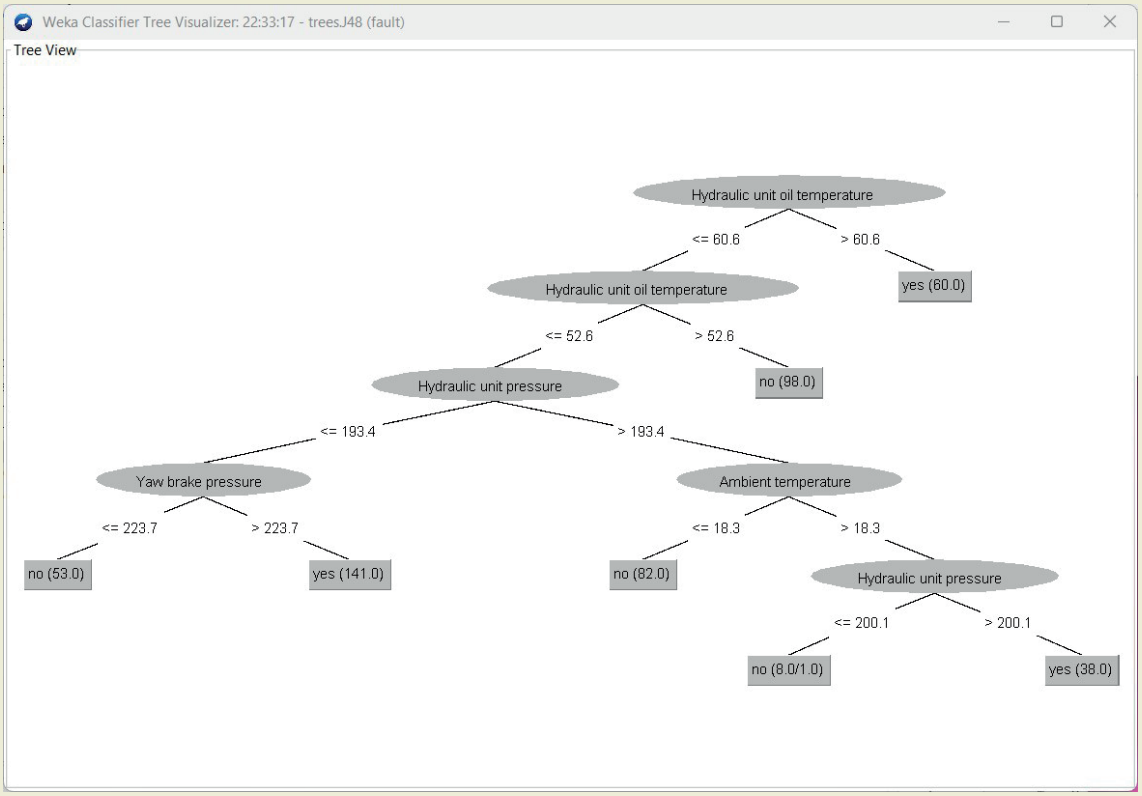

Figure 1. J48 Decision Tree

Figure 2. Relationship between Hydraulic Unit Oil Temperature, and Failure Prediction

Figure 3. Relationship between Hydraulic Unit Pressure, and Failure Prediction

Figure 4. Relationship between Yaw Brake Pressure, and Failure Prediction

indicated that the MLP algorithm, with a distribution of 66% training, and 33% testing, yielded the most successful result with an accuracy rate of 96.32%.

5. Conclusions

The uninterrupted generation of electricity is a critical issue that affects electricity market operations, production, and distribution processes. Additionally, it can lead to significant financial losses for investors. Preventive maintenance to avoid electrical outages is the most economical approach. This study aims to establish preventive maintenance activities by predicting hydraulic failures in advance.

Based on the results of this study, it is recommended to directly integrate the Multilayer Perceptron (MLP) algorithm from artificial neural networks into the SCADA system to test its success rate with real data. This would allow for continuous live reading of data, facilitating the early prediction of failures.

Additionally, forecasting downtime caused by past failures for future months could provide financial insights by establishing predictions between operational costs, and revenue.

To determine the optimal parameter values for the algorithms used in WEKA, the use of optimization algorithms is considered to achieve effective results.

Increasing the diversity, and quantity of data may help uncover different relationships within the dataset. Furthermore, by working with various decision tree algorithms, the most accurate data for failure classification is selected, and incorporated into the algorithm.

Within the scope of preventive maintenance, the failures addressed in this study is evaluated, leading to the creation of preventive activities.

By examining classification errors, the range in which the program makes the most errors identified. The causes of errors within this range will investigate.

Acknowledgments

We would like to thank Necmettin Erbakan University Scientific Research Projects Coordinator ship for supporting this study with project number 23YL19008.

Research ethics

Ethical approval not required.

Author contributions

Conceptualization: Mustafa Yağcı, Tacettin Ahmet Döndüren. Methodology: Tacettin Ahmet Döndüren. Formal Analysis: Mustafa Yağcı, Tacettin Ahmet Döndüren. Investigation: Tacettin Ahmet Döndüren, Resources: Tacettin Ahmet Döndüren. Data Curation: Tacettin Ahmet Döndüren. Writing – Original Draft Preparation: Tacettin Ahmet Döndüren. Writing – Review & Editing: Mustafa Yağcı. Visualization: Tacettin Ahmet Döndüren. Supervision: Mustafa Yağcı.

Competing interests

There is no conflict of interest. The funders had no role in the design of the study; in the collection, analyses, or interpretation of data; in the writing of the manuscript, or in the decision to publish the results.

Research funding

Not reported.

Data availability

Not applicable

Peer-review

Externally peer-reviewed.

Orcid

Tacettin Ahmet Döndüren https://orcid.org/0000-0002-4230-0330
Mustafa Yağcı https://orcid.org/0000-0002-8336-5261

References

[1] Tang, M., Zhao, Q., Wu, H., Wang, Z., Meng, C., & Wang, Y. (2021). Review and perspectives of machine learning methods for wind turbine fault diagnosis. *Frontiers in Energy Research*, 9. https://doi.org/10.3389/fenrg.2021.751066

[2] Zhang, F., Chen, M., Zhu, Y., Zhang, K., & Li, Q. (2023). A review of fault diagnosis, status prediction, and evaluation technology for wind turbines. *Energies, 16*(3). https://doi.org/10.3390/en16031125

[3] Tezer, D. (2024). *Comparison of classification success of artificial neural network factor analysis Hybrit model and artificial neural network models* (Doctoral dissertation). Osmangazi University.

[4] Korkmaz, E. (2022). *Analysis of solar radiation with artificial neural networks and machine learning: Example of Bursa and Çanakkale* (Master's thesis). Onyedi Eylul University.

[5] Sarıkaya, T. A. (2023). *FPGA based artificial neural network motor control of PM assisted synchronous reluctance motor in washers* (Master's thesis). Istanbul Technical University.

[6] Yüksel, F. Ş. (2023). *Estimation of passenger demand in Turkey according to airline carrier models using multiple linear regression, ANFIS and YSA techniques* (Doctoral dissertation). Cukurova University.

[7] Geçmez, A. (2022). *Estimation of production values in solar and wind power plants with artificial intelligence methods based on climate parameters and production estimation by developing solar energy feasibility software* (Doctoral dissertation). Fırat University.

[8] Kiriş, Z. N. (2021). *Wind speed load forecasting models and an application in Yalova* (Master's thesis). Istanbul Technical University.

[9] Shakiba, F. M. (2022). *Artificial neural networks and their applications to intelligent fault diagnosis of power transmission lines* (Order No. 28971262) [Doctoral dissertation, ProQuest Dissertations & Theses

Global].

[10] Zhang, Y., Liu, Q., Liu, W., & Zheng, W. (2022). Deployable lightweight ANN-based approach for wind turbine fault detection. In Proceedings of the *13th International Conference on Reliability, Maintainability, and Safety: Reliability and Safety of Intelligent Systems* (pp. 28–34). https://doi.org/10.1109/ICRMS55680.2022.9944585

[11] Bangalore, P., & Tjernberg, L. B. (2015). An artificial neural network approach for early fault detection of gearbox bearings. I*EEE Transactions on Smart Grid, 6*(2), 980–987. https://doi.org/10.1109/TSG.2014.2386305

[12] Samawi, V. W., Yousif, S. A., & Al-Saidi, N. M. G. (2022). Intrusion detection system: An automatic machine learning algorithms using Auto-WEKA. In *Proceedings of the 2022* IEEE *13th Control and System Graduate Research Colloquium* (pp. 42–46). https://doi.org/10.1109/ICSGRC55096.2022.9845166

[13] Işık, M. A. (2024). *Ranking of machine learning algorithms used to detect bug-containing software modules with multi-criteria decision making methods* (Master's thesis). Baskent University.

[14] Syahrini, Z., Priyadi, Y., & Herdiani, A. (2023). Validity of cosine similarity measurement of functional requirements and steps performed using Cohen Kappa on SRS scenery artifacts. In *Proceedings of the International Conference on Electrical Engineering, Computer Science and Informatics* (pp. 631–636). https://doi.org/10.1109/EECSI59885.2023.10295586

[15] Femi, D., & Thylashri, S. (2022). Human voice emotion recognition using multilayer perceptron. In *Proceedings of the 2022 International Conference on Innovative Computing, Intelligent Communication and Smart Electrical Systems* (pp. 1–6). https://doi.org/10.1109/ICSES55317.2022.9914335

[16] Aryan, B.K., Sobhana, O., Prabhakar, G.C., & Reddy, N.A.(2022). Fault detection and classification in micro grid using AI technique.In *Proceedings - 2022 International Conference on Recent Trends in Microelectronics Automation Computing and Communications Systems* (pp517-522) https://doi.org/10..1109/ICMACC54824..10093359

[17] Fu, X., & Wang, L. (2003). Data Dimensionality Reduction with Application to Simplifying RBF Network Structure and Improving Classification Performance. *IEEE Transactions on Systems, Man, and Cybernetics, Part B: Cybernetics, 33*(3), 399–409. https://doi.org/10.1109/TSMCB.2003.810911